

**3D-MODELING OF UNSATURATED
FLOW DYNAMICS AND PATTERNS**

**POTENTIALS AND LIMITATIONS AT DIFFERENT
SPATIAL AND TEMPORAL SCALES**

Dissertation

zur Erlangung des Doktorgrades (Dr. rer. nat.)

der

Mathematisch-Naturwissenschaftlichen Fakultät

der

Rheinischen Friedrich-Wilhelms-Universität Bonn

vorgelegt von

Thomas Daniel Cornelissen

aus

Köln

Bonn, November 2015

Angefertigt mit Genehmigung der Mathematisch-Naturwissenschaftlichen Fakultät der
Rheinischen Friedrich-Wilhelms-Universität Bonn

1. Gutachter: Prof. Dr. Bernd Dieckrüger
2. Gutachter: Prof. Dr. Clemens Simmer
Datum der Promotion: 11. April 2016
Erscheinungsjahr: 2016

Danksagung

An dieser Stelle möchte ich mich bei allen bedanken, die diese Arbeit möglich gemacht haben.

Ich möchte mich ganz herzlich bei Prof. Bernd Diekkrüger für seine umfassende Betreuung und seine unermüdliche Hilfsbereitschaft bedanken. Ganz besonderer Dank gilt auch Dr. Heye Bogena für die Bereitstellung der Bodenfeuchtedaten. Für die konzeptionelle Unterstützung meiner Arbeit möchte ich mich bei Dr. Heye Bogena, Prof. Clemens Simmer, Dr. Matthieu Masbou und Dr. Wolfgang Korres bedanken. Bedanken möchte ich mich außerdem bei Prof. René Therrien, Prof. Rob McLaren und Dr. Daniel Partington für ihre umfassende und geduldige Beantwortung meiner Fragen zum Modell HydroGeoSphere sowie für die Behebung von Modellfehlern.

Ebenso herzlich danke ich den Mitgliedern der „Hydrology Research Group“, insbesondere Nicolas Hagemann, Ann-Christine Hartmann, Britta Höllermann, Thomas Jütten, Jenny Kebschull, Constanze Leemhuis, Kristian Näschen und Inken Rabbel für ihre Hilfsbereitschaft und Aufmunterung.

Gleichermaßen bedanken möchte ich mich auch bei meiner Familie und den Freunden unserer Familie, Herrn Dr. Winter und Frau Winter, für ihre häufigen Ermutigungen.

Abstract

The aim of this thesis was to evaluate the suitability of the physically based, distributed 3D hydrological model HydroGeoSphere for the simulation of spatio-temporal soil moisture variability as well as unsaturated flow processes and to investigate the models' applicability at large spatial and temporal scales.

To achieve these aims, hydrological simulations of a forested headwater catchment in the Eifel region were used to evaluate the suitability of the model. The headwater catchment offered not only site specific measurement of discharge, evapotranspiration and interception, but the instrumentation in the catchment also provided the unique possibility to compare simulated to continuously measured soil moisture variability for two years. As model results heavily depend on the chosen spatial and temporal model resolution, the catchment was simulated at 2 different spatial and 2 different temporal discretizations.

All simulations showed a satisfactory agreement to annual water balance components and discharge dynamics. A dominance of subsurface flow was also simulated for every simulation which corresponds to previous findings in forested catchments. The quality of simulated soil moisture variability exhibited large variations between the temporal dynamics and spatial patterns. Dynamics were well simulated, but the simulation missed short term variations probably due to a lack of bypass flow in the model structure. On the contrary, simulated and measured soil moisture patterns showed large differences indicating a simplified representation of spatial heterogeneity in the model. Simulation of flow processes and water balance components only showed a weak sensitivity to spatial or temporal resolution while higher spatial resolution was identified as an important factor in the successful simulation of soil moisture patterns.

The potential of using the model at larger spatial and temporal scales was tested with simulations at a mesoscale catchment including the above described headwater catchment. The challenge of simulating large catchments refers to the incorporation of spatial variability in climate and land use, especially the land use specific parameter estimation. With a step-wise introduction of spatial heterogeneity in soil, land use, potential evapotranspiration and precipitation into the simulation, the precipitation pattern was identified as the most and the potential evapotranspiration pattern as the least important for discharge simulation.

The land use specific parameter estimation was done by transferring calibrated evapotranspiration parameters from the headwater catchment to the land use of the mesoscale catchment. This method results in very good agreement of annual and monthly simulated actual evapotranspiration rates to measured data and literature values. Thus, this thesis introduced the

transfer of model parameters from smaller to larger catchment as a promising method of parameter estimation of large catchments.

Additional model validation was performed with a 50 years simulation run of forest growth for the mesoscale catchment. Results showed that the model is able to maintain a balance between inputs (precipitation) and outputs (discharge, evapotranspiration) over several decades and that it provides reasonable simulation of discharge dynamics for this time period.

Zusammenfassung

Ziel dieser Arbeit war es, die Eignung des physikalisch basierten und dreidimensionalen hydrologischen Modells HydroGeoSphere für die Simulation räumlicher und zeitlicher Bodenfeuchtevariabilität und ungesättigter Fließbewegungen zu bewerten sowie Möglichkeiten einer Modellanwendung auf großen Raum- und Zeitskalen zu ergründen.

Bewertungsgrundlage sind hydrologische Simulationen eines bewaldeten Quellgebietes der Eifel, das, neben Messungen des Abflusses, der Evapotranspiration und der Interzeption, die seltene Möglichkeit bot, simulierte Bodenfeuchtevariabilität mit mehrjährigen Messdaten zu vergleichen. Da Modellierungsergebnisse stark von der räumlichen und zeitlichen Modellauflösung abhängen, wurde das Einzugsgebiet mit jeweils 2 unterschiedlichen räumlichen und zeitlichen Diskretisierungen simuliert.

Alle Simulationen ergaben eine gute Übereinstimmung mit jährlichen Wasserbilanzkomponenten sowie der Abflussdynamik und zeigten auch eine Dominanz unterirdischer Abflussprozesse, die schon in vielen Studien in bewaldeten Einzugsgebieten nachgewiesen wurde. Die Qualität der simulierten Bodenfeuchtevariabilität zeigte starke Unterschiede zwischen der zeitlichen Dynamik und den räumlichen Mustern. Während die Dynamik bis auf kurzfristige Schwankungen, die auf das Fehlen von präferentiellen Fließbewegungen in der Modellstruktur zurückzuführen sind, zufriedenstellend simuliert wurde, wies die schlechte Übereinstimmung von simulierten und gemessenen Bodenfeuchtemustern jedoch auf eine vereinfachte Repräsentation räumlicher Heterogenität hin. Die Simulation der Fließprozesse und Wasserbilanzkomponenten wurde nur schwach von der zeitlichen und räumlichen Auflösung beeinflusst. Jedoch konnte eine höhere räumliche Auflösung als wichtiger Einflussfaktor bei der Simulation der Bodenfeuchtemuster beobachtet werden.

Die Möglichkeiten einer Modellanwendung auf großen Raum- und Zeitskalen wurden mit Hilfe der Simulationen eines mesoskaligen Einzugsgebietes, in das das oben beschriebene Quellgebiet entwässert, untersucht. Die Herausforderungen der Simulation großer Einzugsgebiete liegen in der Berücksichtigung der räumlichen Variabilität des Klimas und der Landnutzung, insbesondere der landnutzungsspezifischen Modellparametrisierung. Mit schrittweiser Einführung von Heterogenitäten des Bodens, der Landnutzung, der potentiellen Evapotranspiration und des Niederschlags in das Modell konnte die räumliche Niederschlagsvariabilität als wichtigste und die Variabilität der potentiellen Evapotranspiration als unwichtigste Eingangsgröße für die Abflusssimulation identifiziert werden.

Bei der Parametrisierung der verschiedenen Landnutzungen des mesoskaligen Gebietes wurden die kalibrierten Verdunstungsparameter des Quellgebietes auf die Landnutzungen des größeren Einzugsgebietes übertragen. Diese Methode lieferte sehr gute Übereinstimmungen der

simulierten monatlichen und jährlichen Verdunstungswerte mit gemessenen Daten und Literaturwerten. Damit konnte diese Arbeit den Transfer von kalibrierten Modellparametern als vielversprechende Methode zur Parametrisierung mesoskaliger Einzugsgebiete aufzeigen.

Darüber hinaus wurde das Modell an Hand eines 50-jährigen Simulationslaufes, der das Forstwachstum des mesoskaligen Einzugsgebietes simuliert, validiert. Das Modell ist demnach in der Lage, eine Balance zwischen der Inputgröße Niederschlag und den Outputgrößen Abfluss und Evapotranspiration über mehrere Dekaden zu gewährleisten und außerdem die Abflussdynamik in zufriedenstellender Weise wiederzugeben.

Table of Contents

Danksagung.....	3
Abstract.....	5
Zusammenfassung.....	7
Table of Contents	9
Figures.....	11
Tables.....	16
Equations	17
Abbreviations	18
Equation Notations.....	19
1 Motivation and outline.....	22
2 Hydrological Processes in Forested Catchments	26
2.1 General hydrology.....	26
2.2 Relevance of soil moisture	31
3 Hydrological Modeling of Forested Catchments	33
3.1 General overview about hydrological modeling.....	33
3.2 Treatment of subsurface flow in physically based models: Richards' equation	36
3.3 Parameter estimation for hydrological models.....	37
3.4 Measures of model performance.....	40
4 Spatial and temporal scales in hydrological modeling.....	42
5 Quantification of spatial patterns.....	48
6 Study areas "Erkensruhr" and "Wüstebach"	54
6.1 Catchment description	54
6.2 Data base and data processing.....	56
6.2.1 Land use in the Erkensruhr and the Wüstebach catchment.....	56
6.2.2 Climate and precipitation data.....	58
6.2.3 The Wüstebach measurement network	70
6.2.4 Discharge data.....	73
6.2.5 Soil Data	75
7 Model setup with HydroGeoSphere	79
7.1 Model description	79
7.2 Spatial and temporal discretization.....	88
7.3 Parameterization and calibration	91
7.3.1 Land use	91

7.3.2	Soil.....	95
7.3.3	Hydrological parameters	97
7.3.4	Calibration and validation	98
7.4	Simulation procedure.....	99
7.5	Application of Variogram and Kriging methods.....	104
8	Results and Discussions	105
8.1	Sensitivity analysis.....	105
8.2	Wüstebach	113
8.2.1	Influence of spatio-temporal resolution and of bedrock inclusion on water balance and discharge simulation	113
8.2.2	Influence of spatial resolution and of bedrock inclusion on temporal and spatial soil moisture variability at daily time steps.....	118
8.2.3	Influence of calibration period on water balance and soil moisture dynamics	136
8.2.4	Event scale soil moisture hysteresis	139
8.3	Erkensruhr.....	144
8.3.1	Influence of mesoscale soil and land use parameters on the simulation of the headwater catchment	144
8.3.2	Influence of parameter regionalization and spatially distributed input data on the simulation of the mesoscale catchment.....	151
8.3.3	Influence of HydroGeoSphere version on water balance and soil moisture results at the Wüstebach and the Erkensruhr	157
8.4	Long-term Simulation.....	163
9	Conclusion and Outlook	172
10	Bibliography	175

Figures

Figure 2.1: Hydrological processes at an idealized hillslope. Redrawn from Bronstert (1994).....	26
Figure 2.2: Conceptualized illustration of hillslope runoff response induced by bypass flow. Abbreviations t_0 and t_1 indicate the location of the water before rainfall (t_0) and during/after rainfall (t_1). Redrawn from Anderson and Brooks (1996).	28
Figure 4.1: Characteristic time and length of hydrological processes (Blöschl and Sivapalan, 1995)...	43
Figure 4.2: Spatial and temporal properties of processes and patterns. Top: Definition according to Blöschl and Sivapalan (1995): a) Extent, b) Period, c) Correlation Length; Bottom: Scale triplet of Western et al. (2002): a) Extent, b) Spacing, c) Support.	44
Figure 5.1: Illustration of variogram features: sill variance, nugget variance and range.	49
Figure 5.2: Illustration of spherical, Gaussian and exponential theoretical variogram models with sill and effective range value.	50
Figure 5.3: Parameters required for calculating the experimental variogram (adapted after Deutsch and Journel, 1998).....	51
Figure 6.1: Location of the Erkenruhr catchment (top left), distribution of land use classes (top) and topography at 10x10 m resolution (bottom).....	55
Figure 6.2: Land use distribution in the Erkenruhr catchment at a 100x100 m resolution in 2008 and 2012.	58
Figure 6.3: Location and topographic situation of climate stations near the Erkenruhr catchment...	59
Figure 6.4: Daily actual evapotranspiration measured at the Wüstebach catchment between May 2010 and April 2013.	63
Figure 6.5: Comparison between measured and simulated snow storage for the winter periods between end of 2009 and end of 2011.	63
Figure 6.6: Mean annual precipitation between 2006 and 2012 for 5 stations in the Erkenruhr catchment.	64
Figure 6.7: Location of climate stations with annual precipitation sum and pattern of annual precipitation as measured with the radar data of 1x1 km resolution by the Wasserverband Eifel-Rur.	66
Figure 6.8: Mean annual temperatures between 2005 and 2012 at 6 stations in the Erkenruhr catchment. Stations are sorted from the highest (Schleiden) to the lowest (Rurberg) elevation.	67
Figure 6.9: Linear regression between elevation and temperature line calculated with (top) and without (bottom) the station Kalterherberg (Meteomedia).	68
Figure 6.10: Measurement Location of the SoilNet, the Gauging Station and the Eddy-Covariance Tower at the Wüstebach test site. The measurement locations of the interception network are equal to those of the SoilNet.	71
Figure 6.11: Observed mean daily soil moisture dynamics for 2010 and 2011 in 5, 20 and 50 cm depth.....	72
Figure 6.12: Observed weekly precipitation values for 2011 and 2012.	72
Figure 6.13: Measured discharge curve at the Wüstebach and Erkenruhr outlets between 2008 and 2012.	74
Figure 6.14: Soil Type distribution of the Wüstebach test site.....	75
Figure 6.15: Influence of aggregation and of discretization on the soil type distribution in the Erkenruhr catchment.....	78
Figure 7.1: Illustration of the water content-pressure head and hydraulic conductivity-pressure head relationships calculated with $\alpha=0.0217$ (1/cm), $n=1.3366$, $\theta_r=0.0344$ and $\theta_s=0.2833$	80

Figure 7.2: Illustration of the non-linear relationship between soil moisture and transpiration as calculated with Equation 18.	83
Figure 7.3: Normalized root depth functions implemented in HydroGeoSphere.....	83
Figure 7.4: Overview about processes of different complexity implemented in HydroGeoSphere and their solution technique.	85
Figure 7.5: Illustration of node connections in the (a) finite element and (b) finite difference method (redrawn after Panday et al. 1993).	85
Figure 7.6: Illustration of the horizontal (top) and vertical (bottom) spatial discretization of the Wüstebach test site at 25 m (left) and 100 m (right) resolution. Numbers refer to different layers of the bedrock model setup.	89
Figure 7.7: Illustration of the horizontal spatial discretization with river network and outlet of the Erkensruhr catchment.	91
Figure 7.8: Mean monthly LAI for the three land use classes “crops, deciduous broadleaf forest and grassland” derived from MODIS data.	92
Figure 7.9: Comparison between empirically derived root extraction functions (r_r) for deciduous forest and extensive grassland with standard HydroGeoSphere root distribution functions.....	94
Figure 7.10: Minimum, maximum and mean annual LAI used for the long-term simulation study of forest growth in the Erkensruhr catchment (Hammel and Kennel, 2001).The mean LAI of 2.73 is highlighted with a black circle.	94
Figure 7.11: Illustration of the pressure-saturation curve for three example soil types from the Wüstebach catchment.	96
Figure 8.1: Maximum and minimum deviations of water balance components and run time from the mean of 31 simulations with equal parameter values. The figure expresses the sensitivity to the numerical solution procedure.	105
Figure 8.2: Sensitivity of water balance components to parameter change of $\pm 10\%$ (top) and $\pm 50\%$ (bottom) at 25 m resolution. Symbol size refers to relative changes in water balance components compared to the reference simulation. Filled circles indicate a decrease, “Plus” symbols an increase in water balance component due to a positive (green color) or negative parameter change (red color). Abbreviations: Spec. Stor. =Specific Storage; C.L. =Coupling Length; Obs.-Stor = Obstruction-Storage Length; Rill-Stor. =Rill-Storage Length; Overl. =Overland; Conv.=Convergence; Iter.= Iterations; Canopy Stor.=Canopy Storage.	107
Figure 8.3: Sensitivity of water balance components to parameter change of $\pm 10\%$ (top) and $\pm 50\%$ (bottom) at 100 m resolution. Symbol size refers to relative changes in water balance components compared to the reference simulation. Filled circles indicate a decrease, “Plus” symbols an increase in water balance component due to a positive (green color) or negative parameter change (red color). Abbreviations: Spec. Stor. =Specific Storage; C.L. =Coupling Length; Obs.-Stor = Obstruction-Storage Length; Rill-Stor. =Rill-Storage Length; Overl. =Overland; Conv.=Convergence; Iter.= Iterations; Canopy Stor.=Canopy Storage.	108
Figure 8.4: Sensitivity of the annual mean and coefficient of variation (CV) of soil moisture (SM) and its standard deviation (STD) in 5, 20 and 50 cm depth and the coefficient of variation (CV) of discharge (Q) to parameter change of $\pm 10\%$ (top) and $\pm 50\%$ (bottom) at 25 m resolution. Symbol size refers to relative changes in water balance components compared to the reference simulation. Filled circles indicate a decrease, “Plus” symbols an increase in water balance component due to a positive (green color) or negative parameter change (red color). Abbreviations: Spec. Stor. =Specific Storage; C.L. =Coupling Length; Obs.-Stor = Obstruction-Storage Length; Rill-Stor. =Rill-Storage Length; Overl. =Overland; Conv.=Convergence; Iter.= Iterations; Canopy Stor.=Canopy Storage.	111

Figure 8.5: Sensitivity of the annual mean and coefficient of variation (CV) of soil moisture (SM) and its standard deviation (STD) in 5, 20 and 50 cm depth and the coefficient of variation (CV) of discharge (Q) to parameter change of $\pm 10\%$ (top) and $\pm 50\%$ (bottom) at 100 m resolution. Symbol size refers to relative changes in water balance components compared to the reference simulation. Filled circles indicate a decrease, “Plus” symbols an increase in water balance component due to a positive (green color) or negative parameter change (red color). Abbreviations: Spec. Stor. =Specific Storage; C.L. =Coupling Length; Obs.-Stor = Obstruction-Storage Length; Rill-Stor. =Rill-Storage Length; Overl. =Overland; Conv.=Convergence; Iter.= Iterations; Canopy Stor.=Canopy Storage.....112

Figure 8.6: a: Observed and simulated total discharge and simulated baseflow for non-bedrock setup at 25 m resolution for daily time steps. b: Difference between non-bedrock setup at 25 m and 100 m resolution. Positive values indicate larger discharges at 25 m resolution. c: Difference between non-bedrock setup at 25 m resolution on daily and hourly time step. Positive values indicate larger discharges on daily resolution.....114

Figure 8.7: a: Difference in discharge between non-bedrock and bedrock setup at 25 m on hourly time steps. Discharges at hourly time steps were aggregated to daily time steps. Positive values indicate larger discharges for non-bedrock. b: Difference between 25 m and 100 m resolution for bedrock setup. Positive values indicate larger discharges at 25 m resolution. c: Difference between daily and hourly time step for the bedrock setup at 25 m resolution. Positive values indicate larger discharges on daily resolution.....117

Figure 8.8: Upper part: Observed and simulated daily soil moisture dynamics at 25 m resolution for non-bedrock setup. Lower part: Difference between non-bedrock and bedrock setup at 25 m resolution. Positive values indicate larger soil moistures of the non-bedrock setup at 25 m resolution.119

Figure 8.9: Relationship between mean soil moisture and its standard deviation in the topsoil for both model resolutions and both model setups compared with the measured soil moisture data at 5 cm (top), 20 cm (middle) and 50 cm (bottom). Beware of the different x- and y-axis limits in the bottom part of the figure!121

Figure 8.10: Relationship between mean soil moisture (SM) and its standard deviation (STD) at 50 cm depth for the d25 setup. The relationship is classified in six categories according to the temporal evolution of soil moisture and standard deviation.....122

Figure 8.11: Variograms of measured (top row) and simulated soil moisture (second to last row) at the wettest (left column) and driest (right column) day in 5 cm depth. Variograms correspond to soil moisture patterns shown in Figure 8.14 and Figure 8.15.125

Figure 8.12: Variograms of measured (top row) and simulated soil moisture (second to last row) at the wettest (left column) and driest (right column) day in 20 cm depth. Variograms correspond to soil moisture patterns shown in Figure 8.16 and Figure 8.17.126

Figure 8.13: Variograms of measured (top row) and simulated soil moisture (second to last row) at the wettest (left column) and driest (right column) day in 50 cm depth. Variograms correspond to soil moisture patterns shown in Figure 8.18 and Figure 8.19.127

Figure 8.14: Spatial distribution of absolute soil moisture (vol. %) at 5 cm depth on 13.1.2011 for measured (top) and simulated data for 25 m (left) and 100 m (right) resolutions. The values in brackets refer to the mean standard deviation of the kriging algorithm.129

Figure 8.15: Spatial distribution of absolute soil moisture (vol. %) at 5 cm depth on 30.5.2011 for measured (top) and simulated data for 25 m (left) and 100 m (right) resolutions. The values in brackets refer to the mean standard deviation of the kriging algorithm.129

Figure 8.16: Spatial distribution of absolute soil moisture (vol. %) at 20 cm depth on 13.1.2011 for measured (top) and simulated data for 25 m (left) and 100 m (right) resolutions. The values in brackets refer to the mean standard deviation of the kriging algorithm.	130
Figure 8.17: Spatial distribution of absolute soil moisture (vol. %) at 20 cm depth on 30.5.2011 for measured (top) and simulated data for 25 m (left) and 100 m (right) resolutions. The values in brackets refer to the mean standard deviation of the kriging algorithm.	130
Figure 8.18: Spatial distribution of absolute soil moisture (vol. %) at 50 cm depth on 13.1.2011 for measured (top) and simulated data for 25 m (left) and 100 m (right) resolutions. The values in brackets refer to the mean standard deviation of the kriging algorithm.	131
Figure 8.19: Spatial distribution of absolute soil moisture (vol. %) at 50 cm depth on 30.5.2011 for measured (top) and simulated data for 25 m (left) and 100 m (right) resolutions. The values in brackets refer to the mean standard deviation of the kriging algorithm.	131
Figure 8.20: Upper part: Observed and simulated daily soil moisture dynamics calibrated for the year 2011. Lower part: Comparison between simulated soil moisture for the two different calibration periods 2010 and 2011.	138
Figure 8.21: Hysteresis reaction after a convective rainfall at the intermediate soil moisture state between 10.7.2010 and 11.7.2010. Top part shows precipitation, center part soil moisture and standard deviation development, bottom part the soil moisture-to-standard deviation relationship for measured and simulated data.	142
Figure 8.22: Hysteresis reaction after an advective rainfall at the dry soil moisture state between 31.5.2011 and 4.6.2011. Top part shows precipitation, center part the soil moisture and standard deviation development, bottom part the soil moisture-to-standard deviation relationship for measured and simulated data.	143
Figure 8.23: Top: Comparison of observed and simulated discharge of the Wüstebach for simulations with high-resolution soil data (Wbach) and low-resolution soil data (WbachEsoilConi). Middle: Discharge difference between simulations with changing land use. Bottom: Discharge difference between simulations with changing land use and soil data.	145
Figure 8.24: Bias (black line), coefficient of variation (CV; green line) and correlation coefficient (red line) in hydrological summer (solid lines) and winter (dashed lines) for the Wüstebach discharge simulations.	146
Figure 8.25: Soil moisture dynamics of the Wüstebach simulations at 20 cm depth.	148
Figure 8.26: Relationship between mean soil moisture and its standard deviation for Wüstebach simulations at 5 cm depth with (top) Wüstebach and (bottom) Erkensruhr soil data.	149
Figure 8.27: Observed and simulated discharge of the Erkensruhr for simulations with heterogeneous soil (Erk), heterogeneous soil and land use (Erk_LN), heterogeneous soil, land use and potential evapotranspiration (Erk_LN_PET).	152
Figure 8.28: Observed and simulated discharge of the Erkensruhr for simulations with homogeneous (Erk_LN_PET) and distributed precipitation (Erk_LN_PET_P).	152
Figure 8.29: Bias (black line), coefficient of variation (CV; green line) and correlation coefficient (red line) in hydrological summer (solid lines) and winter (dashed lines) for the Erkensruhr discharge simulations.	153
Figure 8.30: Measured and simulated mean monthly fraction of evapotranspiration rates for (A) coniferous, (B) grassland and (C) deciduous vegetation. Measured data refer to (A) eddy-covariance data from Graf et al. (2014), (B) eddy-covariance data from Schmidt (personal communication) and (C) mean monthly data from a low mountain catchment in northern Germany between 1969-1972 with a mean rainfall of 1066 mm (Mendel, 2000).	155

Figure 8.31: Pattern of actual evapotranspiration (ET) for simulations Erk (top left), Erk_LN (top right), Erk_LN_PET (bottom left) and Erk_LN_PET_P (bottom right). Evapotranspiration is given relative to the maximum of the actual evapotranspiration sums of 2010 and 2011 as specified in the brackets.	157
Figure 8.32: Comparison of measured and simulated discharge rates at the Wüstebach catchment with two different model versions.	158
Figure 8.33: Upper part: Observed and simulated daily soil moisture dynamics with the new HydroGeoSphere version. Lower part: Comparison between soil moisture simulated with two different versions.	159
Figure 8.34: Observed and simulated discharge of the Erkensruhr for simulations with the old and new HydroGeoSphere model version.....	161
Figure 8.35: Observed and simulated total discharge of the Erk setup for different climate inputs. .	164
Figure 8.36: Observed and simulated total discharge of the WbachEsoilConi setup for different climate inputs.....	165
Figure 8.37: Annual fractions of interception between 1951 and 2000 calculated with HydroGeoSphere (black line), the equation given in the model manual (blue line), the equation given in Panday & Huyakorn (2004) with a canopy storage of 0.8 mm (solid red line) and 0.45 mm (dashed red line) and mean LAI (grey line).	166
Figure 8.38: Simulated Water balance components per 5-year period of the 50-year simulation with the WbachEsoilConi setup. Error bars indicate maximum and minimum values during a five-year period.....	167
Figure 8.39: Actual evapotranspiration components and mean LAI per 5-year period between 1951 and 2000. Error bars indicate maximum and minimum values during a five-year period.....	168
Figure 8.40: Simulated water balance components and measured discharge amount between 1970 and 1973.	169
Figure 8.41: Comparison of upscaled simulated discharge to measured discharge amount between 1961 and 2000.....	170

Tables

Table 6.1: Proportional coverage of land use classes in 2008 and 2012 at 15x15 m and 100x100 m resolution.	56
Table 6.2: Percentual distribution of land use classes of the gridded input data and of the HydroGeoSphere simulation grid.	57
Table 6.3: Summary of available climate and precipitation data for the Erkensruhr catchment.	60
Table 6.4: Measured annual discharge, precipitation, actual and potential evapotranspiration sums between 2010 and 2012 for the Wüstebach catchment.	61
Table 6.5: Land use fraction per altitude layer and computed mean albedos per altitude layer.	69
Table 6.6: Annual sums of potential evapotranspiration per altitude layer between 1 st July 2009 and 2012 and area fraction per altitude layer.	70
Table 6.7: Amount of target and credit hours and their residual at the Wüstebach outlet.	73
Table 6.8: Area weighted mean values of characteristic soil properties for the three top layers in the Wüstebach catchment.	76
Table 6.9: Mean values of characteristic soil properties for the two top layers in the Erkensruhr catchment.	77
Table 6.10: Area fraction of original vectorized soil data and area fraction of soil types in the model.	78
Table 7.1: Summary of used parameters for the Erkensruhr simulation study.	93
Table 7.2: Area weighted mean values of van-Genuchten parameters for the top two soil layers in the Wüstebach catchment (θ_s =porosity, θ_r =residual saturation, α and n being fitting parameters).	95
Table 7.3: Area weighted mean values of van-Genuchten parameters for the top two soil layers in the Erkensruhr catchment (θ_s =porosity, θ_r =residual saturation, α and n being fitting parameters).	97
Table 7.4: Parameters chosen for channel and surface flow. Parameter explanations can be found in chapter 7.1.	97
Table 7.5: Overview about parameters and corresponding change per simulation run considered in the sensitivity analysis.	100
Table 7.6: Spatio-temporal resolution, applied soil and land use and abbreviation of simulations.	102
Table 8.1: Measured and simulated water balance components for the calibration (2010) and the validation period (2011) for all model setups.	116
Table 8.2: Calibrated parameters at 25 m and 100 m resolutions for daily and hourly time steps.	119
Table 8.3: Mean, minimum, maximum and standard deviation of range and sill values for simulated and measured soil moistures at 5, 20 and 50 cm depth. Green and red colors highlight increases and decreases in range or sill between 5 to 20 cm depth and 20 to 50 cm depth by $\geq 10\%$	124
Table 8.4: Kappa location, Kappa histogram and combined Kappa values for simulated and measured soil moistures at 5, 20 and 50 cm depth. Green and red colors highlight increases and decreases between 5 to 20 cm depth and 20 to 50 cm depth by $\geq 10\%$	132
Table 8.5: Mean Spearman coefficients among topographic variables, porosity distributions and soil moisture patterns. Values in bold are significant at an alpha of 0.05. Green and red colors highlight increases and decreases between 5 to 20 cm depth and 20 to 50 cm depth by $\geq 10\%$	135
Table 8.6: Measured and simulated water balance components in 2010 and 2011 for two simulations with different calibration periods.	136
Table 8.7: Measures of soil moisture simulation performance at 5, 20 and 50 cm depth for two simulations with different calibration periods.	137
Table 8.8: Calibrated parameters for two simulations with different calibration periods.	137

Table 8.9: Changes in simulated and measured soil moisture and standard deviation during four rainfall events with different rainfall characteristics and soil moisture contents.....	139
Table 8.10: Water balance components for Wüstebach simulations.....	147
Table 8.11: Water balance components for simulations of the Erkensruhr catchment.	154
Table 8.12: Measured and simulated water balance components at the Wüstebach in 2010 and 2011 for two simulations with different model versions.	160
Table 8.13: Measures of soil moisture simulation performance at 5, 20 and 50 cm depth for two simulations with different model versions.	160
Table 8.14: Water balance components for the Erkensruhr in simulations with the old and new HydroGeoSphere model version.	162
Table 8.15: Measured and simulated water balance components for simulations of the Wüstebach and the Erkensruhr with new and original climate data for 2010 and 2011.	164

Equations

Equation 1: Water balance.....	26
Equation 2: Darcy’s law.....	36
Equation 3: Components of the hydraulic conductivity.....	37
Equation 4: Richards’ equation.....	37
Equation 5: Percent Bias.....	41
Equation 6: Bias.....	41
Equation 7: Coefficient of Variation.....	41
Equation 8: Semivariance.....	48
Equation 9: Relation between semivariance and covariance.....	49
Equation 10: Potential Evapotranspiration.....	68
Equation 11: Richards’ equation: model notation.....	79
Equation 12: Mualem parameterization of unsaturated conductivity.....	80
Equation 13: Van Genuchten parameterization of pressure head – water content relation.....	80
Equation 14: Coupling term for dual node approach.....	81
Equation 15: Saint Venant equation for surface flow.....	81
Equation 16: Transpiration rate.....	82
Equation 17: Dependency of Transpiration on LAI.....	82
Equation 18: Dependency of Transpiration on water content.....	82
Equation 19: Root distribution function.....	83
Equation 20: Surface Evaporation.....	84
Equation 21: Dependency of Evaporation on water content.....	84
Equation 22: Discretized Richards’ equation.....	86
Equation 23: Newton-Raphson method: one-dimensional.....	86
Equation 24: Newton-Raphson method: multidimensional.....	87
Equation 25: Decomposition of Jacobi Matrix.....	87
Equation 26: Calibration.....	98

Abbreviations

CV	Coefficient of V ariation
DEM	D igital E levation M odel
DREAM	D ifferential E volution A daptive M etropolis Algorithm
DWD	D eutscher W etter d ienst
EOF	E mpirical O rthogonal F unctions
FAO	F ood and A griculture O rganization of the United Nations
GLUE	G eneralized L ikelihood U ncertainty E stimation
HBV	H ydrologiska B yråns V attenavdelning
LAI	L eaf A rea I ndex
LU decomposition	L ower U pper decomposition
LWF-Brook 90	Version of the B rook 90 Model by the Bayerische Landesanstalt für W ald- und F orstwirtschaft
MODIS	M oderate R esolution I maging S pectroradiometer
NSE	N ash- S utcliffe- E fficiency
ParFlow-CLM	P arallel F low coupled to C ommon L and M odel
PBIAS	P ercent B ias
r	Correlation Coefficient
R ²	Coefficient of Determination
RMSE	R oot M ean S quare E rror
SWAT	S oil W ater A ssessment T ool
TERENO	T errestrial E nvironmental Observatories
TR32	T ransregional Collaborative R esearch Center 32
WaSiM	W ater F low and B alance S imulation M odel
WASMOD	W ater A nd S now balance M odeling system
WVER	W asserverband E ifel- R ur

Equation Notations

Unit

P	precipitation	[L/T]
Q	discharge	[L/T]
ET	evapotranspiration	[L/T]
ΔS	storage change	[L/T]
q	flow through specified area	[L/T]
h	hydraulic head (sum of elevation and pressure head)	[L]
l	flow distance	[L]
K	hydraulic conductivity	[L/T]
K_s	saturated conductivity	[L/T]
K_r	relative conductivity	[-]
θ	water content	[-]
t	time	[T]
∇	nabla operator	[1/L]
ψ	pressure head	[L]
z	elevation	[L]
N	total number of values	[-]
i,j	value indices (i.e. number of observed discharge values)	[-]
μ	mean	[input unit]
σ	standard deviation	[input unit]
γ	semivariance	[squared input unit]
X,x	a variable and a value of the variable X	[input unit]
u	location	[-]
σ^2	variance	[squared input unit]
g	lag distance	[L]
C	covariance	[squared input unit]
PET	potential evapotranspiration	[L/T]
R_n	net radiation	[MJ/L ² *T]

G	ground heat flux	[MJ/L ² *T]
T	temperature	[°C]
u	wind speed	[L/S]
e _s	saturation vapor pressure	[kPa]
e _a	actual vapor pressure	[kPa]
Δ	slope vapor pressure	[kPa/°C]
flux _o	exchange rate between surface and subsurface	[1/T]
O	sources/sinks	[1/T]
S _w	relative saturation (θ/θ_s)	[-]
S _s	specific storage	[1/L]
θ _s	saturated water content	[-]
S _e	effective water content	[-]
θ _r	residual water content	[-]
n, m	fitting parameters of the van-Genuchten-Mualem parameterization	[-]
α	fitting parameter of the van-Genuchten-Mualem parameterization	[1/L]
d _o	depth of surface flow	[L]
k _{ro}	relative permeability of the surface	[-]
Γ _{ex}	coupling length	[L]
φ _o	surface porosity	[-]
T _p	transpiration rate	[1/T]
C ₁ , C ₂ , C ₃	fitting parameter of the evapotranspiration module	[-]
E _{can}	canopy evaporation	[1/T]
RDF	root distribution function	[-]
θ _{fc}	field capacity	[-]
θ _{wp}	wilting point	[-]
θ _{an}	anoxic water content limit	[-]
θ _o	oxic water content limit	[-]
E _s	surface evaporation	[-]

EDF	evaporation distribution function	[-]
r_f	root extraction function	[-]
L_r	root depth	[L]
λ	weighted relative permeability	[-]
v	volume	[L ³]
J	Jacobi matrix	[-]
$\Theta_{\text{sat_new}}$	calibrated saturated water content	[-]
$\theta_{\text{res_old}}$	given residual water content	[-]
a	calibration parameter	[-]
$\theta_{\text{sat_old}}$	given saturated water content	[-]

1 Motivation and outline

Fresh water used by industry, agriculture and households is taken from rivers, lakes, aquifers or artificial reservoirs. The amount of available water depends on the interplay of processes in the soil-plant-atmosphere system, namely precipitation, transpiration and evaporation and their spatial and temporal variability. This spatio-temporal variability controls and at the same time results from soil moisture dynamics and patterns. Spatio-temporal soil moisture variability is for example influenced by climatic conditions (Western et al., 2004), vegetation type (Jost et al., 2004; Schume et al., 2004; Schwärzel et al., 2009), topography (Grayson et al., 1997), soil properties (Vereecken et al., 2007), antecedent soil moisture (Pan and Peters-Lidard, 2008) and hysteresis (Ivanov et al., 2010; Rosenbaum et al., 2012). In turn, vertical and lateral soil moisture variability influences the prediction of convection (Hauck et al., 2011), discharge generation (Blume et al., 2009; Partington et al., 2013; Stockinger et al., 2014) and transpiration.

A major challenge to the investigation of soil moisture variability and its feedbacks with other state variables and fluxes originates from the scale dependency of these feedbacks. For example, soil moisture influences convection at mesoscale study sites ($>10 \text{ km}^2$) but discharge generation processes occur at the hillslope scale (a few hundreds of meters).

A possible solution for the challenge of investigating soil moisture variability at different spatial and temporal scales could be provided by distributed hydrological models, for example HydroGeoSphere (Panday and Huyakorn, 2004), ParFlow-CLM (Kollet and Maxwell, 2008), MIKE-SHE (Graham and Butts, 2005), Cathy (Camporese et al., 2010). It is widely acknowledged that hydrological models integrating the surface and subsurface flow systems have a great potential to give insights into temporal and spatial patterns of fluxes, state variables and their feedbacks (Li et al., 2008; Weill et al., 2013; Frei and Fleckenstein, 2014; Voeckler et al., 2014; Ala-aho et al., 2015). Part of the potential lies in the models' ability to provide horizontally and vertically continuous soil moisture information at different catchment sizes for different spatial and temporal resolutions.

Yet, only few studies investigate the quality of soil moisture simulations (Herbst and Diekkrüger, 2003; Zhang and Wegehenkel, 2006; Mahmood and Vivoni, 2011). In addition, distributed hydrological 3D-models are currently predominantly used for small-scale applications (e.g. Cornelissen et al., 2014; Frei and Fleckenstein, 2014; Voeckler et al., 2014). Rare examples at large scales include the study of Goderniaux et al. (2009) who estimated climate change effects on groundwater reserves in a 480 km^2 large catchment with HydroGeoSphere, and the study of Rahman et al. (2014) who applied ParFlow-CLM to a 2364 km^2 large catchment to investigate spatio-temporal patterns of land surface mass and energy fluxes.

The lack of knowledge about potentials and limitations of soil moisture modeling especially at large scales is due to the high data requirements for temporal and spatial discretization, parameterization, calibration and validation of distributed models.

Necessary soil moisture data for the usage of distributed models at small scales can be provided by a range of measurement techniques. Invasive methods like the capacitance (spade sensors) or the time-domain-reflectometry technique offer a high vertical and lateral differentiation but they only provide point data. This limits their application to headwater scale catchments, for example the Wüstebach catchment in Germany (Graf et al., 2014) or the Little Washita catchment in the United States (Kollet and Maxwell, 2008). In addition, point data have to be interpolated to create patterns of a state variable which adds an additional error source. Geophysical methods (e.g. electromagnetic inductance) and the cosmic ray sensor technology provide spatially continuous measurements but their low penetration depth limits the resolution of vertical soil moisture variability. Comparable to point measurements, their application scale is confined to headwater catchments (Vereecken et al., 2008; Romano, 2014).

Modeling large catchments is closely connected to a decrease in quantity and quality of available calibration data, especially concerning their spatial distribution. For example, satellite and remote sensing data provide the necessary spatial coverage for mesoscale catchments (>10 km²) but suffer from low vertical resolution and spatial averaging (Vereecken et al., 2008) and from the inability to measure soil moisture below forest canopies. Often, a reliable calibration of distributed and process-based models is not possible without running into equifinality (Beven, 2001). If a sophisticated model calibration is not possible, model parameters can be transferred between catchments of different size and characteristics. The transfer of model parameters between catchments with different conditions is commonly done with regionalization techniques. Regionalization of parameters or resulting state variables and fluxes is one of the main challenges in hydrological modeling and has been long under debate. One major drawback of commonly used parameter regionalization techniques is the large number of test sites typically required to acquire statistically sound results (between 38 (Samaniego et al., 2010) and 913 catchments (Oudin et al., 2008)).

The high complexity of these models also demands for a strong model validation. Model validation is done in most studies with a simple split sample test where the model is calibrated and validated for the same climate and land use conditions. Kirchner (2006) recommends that model validation should include an application of calibrated models to different land use and climate conditions.

High demand in data and modeling expertise arising from above mentioned research topics requires a broad measurement infrastructure and interdisciplinary work between different natural sciences. The Transregional Collaborative Research Center 32 project (TR32) supplies the necessary framework both in data provision and interdisciplinary expertise (Simmer et al., 2014).

It is a joint collaboration project, funded by the Deutsche Forschungsgesellschaft, between the universities of Cologne, Bonn, Aachen and the Research Center Jülich with approximately 120 participants from various disciplines of natural sciences. The general aim is to increase knowledge about patterns, processes and structures of the soil-plant-atmosphere system from the point scale to the basin scale using different measurement, modeling and data assimilation techniques. In close collaboration with the Terrestrial Environmental Observatories (TERENO) project (Zacharias et al., 2011) several highly instrumented test sites including continuous measurements of soil moisture dynamics and measurements of water balance components were set up. One of these test sites, the forested headwater catchment Wüstebach (0.27 km²) in the Eifel National Park, was chosen as study area for this thesis.

Given the importance of soil moisture in the soil-plant-atmosphere system and the challenges of soil moisture measurement and simulation of different scales, this thesis investigates potentials and limitations of distributed hydrological models to simulate temporal and spatial soil moisture patterns and contributes to the topics of parameter regionalization and model validation.

The **first part** of the thesis investigates model related issues of simulation quality with the distributed hydrological 3D model HydroGeoSphere. The specific objectives are the investigation of:

- (1) the influence of spatial model discretization,
- (2) the influence of temporal model discretization
- (3) and the influence of lower boundary condition.

In the **second part**, model validation is done by transferring calibrated parameters from the Wüstebach catchment to different land use and climate conditions of the mesoscale Erkensruhr catchment (41.7 km²) and by applying in return land use and soil parameter sets of the Erkensruhr to the Wüstebach catchment. Objectives of this part are the investigation of:

- (1) the sensitivity of a headwater catchment simulation to mesoscale land use and soil parameters,
- (2) the sensitivity of a mesoscale simulation to spatial heterogeneity in potential evapotranspiration and precipitation
- (3) and the applicability of evapotranspiration parameters calibrated at a homogeneously covered catchment for water balance simulation of a heterogeneously covered catchment.

In the **third part** of this thesis, additional model validation is done with a 50-year long simulation run for forest growth in the Erkensruhr catchment. Objectives include:

- (1) the ability of the model to sustain the water balance over several decades
- (2) and the quality of discharge simulation.

The thesis is organized in 9 chapters starting with an introduction (chapter 1). Chapter 2 gives an overview about hydrological processes in forested catchments and feedbacks between processes and soil moisture, followed by chapter 3 summarizing the current state of knowledge in hydrological modeling including methods for describing subsurface flow and measuring model success. Chapter 4 discusses the question of scale in hydrological modeling and chapter 5 gives an introduction into geostatistical methods for quantifying spatial patterns. Chapter 6 describes characteristics of the studied catchments Wüstebach and Erkensruhr, the available data base and the process of data selection and processing. Chapter 7 outlines the applied model, its discretization and parameterization. Chapter 8 presents results and discussion of soil moisture, water balance and discharge simulations at the headwater and the mesoscale catchment. Finally, chapter 9 summarizes potentials and limitations of soil moisture modeling with distributed hydrological models at different spatial and temporal scales and gives an outlook for future research demands.

2 Hydrological Processes in Forested Catchments

2.1 General hydrology

The water balance describes the interconnection between **Precipitation (P)**, **Discharge (Q)**, **Evapotranspiration (ET)** and **Storage Change (ΔS)** in the following equation:

$$P = Q + ET + \Delta S \text{ [L/T]} \quad \text{Equation 1}$$

Of the four different water balance components, storage change exhibits largest spatial and temporal variability. While precipitation is often in balance with discharge and evapotranspiration on large time scales (e.g. annual), storage changes can occur very quickly during heavy rain events. Subsequent drying by evapotranspiration may take a lot longer. In this thesis, water balance is observed and simulated at a headwater catchment (0.385 km²; Wüstebach) and a mesoscale catchment (41.9 km²; Erkensruhr) for annual periods. Details about measured water balance components at the two catchments are given in chapter 6.2.

Each water balance component can be divided into different contributing processes which are illustrated at an idealized hillslope in Figure 2.1.

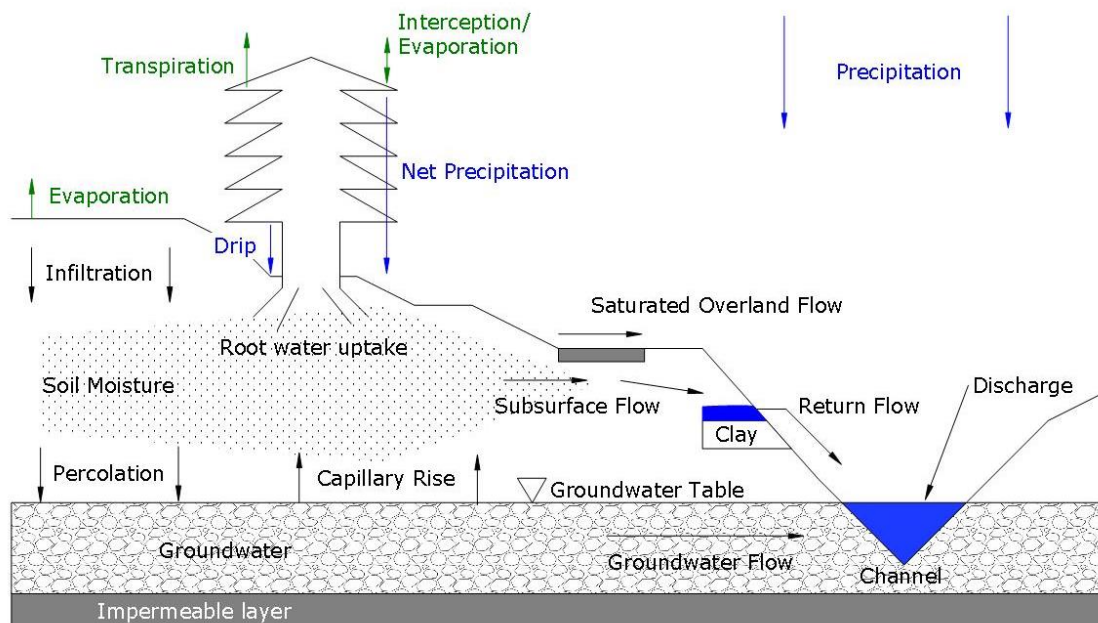


Figure 2.1: Hydrological processes at an idealized hillslope. Redrawn from Bronstert (1994).

Precipitation is divided into interception – water storage on leaves - , stemflow and net rainfall which manifests as direct precipitation to the surface underneath a canopy and as direct rainfall into lakes or rivers. The amount of interception depends on the intensity, length and frequency of rainfall events, on the height and Leaf Area Index (LAI) of trees and on the storage capacity of

leaves. Intercepted water either evaporates or falls to the ground as dripping water. The rate of interception evaporation depends on the storage capacity of leaves, the post-rainfall potential evapotranspiration rate (the rate of evapotranspiration at unlimited water supply) and the aerodynamic roughness of the canopy which expresses the resistance of leaves to turbulent mixture with the atmosphere (Davie, 2008).

Once precipitation has reached the surface, different **runoff generating processes** can develop depending on the infiltration capacity of the underlying soil. Infiltration capacity depends on the current soil moisture and the hydraulic conductivity being a function of soil texture, bulk density and current soil moisture status (Bronstert, 1994). If rainfall intensity is larger than the infiltration capacity of the soil, infiltration excess or Horton **overland flow** (Horton, 1933) occurs. If the infiltration capacity has reached its limit due to soil saturation or sealing, saturation excess overland flow occurs.

Horton infiltration was the dominant paradigm for explaining storm runoff until the 1960s. During the 1970s, this theory was questioned due to missing evidence of overland flow during storm flow events (Kirkby, 1988). Thus, **subsurface flow** came into attention. Subsurface flow can either originate from the soil matrix or from bypass flow. In the soil matrix, water is flowing due to gradients in capillary forces and gravity and can be described in the saturated case by Darcy's law and in the unsaturated case by the Richards' equation (refer to chapter 3.2, Equation 4). In contrast, bypass flow is a fast, turbulent flow transporting water through the soil via connected hollows originating e.g. from decayed roots, earthworm channels or cracks (Kirkby, 1988). It is only driven by gravity and avoids the soil matrix (McDonnell, 1990). Bypass flow through the unsaturated zone is called macropore flow while flow through the saturated zone is denoted pipeflow (Kirkby, 1988). According to McDonnell (1990), shallow soil depth, an impermeable bedrock layer, root growth and decay are conditions favoring the development of pipes. Matrix and bypass flow can be conceptualized as two different "domains" with different hydraulic properties, most important being hydraulic conductivity. Following this conceptualization, bypass flow occurs when the rainfall rate exceeds the hydraulic conductivity of the soil matrix. Unlike matrix flow which reduces with increasing soil saturation ($\hat{=}$ decreasing infiltration capacity), bypass flow increases with increasing soil saturation (Kirkby, 1988).

Anderson and Brooks (1996) distinguish between four different conceptualizations of bypass flow induced streamflow (refer to Figure 2.2). These concepts also mirror the advancement in understanding of hillslope processes. In the first case bypass flow was assumed to transport water rapidly from a current rainfall event to the stream (new water), while the second case assumed the displacement of old water stored in the subsurface in addition to new water.

The third case provided evidence of bypass flow induced release of old water by tensiometer measurements showing rapid responses to heavy rainfall events (McDonnell, 1990). According to this conceptualization, macropore flow delivers new water into the subsurface causing a rise in

groundwater level. The groundwater level rise activates pipeflow and results in the release of old and new water into the channel. The fourth case introduced by Brammer and McDonnell (1996) emphasized the role of bedrock topography in storing water in isolated depressions. During groundwater rise, these depressions become connected leading to mobilization of old water.

Tracer experiments by Sidle et al. (2000) approved the understanding of streamflow generating processes presented by Brammer and McDonnell (1996). For a steep forested headwater catchment in Japan, they found a contribution of macropore flow to peak discharge and the recession limb of the hydrograph and noted the importance of bedrock microtopography for streamflow. During wet soil moisture conditions, the maximum contribution of macropore flow accounted for 30% of matrix flow.

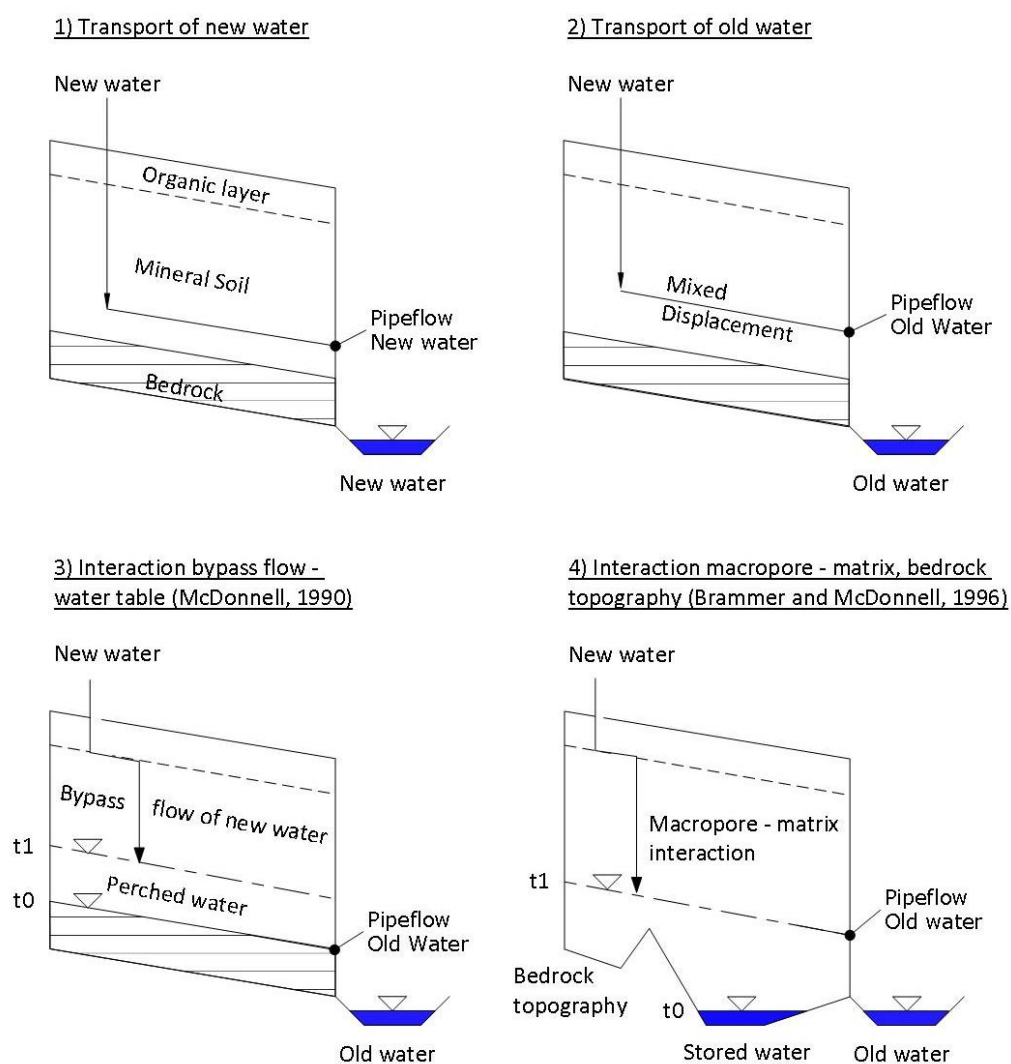


Figure 2.2: Conceptualized illustration of hillslope runoff response induced by bypass flow. Abbreviations t_0 and t_1 indicate the location of the water before rainfall (t_0) and during/after rainfall (t_1). Redrawn from Anderson and Brooks (1996).

More recently, Stockinger et al. (2014) used tracer experiments in a forested headwater catchment to find that hillslope and riparian zone switch between a state of hydrological connection and disconnection depending on the seasonal change in catchments wetness. During connection, old water stored in hillslopes can be quickly released to the riparian zone thus contributing to runoff. Kosugi et al. (2011) stressed the importance of bedrock aquifers by explaining immediate and lagged discharge peaks after a rainfall event by the interconnection of upslope, midslope and downslope aquifers.

Apart from tracers, discharge generating processes can be quantified by simulations with hydrological models (refer to chapter 3). Partington et al. (2013) studied temporal and spatial variation in discharge generation processes for a spruce dominated catchment with well-developed wetlands beside the river channel using a baseflow filter coupled to the model HydroGeoSphere. They found that the groundwater flow to the stream constituted flow in the dry period, but rainfall onto wetland areas inducing overland flow and rainfall into the channel produced peak discharge rates. Forests did not directly contribute to stream flow but supplied over 90% of the water necessary to maintain groundwater contribution to the stream.

A special case of subsurface flow is called **return flow**. According to Kirkby (1988), return flow requires the development of a saturated area in the subsurface producing saturation excess overland flow. Anderson and Burt (1990) note that topography plays a key role in the development of source areas for saturation excess overland flow and return flow because contributing areas develop e.g. due to flow convergence or when soil permeability decreases downslope.

The **impact of forests on total discharge** has already been noted by Pliny the Elder in the first century AD. He observed that tree cutting had an influence on spring flow (which he found to be intensified) and on rainfall (cited after Andréassian (2004)). During the last decades, quantitative observations from deforestation and reforestation experiments have highlighted some key impacts of forests on discharge: while it is widely accepted that reforestation decreases and deforestation increases low flows, the effect of forests on floods is arbitrary. Deforestation experiments showed an increase in flood peaks and their volumes, but the reverse effect could not be observed during reforestation experiments. In addition, forests reduce discharge rates if their evaporative potential is higher than the vegetation they replaced (Andréassian, 2004). Tesemma et al. (2015) investigated the effect of drought on simulated LAI and discharge for a range of subcatchments with varying degree of forest cover. They found a higher resilience of catchments with a higher degree of forest cover to climate changes in terms of discharge and LAI reduction.

Water infiltrating into the subsurface does not only feed discharge generation but also provides water for **evapotranspiration**. Evapotranspiration is generally divided into interception evaporation (described above), ground evaporation and transpiration. While potential

evapotranspiration is the rate of evapotranspiration at unlimited water supply, actual evapotranspiration defines the rate of evapotranspiration under given moisture conditions. Transpiration is driven by the difference in water pressure between atmosphere and leaf and occurs as a flux inside a tree's xylem (also called sap flux) transporting water and nutrients. Actual transpiration rate is controlled by current soil moisture, relative air saturation and the aerodynamic and stomatal resistances (ability of the vegetation to control transpiration from stomatal closure and opening). Evaporation refers to interception evaporation (already introduced) and ground evaporation. Ground evaporation is either evaporation of water ponding on the forest surface or evaporation from mineral soil. In forests, ground evaporation from the mineral soil is unlikely because the litter layer blocks capillary soil moisture exfiltration (Mendel, 2000).

Direct estimation of evapotranspiration can be done with the eddy-covariance technique which is based on the measurement of sensible and latent heat transport by turbulence (a detailed description of methodology and measurement in the study catchment can be found in chapter 6.2.2) while sap flow measurements provide estimates of transpiration (Granier, 1987).

There are large differences in total evapotranspiration and its components depending e.g. on the tree species composition and the age of the forest stand (refer to detailed description in Mendel (2000)). As spruce and beech stands of uniform age are dominant in the studied catchment, a short overview about evapotranspiration estimates will follow. According to data in Mendel (2000), Harsch et al. (2009) and Ringgaard et al. (2014) – the latter reporting eddy-covariance measurements – total evapotranspiration of a spruce forest accounts for ~61% of rainfall with large deviations between summer and winter while interception accounts for ~31% of rainfall according to data from Mendel (2000), Patzner (2004) and Ringgaard et al. (2014). Regionalized sap flux measurements from Patzner (2004) suggest a fraction of transpiration of 16% while simulated data from Ringgaard et al. (2014) amount to a fraction of 36%. Mendel (2000) reports a rather broad range of possible transpiration fractions between 21 and 95% of precipitation.

According to Mendel (2000), Oishi et al. (2008) and Harsch et al. (2009), total evapotranspiration of deciduous forest reaches ~53% of rainfall. Also, according to Mendel (2000), interception accounts for 28% of total rainfall while Oishi et al. (2008) report an interception fraction of 17% for deciduous hardwood forest. Transpiration estimates from Oishi et al. (2008) and Hentschel et al. (2013) are very similar with a fraction of ~32% while Mendel (2000) reports a fraction of only 19%. In addition, Oishi et al. (2008) give a fraction of evaporation of 9% from total rainfall for a hardwood forest.

While above cited studies mostly agree on the fraction of actual evapotranspiration, their estimates of evapotranspiration components revealed large uncertainty. This observation stresses the demand for catchment specific estimates of actual evapotranspiration and its components. The **storage term** of the water balance equation refers to water stored in the form

of ice and snow, to the soil water stored in the unsaturated zone and to groundwater in the saturated zone (Davie, 2008).

2.2 Relevance of soil moisture

In the previous chapter, the relevance of soil moisture for runoff formation (e.g. by influencing hydraulic conductivity or by the development of saturated areas) and transpiration has been outlined. Results by Blume et al. (2009), Partington et al. (2013) and Stockinger et al. (2014) showed that spatio-temporal soil moisture patterns are a useful tool to study runoff generation processes and their patterns.

The following two paragraphs (taken from Cornelissen et al., 2014) will therefore outline two major frameworks for exploring the interconnection of processes and catchment properties with spatial variability of soil moisture.

¹A first framework provided by Grayson et al. (1997) separated the spatial soil moisture patterns into a dry state when evapotranspiration exceeds precipitation and a wet state when precipitation exceeds evapotranspiration. At the dry state, the soil moisture pattern reflects soil and vegetation differentiation (local controls). At the wet state, lateral water movements by surface and subsurface pathways dominate (nonlocal controls). When macropores are activated and areas of high topographic convergence are saturated, only a small amount of precipitation is needed to produce runoff. Bogaen et al. (2010) noted that an influence of topographic features such as slope depends on the current soil moisture and soil depth.

The second major framework to study the contribution of different processes on spatial soil moisture variability is the relationship between mean soil water content and its standard deviation. This framework has received special attention in research because a clear pattern can be observed (Vereecken et al., 2007; Famiglietti et al., 2008; Pan and Peters-Lidard, 2008; Rosenbaum et al., 2012). In an idealized test case for only two soil types with contrasting soil texture, Pan and Peters-Lidard (2008) found a unimodal relationship between mean soil moisture and its standard deviation with a peak in the intermediate soil moisture range. This finding suggests that spatial soil moisture variability increases during wetting from dry to intermediate soil moistures and decreases during further wetting. In addition, Pan and Peters-Lidard (2008) observed that the range of studied soil moistures predefines the relationship between mean soil moisture and its standard deviation. This could explain the finding of Hu et al. (2011), who reported an increase in soil moisture variability with increasing soil moisture content. Vereecken et al. (2007) explored the dependence of the relationship between mean soil moisture and its standard deviation on soil properties and found that the relationship shows a clear peak for fine textured soils, while coarser textured soils exhibit a continuous decreasing standard deviation from the wet to the dry state. Based on a geostatistical analysis of soil

¹ Text taken from Cornelissen et al. (2014)

moisture data from a forested headwater in Germany, Rosenbaum et al. (2012) could observe this unimodal relationship. Based on their own results and on previous studies, Rosenbaum et al. (2012) summarized that the variability of soil moisture in wet soils is mainly controlled by lateral¹ and vertical flow processes and the spatial distribution of soil porosity. As the soil dries, the influence of evaporation and root water uptake increases and reduces spatial soil moisture variability. Finally, the variability of soil moisture of dry soils is mainly controlled by the soil's clay content (Rosenbaum et al., 2012)¹.

In the context of this thesis, the second framework - the relationship between mean soil moisture and its standard deviation - is used, because it is an illustrative method to analyze the linkage of temporal to spatial soil moisture variability and to efficiently compare different soil moisture data sets. In addition, it can be used to analyze characteristics and control mechanisms of different soil moisture states as suggested by Grayson et al. (1997).

¹ Text taken from Cornelissen et al. (2014)

3 Hydrological Modeling of Forested Catchments

3.1 General overview about hydrological modeling

The need for hydrological modeling arises from restrictions of measurement technology and from the challenge of predicting climate and land use change impacts on water availability and flood prediction (Beven, 2001). Restrictions of measurement technology in spatial and temporal coverage relate to surface but especially to subsurface state variables and fluxes. In chapter 2, subsurface state variables such as soil moisture have been identified as one key source of hydrological variability in forested catchments. If we attempt to understand the hydrological behavior of a forested catchment, modeling is an intrinsic part of the research process.

Hydrological models can be categorized by the nature of their equations (deterministic or stochastic), their representation of spatial variability in state variables, fluxes and parameters (lumped or distributed) or their description of hydrological processes (conceptual or physically-based).

The first rainfall-runoff model was developed by the Irish engineer Thomas James Mulvaney in 1851 to simulate peak flow rates (Beven, 2001). Peak flow was calculated by a linear combination of the catchment area, its mean rainfall and a conceptual parameter which had to be manually adjusted. The major drawback of this simplified approach was that processes affecting discharge amount (i.e. interception) could not be separated from those affecting the temporal arrival of discharge at an outlet (discharge routing). This first model can be classified as a deterministic one because it had a predefined set of equations and produced equal results with same parameters, input data and boundary conditions. Contemporary deterministic models contain non-linear equations and thus the statement above is only valid in the range of a mathematical inaccuracy. Before the onset of first computer models, the introduction of the unit hydrograph which characterizes the reaction of a watershed in terms of surface runoff response to a unit input excess rainfall rate (Sherman in 1932 cited after Beven, 2001) and the concept of infiltration excess flow (Horton, 1933) led to major improvements in hydrological science.

First computer models developed in the 1960s were of lumped conceptual type due to restrictions in computer power (Beven, 2001). These models represent the hydrological cycle as storages interlinked by simplified equations (conceptual) and do not account for spatial variability of input data, parameters, fluxes and state variables because catchment characteristics are lumped into one single value (Beckers et al., 2009). An important aspect of conceptual models refers to their parameters which often lack physical background and thus have to be determined through calibration. Modern examples of conceptual models include the '3 parameter monthly water balance model WASMOD' (Xu, 2002) and the more complex UHP model capable of representing the discharge components as independent storages (Bormann

and Diekkrüger, 2004). One of the most frequently used conceptual models is the HBV model (Bergström, 1976).

Physically based models represent processes and storage changes with equations based on conservation of mass, momentum and energy. The parameters of these equations can – in the best case – all be acquired by measurements. Of course, physically based models still contain conceptual parts, as for example HydroGeoSphere does for the description of the interception process. Conceptual models can be either lumped or distributed while physically based models are always distributed. Distributed models are able to incorporate the spatial variability of parameters, input variables and flow paths of water by dividing the catchment into a number of elements with structured (grid) or unstructured shape (e.g. triangles; Kampf and Burges, 2007).

The blueprint for distributed physically based models was provided by Freeze and Harlan (1969). They described the basic prerequisites for distributed and physically based modeling: (1) meteorological input data, (2) definition of flow boundaries, (3) information about flow barriers like clay layers, (4) definition of a grid, (5) data about spatial and temporal discretization and (6) flow parameters to represent heterogeneity in the soil. One of the first models incorporating spatially distributed hydrological responses was the TOPMODEL by Beven and Kirkby (1979) considering the effect of soil moisture status on overland flow generation. The distributed part was based on the variable contributing area concept that determines the fraction of saturated area of a sub-basin by comparing its soil average soil moisture status to its topographical structure represented in a distributed way. Areas determined as saturated contributed to overland flow. Though Beven and Kirkby (1979) emphasize the physical basis of the contributing area concept, the equation for calculating the saturated area contains conceptual parameters and is thus not physical in a strict meaning.

Contemporary examples of distributed physically based models include HydroGeoSphere (Panday and Huyakorn, 2004), ParFlow-CLM (Kollet and Maxwell, 2008), MIKE-SHE (Graham and Butts, 2005), Cathy (Camporese et al., 2010) and WaSiM (Schulla, 2015). The physical background of these models does not make parameter calibration redundant but in contrast demands for a thorough sensitivity and calibration process. This demand arises from the fact that the higher physical sophistication leads to an increase in the number of parameters and to non-linearity in equations. In addition, these parameters are often unknown or very uncertain due to a lack of measurements. Thus, one of the most common problems in distributed physically based models is overparameterization (Kirchner, 2006) and compensation effects in the parameters - which will be discussed in chapter 3.3 - leading to equifinality (Beven, 2001). The distributed nature of physically based models requires spatial variability in parameters and thus a large quantity of spatial and temporal data. Beckers et al. (2009) state that the “higher intrinsic accuracy of physically based models” (ibid., pp. 15) can only be fully exploited with an adequate data base and an assessment of consequences of parameterization and calibration.

Due to the high data demand and uncertainty in parameterization, distributed physically based models are not automatically superior to conceptual models in simulation results. For example, Cornelissen et al. (2013) compared the ability of conceptual and distributed physically based model types to simulate hydrological processes in a data sparse West African catchment. They concluded that the structure and parameter estimation effort of the physically based models WaSiM (Schulla, 2015) and SWAT (Arnold et al., 1998) hindered the correct representation of hydrological processes. For an overview about data, resource and time requirements of models with varying complexity, the reader is referred to Beckers et al. (2009).

Both physically based and conceptual models require the definition of boundary conditions with neighboring systems - for example the atmosphere - and the usage of coupling techniques between the subsystems of a model. First-type or Dirichlet boundary conditions prescribe state variable at a boundary of a system, for example a fixed pressure at the boundary of a catchment. Second-type or Newman boundary conditions specify a flux at a boundary, for example a constant inflow into the subsurface system or a precipitation rate (Fetter, 2001). At the lateral surface boundaries of the catchment and at the outlet of a catchment, the critical depth boundary condition is most widely used to constrain discharge outflow. In an open channel, discharge is a function of velocity, flow depth and channel width. The critical depth is a flow depth for which the discharge only depends on the flow depth and not on velocity. The critical depth boundary condition represents the effect of a broad-crested weir. These weirs are designed to create critical flow conditions at one point on top the weir. It is thus enough to measure the upstream surface elevation to determine the discharge rate (Chanson, 2004²).

The term 'coupling' can refer to techniques of interlinking or solving equations. Linking equations of the surface and subsurface system is done –among others - with first order exchange or continuity of pressure. First order exchange allows for a difference in pressure head between the surface and subsurface systems whereas continuity of pressure assumes equality in the pressure heads of the surface and subsurface system (Ebel et al., 2009). Furmann (2008) summarizes three types of solution techniques for coupled surface and subsurface systems: In the (1) fully coupled approach, equations of the surface and subsurface and the boundary condition between the two are assembled into one equation system and solved simultaneously whereas in the (2) iterative coupling approach, the solution of the subsurface is used to update the boundary condition which is subsequently used to recalculate the surface equations. When used (3) uncoupled, equations are solved step-wise without feedbacks between them. The fully coupled solution technique is most demanding in numerical sense and not necessarily superior to the other solution techniques (Furman, 2008).

Recently, physically based distributed hydrological models were coupled to land surface and atmospheric models to gain an holistic picture of the soil-plant-atmosphere continuum (e.g. Shrestha et al., 2014). The integration of processes covering the whole soil-plant-atmosphere continuum is especially sensitive to the discrepancy in time scales between the subsystems as

described in Furman (2008) and is thus one of the major challenges in coupled modeling (Maxwell, 2009). For a more complete review of the historical development of rainfall-runoff modeling and an overview of available conceptual and physically based models, the reader is referred to Singh and Woolhiser (2002) and Beckers et al. (2009).

When modeling hydrological processes of forested catchments, the dominance of subsurface processes requires special attention to the treatment of unsaturated subsurface flow. The next chapter gives an overview about methods to simulate subsurface flow with a focus on Richards' equation.

3.2 Treatment of subsurface flow in physically based models: Richards' equation

As unsaturated flow is one of the most important compartments in the hydrological cycle, it has been described in many different ways. Early physically-based models like the TOPMODEL (Beven and Kirkby, 1979) did not explicitly account for unsaturated flow but represented the unsaturated zone as an infiltration storage and the saturated zone as a second storage. The unsaturated flow was split into fast runoff and percolation into the saturated zone. Later, conceptual models like UHP (Bormann and Diekkrüger, 2004) contained a separate storage for each individual runoff component. Another conceptual approach is the simulation of unsaturated flow by cascades of non-linear reservoirs in which the time constant of each reservoir relates to the unsaturated hydraulic conductivity in a prescribed way, for example in an inversely proportional fashion (Gandolfi et al., 2006).

In contemporary physically based models, Richards' equation is implemented in all possible ways ranging from 1D (Hydrus-1D; Šimůnek et al., 2005) and combined way (Mike-SHE; 1D for unsaturated zone and 2D or 3D for groundwater flow; Graham and Butts, 2005) to a fully 3D way (HydroGeoSphere; Panday and Huyakorn, 2004).

Richards' equation is based on Darcy's law found in the mid-1800s by the French engineer Henry Darcy. It expresses that a flow through a specified area q (L/T) is proportional to the difference in the height of the water h (hydraulic head, the sum of pressure and elevation head, with the dimension L) between an inlet and an outlet and inversely proportional to the flow distance (Fetter, 2001):

$$q = K \frac{dh}{dl} \tag{Equation 2}$$

The hydraulic conductivity K (L/T) is a function of the intrinsic permeability (a function of the diameter through which a fluid flows), the dynamic viscosity and the density of the fluid and the gravity force (Hubbert (1956) cited after Fetter, 2001). Darcy's law is only valid for saturated flow but when used with the Buckingham extension, it is commonly assumed that it can also be applied to unsaturated conditions (Furmann, 2008).

The extension splits the hydraulic conductivity K into a saturated part K_s and a relative part K_r :

$$K = K_s K_r \quad \text{Equation 3}$$

K_s (L/T) can be measured with permeameters while K_r (-) describes the dependence of conductivity on water content or pressure head and has to be parameterized for example with the model by Mualem (1976). Embedding Darcy's law into a mass conservation formulation yields the Richards' equation:

$$\frac{\partial \theta}{\partial t} = \nabla [K(\psi) \nabla \psi] + \frac{\partial K}{\partial z} \quad \text{Equation 4}$$

where θ is the volumetric water content (dimensionless), t is time, K is hydraulic conductivity (L/T), ψ is the pressure head (L) and z (L) is elevation. The largest source of uncertainty in Richards' equation arises from the curvilinear nature of the relations between head and water content, and between unsaturated conductivity and head (Smith and Woolhiser, 1971). They can be derived for example with the model of van Genuchten (1980). Due to the strong nonlinear nature of the equation and the curvilinear nature of relations described above, Smith and Woolhiser (1971) and Dye et al. (2011) emphasize the importance of the time step in the numerical solution technique for the accuracy of simulations with Richards' equation.

Kirchner (2006) is critical about the usage of Richards' and Darcy equations for studies in large catchments. Because both were derived at small scales, the application at larger scales automatically assumes that involved state variables (flux, θ , h) and effective parameters (K_s , $\theta(h)$) adequately subsume the heterogeneity of the subsurface. Clark et al. (2009) add that Richards' equation and Darcy's law cannot represent hillslope processes like preferential flow or flow through fractures because both lead to nonequilibrium situations in the head which cannot be characterized by Richards' equation. With extensions like the dual-porosity model using two different parameters sets to characterize the matrix and the macropore flow media independently and a transfer term between the two media, it is possible to simulate matrix and bypass flow with the Richards' equation (Gerke and van Genuchten, 1993).

In summary, the application of Richards' equation at larger scales is based on the assumption that averaged state variables like the hydraulic potential or water content and effective parameters like saturated conductivity adequately subsume the subsurface heterogeneity (Kirchner, 2006). Diekkrüger (2003) provides an overview of available methods to determine effective parameters.

3.3 Parameter estimation for hydrological models

Hydrological models contain conceptual and physical parameters. An example for a physical parameter is the saturated hydraulic conductivity; the maximum storage capacity of the unsaturated zone is an example for a conceptual parameter. Depending on their level of physical

representativeness and number of equations, the amount of parameters in hydrological models varies between 3 (e.g. WASMOD; Xu, 2002) and more than 75 (e.g. HydroGeoSphere; Panday and Huyakorn, 2004). The physical representativeness of parameters depends on their application scale. For example, the saturated hydraulic conductivity applied at a certain spatial model resolution may originate from point measurements. When applied in a distributed model, it is assumed that the point measurement adequately subsumes the spatial heterogeneity and the parameter is denoted as an effective parameter. Blöschl and Sivapalan (1995) are critical about the usage of effective parameters for non-linear processes such as unsaturated flow and suggest distribution functions for the definition of subgrid variability.

Parameter estimation is the process of quantifying unknown or uncertain parameters by measurements or calibration while during parameterization, the spatial or temporal dimension (e.g. a unique soil type) for which a parameter is representative, is defined (Refsgaard and Storm, 1996). The necessity for adjustment of parameters originates from incomplete knowledge of the true parameter value and their spatial and temporal variability. During calibration, the modeler seeks to find a combination of parameter values which optimally fits simulated to observed data (Morton and Suárez, 2001). The success of the calibration is evaluated by measures of model performance outlined in chapter 3.4. Model calibration is followed by a validation process where the model is applied unchanged to a different data set (Refsgaard and Storm, 1996). Due to restrictions in the amount and quality of measurements, this is typically done by subdividing the data set (e.g. discharge) into two parts (split sample test; Refsgaard and Storm, 1996).

Calibration and parameter estimation is linked to a number of problems. Beven and Binley found in Monte Carlo experiments conducted in the 70s about parameter sensitivity that no clear optimum parameter set exists but rather a group of parameter sets providing equally good fits (cited after Beven and Binley (2013)). This phenomenon has become known under the term “equifinality”. A second major problem refers to the effect of parameter compensation. With the number of parameters, the probability increases that an error in one parameter is compensated by another parameter. Both problems become especially virulent if a distributed physically based model is calibrated to integrated hydrological values like discharge (Kirchner, 2006). These weaknesses lead to the opinion expressed by many authors (e.g. Woolhiser, 1996 and Kirchner, 2006) that physically based models require too many parameters and are thus likely to be misused and inaccurate. In addition, Kirchner (2006) criticizes the commonly used split-sample test as insufficient and proposes to test models for conditions different in land use and climate data to those during calibration period (differential split sample test). Anderson and Bates (2001, p.8) state that “models can never be conclusively validated, only falsified”.

One of the prerequisites to a successful calibration is a sensitivity analysis which is the “process of determining the rate of change in model output with respect to changes in model inputs” which can be data or parameters (Moriassi et al., 2007, p.885). Thus a sensitivity analysis reveals

parameters and parameter combinations which are sensitive to the simulated output variable. A sensitivity analysis can be part of an uncertainty analysis which quantifies the total error of a simulation. According to Moriasi et al. (2007) uncertainty analysis assesses the level of confidence in simulation results regarding (1) quality and amount of measured data, (2) state of knowledge about processes, (3) nature of mathematical equations and (4) quality of the sensitivity and calibration procedure. The most frequently used uncertainty analysis methods are Generalized Likelihood Uncertainty Estimation (GLUE; Beven and Binley, 1992) and formal Bayesian approaches (e.g. the Differential Evolution Adaptive Metropolis (DREAM) algorithm by Vrugt et al. 2008). Both methods involve a sampling strategy to choose parameter sets from a parameter distribution, the definition of a likelihood function quantifying the level of agreement between simulated and observed data for each parameter set and the definition of a threshold value of the likelihood function to identify acceptable simulation results. The main difference between GLUE and Bayesian approaches refers to the definition of the likelihood function which is purely subjective in the GLUE method but originates from statistical probabilities in the case of Bayesian approaches. Beven and Binley (2013) state that a formal (Bayesian) likelihood results in a very constrained cumulative likelihood function because it does not allow for zero likelihood. That leads to reduced differentiation among parameter sets with high likelihood value. In addition, a formal likelihood function is restricted to aleatory – statistical - errors whereas informal likelihood measures implicitly allow for epistemic uncertainties which are related to possibly unknown parts of the system behavior. According to Beven and Binley (2013), allowing for purely aleatory errors in uncertainty estimation results in an overestimation of the information content in observation data. In contrast, Vrugt et al. (2003) state that formal approaches are able to separate the contribution of error in input data, output, parameters and model structure. At the same time, inferring a formal likelihood function capable of separating these errors is difficult because of interactions between these errors. Nevertheless, Vrugt et al. (2003) and Jin et al. (2010) find that both methods produce very similar confidence intervals for simulated discharge. Diekkrüger et al. (1995) provided 19 different modelers with the same data set covering water, nitrogen and pesticide dynamics and plant growth. Their modeling comparison revealed that the process knowledge of a modeler is an equally important determinant of simulation results than the chosen modeling approach. Recently, Holländer et al. (2014) added that the knowledge of soft information about the catchment's processes via field inspection was equally important as measured data for improving simulation results. Uncertainty and sensitivity analysis together with calibration and validation constitute the process of model evaluation (Moriasi et al., 2007). The author of this thesis thinks that model intercomparison either with synthetic experiments (e.g. Maxwell et al., 2014) or preferably with real test cases (e.g. Sulis et al., 2010, Cornelissen et al., 2013, Koch et al., in preparation) is an important part in model evaluation as it allows for separating shared and model-specific limitations.

3.4 Measures of model performance

Measures of model performance are used to quantify the level of agreement between simulated and observed temporal variables like discharge or soil moisture. Each of these measures is sensitive to different characteristics of the data set – e.g. dynamics or absolute deviations - and thus the choice of applied measures greatly influences calibration and simulation results. This chapter gives a brief overview of advantages and disadvantages of commonly used measures of model performance.

Measures of model performance commonly applied in hydrological modeling can be grouped into 3 categories (Moriassi et al., 2007): (1) standard regression, (2) dimensionless measures and (3) error indices.

The first category measures the strength of the linear relationship between simulated and measured data. It includes Pearson's correlation coefficient (r ; ranging from -1 to +1) describing the degree of linear relationship between two variables, and the coefficient of determination (the square of Pearson's r) measuring the proportion of the variance in observed data which is explained by simulated data (R^2 ; ranging from 0 to +1). Both coefficients are oversensitive to outliers or extreme values but insensitive to additive and proportional differences between simulated and measured data (Moriassi et al., 2007). This insensitivity can cause the R^2 to reach its maximum if two time series have the same dynamics although their magnitudes differ substantially.

The dimensionless measures 'Index of Agreement' (Willmott, 1981) and 'Nash-Sutcliffe Efficiency' (NSE; Nash and Sutcliffe, 1970) overcome the insensitivity to proportional differences between simulated and measured data but are both still oversensitive to extreme values due to the usage of squared differences between simulated and observed data. The NSE determines the relative magnitude of the residual variance between measured and simulated data (noise) compared to the variance of measured data (ranging from $-\infty$ to +1) and is a measure of noise (Moriassi et al., 2007). If the NSE is smaller than the R^2 , this indicates a bias in the simulated data (Aitken, 1973). Gupta et al. (2009) decompose the NSE into correlation coefficient, bias and standard deviation and observe a variation in the relative importance of each component e.g. across different years and basins. They apply an equal weighting to each measure and combine them into a new measure, the Kling-Gupta-Efficiency.

The third category – error indices – includes, among others, the 'Percent Bias' (PBIAS, ranging from $-\infty$ to $+\infty$ with 0 as the optimal value) and the 'Root Mean Square Error' (RMSE; ranging from $+\infty$ to the optimal value of 0). The first index measures the average tendency of simulated data to differ from observed values (Gupta et al., 1999) and the second index is the squared mean of the quadratic deviations between simulated and observed data.

The PBIAS is defined in the context of this thesis as follows:

$$PBIAS = \frac{\sum_{i=1}^N (Obs - Sim)}{\sum_{i=1}^N Obs} * 100 \quad \text{Equation 5}$$

with N being the total number of measured (Obs) and simulated (Sim) values.

Other error indices include for example the average error (or Bias) which is the difference between the mean of simulated and observed values. They are sometimes used in a normalized way for example by dividing the bias by the observed mean (Janssen and Heuberger, 1995).

Measures relying on average values are generally oversensitive to outliers (Janssen and Heuberger, 1995).

In the framework of the Wüstebach study (chapter 8.2), the PBIAS, the R^2 and the NSE are used. For the Erkensruhr simulations (chapter 8.3), the correlation coefficient (r), the Bias and the coefficient of variation (CV) are used as measures of model performance. The bias is defined in Gupta et al. (2009) as the relation between the mean of simulated $\mu(Sim)$ and observed values $\mu(Obs)$. It ranges between $-\infty$ and $+\infty$:

$$Bias = \frac{\mu(Sim)}{\mu(Obs)} \quad \text{Equation 6}$$

The coefficient of variation (CV) is usually defined as the ratio between standard deviation and mean of a variable and expresses the relative spread of a distribution. In this thesis, the coefficient of variation is used as a ratio between the coefficients of simulated and observed data. It is used as a measure for the over- or underestimation of the relative spread in simulated data and ranges between -1 and $+1$:

$$CV = \frac{\frac{\sigma(Sim)}{\mu(Sim)}}{\frac{\sigma(Obs)}{\mu(Obs)}} \quad \text{Equation 7}$$

with $\mu(Sim)$ and $\mu(Obs)$ being the mean of simulated and observed values and $\sigma(Sim)$ and $\sigma(Obs)$ being the standard deviation of the simulated and observed values.

Refsgaard and Storm (1996) state that measures of model performance assess the simulation quality of a hydrological variable in a statistical sense but not its representation of hydrological processes. Many authors deduce that a thorough model evaluation should include several of the above described metrics in addition to measures which can provide hydrological interpretation (e.g. Janssen and Heuberger, 1995; Legates and McCabe, 1999; Moriasi et al., 2007, Gupta et al., 2009). In this thesis, geostatistical measures and the relation between mean soil moisture and its variance (refer to chapters 5 and 2.2) are applied as additional measures for model evaluation beyond single measures of model performance.

4 Spatial and temporal scales in hydrological modeling

Catchments are highly heterogeneous and variable in time and space. Interestingly, the sources for heterogeneity and variability change with temporal and spatial scale. For example, variability in runoff at the event scale (1 day) may be controlled by the characteristics of a storm but at seasonal scale (1 year), runoff may be dominated by the annual cycle in precipitation and evapotranspiration (Blöschl and Sivapalan 1995). This chapter briefly introduces the concept of scale dependent hydrological processes, discusses consequences for hydrological modeling and describes methods to transfer information between scales.

In the context of this thesis, the term 'scale' refers to a characteristic time or length of a process, observation or model discretization (Blöschl and Sivapalan, 1995). Klemes (1983) notes that, in any science, dominant levels of scale characterized by different forces exist. Identifying these scales will help to develop conceptualization of hydrologic processes (Klemes, 1983, Blöschl, 2001). Blöschl and Sivapalan (1995) give an example of such a conceptualization by summarizing dominant time and length scales of hydrological processes (Figure 4.1). The figure shows that each process occurs at a range of different temporal and spatial scales and thus specific pairs of temporal and spatial scales correspond to unique combinations of different processes. For example, infiltration excess overland flow is characteristic for short time steps (minutes), but at larger time scales (days) unsaturated flow is characteristic. ¹ Western et al. (2002) illustrate this relationship for the spatial variability of soil moisture which may be dominated by differences in soil type on the catchment scale (10 km) and by macropore flow on the local scale (1 m). On large temporal scales (1 year), variability of soil moisture is caused by changes in evapotranspiration and precipitation, but on a small temporal scale (1 hour) the seasonal trend might be superimposed by a series of wetting and drying events (Western et al., 2002) ¹. Kirchner (2006) and Tetzlaff et al. (2008) advocate the usage of tracers to support the investigation of scale-dependencies in hydrological processes because tracers are able to provide information about geographical sources of runoff. For example, Soulsby et al. (2006) used tracers for a mesoscale catchment and its nested subcatchments to investigate the scaling of groundwater contribution and residence time. They found a clear correspondence of residence time to the percentage of hydrological responsive soils (Histosols, Leptosols) but not to catchment area. Stockinger et al. (2014) conducted tracer experiments in a forested headwater catchment and found that the catchment changes between a state of hydrological connection between hillslopes and riparian areas and a state of disconnection. They attributed this behavior to the current soil moisture state of the catchment while soil moistures below 30 vol.% favored disconnection.

¹ Text taken from Cornelissen et al. (2014)

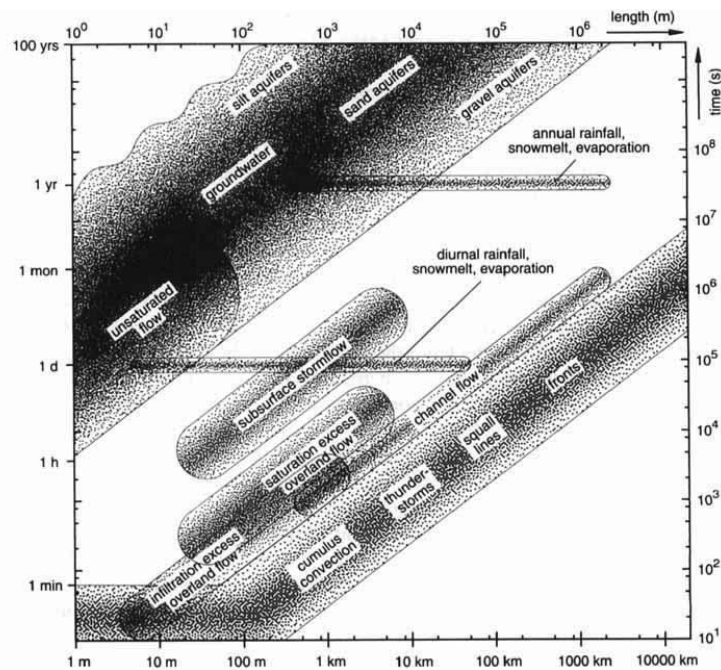


Figure 4.1: Characteristic time and length of hydrological processes (Blöschl and Sivapalan, 1995).

In hydrological science, two different frameworks describing temporal and spatial properties of processes, measurements and patterns have been proposed. The framework of Blöschl and Sivapalan (1995) focuses on the characterization of spatial and temporal properties of processes and measurements and it distinguishes between the extent, the period and the correlation length of a process (refer to top part of Figure 4.2). Western et al. (2002) apply this framework to characterize soil moisture patterns and differentiate into extent (total time or spatial coverage), spacing (distance between sample points) and support (area for which the measurement is assumed representative) as illustrated in the bottom part of Figure 4.2. This so called scale triplet has been proven to be a valuable tool to analyze the scaling behavior of soil moisture. For example, Korres et al. (2015) used the scale triplet to analyze similarities and differences in spatial variability of measured and simulated soil moisture data originating from different catchment sizes. Like Famiglietti et al. (2008) and Manfreda et al. (2007), Korres et al. (2015) found a variation of spatial soil moisture variability with spatial extent and support. More specifically, Famiglietti et al. (2008) found that the variance of measured soil moisture not only depends on its mean value but also on the extent of measurements. Koyama et al. (2010), Korres et al. (2013) and Bogena et al. (2010) were able to attribute a specific trend in spatial variability to a trend in a dimension of the scale triplet. Ryu and Famiglietti (2006) examined the scaling behavior of surface soil moisture variance with increasing support scale and identified three distinct spatial patterns each correlated to a specific theoretical semivariogram (refer to chapter 5) and to variations in precipitation, land use and soil texture.

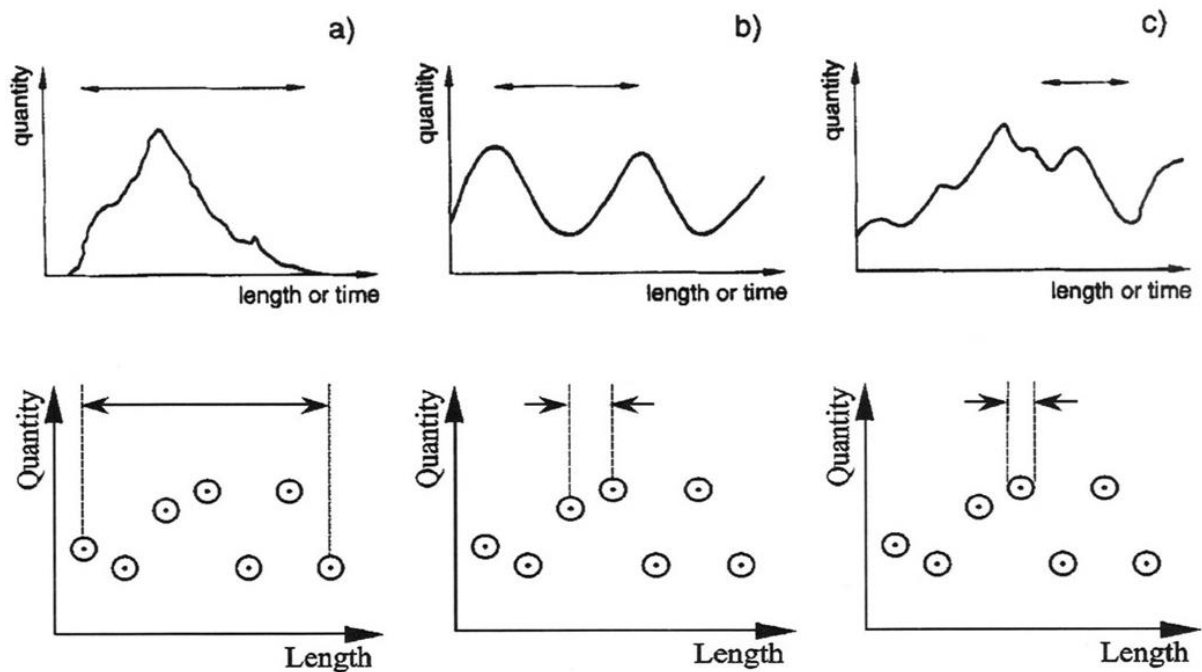


Figure 4.2: Spatial and temporal properties of processes and patterns. Top: Definition according to Blöschl and Sivapalan (1995): a) Extent, b) Period, c) Correlation Length; Bottom: Scale triplet of Western et al. (2002): a) Extent, b) Spacing, c) Support.

Specific pairs of temporal and spatial scales do not only occur for hydrological processes, but also for measurement techniques providing information only for a unique combination of the dimensions of the scale triplet. Blöschl and Grayson (2000, p.21) explain that “from a particular measurement one can only “see” processes within a limited window (determined by the scale triplet), and processes at larger and smaller scales will not be reflected in the data”. Applying the dimensions of the scale triplet, Blöschl and Grayson (2000) state that small-scale variability will not be captured by a measurement if the spacing is too large and will be smoothed if the support is too large. Variability will appear as trends if the extent scale is too small (Blöschl and Grayson, 2000). Vereecken et al. (2008) presented a review of soil moisture measurement methods. They found that current measurement technologies have the largest overlap for spatial extents between 10 and 1.000 m. At the same time, their support scale greatly varies between centimeters (soil moisture probes) and hundreds of meters (airborne sensors). This overlap provides a great potential to investigate advantages and disadvantages of the different measurement techniques. Xu et al. (2013) investigated the relationship between the number of rain gauges used for the estimation of areal precipitation and simulated runoff in a Chinese watershed. They found that the simulation performance increased to a threshold value beyond which the number of additional rainfall information had no additional effect on simulation performance. Blume et al. (2009) confirmed the value of using a combination of data sets with different spatiotemporal resolution for analyzing dynamics of unsaturated flow.

These examples illustrate the necessity to develop a measurement framework which is as consistent in its extent, support and spacing as possible with investigated processes prior to a modeling application.

In chapter 3.3, overparameterization, equifinality and parameter compensation have been identified as challenges to successful application of distributed physically based hydrological models. One consequence of scale dependency of processes and state variables is the change in parameter sensitivity with temporal and spatial model discretization. For example Sciuto and Diekkrüger (2010) observed temporal and spatial scaling issues in discharge and water balance modeling resulting from a high sensitivity of evapotranspiration parameters to spatial discretization. In addition, equations derived at certain scales may not adequately represent dominant processes at a different scale (refer to chapter 3.2).

A large challenge arises from a change in one or more dimensions of the scale triplet. For example, if a larger catchment (extent increase) is simulated, the increase in heterogeneity of the catchment concerning soil properties, land use types and topography does not correspond to an increase in information density (Bormann et al., 1999).

This problem is also encountered in the framework of this thesis. The same model with the same structure is applied at two different scales with a strong contrast in heterogeneity which is accomplished with a decrease in the information density (i.e. resolution of soil data, measured water balance components, precipitation measurements; refer to chapter 8.3).

Scale dependency of processes, patterns and parameters leads to the question of ‘scaling’ which is understood as the transfer of information across scales (Blöschl and Sivapalan, 1995). In the words of Western et al. (2002) “the essence of scaling is to distill the key patterns from information at one scale and to use these to make good predictions at another scale”. Scaling of parameters and state variables can be done with up-/downscaling methods or with regionalization (Sivapalan and Kalma, 1995). According to Blöschl and Sivapalan (1995), upscaling (downscaling) involves distributing the small-scale variable over the catchment – e.g. increasing precipitation with elevation – and aggregating the spatial distribution into one value. Downscaling involves singling out the variable to a smaller scale which is accompanied by disaggregation. Regionalization denotes the transfer of information to a different catchment without a change in parameter values. Western et al. (2002) separate process-based scaling from behavioral scaling techniques. While the first one uses process understanding to investigate the effect of scale on spatial patterns e.g. in a modeling framework, the second technique quantifies characteristics or the behavior of spatial patterns at different scales and uses these information to predict the effect of scale changes.

Influence of up- and downscaling techniques on simulation results has been long under debate. Stephan (2003) investigated the influence of aggregation of topography and land use data on water balance simulation. He found that a change in raster cell size (extent) and corresponding

aggregation of topography did not lead to significant variations in actual evapotranspiration and discharge. In contrast, aggregation of land use data resulted in significant differences in water balance components which increase with increasing heterogeneity in land use. Diekkrüger (2003) summarizes methods of upscaling soil hydraulic parameters commonly used in hydrological modeling. Comparing latin hypercube sampling and inverse modeling for determining effective parameters with the usage of aggregation and methods which consider subgrid variability, he recommended to use different methods because applicability and uncertainty of methods depend on the simulation aim, the data availability and their quality. In contrast, Stephan (2003) recommended the geometric mean as the best method for the aggregation of soil hydraulic properties. The spatial scaling of soil hydraulic parameters on water balance modeling has for example been investigated by Sciuto und Diekkrüger (2010) in the Wüstebach catchment with HydroGeoSphere. They concluded that upscaling soil hydraulic properties by taking a volume-average of the distributed parameters while keeping the spatial discretization of the model leads to a good match in terms of water balance simulation.

Alternatively, model parameters can be transferred between catchments of different sizes by regionalization techniques.

The transfer of model parameters between catchments with different conditions is commonly done with regionalization techniques. According to Oudin et al. (2008), three regionalization techniques can be distinguished: (1) regression, (2) spatial proximity and (3) physical similarity. The regression based method seeks for transfer functions at gauged catchments between calibrated parameters and physical/climatological descriptors of the catchment. Regression parameters are applied to descriptors of an ungauged catchment to calculate necessary model parameters. Bossa and Diekkrüger (2012) used a multiple linear regression approach between calibrated model parameters and catchment attributes (e.g. fraction of land use types) to calculate model parameters for catchments with varying size. With the derived scale-dependent model parameters, discharge was well simulated at different catchments. The authors also stressed the ability of this method to provide reliable estimates of water, sediment and nutrient transport in ungauged catchments. The spatial proximity method transfers parameters to geographically close catchments while the physical similarity method transfers parameters to catchments which are hydrological similar to the gauged catchment.

Among regionalization methods, regression is the most criticized. Kling and Gupta (2009) stated that parameter calibration undertaken prior to regression might lead to parameter values without relationship to observed catchment predictors. Li et al. (2010) added that the hypothesis of linear relationships between catchment predictors and parameters ignores the spatial variability in catchment predictors. As lumped models are predominantly used for regression based regionalization, Kling and Gupta (2009) quantified the noise involved when using spatially lumped models for catchments with spatially distributed physical and climatological variables.

They found that parameters controlling processes that are less visible in the output signal produced the largest noise.

There is an ongoing debate about the most suitable regionalization technique because results are still inconsistent. For example, Li et al. (2010) found a clear superiority of linear regression over the two other methods while Bao et al. (2012) found that similarity is superior to linear regression especially for data sparse regions.

Another major drawback of all regionalization techniques is that they typically require a large number of test sites to acquire statistically sound results. For the studies cited above, the number of used catchments varies between 38 (Samaniego et al., 2010) and 913 catchments (Oudin et al., 2008).

In this thesis, the problem of interconnection between scales is explicitly investigated by running the HydroGeoSphere at different spatial and temporal resolutions to investigate scale dependencies in soil moisture dynamics and patterns, runoff components and parameters involved in the calculation of soil moisture (process-based scaling). The behavioral scaling techniques - variogram and kriging - permit a scale dependent comparison of simulated to measured soil patterns and their statistical properties. In the second part of this thesis, calibrated evapotranspiration parameters from the headwater simulation are applied to a mesoscale catchment to investigate their applicability for and sensitivity to mesoscale water balance and discharge simulation under different climate and land use conditions.

5 Quantification of spatial patterns

Chapter 2 showed that variability in hydrological processes is connected to variability in the state variable 'soil moisture' and to catchment characteristics. Analyzing and illustrating spatial and temporal variability is thus an important step in understanding catchment response and feedbacks between state variables. It requires quantifications of spatial correlations and interpolations to support the comparison between point measurements and point based simulation results. Geostatistics provide a broad range of methods to examine the temporal and spatial heterogeneity (Deutsch and Journel, 1998). As this thesis concentrates on spatial patterns, the following chapter only deals with methods to analyze spatial variability. These methods include (i) the widely used variogram for analyzing spatial autocorrelation, (ii) empirical orthogonal functions for separating random from non-random spatial patterns of datasets, (iii) entropy as a measure of uncertainty and (iv) interpolation techniques like Thiessen Polygons, Inverse Distance Weighting and Kriging.

Spatial variability and spatial dependence of localized variables like soil moisture can be expressed by the **covariance**. In a statistical sense, each soil moisture measurement is a localized random variable with a certain distribution from which the realization of the variable is drawn. Like variance, the covariance requires a definition of the distribution mean for every measurement at each location. However, a random distribution can only be sampled once at a given time and thus the distribution mean cannot be calculated. To solve this problem, stationarity is assumed which means that the mean value and the variance of the random distributions are constant over the entire domain (i.e. measurement test site). In addition, it is assumed that the stationary covariance only depends on the difference between the soil moisture values at different locations and not on their absolute position.

An alternative formulation of the covariance is the (semi-)**variogram** which measures the variance of the difference between a number of points separated by the vector h . Definition of the variogram requires the so called "intrinsic hypothesis" which equals the concept of stationarity except that the variance may vary over the measurement domain. The variogram of a random variable is defined as:

$$\gamma(g) = \frac{1}{2N(g)} \sum_{i=1}^{N(g)} (x(u_i) - x(u_i + g))^2 \quad \text{Equation 8}$$

with $x(u_i)$ and $x(u_i+g)$ being the actual values of the variable X at the locations u_i and u_i+g , and $N(g)$ being the number of paired comparisons at lag g . Depending on the calculation method of variograms, Oliver (2010) reports a minimum number of sample points between 50 and 100 to achieve reliable estimations. Problems can occur for example when the data exhibit a trend which in a statistical sense shows that the assumption of stationarity is not valid any more. Of

course, trends depend on the scale at which data are examined. The variogram equation can be extended to investigate the cross variability of two different attributes (e.g. soil moisture and saturated conductivity); logarithms of $x(u_i)$ and $x(u_i+g)$ can be used for negative values of a random variable.

The variogram relates to the covariance under the assumption of stationarity as follows:

$$\gamma(g) = \sigma^2(X(u)) - \left[\frac{1}{N(g)} \sum_{i=1}^{N(g)} (x(u_i)x(u_i + g)) - (\mu(X(u)))^2 \right] \quad \text{Equation 9}$$

$$\gamma(g) = C(0) - C(g)$$

with $\sigma^2(X(u))$ being the variance of the random variable at the location u , $(\mu(X(u)))^2$ being the squared mean of the random variable at the location u , $x(u_i)$ and $x(u_i+g)$ being the actual values of the variable Z at the locations u_i and u_i+g ; finally, $N(g)$ is the number of paired comparisons at lag g . The variance of the random variable $\sigma^2(X(u))$ is identical to the covariance $C(0)$ at lag distance zero, and the second term denotes the stationary covariance $C(g)$ between the value at location u and another value at a location separated by the vector g .

The variogram is a measure of the autocorrelation structure of spatially distributed data and can be characterized by three different features: **sill**, **range** and **nugget variance** (refer to Figure 5.1).

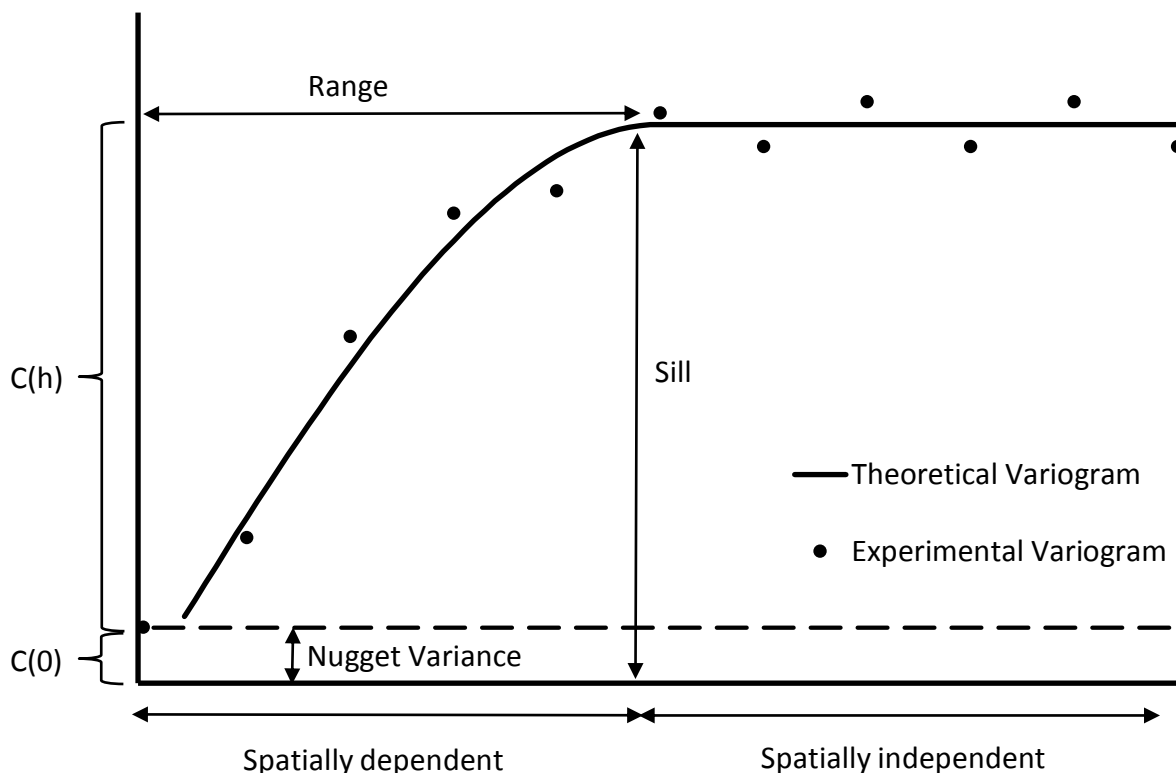


Figure 5.1: Illustration of variogram features: sill variance, nugget variance and range.

The nugget variance results from discontinuities in the data that are e.g. due to measurement errors; it equals $C(0)$ which is the covariance at lag distance zero. A high nugget effect means weak spatial correlation between analyzed values. Sill is the maximum variance reached at a

certain lag distance h and consists of the spatially correlated variance $C(g)$ and the nugget variance $C(0)$. The lag distance at which the sill reaches its maximum value is called range. Values separated by a lag distance at or below the range are spatially dependent; values separated at a lag distance above the range are spatially independent. High range and low sill values indicate large spatial homogeneity in the dataset while low range and high sill indicate large heterogeneity (Oliver, 2010).

A **theoretical variogram** can be fitted to the experimental variogram in order to calculate the spatial correlation for each lag distance. Most frequently used theoretical variograms include the spherical, the Gaussian and the exponential models (refer to Figure 5.2 for illustration). Due to the fact that the Gaussian and exponential variogram models reach their sill values in an asymptotic way, the range value is defined as the lag distance at which the variance reaches 95% of the sill variance. In this case, the range value is denoted as “effective range”.

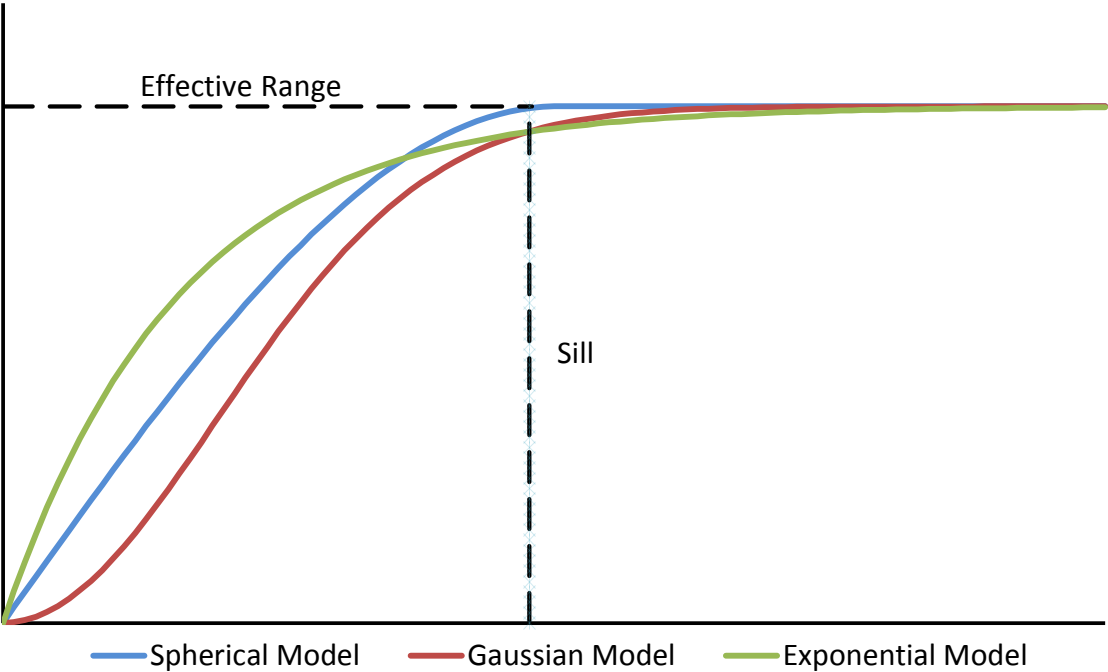


Figure 5.2: Illustration of spherical, Gaussian and exponential theoretical variogram models with sill and effective range value.

When fitting a theoretical variogram to an empirical variogram, the quality of the experimental variogram is of high importance. Best results are achieved if the experimental variogram has the same number of pairs in each lag. To achieve a good distribution of sample points to the lags, several parameters can be adjusted (refer to Figure 5.3 for illustration). First of all, the lag distance and the maximum allowed lag distance influence the number of lags for which pairs will be calculated. As the lags are defined as a vector, the search angle (the direction in which is looked for pairs) can be altered which is helpful if the data exhibit anisotropy. Furthermore, lag and angle tolerances can be used to adjust the number of pairs in each lag (Deutsch and Journel, 1998).

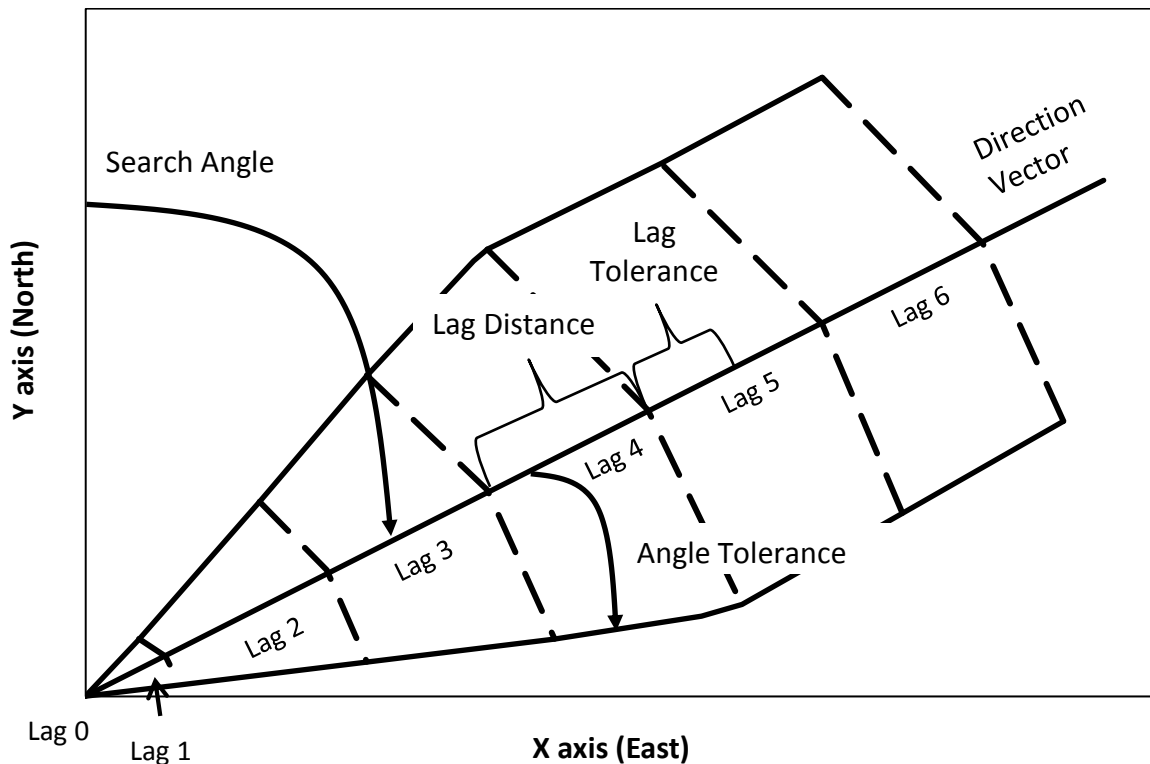


Figure 5.3: Parameters required for calculating the experimental variogram (adapted after Deutsch and Journel, 1998).

The variogram method has been used to compare the statistical properties of soil moisture products of different origin (measured or simulated) and different spatial scale (from plot to mesoscale catchment). For example, Korres et al. (2014) investigated the variogram properties for measured and simulated soil moisture data from different catchments. They were able to identify three unique combinations of sill and range values that corresponded to a certain catchment size and to either modeled or measured soil moisture data.

The variogram method is not able to appropriately describe heterogeneity of complex patterns like strong heterogeneity in saturated conductivity due to a change in soil texture. Multi-point geostatistics are therefore used to calculate correlations for more than two locations at each time step. This approach requires three-dimensional information. As these are usually not available, “training images” are used in multi-point geostatistics. Training images are conceptualizations of the expected pattern, for example the soil texture distribution of a test site derived from measurement data or other proxy data. For example, Huysmans and Dassargues (2009) applied this approach to derive hydrological conductivities for an aquifer with complex heterogeneity and utilized photographs and observations of sedimentary structures to construct the training image. They used the derived hydrological conductivities for a simulation of contaminant transports and found that the multi-point geostatistical method leads to superior simulations compared to those achieved with the commonly used variogram approach.

Apart from the variogram approach, **empirical orthogonal functions** (EOF) and **entropy** are used to characterize patterns. Empirical orthogonal functions decompose patterns of e.g. soil moisture into stable (non-random) and random spatial patterns revealing the explained variance of each derived spatial pattern (for a detailed description refer e.g. to Korres et al., 2010). Korres et al. (2010) derived empirical orthogonal functions for surface soil moisture measured at a grassland and an agricultural test site. They correlated the resulting patterns to time invariant patterns of topographical characteristics and soil texture distributions and found that the most stable EOF explained 57.5% of total spatial soil moisture variance; the correlation analysis revealed that this pattern was mainly controlled by the existence of gleyic or non-gleyic soils thus indicating a strong link to infiltration. Graf et al. (2014) applied the EOF method to soil moisture measurements in a forested catchment. They found that the spatiotemporal variability of the soil water storage was to a large degree explained by two underlying patterns that were related to the spatial average of soil moisture. The first EOF pattern explained ~86% of soil moisture variance and basically resembled the relationship between standard deviation and mean soil moisture.

Entropy is a measure of uncertainty. When applied to Hortonian infiltration, entropy illustrates that the uncertainty of the Horton equation increases with increasing dryness prior to a rainfall event. This means that the information content included in the observation of the uncertain event of Hortonian runoff above dry areas is large (reported in Singh, 2010). In the case of Hortonian infiltration, the uncertain event is connected to a low probability. On the contrary, occurrence of Hortonian overland flow on saturated areas is very likely and thus the entropy value and the information content included in the observation of such an event is low. Singh (2011) and Hao and Singh (2015) provide an overview about the theory and application of entropy in the field of hydrology. Castillo et al. (2015) developed an entropy-based index of model complexity which compares a given soil moisture distribution to assumed soil moisture distributions reflecting the maximum and minimum possible complexity of soil water deficit distribution throughout a catchment. Castillo et al. (2015) found a clear dependency of complexity in soil water deficit distribution on climate and topographic catchment attributes.

Kriging is a statistical spatial **interpolation** method. In contrast to deterministic interpolation techniques like Inverse Distance Weighting or Thiessen Polygons, the Kriging method considers information on the spatial variability of a variable as measured by the variogram. In its most basic form, Ordinary Kriging estimates an unknown value of a random variable at a given location by applying weights to known values in proximity to the location with the unknown value. The weights are determined by minimizing the Kriging variance (mean squared error between the real and the estimated value) in a least-square sense (for detailed description of the Kriging method, the reader is referred to Deutsch and Journel, 1998). Weights are sensitive to nugget variance and anisotropy (trend in the variable in at least one direction). A high nugget-to-sill ratio or a low range causes high weights of known values with a large distance to the

location of the unknown value. **Kriging interpolation** can be performed block- or pointwise. When Kriging is performed blockwise, the covariance matrix includes random variables at the sample location and locations inside the block, while for point Kriging only important locations are taken into account for the interpolation. Deutsch and Journel (1998) give details about strategies for searching nearby data whereas Oliver (2010) remarks that the number of nearby data should be between 16 and 20 data points for a reliable interpolation. Block Kriging generally allows for smoother interpolation results than point Kriging and is therefore commonly used when the area for which a prediction is required is larger than the sample extent (Oliver, 2010). Ordinary Kriging can be extended with a trend model (Universal Kriging) to incorporate data trends. Furthermore, a second variable can be used for the interpolation in a linear regression approach (Cokriging).

In this thesis, the variogram method is applied to analyze the autocorrelation structure of simulated and measured soil moisture data. Based on this analysis, kriging interpolation is used to obtain an illustrative representation of spatial soil moisture patterns. ¹The level of agreement between interpolated patterns is quantified with Kappa statistics (Viera and Garrett, 2005). The Kappa value consists of two factors: KLoc and KHisto. A KLoc of 1 indicates that observed and simulated soil moisture values are identical at a given location. A KHisto value of 1 indicates a perfect agreement between the histograms of the observed and simulated soil moisture values. The multiplication of KLoc and KHisto results in the Kappa value. A Kappa value of 1 indicates optimal concordance while values below zero indicate complete dissimilarity ¹.

To explore drivers of soil moisture patterns, a Spearman correlation analysis between catchment characteristics (topography, porosity distribution) and measured and simulated soil moisture patterns was performed. The EOF method was not used in the context of this thesis because results from recent studies using EOF (Korres et al., 2010; Graf et al., 2014; Fang et al., 2015) revealed that one EOF pattern already explained over 50% of the total variance. This pattern was highly correlated to soil properties (e.g. Korres et al., 2010; Fang et al., 2015) or the relationship between soil moisture and its standard deviation (Graf et al., 2014). Results of the Spearman correlation analysis conducted in the context of this thesis showed strong correlations between simulated soil moisture patterns and porosity distribution. As this finding was in line with those by Korres et al. (2010) and Fang et al. (2015), the application of the EOF analysis was not expected to reveal additional insights into simulated soil moisture patterns.

¹ Text taken from Cornelissen et al. (2014)

6 Study areas “Erkensruhr” and “Wüstebach”

6.1 Catchment description

Figure 6.1 gives an overview about the study areas Erkensruhr and Wüstebach showing their location, land use distribution and topography. The Erkensruhr catchment is located in western Germany close to the Belgian border (Figure 6.1). It is part of the larger Rur catchment with a size of 2354 km². The Erkensruhr catchment itself is 41.9 km² large with an elevation ranging from 286 m to 631 m above sea level. Highest elevations occur in the south-western area of the catchment, lowest elevations in the northern part of the catchment (Figure 6.1).

The 0.385 km² large (Stockinger et al., 2014) headwater catchment Wüstebach is situated at the southern border of the Erkensruhr catchment (see Figure 6.1).¹ The Wüstebach test site is the central part of the catchment and a major monitoring area of the TR32 project with a size of 0.27 km². Its elevation ranges between 595 and 628 m, with an average slope of 3.6% and a maximum slope of 10.4% (Bogena et al., 2010). The local topography of the headwater catchment is influenced by anthropogenic landforms that date back to the Second World War, e.g. gun emplacements and trenches¹.

The Erkensruhr catchment is part of the Eifel National Park which was established in 2004 covering an area of 110 km². During the Second World War, forests were cut to provide firewood. In the 1950s, fast growing Norwegian spruce (*Picea abies* (L.); Lehmkuhl et al. (2010)) forests were planted to prevent erosion. In the future, the landscape of the Eifel National Park is supposed to develop independently from human impact or control, following ‘natural’ processes. By the year 2034, 75% of the area of the Eifel National Park are supposed to have reached this status. The ‘potentially natural vegetation’ on these areas will then be dominated by slow growing deciduous trees like beech and oak. In order to reintroduce these species, large areas of coniferous stands are about to be cleared. Particularly, the renaturation of river valleys required major clearcuttings in 2011 (Forestry Commission Office of the National Park Eifel, 2012). Coniferous trees will only remain in the southern areas with high precipitation (Forestry Commission Office of the National Park Eifel, 2008). Currently, the Erkensruhr catchment is dominated by coniferous forest (mainly *Picea abies*) in the southern part (including the Wüstebach catchment) and by beech forest (*Fagus sylvatica*) in the northern part. Oak forest, grassland and pasture occupy the central part while a mixture of grassland and pasture dominates the eastern parts of the catchment. In the south-eastern part, a few areas are cultivated (Figure 6.1).

There are two different river types in the catchment: fast flowing rivers in narrow valleys which partly dry out in summer (e.g. Wüstebach) and rivers flowing in grassland and pasture areas with

¹ Text taken from Cornelissen et al. (2014)

slower flow velocities (e.g. Mückenbach, Funkenbach; refer to Figure 6.1). The Wüstebach flows from higher elevated southern areas to the outlet in the north in an asymmetrical v-shaped valley with a steeper eastern and a flatter western flank.

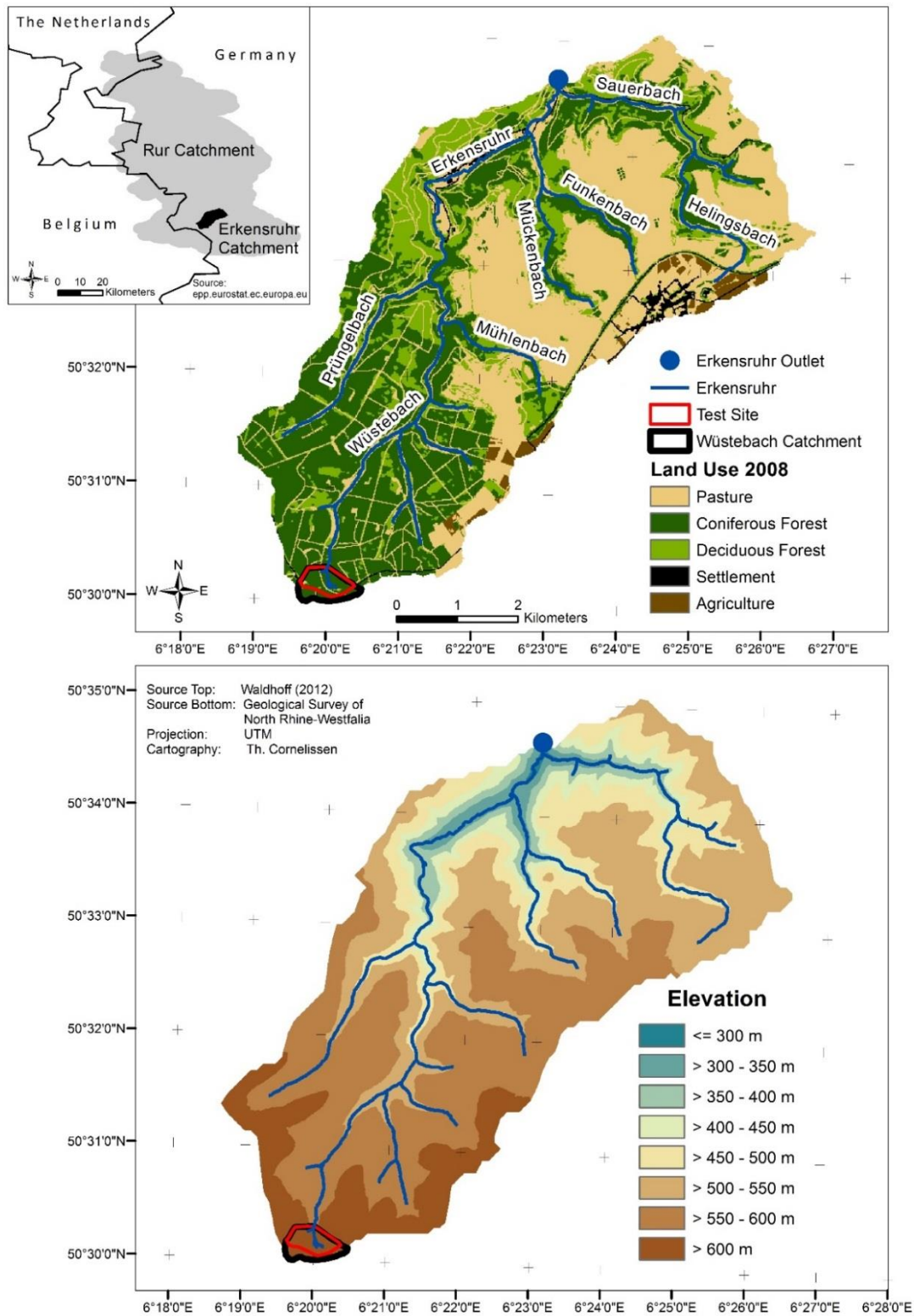


Figure 6.1: Location of the Erkersruhr catchment (top left), distribution of land use classes (top) and topography at 10x10 m resolution (bottom).

The climate is warm-temperate with mean annual temperatures ranging between 7.6°C at high and 10°C at low altitudes. The catchment is characterized by a strong west-east gradient in precipitation with a mean annual precipitation of 1150 mm in western and 740 mm in eastern parts of the catchment (Cornelissen et al., submitted). For the Wüstebach, the mean annual precipitation amounts to 1220 mm (1979-1999; Bogena et al. (2010)). Cambisol is the dominant soil type of the catchment (refer to chapter 6.2.5). Bedrock consists of Devonian clayshales with sandstone intrusions and fractures (Stoltidis and Krapp, 1980). For a detailed description of catchment characteristics, the reader is also referred to Lehmkuhl et al. (2010) and Borchardt (2012).

6.2 Data base and data processing

This chapter summarizes data resolution and availability and justifies the choice of data for simulations of the Wüstebach and the Erkensruhr.

6.2.1 Land use in the Erkensruhr and the Wüstebach catchment

The description of land use data and their processing only refers to the Erkensruhr catchment because the Wüstebach catchment is homogeneously covered with spruce (*Picea abies*) and as such, no spatial land use data had to be prepared.

Table 6.1: Proportional coverage of land use classes in 2008 and 2012 at 15x15 m and 100x100 m resolution.

Land Use Class	Percentage (%) in 2008	Percentage (%) in 2012	Difference (%) 2012-2008
15x15 m resolution			
Agriculture	2	2	0
Grassland	38	36	-2
Coniferous Forest	34	33	-1
Deciduous Forest	20	22	+2
Settlement	2	2	0
Copse	1	2	+1
Heath	3	3	0
100x100 m resolution			
Agriculture	2	2	0
Grassland	35	33	-2
Coniferous Forest	38	36	-2
Deciduous Forest	20	22	+2
Settlement	1	1	0
Copse	1	1	0
Heath	2	3	+1

Land use data were available for the entire Rur catchment at 15x15 m resolution on an annual basis between 2008 and 2012 distinguishing 26 classes for the Erkersruhr catchment (Waldhoff, 2012; Lussem and Waldhoff, 2013). Some land use classes only accounted for less than one percent of the total catchment area and therefore the 26 land use classes were reclassified to 7. The proportional coverage of the classified land uses for 2008 and 2012 and the difference between the two years are given in Table 6.1.

Differences in land use cover between 2008 and 2012 were minor ($\leq 2\%$), thus land use was assumed constant for the hydrological modeling period. As the Erkersruhr was discretized at a 100x100 m resolution, the aggregation of land use data to the required resolution was performed with the corresponding ArcGIS tool, applying the ‘majority’ option which assigns the dominant land use type to the new (larger) grid cell. This causes deviations in the proportional coverage of land use (see Table 6.1). There were large deviations in coverage for pasture (3%) and coniferous forest (4%) classes but only small deviations for the other classes. Despite these deviations, land use change between 2008 and 2012 at 15x15 m resolution was well preserved at the 100x100 m resolution. The resulting spatial land use patterns are given for 2008 and 2012 in Figure 6.2 at a 100x100 m resolution.

Distribution and characteristics of ‘Heath’ and ‘Copse’ were unclear because (1) both land use classes were not sufficiently described in the data source and (2) ‘Heath’ did not occur in the catchment. As ‘Heath’ mainly occurred next to ‘Grassland’, all elements of this class were allocated to ‘Grassland’. Elements with class ‘Copse’ were evenly distributed between ‘Deciduous’ and ‘Coniferous’ land use classes. As land use was assumed constant over the period 2008 to 2012, the land use distribution of 2008 was chosen as reference distribution for the simulation.

The triangular shape of the elements in HydroGeoSphere (see chapter 7.2) made the direct implementation of gridded land use data impossible. Instead, the dominant land use fraction for each HydroGeoSphere element had to be computed from the gridded information. Table 6.2 shows that deviations between the gridded and triangulated distributions remain small ($< 2.5\%$).

Table 6.2: *Percentual distribution of land use classes of the gridded input data and of the HydroGeoSphere simulation grid.*

Land Use Class	Land use cover grid (%)	Land use cover triangulated (%)	Difference (%)
Agriculture	1.82	1.65	-0.17
Grassland	35.44	37.77	2.33
Coniferous Forest	38.38	40.41	2.03
Deciduous Forest	20.18	19.43	-0.75
Settlement	1.03	0.75	-0.28
Copse	0.98	0.00	-0.98
Heath	2.17	0.00	-2.17

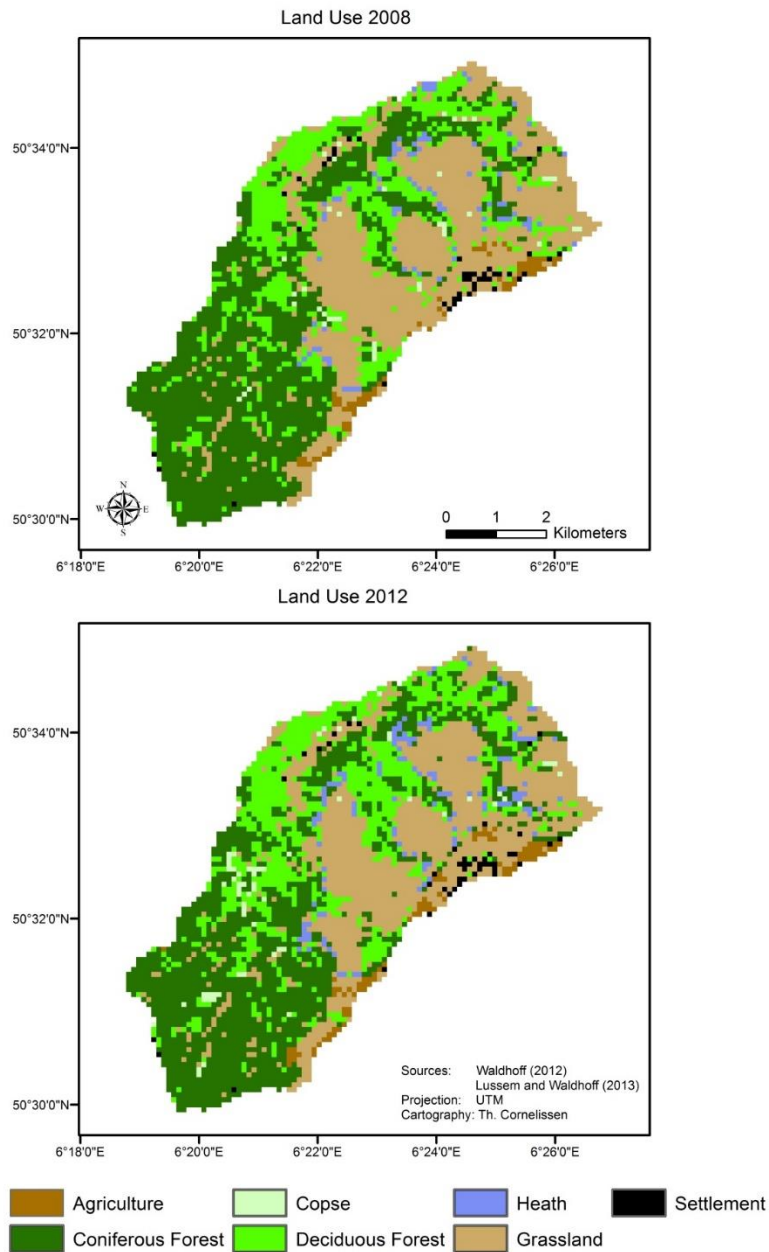


Figure 6.2: Land use distribution in the Erkersruhr catchment at a 100x100 m resolution in 2008 and 2012.

6.2.2 Climate and precipitation data

Figure 6.3 shows the locations of meteorological stations near the Erkersruhr catchment and Table 6.3 specifies type, availability and resolution of measured data. Necessary climate data for the calculation of potential evapotranspiration with the FAO Penman-Monteith method (Allen et al., 1998) include vapor pressure (or relative humidity), wind speed, temperature and radiation (or sunshine duration).

As shown in Table 6.3, radiation or sunshine duration data was rarely available. The stations Kalterherberg and Schleiden (Meteomedia) did not provide enough data because global

radiation was not recorded before the end of 2010, and sunshine duration data of the station at Kall-Sistig were not representative due to their distance to the Wüstebach catchment (Figure 6.3).

The relevant climate data was finally taken from the station at Schöneiseffen operated by the TERENO project. As measurements at this station began on 1st of July 2009, all simulations also started at this date.

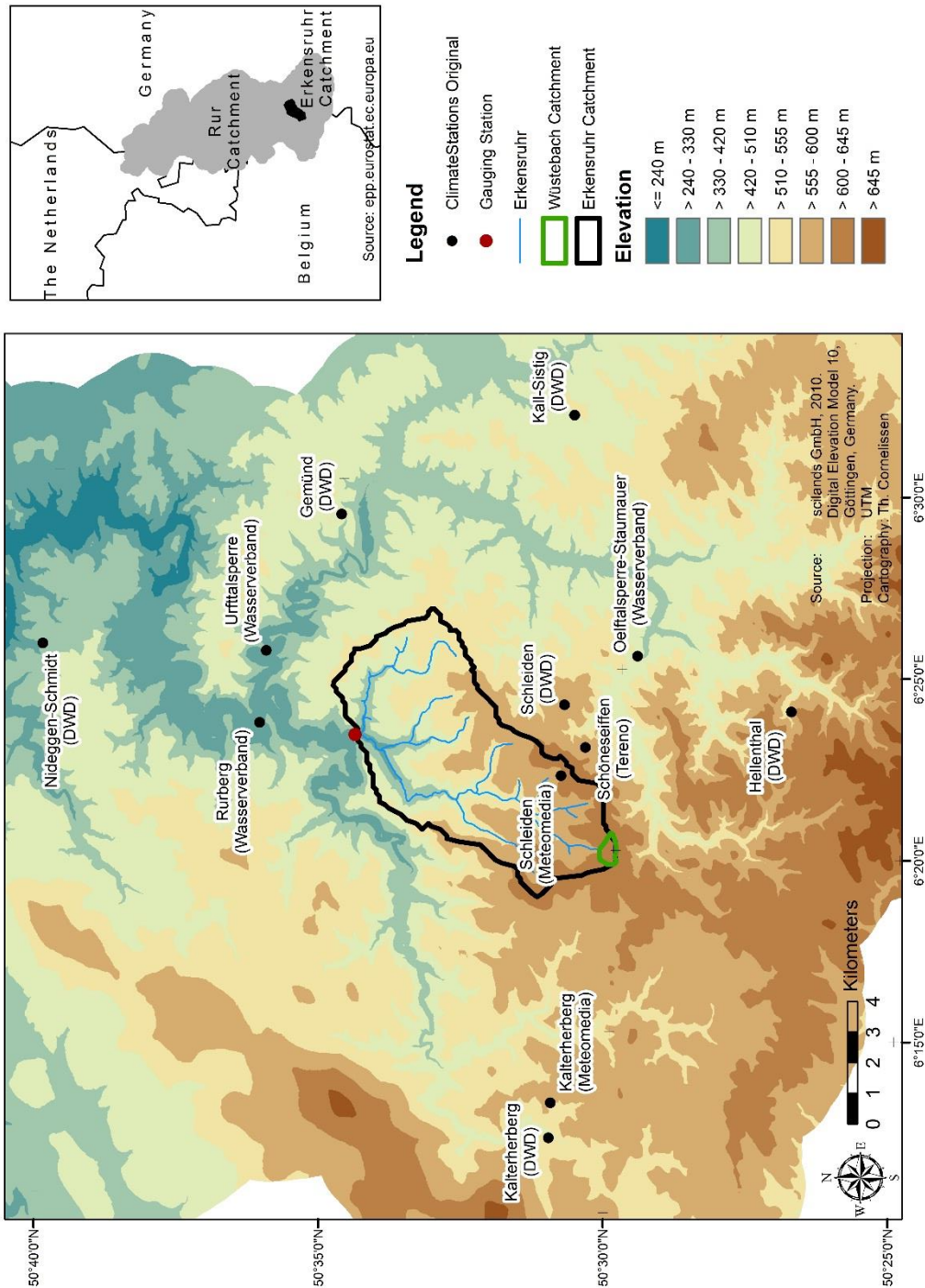


Figure 6.3: Location and topographic situation of climate stations near the Erkersruhr catchment.

Table 6.3: Summary of available climate and precipitation data for the Erkensruhr catchment.

Station Name	(Operator)	Precipitation	Climate ¹	Additional Data
Monschau-Kalterherberg	DWD	1.1.1941 (daily) 1.9.2006 (hourly)	-	6-hourly 1.9.2006 Height of new snow; Snow height; Water equivalent of 1cm snow
Kall-Sistig	DWD	1.8.2004 (hourly)	1.8.2004 (T, V, SSD, hourly) 17.10.2007 (RH, hourly)	Hourly 1.8.2004 Dew point temperature; Temperature at ground 6-hourly 17.10.2007 Snow height
Hellenthal-Hollerath	DWD	1.1.1951 - 31.12.2006 (daily)	-	-
Schleiden-Gemünd	DWD	1.1.1951 - 28.2.2006 (daily)	-	-
Schleiden-Schöneseiffen	DWD	1.1.1959 – 31.7.2007 (daily)	-	-
Nideggen-Schmidt	DWD	1.1.1994 (daily) 1.6.2004 (hourly)	1.1.1994 (T,RH,V, daily) 1.8.2007 (T,RH,V, hourly)	1.1.1994 (Height of new snow; Snow height; daily) 1.6.2004 (Dew point temperature; Temperature at ground; Height of new snow; Snow height; hourly)
Schöneseiffen	Tereno	-	1.7.2009 (T,V, atmospheric and vapor pressure, shortwave incoming radiation, hourly)	-
Schleiden	Meteoedia	29.10.2001-10.10.2012 (hourly)	29.10.2001 (T, RH, V, hourly) 31.12.2010 (Global radiation, hourly)	-
Kalterherberg	Meteoedia	2.10.1998 - 9.10.2012 (hourly)	2.10.1998 (T, RH, V, hourly) 31.12.2010 (Global radiation, hourly)	-
Oelftalsperre – Staumauer	Wasserverband Eifel-Rur	1.5.2000 - 31.1.2010 (hourly)	1.5.2000 - 28.2.2010 (T, hourly)	-
Rurberg	Wasserverband Eifel-Rur	10.5.2001- 1.2.2010 (hourly)	10.5.2001 - 1.3.2010 (T, hourly)	-
Urfttalsperre	Wasserverband Eifel-Rur	1.5.2000 -1.2.2010 (hourly)	1.5.2000 - 1.3.2010 (T, hourly)	-

¹ T=Temperature; V= Wind Speed; RH=Relative Humidity; SSD=Sunshine Duration

Due to their proximity to the catchment and their temporal availability, the stations at Schleiden and Kalterherberg (Meteoedia) and a second station at Kalterherberg operated by the German

Weather Service (DWD) could eventually provide necessary precipitation data for the simulation of the **Wüstebach** catchment. To decide which data to select, measured precipitation of the three stations was compared to other components of the water balance (discharge, actual and potential evapotranspiration) in the form of annual sums between 2010 and 2012 (Table 6.4). The last column in Table 6.4 depicts the water balance residual in percentage of total rainfall. As measurements of actual evapotranspiration started on 5th of May 2010 and measurements of climate data from the Schönesseiffen station (TERENO) started on 1st of July 2009, the table also gives sums of water balance components for these sub-periods.

Table 6.4: Measured annual discharge, precipitation, actual and potential evapotranspiration sums between 2010 and 2012 for the Wüstebach catchment.

	Precipitation (mm)	Discharge (mm)	PET (mm) ¹	AET (mm) ²	Residual (%)
Station Name					
01.07.2009 - 31.12.2009					
Schleiden (Meteoedia)	548	200	352		
Kalterherberg (Meteoedia)	654	200	352		
Kalterherberg (DWD)	681	200	352		
Kalterherberg (DWD) corrected	768	200	352		
Kalterherberg (DWD) corrected; with snow	768	200	352		
01.05.2010 - 31.12.2010					
Schleiden (Meteoedia)	783	248	556	377	20
Kalterherberg (Meteoedia)	811	248	556	377	23
Kalterherberg (DWD)	880	248	556	377	29
Kalterherberg (DWD) corrected	990	248	556	377	37
Kalterherberg (DWD) corrected; with snow	881	248	556	377	29
2010					
Schleiden (Meteoedia)	986	608	694		
Kalterherberg (Meteoedia)	1077	608	694		
Kalterherberg (DWD)	1178	608	694		
Kalterherberg (DWD) corrected	1334	608	694		
Kalterherberg (DWD) corrected; with snow	1226	608	694		
2011					
Schleiden (Meteoedia)	818	630	756	596	-50
Kalterherberg (Meteoedia)	1008	630	756	596	-22
Kalterherberg (DWD)	1096	630	756	596	-12
Kalterherberg (DWD) corrected	1239	630	756	596	1
Kalterherberg (DWD) corrected; with snow	1348	630	756	596	9
2012					
Schleiden (Meteoedia)	794	589	689	606	-50
Kalterherberg (Meteoedia)	938	589	689	606	-27
Kalterherberg (DWD)	1294	589	689	606	8
Kalterherberg (DWD) corrected	1462	589	689	606	18
Kalterherberg (DWD) corrected; with snow	1462	589	689	606	18

¹PET=Potential Evapotranspiration; ²AET=Actual Evapotranspiration

The comparison between the stations shows that only the station at Kalterherberg (DWD) provided a reasonable closure of the water balance (also refer to Graf et al., 2014). Precipitation data were corrected following the method described by Richter (1995). The correction resulted in an annual increase of 13 % in precipitation, reducing the water balance residual in 2011 from -12% to +1%, but increasing the residual in 2012 from +8% to +18%.

Actual Evapotranspiration at the Wüstebach catchment has been measured on top of a 38 m measurement tower by the **eddy-covariance** technique since May 2010 (Drüe et al., 2012). The technique is based on the phenomenon that air parcels having e.g. a specific water vapor, are transported by turbulence (eddy). The vertical flux of e.g. latent heat can thus be interpreted as the covariance between vertical wind velocity and the concentration of water vapor. The measurements of the eddy-covariance technique are not associated to a certain point, but to a footprint (comparable to the “spacing” dimension of the scale triplet) which changes with wind direction and speed. According to Mauder et al. (2013) the changes in footprint - in addition to instrumental noise and the stochastic nature of turbulence - comprise the sources of random errors. Systematic errors may arise from the closure of the energy balance originating from the systematic underestimation of turbulent fluxes related to advection. At the Wüstebach catchment, a systematic error arises during periods of northern wind directions because under these wind conditions, an anemometer backwind arises (Graf et al., 2014). The data gathered during northern wind conditions amounts to roughly 8% of total data between the period May 2010 and April 2013 and was excluded a priori from the data set. In total the fraction of missing or dismissed data amounted to ~54% for the Wüstebach. Therefore, a gap-filling was necessary as described in Graf et al. (2014). The following figure (Figure 6.4) shows the gap-filled eddy covariance data set at daily resolution.

Due to the lack of a snow model in HydroGeoSphere, snow storage dynamics were simulated with the **degree-day-method** (Maidment, 1993). This method simplifies the heat balance of the snow pack by assuming that temperature is the only influencing factor and that the snow surface keeps a temperature of 0°C. Snow is accumulated when the air temperature is below or equal to zero and melts for temperatures above zero. The amount of melted snow equals the precipitation rate at that time step plus the temperature multiplied by the degree-day factor. Snow storage is reduced by the amount of melted snow. The degree-day-factor was calibrated at hourly time steps by comparing simulated to measured snow storage which was calculated by multiplying measured snow height with snow water equivalent data from Kalterherberg (DWD).

Figure 6.5 compares calibrated (with a degree-day-factor of 0.25) to measured snow storage at the station Kalterherberg (DWD). The figure shows that the dynamics and the amount of snow storage were well captured by the model ($R^2 = 0.94$ during winter 2010/2011). The resulting precipitation rate at hourly resolution was aggregated to daily time steps, thus avoiding differences in precipitation between simulations at hourly and daily resolution.

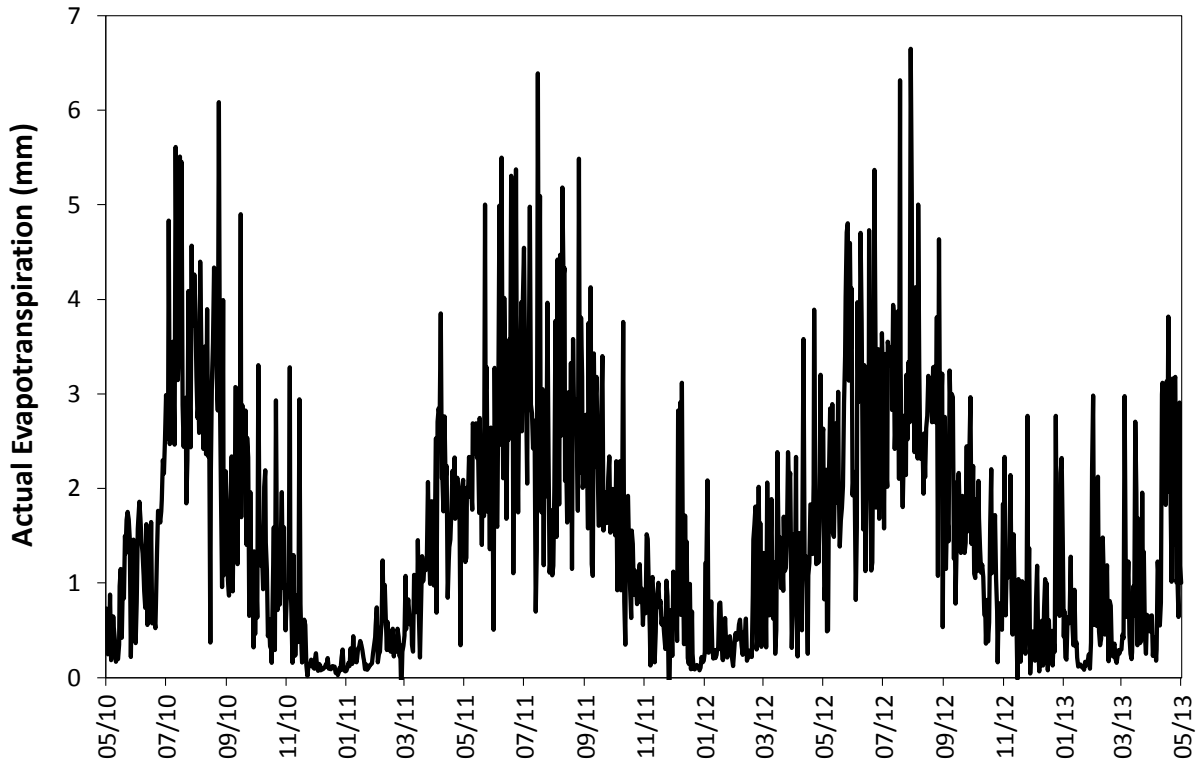


Figure 6.4: Daily actual evapotranspiration measured at the Wüstebach catchment between May 2010 and April 2013.

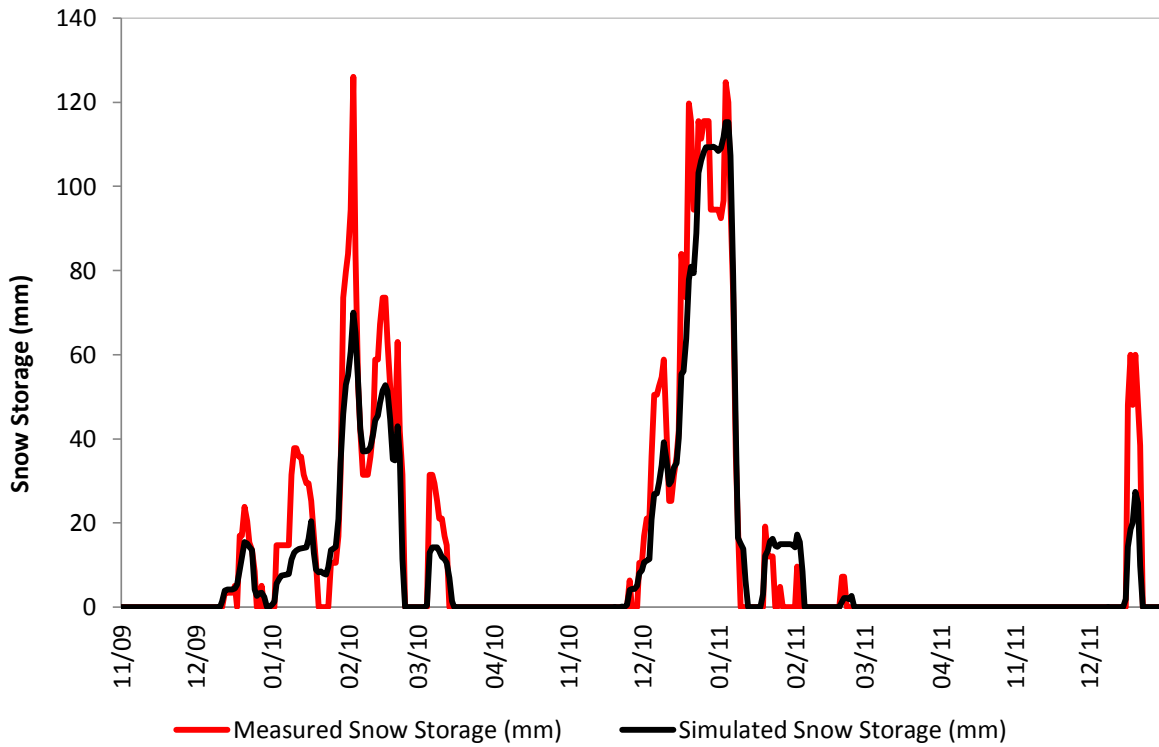


Figure 6.5: Comparison between measured and simulated snow storage for the winter periods between end of 2009 and end of 2011.

In the following sections, data availability and processing for the incorporation of spatial variability in precipitation and potential evapotranspiration for the **Erkensruhr** simulation is described.

Figure 6.6 shows mean annual **precipitation** sums between 2006 and 2012 for 5 stations. Precipitation decreased by at least 340 mm from stations in the west e.g. Kalterherberg (DWD) to stations in the east e.g. Kall-Sistig (DWD). Correlation coefficients (R^2) between longitude and precipitation ranged between 0.82 (2007) and 0.98 (2011). Weaker correlations existed between latitude and precipitation (0.1 to 0.7) and elevation and precipitation (0.33 to 0.72). Thus, the spatial distribution of precipitation has to be taken into account for the discharge and water balance simulation at the Erkensruhr catchment.

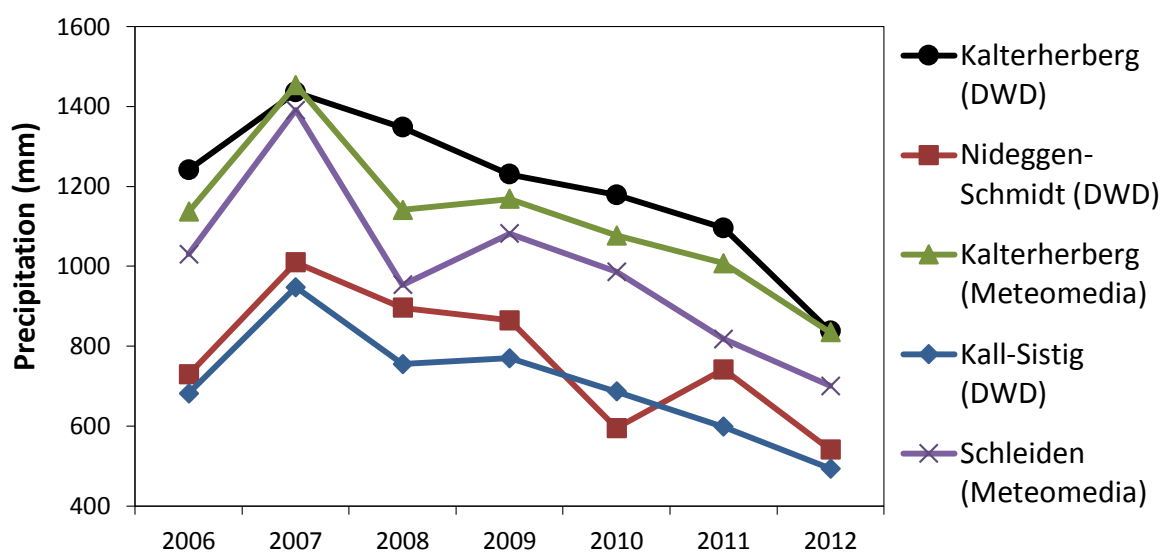


Figure 6.6: Mean annual precipitation between 2006 and 2012 for 5 stations in the Erkensruhr catchment.

The incorporation of spatially heterogeneous precipitation data can be acquired by the usage of spatial interpolation methods. As HydroGeoSphere does not offer any internal routine for the interpolation of climate data, interpolation had to be done in advance. Generally, interpolation methods are either exclusively distance based (Inverse Distance, Thiessen Polygons) or they take into account mean and variance (Kriging; refer to chapter 5). Precipitation data interpolated with distance based methods heavily exaggerated the influence of the station Schleiden (Meteoedia) due to the large distances between Schleiden (Meteoedia) and other stations e.g. Kalterherberg (DWD; refer to Figure 6.3). Other methods that include mean and variance require a certain amount of data points to achieve statistically sound results (refer to chapter 5). The maximum number of only five available stations was far below the recommended minimum amount of sampling points. Thus, interpolation methods failed in mapping the precipitation pattern.

Due to the difficulty in spatial interpolation, **radar data** of the catchment were acquired from the Wasserverband Eifel-Rur (WVER). The data originate from the radar station Neuheilenbach (operational since 1998) which is situated approximately 46 km south of the Wüstebach catchment at an elevation of 585 m (hydro & meteo GmbH & Co. KG, 2012). The radar has a spatial resolution of 1x1 km and a temporal resolution of 5 minutes. The data have been corrected for soil echoes and attenuation (weakening of the radar beam behind a pixel with heavy rainfall). In addition, data were adjusted to precipitation stations in order to correct for the bright band effect which describes the influence of snow melting on the detection of rainfall and snow. Data gaps were closed with data from the radar station at Essen (hydro & meteo GmbH & Co. KG, 2012). Figure 6.7 compares the annual precipitation sums of the radar data with station data close to the Erkersruhr catchment.

To properly incorporate the spatial variation of **potential evapotranspiration at the Erkersruhr catchment**, a mean temperature gradient per elevation had to be defined. In Figure 6.8, mean annual temperatures between 2006 and 2012 are shown for 6 stations (locations are given in Figure 6.3). As can be seen in Figure 6.8, stations at higher elevations (Schleiden, Kalterherberg and Kall-Sistig) had a significantly lower mean annual temperature than those at lower elevations (Nideggen-Schmidt, Urfttalsperre and Rurberg). Significance was tested with a one-sided t-test with unknown variances and a significance level of 5%. The correlation between temperature and elevation was found to be very strong with correlation coefficients between 0.92 (2008, 2011) and 0.97 (2009). The effect of changing temperatures on the amount of potential evapotranspiration (FAO Penman-Monteith; Allen et al. (1998)) was tested by altering given hourly temperatures by $\pm 10\%$. The resulting change in potential evapotranspiration equaled the temperature change. Thus, spatial variability in potential evapotranspiration had to be included in the simulation of the Erkersruhr catchment.

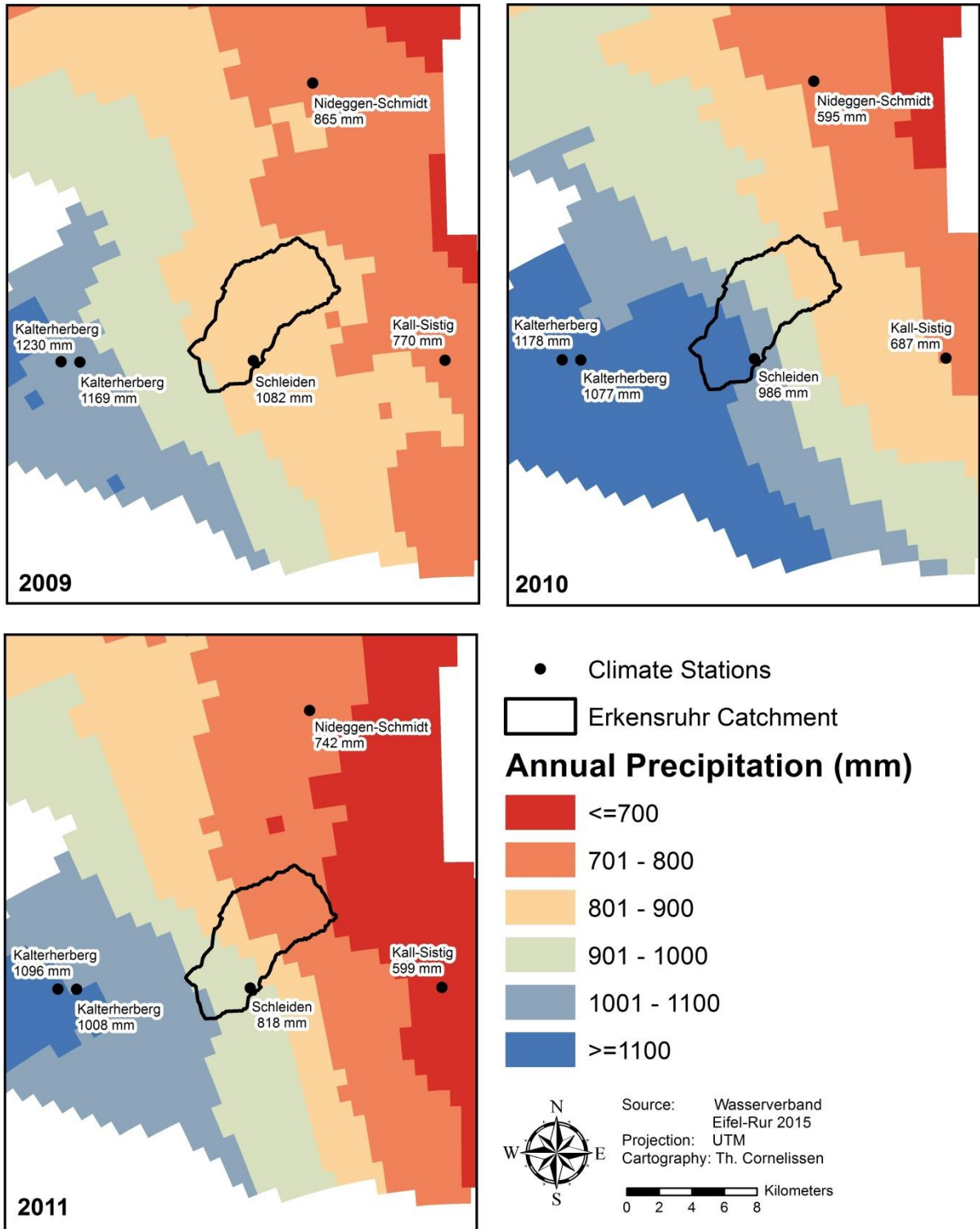


Figure 6.7: Location of climate stations with annual precipitation sum and pattern of annual precipitation as measured with the radar data of 1x1 km resolution by the Wasserverband Eifel-Rur.

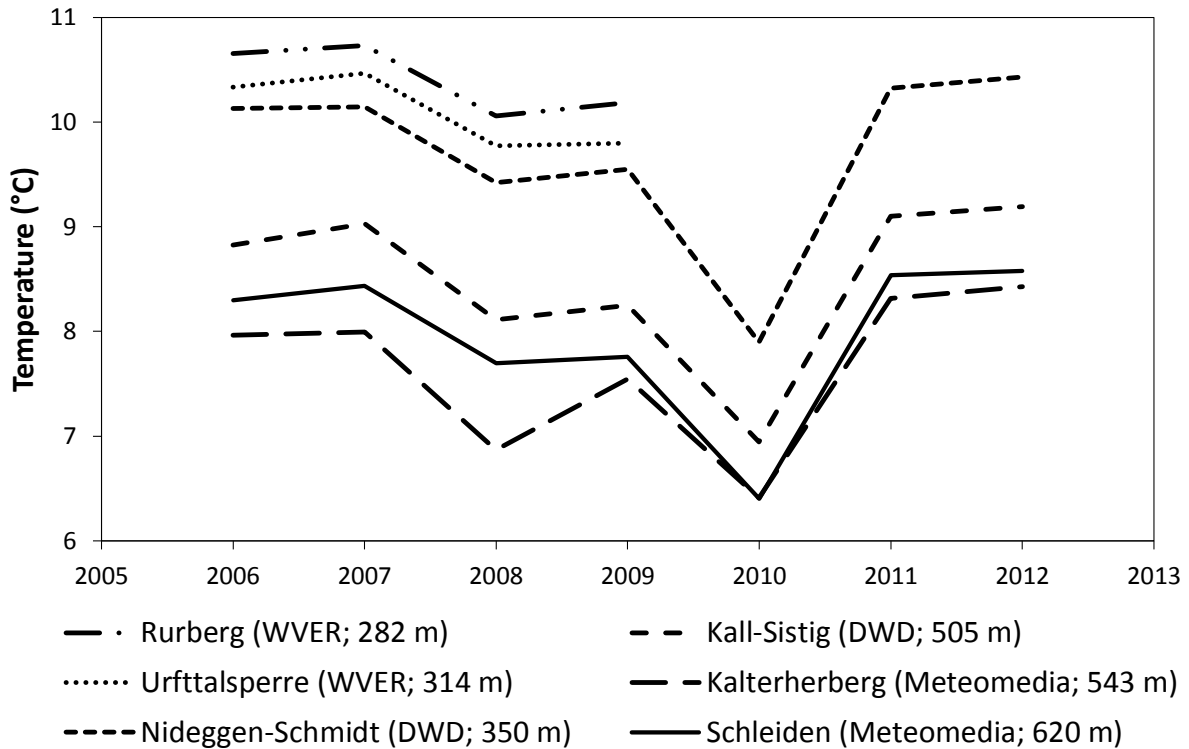


Figure 6.8: Mean annual temperatures between 2005 and 2012 at 6 stations in the Erkensruhr catchment. Stations are sorted from the highest (Schleiden) to the lowest (Rurberg) elevation.

To include the spatial variation of potential evapotranspiration, a temperature gradient per elevation was required and computed with two linear regressions performed with mean annual temperature values between 2006 and 2009 for 5 stations (Rurberg, Urfttalsperre, Nideggen-Schmidt, Kall-Sistig and Schleiden) and between 2010 and 2012 for 3 stations (Nideggen-Schmidt, Kall-Sistig and Schleiden). The station at Kalterherberg (Meteomedia) was removed from the regression analysis because – although located at a lower elevation - its mean annual temperatures were lower in comparison to the station Schleiden (Meteomedia). The combination of the regression curves of the two time periods (without Kalterherberg (Meteomedia)) led to a mean temperature gradient of 0.66°C per 100 m and an R^2 of 0.99 between simulated and measured mean annual temperatures. When including the station Kalterherberg in the regression analysis, R^2 dropped slightly to 0.91 but the temperature gradient increased from 0.66°C to 0.73°C per 100 m. Figure 6.9 illustrates the effect of the station on the linear trend lines for the two time periods.

In order to distribute the temperature measured at the station Schöneiseiffen (TERENO) according to the calculated temperature gradient, altitude layers were defined. Temperature at Schöneiseiffen (TERENO) was arbitrarily defined to be valid for 50 m above and below the station height of 610 m. Therefore, the following altitude layers were defined: below 360 m, ≥ 360 m to < 460 m, ≥ 460 m to < 560 m and higher than 560 m.

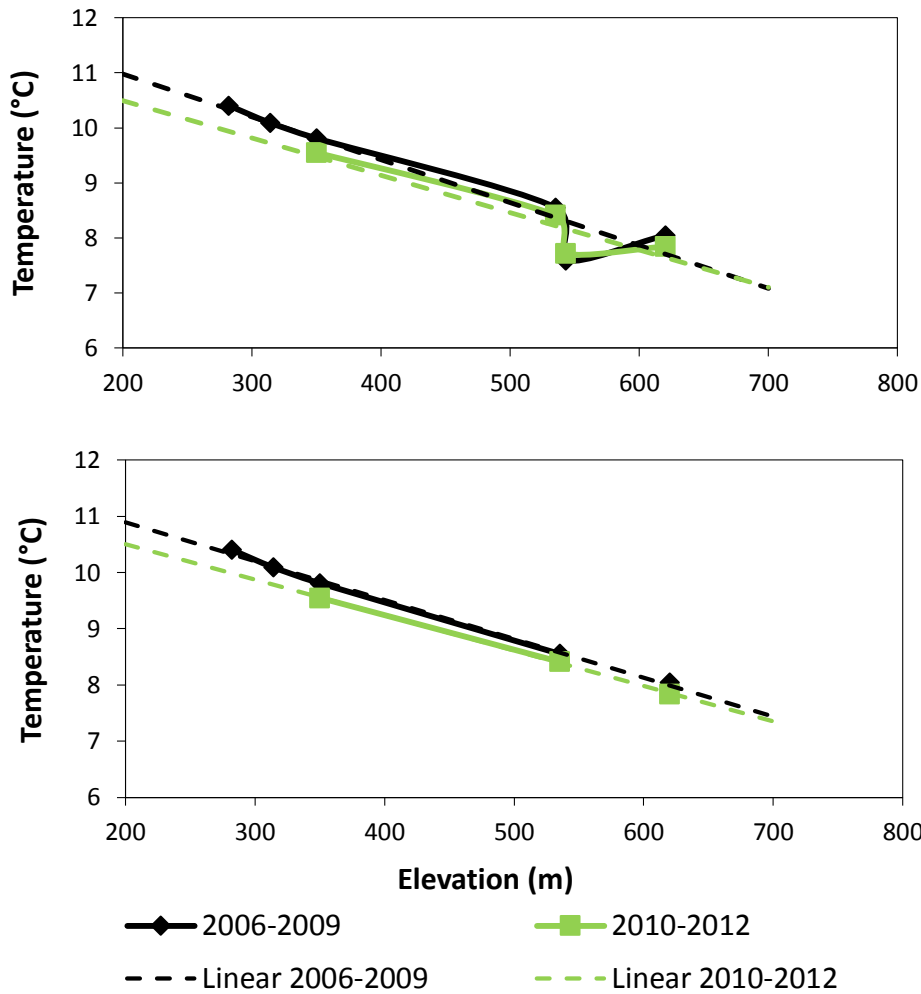


Figure 6.9: Linear regression between elevation and temperature line calculated with (top) and without (bottom) the station Kalterherberg (MeteoMedia).

Potential evapotranspiration was computed for the **Wüstebach** and the **Erkensruhr** simulations at hourly time steps following the FAO Penman-Monteith crop-reference equation (Allen et al., 1998). The results were aggregated to daily resolution:

$$PET = \frac{0.408\Delta(R_n - G) + \gamma \frac{900}{T + 273} u (e_s - e_a)}{\Delta + \gamma(1 + 0.34u)} \quad \text{Equation 10}$$

where Δ is the slope vapor pressure curve (kPa/°C), R_n is net radiation (MJ/m²*day), G the soil heat flux density (MJ/m²*day), γ is the psychrometric constant (kPa/°C), T is temperature (°C), u is wind speed (m/s) and $e_s - e_a$ is the saturation vapor pressure deficit (kPa). The calculation of net radiation requires the definition of an albedo value.

The equation is valid for extensive grassland with uniform height, a given aerodynamic resistance of 208 divided by wind speed (s/m) and a surface resistance of 70 (s/m) (Allen et al, 1998). If the potential evapotranspiration is calculated for vegetation differing from a well-watered grass reference crop surface, the crop coefficient can be used to include the combined

effects of vegetation characteristics (e.g. stomata resistance) on transpiration and evaporation. For grassland and coniferous forest, the crop coefficient equals 1 (Allen et al., 1998) but for deciduous forest, it ranges between 0.79 and 0.9 (data for *Fagus sylvatica* by Verstraeten et al., 2005).

Due to the fact that the crop coefficient equals 1 for spruce forests, only the albedo had to be changed at the Wüstebach catchment and was set to 0.075 which is an average of values reported by Armbruster et al. (2004) and Bernhofer et al. (2003). Resulting potential evapotranspiration values were already introduced in Table 6.4.

At the Erkensruhr catchment, each altitude layer has its unique mixture of land use types. This circumstance affects the albedo, surface and stomata resistance parameters and the crop coefficient. Based on the fractions of land use types per altitude layer (refer to Table 6.5), the maximum possible difference in annual potential evapotranspiration due to changes in crop coefficient amounts to 9% at altitudes between 360 and 460 m. As this altitude only accounted for 16% of the total catchment area (Table 6.6), the annual potential evapotranspiration sum for the whole catchment could only vary by 4%. Due to the low influence of the crop coefficient on catchment's total potential evapotranspiration combined with the fact that these values cannot be validated, the crop coefficient was not adjusted. Thus, only the albedo value has been adapted to the following values: Coniferous Forest: 0.075 (from Wüstebach study, see above), Deciduous Forest: 0.19 (Breuer et al. 2003), Grassland: 0.2175 (Breuer et al. 2003), Urban: 0.3 (assumption), Crops: 0.22 (Breuer et al. 2003). Table 6.5 shows weighted mean albedos and Table 6.6 annual potential evapotranspiration sums for the different altitude layers of the Erkensruhr catchment.

Table 6.5: Land use fraction per altitude layer and computed mean albedos per altitude layer.

Land use	Land use fraction per altitude layer			
	<360	360<460	460<560	>560
Deciduous (%)	35	39	21	9
Spruce (%)	35	33	41	74
Grassland (%)	30	27	37	17
Urban (%)	1	1	1	0
Agriculture (%)	0	0	1	0
Weighted Mean Albedo (-)	0.16	0.16	0.15	0.11

In the third part of this thesis (chapter 8.4), a **long-term simulation run** was conducted. The aim was to simulate the change of water balance and evapotranspiration components with forest growth between 1951 and 2000. Daily climate and rainfall values from 1951 onwards were available at the station of Kall-Sistig (DWD) except for relative humidity and absolute sunshine starting on 1.1.1961. In addition, the time series at Kall-Sistig had a measurement gap between 1st January 1968 and 31st July 1968. These gaps were filled with data from the DWD station at Aachen which provided gapless climate data from 1.1.1937 on.

Table 6.6: Annual sums of potential evapotranspiration per altitude layer between 1st July 2009 and 2012 and area fraction per altitude layer.

Year	Annual sums of potential evapotranspiration (mm) per altitude layer				Area-Weighted sums
	<360 m	360 m - 460 m	460 m - 560 m	≥560 m	
1.7-1.12 2009	406	378	354	340	355
2010	784	734	692	671	696
2011	858	803	756	732	760
2012	788	735	689	666	693
Fraction of catchment (%)	4	16	49	31	100

Data from Aachen have been corrected by a linear regression model between climate variables measured at Kall-Sistig and Aachen for the period 1st August 1968 to 31st December 2000. Correlation coefficients reached high values for minimum and maximum temperature ($R^2=0.97$) and vapor pressure data ($R^2=0.94$), but only a moderate value for absolute sunshine duration ($R^2=0.85$). Correlations for precipitation and wind speed were lowest ($R^2<0.7$) and the applied regression function did not result in a significant improvement compared to original values from the station at Aachen. Thus, precipitation and wind speed data were transferred without any change from Aachen to Kall-Sistig for the period 1st January 1968 to 31st July 1968. Gap-filled climate data were used to calculate the FAO Penman-Monteith potential evapotranspiration (Allen et al., 1998) and snowfall as previously described.

6.2.3 The Wüstebach measurement network

This chapter describes the ‘Soil Moisture Sensor and Interception Monitoring Network’ that was installed specifically in the Wüstebach catchment. The measurement of actual evapotranspiration is – among other measurements – part of the Wüstebach measurement network and was already described in chapter 6.2.2 because these data were used to justify the choice of precipitation data for the Wüstebach catchment. Figure 6.10 depicts the measurement locations of the Soil Moisture Sensor and Interception Monitoring Network and of the eddy-covariance measurement tower at the Wüstebach catchment. These measurements are confined to the test site area of the catchment. The existence of such high-resolution data was therefore the reason for restricting the simulation area to the test site.

¹ For measuring **soil moisture**, a wireless soil moisture sensor network (SoilNet; Bogena et al., 2010) was installed in the Wüstebach in August 2009 consisting of 900 sensors (see Bogena et al. (2007) for further details on the sensor technology). At 150 locations, sensor pairs were installed at 5, 20 and 50 cm depth with a horizontal distance of 5 cm. The quality-checked data used for this study are reported in Bogena et al. (2013) and comprised a data set of 112 measurement points starting on 1st of July 2009. When comparing the point based soil moisture pattern with ¹

¹ Text taken from Cornelissen et al. (2014)

¹ catchment scale soil moisture patterns measured with electromagnetic induction (EMI), Altdorff (personal communication) identified 7 nodes which showed large deviations from the EMI measurements. Since these deviations were likely to be caused by local processes (e.g. macropore flow), these nodes were excluded from the analysis. The SoilNet nodes finally used in this study are shown in Figure 6.10 as black dots. Figure 6.11 gives the measured soil moisture dynamics between 2010 and 2011 for the Wüstebach catchment in 5, 20 and 50 cm depth ¹.

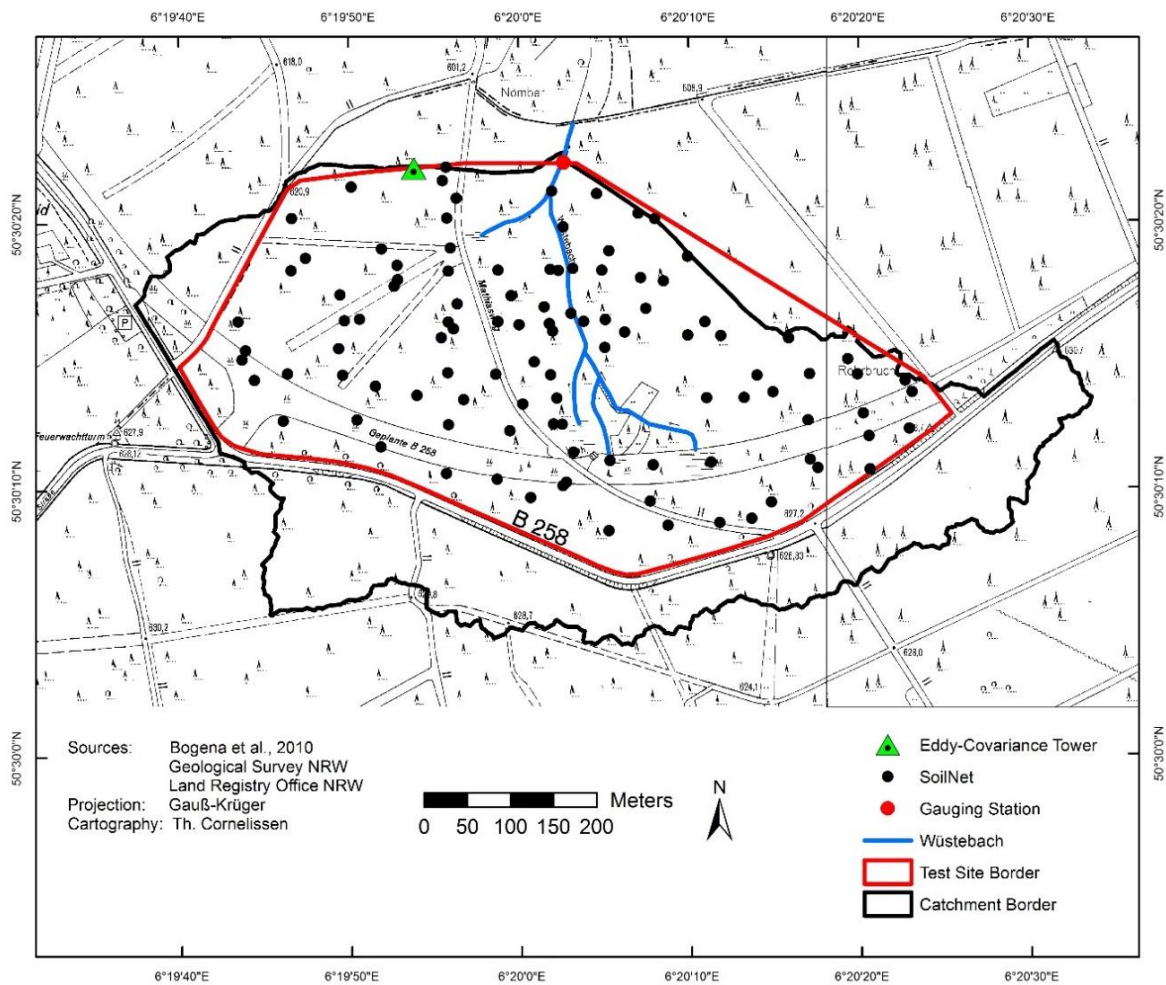


Figure 6.10: Measurement Location of the SoilNet, the Gauging Station and the Eddy-Covariance Tower at the Wüstebach test site. The measurement locations of the interception network are equal to those of the SoilNet.

Since 2011, weekly **throughfall** has been measured in the Wüstebach catchment with cylindrical measuring containers having a maximum storage equal to 50 mm. Measurements are done for all 147 locations of the SoilNet sensors. 144 sensors are placed underneath the vegetation giving an estimate of the sum of throughfall and dripping water while 3 sensors are freestanding to record the net precipitation. The difference between the mean net precipitation and the throughfall gave a raw estimate of the interception loss of about 20%. In Figure 6.12, net and

¹ Text taken from Cornelissen et al. (2014)

field precipitation is plotted against each other for the years 2011 and 2012. These data were used for calibration.

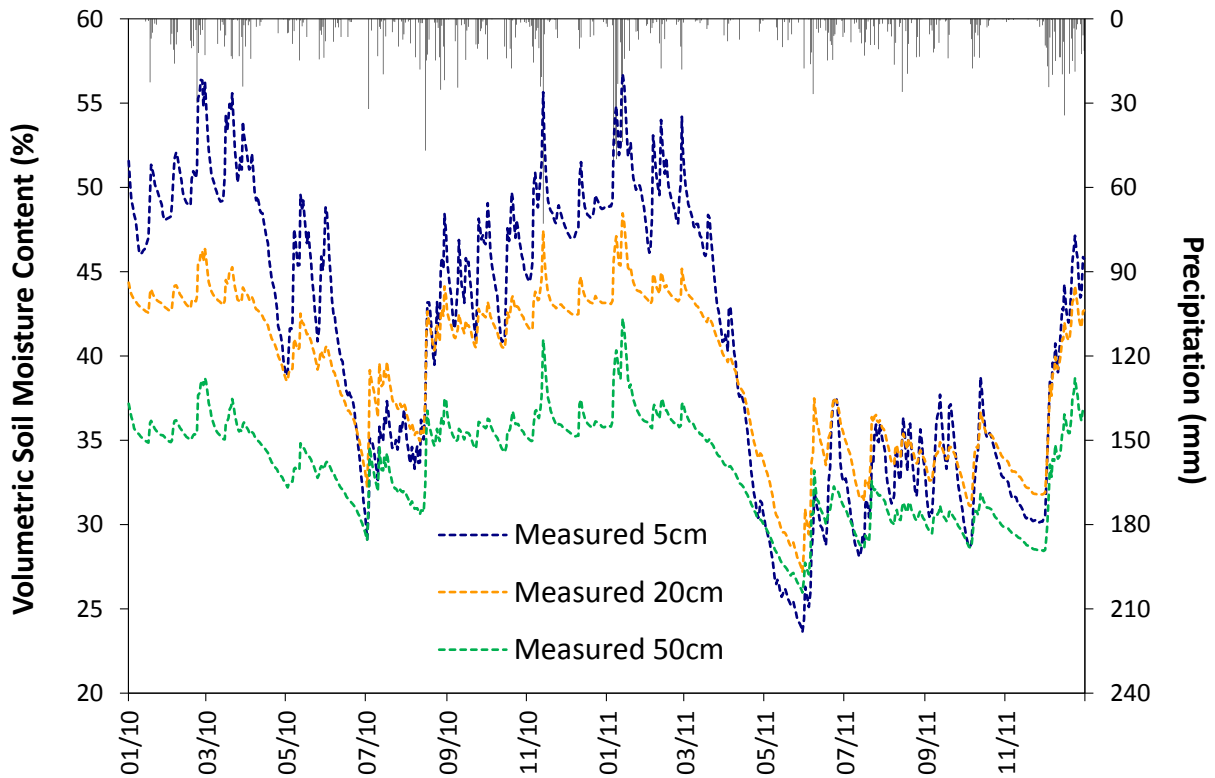


Figure 6.11: Observed mean daily soil moisture dynamics for 2010 and 2011 in 5, 20 and 50 cm depth.

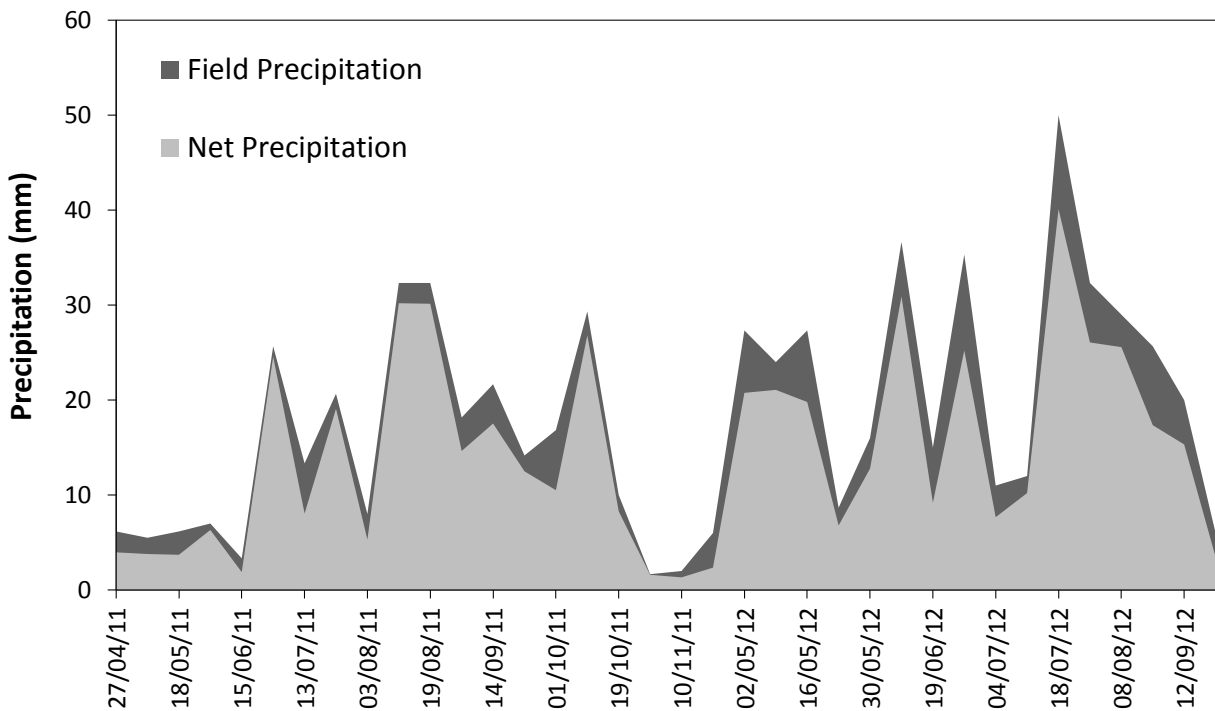


Figure 6.12: Observed weekly precipitation values for 2011 and 2012.

6.2.4 Discharge data

Discharge is monitored at the Wüstebach outlet by a combination of Parshall flumes (Venturi weir) for high flows (5-300 l/s) and V-notch weirs (Thomson weir) for measuring flow rates smaller than 5 l/s at 10 minute intervals (Graf et al. 2014). Discharge is measured in l/s for both weirs and combined to one discharge curve. Table 6.7 gives an overview of the percentage of data gaps in the Wüstebach discharge data at hourly resolution. The percentage of gaps was high in 2008 and 2009 but substantially decreased between 2009 and 2012.

It was already outlined that the size of the Wüstebach simulation area (0.27 km²) and its catchment area (0.38 km²) differed from each other meaning that measured and simulated discharge originate from areas of different size. To enable comparison, discharge in l/s was divided by the corresponding area to determine discharge in mm.

Table 6.7: Amount of target and credit hours and their residual at the Wüstebach outlet.

Year	Target Hours	Credit Hours	Gaps (%)
2008	5088	4545	11
2009	8760	7728	12
2010	8760	8176	7
2011	8760	8241	6
2012	8784	8630	2

At the Erkersruhr, discharge data was available from 1st November 1961 until 31st December 2012. Figure 6.13 depicts measured discharge at the Wüstebach and the Erkersruhr outlets between 2008 and 2012. Discharge rates between 1962 and 2000 are given as mean 5-year values in chapter 8.4. Discharge was characterized by a strong seasonality with a pronounced low flow period during the summer and a high variability during snow dominated periods in the winter. The Wüstebach discharge tended to produce larger and more short-term variations during autumn and higher peak flows during the whole year. The similarity between the outlets (Figure 6.13) was quantified by the coefficient of variation which is a measure for the frequency distribution (see chapter 3.4). It reached comparable values for the Wüstebach (1.5) and the Erkersruhr (1.3).

In this thesis, the long-term simulation run covering the growing period of the spruce forest in the Erkersruhr catchment (50 years) was performed (chapter 8.4). Due to the large similarity in discharge dynamics between the Erkersruhr and the Wüstebach, the Wüstebach catchment was regarded as representative for the whole Erkersruhr catchment. To allow for a comparison between simulated and observed discharge data, the simulated data had to be rescaled from the Wüstebach to the Erkersruhr. This was achieved by a linear regression curve ($y=1.3742x+0.2348$; R^2 of 0.81) between observed discharge rates from the Erkersruhr and the Wüstebach catchments for the period between 2010 and 2011.

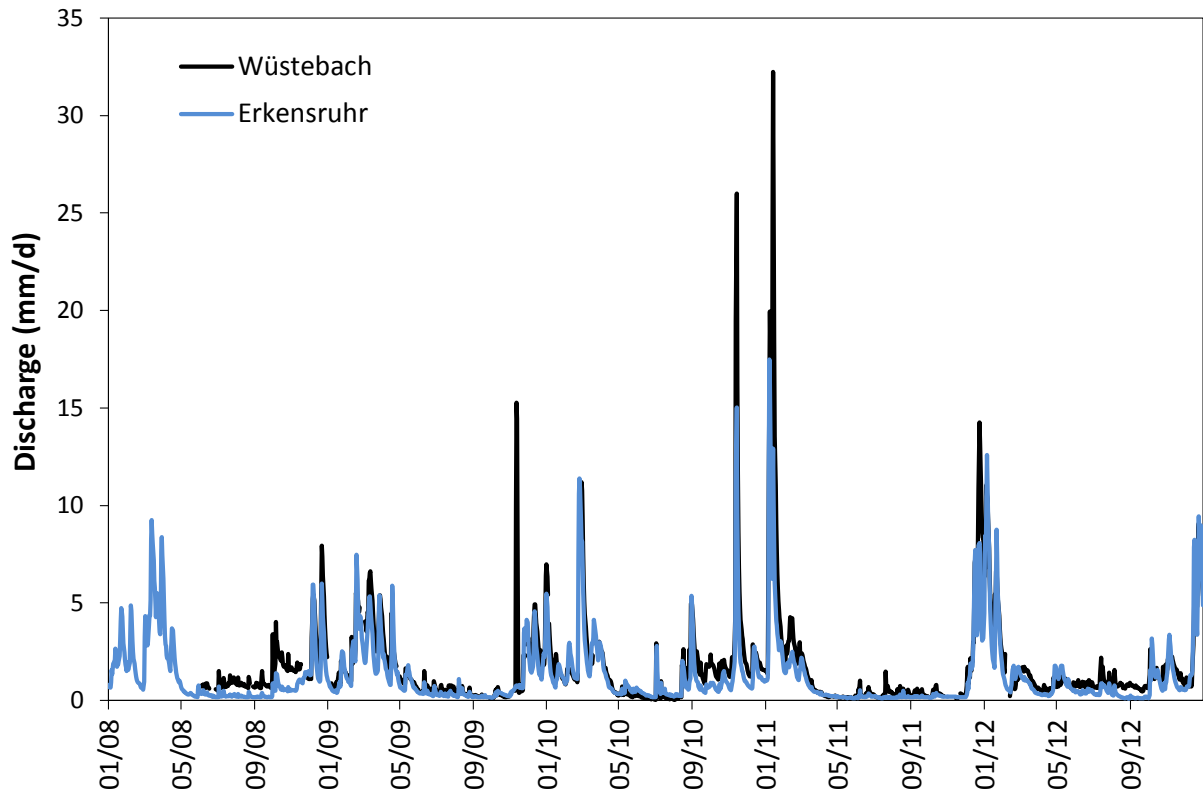


Figure 6.13: Measured discharge curve at the Wüstebach and Erkersruhr outlets between 2008 and 2012.

6.2.5 Soil Data

Soil data for the **Wüstebach** catchment had a resolution of 1:2.500. Figure 6.14 differentiates 8 different soil types from which 6 are located near the river bed and the source areas. The two dominant soil types - Cambisol in the western and Gleyic Cambisol in the eastern part of the catchment – cover 81% of the test site area. Of the 6 other soil types, Gleysol and Stagnic Cambisol account for 7% and 4% of the total area, respectively. For each soil type, Table 6.8 gives basic soil characteristics as an area weighted mean value. Despite the variability in soil types, silt loam is the dominant soil texture of the first two layers in the Wüstebach catchment. In the first layer, soil texture only varies for Histosol and Gleysol (silty clay). In the second layer, only Regosol has a different soil texture class (silty clay). The skeleton content increases with depth from 33% in the first to 66% in the second layer. This increase in skeleton content results in a strong decrease of porosities and residual saturation during parameterization of the model HydroGeoSphere (refer to chapter 7.3.2). Corresponding to the increase in skeleton content, the saturated conductivity also decreases from 2.4E-6 m/s to 8.1E-8 m/s between the two top layers. Comparable to soil texture and skeleton content, the saturated conductivity shows little variation between soil types except for the Histosol soil type.

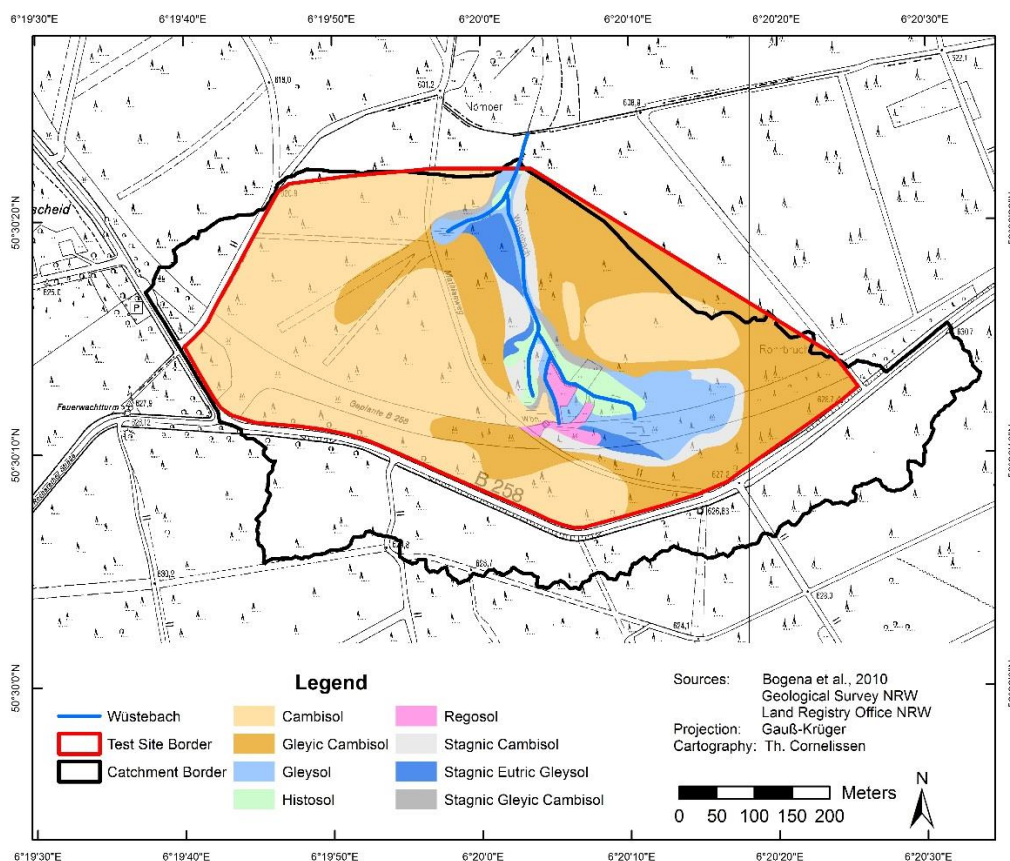


Figure 6.14: Soil Type distribution of the Wüstebach test site.

Table 6.8: Area weighted mean values of characteristic soil properties for the three top layers in the Wüstebach catchment.

	Cambisol	Gleyic Cambisol	Gleysol	Histosol	Regosol	Stagnic Cambisol	Stagnic Eutric Gleysol	Stagnic Gleyic Cambisol
Layer 1								
Thickness (cm)	72	68	52	31	118	72	84	55
Sand (%)	8	9	12	0	19	9	10	10
Silt (%)	73	71	42	0	61	68	65	70
Skeleton (%)	37	31	27	0	40	38	31	38
Humus (%)	1	1	18	100	1	2	1	1
K _s (m/s)	2.7E-07	2.8E-07	1.5E-07	7.3E-05	5.4E-07	2.5E-07	2.7E-07	3.2E-07
Layer 2								
Thickness (cm)	101	102	76	95	120	110	132	106
Sand (%)	11	11	10	10	11	11	11	11
Silt (%)	75	75	69	69	75	75	75	75
Skeleton (%)	66	72	58	40	53	69	53	61
Humus (%)	0	0	0	4	0	0	0	0
K _s (m/s)	8.7E-08	7.2E-08	5.5E-08	9.0E-08	1.2E-07	1.1E-07	1.2E-07	9.9E-08
Layer 3								
Thickness (cm)	133	125	144	166	86	149	156	139
Sand (%)	6	0	7	11	5	3	7	0
Silt (%)	38	0	46	75	31	22	46	0
Skeleton (%)	97	100	93	85	55	99	97	100
Humus (%)	0	0	0	0	0	0	0	0
K _s (m/s)*	3.0E-09	0	3.6E-09	1.3E-08	2.4E-09	1.7E-09	3.6E-09	0

*Saturated conductivity as given by the soil data of the Geological Survey of North Rhine-Westphalia.

As outlined in chapter 7.2, the Wüstebach catchment was discretized at a 25x25 m resolution with a refinement of the river bed. Thus, spatial discretization was detailed enough to support a direct incorporation of the soil type pattern visible in Figure 6.14 without derivations and will therefore not be described in detail.

With a spatial resolution of 1:50.000, the soil data of the **Erkensruhr** catchment had a much coarser resolution than that of the Wüstebach. According to Figure 6.15 (top left), Cambisol is the dominant soil type in the catchment. River valleys are dominated by Gleysol and some source areas of the rivers are characterized by Planosol. Silt is the dominant soil texture in the first soil layer for all soil types except for the Histosol soil type which is characterized by peat in both layers (Table 6.9). In the second layer, Cambisols, Gleysols and Vertisols have a large skeleton content of at least 66% and a maximum of 90%. In contrast, Planosols only have a mean skeleton content of 10% which is consistent with their origin as river source areas.

A comparison of soil properties between the Erkensruhr and the Wüstebach catchment pointed to large differences concerning skeleton content and saturated conductivity. In the first layer, the soil data of the Erkensruhr does not have any skeleton content whereas the mean content in

the Wüstebach amounts to 33%. In the second layer, the area weighted mean skeleton contents are the same in the Wüstebach and the Erkensruhr catchment. Thus, the decrease in porosities is much more pronounced in the Erkensruhr catchment than in the Wüstebach. In addition, the saturated conductivity values are much higher in the Erkensruhr catchment (factor of 2.4 in the first and 2.6 in the second layer).

Table 6.9: Mean values of characteristic soil properties for the two top layers in the Erkensruhr catchment.

	Cambisol	Vertisol	Gleysol	Planosol	Histosol
Layer 1					
Thickness (cm)	60	20	130	60	30
Sand (%)	16	17	12	17	9
Silt (%)	60	58	53	59	9
Peat (%)	0	0	10	0	80
Skeleton (%)	0	0	0	0	0
Saturated Conductivity (m/s)	5.8E-6	5.6E-6	5.7E-6	5.8E-6	1.2E-5
Layer 2					
Thickness (cm)	120	180	80	110	80
Sand (%)	5	1	15	13	0
Silt (%)	20	6	7	45	0
Peat (%)	0	0	0	0	100
Skeleton (%)	66	90	75	10	0
Saturated Conductivity (m/s)	1.9E-6	4.6E-7	4.9E-6	3.5E-6	1.2E-5

Soil data were delivered as vector data. The implementation of these data in the model required the following steps: Conversion of vector data into gridded data, aggregation of the gridded data from 37x37 m to 100x100 m resolution, and assignment of aggregated soil types to the triangulated grid elements used for the simulations with HydroGeoSphere (chapter 7.2). Figure 6.15 depicts the change in distribution of soil types during this implementation process. The conversion of vectorized into gridded data with ArcGIS did not alter the soil type distribution. In contrary, the aggregation from 37x37 m to 100x100 m resolution altered the pattern of the Gleysol distribution (Figure 6.15, left bottom).

In the previous section, it was outlined that the variations in soil properties between the soil types were marginal. In contrast, the clear correspondence between the Gleysol soil type and the river bed pointed to a great relevance of the soil type pattern for the simulation. Therefore, the soil type Gleysol was manually assigned to all elements surrounding the river bed covering the whole riparian area. The lower right part of Figure 6.15 visualizes that this adjustment increased the fraction of the Gleysol soil. Table 6.10 lists the area fraction of all soil types for the original vectorized soil data and the fractions in the model. According to the data in Table 6.10, the fraction of Gleysol increased by 14% which corresponded to the decrease in Cambisol.

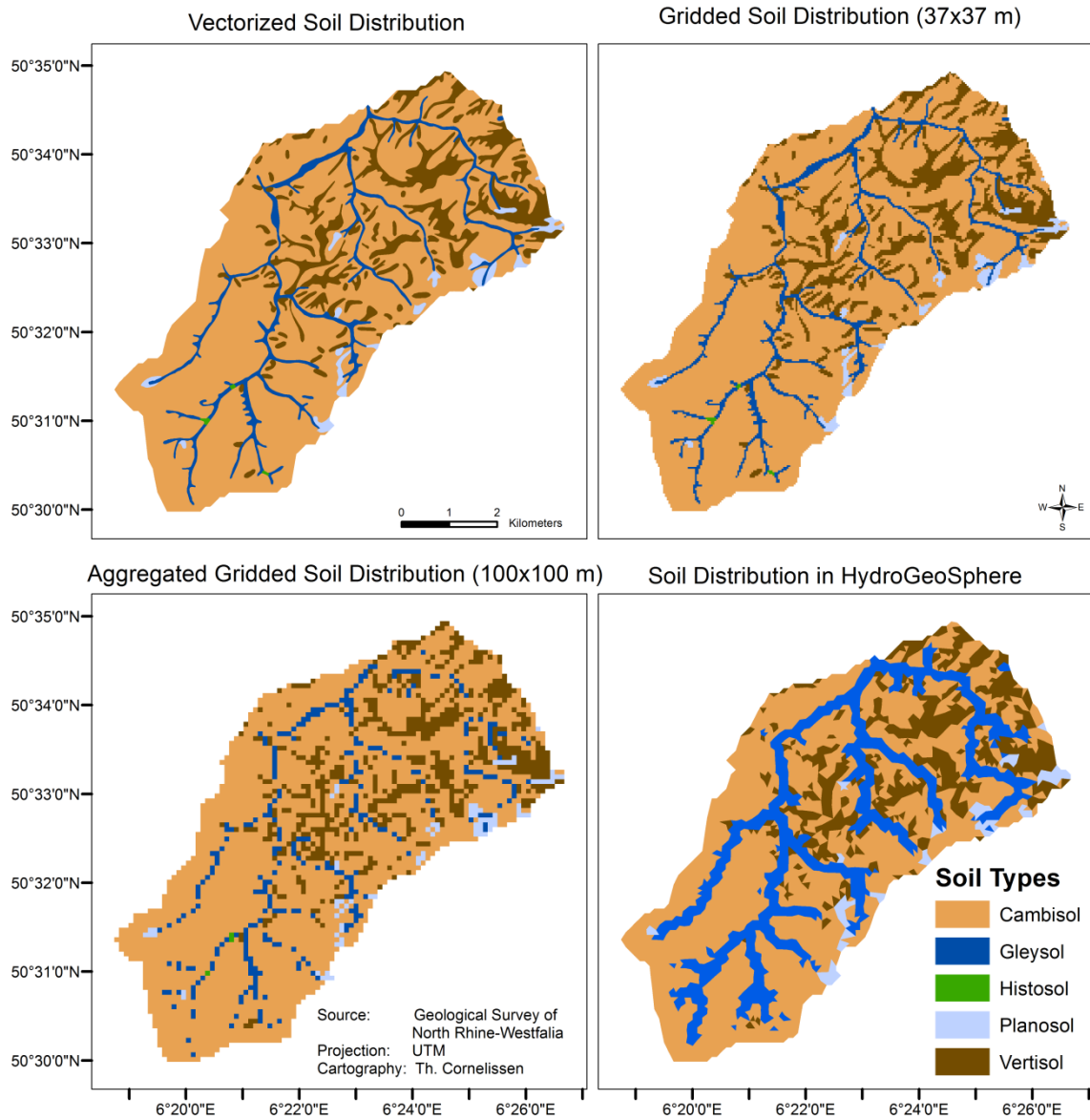


Figure 6.15: Influence of aggregation and of discretization on the soil type distribution in the Erkensruhr catchment.

Table 6.10: Area fraction of original vectorized soil data and area fraction of soil types in the model.

Soil Type	Original Fraction (%)	Fraction in HydroGeoSphere (%)
Cambisol	75	60
Gleysol	8	22
Planosol	2	2
Vertisol	15	16

7 Model setup with HydroGeoSphere

7.1 Model description

In this thesis, the 3D physically based and distributed hydrological model **HydroGeoSphere** was applied. HydroGeoSphere has been successfully used for the simulation of a broad range of applications, e.g. the simulation of the effect of different bank slopes on bank storage (Doble et al., 2011), the discharge of large watersheds (Li et al., 2008), the impact of climate change (Goderniaux et al., 2009), the investigation of surface/subsurface interactions (Brunner et al., 2009a, Brunner et al., 2009b), investigation of vegetation effects on surface/subsurface processes (Banks et al., 2011) and the simulation and illustration of runoff generation processes in a headwater catchment (Partington et al., 2013). One of the main reasons for the application of this model in the context of this thesis, was its unique ability to use an unstructured grid composed of triangles instead of a structured grid composed of rectangles for the spatial discretization of a catchment. The shape of these triangles can vary inside a catchment. It is thus possible to fit the discretization to a pattern assumed to be hydrologically relevant e.g. the topography of a catchment.

The model has been developed in Canada at the Universities of Laval and Waterloo and by the company Aquanty by René Therrien, Edward Sudicky, Rob McLaren and Sorab Panday. It describes 3D saturated and unsaturated subsurface flow and 2D aboveground flow processes in a fully integrated and coupled way meaning that governing equations are solved simultaneously (refer to chapter 3.1). The model is able to incorporate evapotranspiration (using the approach by Kristensen and Jensen, 1975), channels (1D), macropore flow (with the dual-porosity model by Gerke and van Genuchten, 1993), transport and flow of solutes and thermal energy transport. The most important model equation is the Richards' equation which expresses that a divergence in the subsurface flux has to be equal to a change in soil moisture storage (refer to chapter 3.2). In HydroGeoSphere, the equation takes the form:

$$-\nabla q + flux_o + O = S_w S_s \frac{\partial \psi}{\partial t} + \theta_s \frac{\partial S_w}{\partial t} \quad \text{Equation 11}$$

where q is the Darcy flux (L/T; refer to chapter 3.2), $flux_o$ is the exchange rate between the surface and the subsurface (1/T), O are sources and sinks, for example the transpiration rate (1/T). The right hand expression is the storage term and consists of the relative saturation $S_w = \theta / \theta_s$ (-), the specific storage S_s (1/L) - a calibration parameter -, the pressure head ψ (L) - the unknown for which the equations are solved -, θ_s (-) the saturated water content and θ (-) the actual water content. In chapter 3.2 it was outlined that the application of the Darcy equation to unsaturated conditions requires the definition of the unsaturated conductivity K_r (-) which depends on water content or pressure head.

In the model of Mualem (1976), K_r depends on water content as:

$$K_r = S_e^\tau \left[1 - \left(1 - S_e^{1/m} \right)^m \right]^2 \quad \text{Equation 12}$$

where τ is the dimensionless pore connectivity parameter describing the strength of the connection between soil pores and has been determined by Mualem (1976) as equal to 0.5 for most soils. The parameter m has been restricted by Mualem (1976) to $m=1-1/n$ where n is a parameter of the pressure-saturation relationship by van Genuchten (1980). S_e (-) is an effective water content which is given by the van Genuchten (1980) equation describing the dependency between water content and pressure head:

$$S_e = \frac{\theta - \theta_r}{\theta_s - \theta_r} = \begin{cases} \frac{1}{[1 + (\alpha\psi)^n]^m}, & \psi < 0 \\ 1, & \psi \geq 0 \end{cases} \quad \text{Equation 13}$$

where n (-) and α (1/L) are fitting parameters changing the slope (n) and moving the curve parallel to the axis of the pressure head (α); m (-) is dependent on n as $m=1-1/n$; θ_r and θ_s (both dimensionless) are the residual water content and the water content at saturation (porosity); θ is the current water content. Van Genuchten and Nielsen (1985) note that the restriction of m by Mualem (1976) leads to a dependency between the slope and the curvature of the curve for dry and saturated conditions. Figure 7.1 shows the shape of the relationships $\theta(\psi)$ and $K_r(\psi)$ as parameterized with the models of Mualem (1976) and van Genuchten (1980).

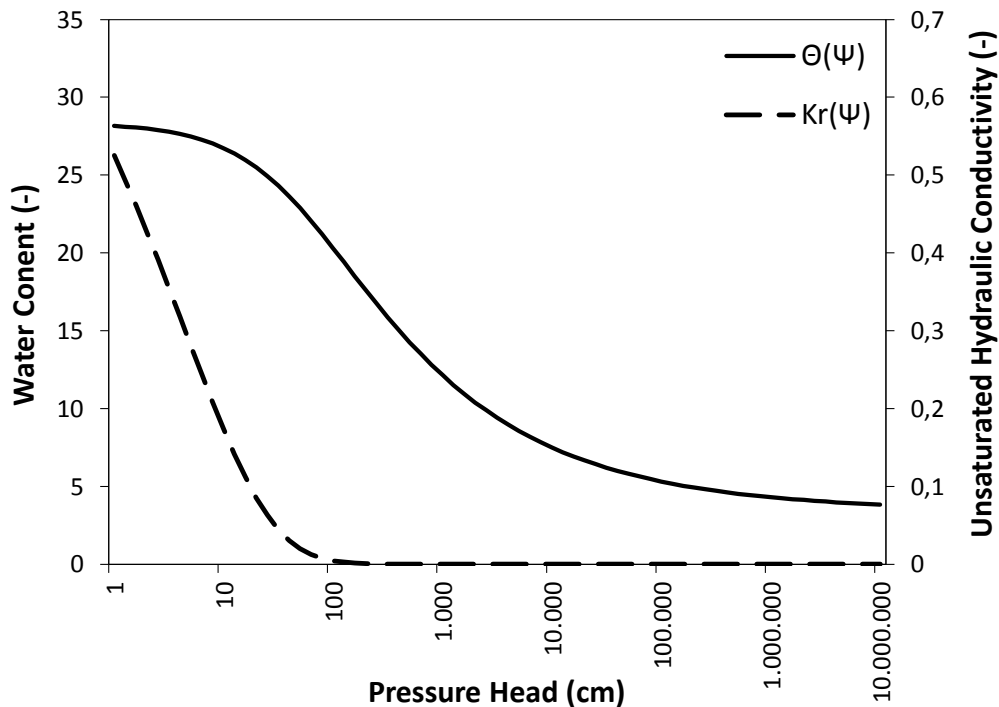


Figure 7.1: Illustration of the water content-pressure head and hydraulic conductivity-pressure head relationships calculated with $\alpha=0.0217$ (1/cm), $n=1.3366$, $\theta_r=0.0344$ and $\theta_s=0.2833$.

The subsurface Richards' equation is coupled to the surface flow or macropore domain via the common node or the dual node approach. While the dual node approach calculates a leakage between the surface and subsurface domains according to the pressure head difference, the common node approach assumes continuity of pressure heads between the surface and the subsurface domains. Due to mass conservation problems arising in the common node approach, the dual node was used in this study.

The coupling term of the dual node approach is given as follows:

$$d_o flux_o = \frac{k_{ro} K_{zz}}{\Gamma_{ex}} (h - h_o) \quad \text{Equation 14}$$

where d_o is the depth of surface flow (L), $flux_o$ is the exchange rate between the surface and the subsurface (1/T), k_{ro} is the relative permeability of the surface (-), K_{zz} is the saturated hydraulic conductivity of the underlying porous media (L/T), Γ_{ex} is the coupling length (L) which has to be calibrated, and h and h_o are the hydraulic heads of the subsurface and surface which equal the sums of the pressure head and the elevation head of their respective domains. When $h > h_o$ water infiltrates from the surface to the subsurface domain and when $h < h_o$ water moves from the subsurface to the surface, respectively. The relative permeability equals 1 if the depth of surface flow d_o equals or is larger than the obstruction storage height (L) which is a calibration parameter. When the surface flow is smaller than the obstruction storage height, the relative permeability approximately follows a Gaussian function (R^2 of 0.97). The obstruction storage subsumes retention effects on surface flow by e.g. vegetation or stones in a river bed or on a forest flow.

Surface flow is calculated with the 2D diffusion wave approximation of the Saint-Venant equation for unsteady shallow water flow. It consists of a mass balance equation and a momentum equation in x- and y-direction. The momentum equation contains bed and friction slopes in x- and y-direction which are parameterized by Manning's equation. Manning's equation contains depth averaged flow velocities, the surface flow depth and a friction coefficient which has to be calibrated. The Saint Venant equation assumes depth-averaged flow velocities, no vertical momentum change in a surface water column (hydrostatic; pressure is only due to gravity) and mild slope (Aquanty, 2013). The equation for surface flow is given as:

$$-\nabla(d_o q_o) - d_o flux_o + O_o = \frac{\partial \phi_o h_o}{\partial t} \quad \text{Equation 15}$$

where d_o is depth of surface flow (L), q_o is the Darcy flux (L/T; refer to chapter 3.2), $flux_o$ is the exchange rate between the surface and the subsurface (1/T), O_o are sources and sinks for example the evaporation rate (L/T) expressed as a volumetric flux rate per unit area, h_o is the hydraulic head of the surface (L) and ϕ_o is the surface porosity (-). HydroGeoSphere incorporates two conceptual parameters – the depression and the obstruction storage – to account for subscale topography. The depression storage accounts for subscale terrain unevenness created by

detention features like rills or furrows. Water hold in the depression storage is dead water, because for the occurrence of lateral flow the surface flow depth has to be higher than the depression storage. The obstruction storage accounts for flow obstruction like plants or stones which may have developed at the surface. If the depth of flow is higher than the sum of depression and obstruction storage, the full area contributes to surface flow and evaporation.

The simulation of interception and evapotranspiration in HydroGeoSphere follows the approach of Kristensen and Jensen (1975). Interception is modeled with a bucket approach, where precipitation reaches the ground when the precipitation rate exceeds the maximum interception storage and its evaporation. Maximum interception storage equals the product of the parameters Leaf Area Index (LAI) and canopy storage. Interception storage is emptied prior to other evapotranspiration processes and calculated prior to all other equations. The interception model does not account for dripping water, so all intercepted water evaporates. Transpiration is calculated with the following equation:

$$T_p = f_1(LAI)f_2(\theta)RDF[PET - E_{can}] \quad \text{Equation 16}$$

The transpiration rate depends on (1) f_1 which linearly correlates the transpiration to the LAI, (2) f_2 which describes the dependency of transpiration on soil moisture in a nonlinear way, (3) a root distribution function which distributed the root water uptake for transpiration among the root zone and (4) the difference between potential and canopy evapotranspiration. The function f_1 is given below:

$$f_1(LAI) = \max\{0, \min[1, (C_2 + C_1LAI)]\} \quad \text{Equation 17}$$

where C_1 and C_2 are dimensionless fitting parameters. The function f_2 describes the dependence of transpiration on soil moisture and is particularly important in the context of this thesis (refer to Figure 7.2 for illustration):

$$f_2(\theta) = \begin{cases} 0, & 0 \leq \theta < \theta_{wp} \\ 1 - \left[\frac{\theta_{fc} - \theta}{\theta_{fc} - \theta_{wp}} \right]^{C_3}, & \theta_{wp} \leq \theta \leq \theta_{fc} \\ 1, & \theta_{fc} \leq \theta \leq \theta_o \\ \left[\frac{\theta_{an} - \theta}{\theta_{an} - \theta_o} \right]^{C_3}, & \theta_o \leq \theta \leq \theta_{an} \\ 0, & \theta_{an} \leq \theta \end{cases} \quad \text{Equation 18}$$

According to this equation, the transpiration is zero for soil moistures (θ) below the wilting point (θ_{wp}) and beyond the anoxic limit (θ_{an}). Between the wilting point (θ_{wp}) and the field capacity (θ_{fc}), as between the oxic (θ_o) and anoxic limits (θ_{an}), the transpiration linearly increases to the potential rate depending on the dimensionless fitting parameter C_3 . Between the field capacity (θ_{fc}) and the oxic limit (θ_o), the actual transpiration occurs at the potential rate.

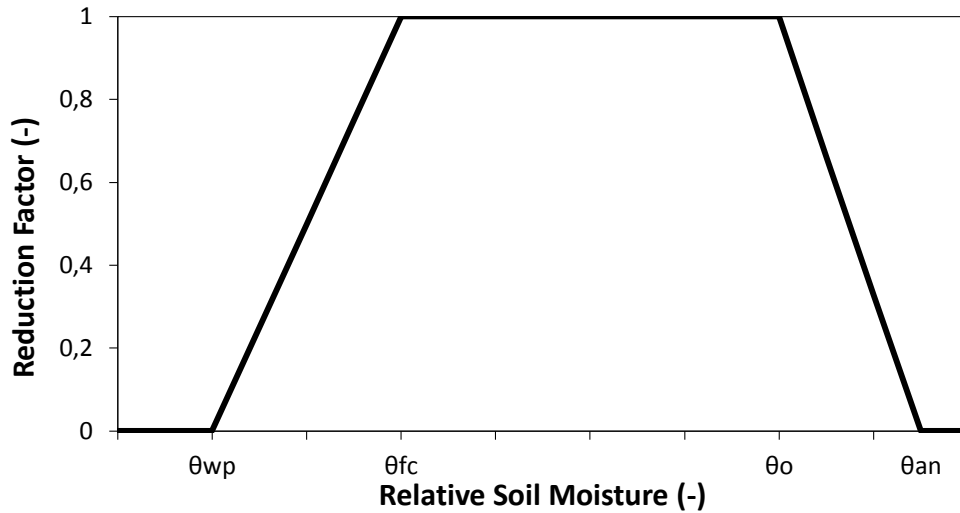


Figure 7.2: Illustration of the non-linear relationship between soil moisture and transpiration as calculated with Equation 18.

The root distribution function RDF calculates the relative contribution to transpiration for each soil layer defined by the vertical model discretization. The relative contribution per soil layer is calculated as:

$$RDF = \int_{z_1}^{z_2} r_F(z) dz / \int_0^{L_r} r_F(z) dz \quad \text{Equation 19}$$

where z_1 and z_2 are the lower and upper depth coordinates of a soil layer (both L) inside the root zone, L_r is the root depth (L) - a calibration parameter - and $r_F(-)$ is the root extraction function. HydroGeoSphere offers four different root extraction functions describing the dependence of root extraction from depth (refer to Figure 7.3).

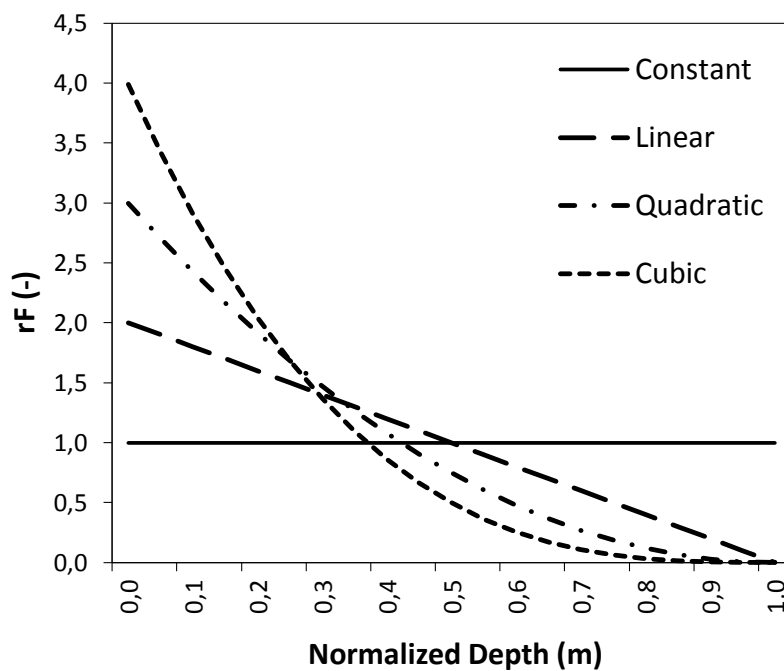


Figure 7.3: Normalized root depth functions implemented in HydroGeoSphere.

Surface and subsurface evaporation occur together with transpiration according to the following equation:

$$E_s = \alpha^* EDF [E_p - E_{can}] [1 - f_1(LAI)] \quad \text{Equation 20}$$

where EDF is the evaporation distribution function which is calculated in the same way as the RDF value. The dimensionless parameter α^* is given for the subsurface as:

$$\alpha^* = \begin{cases} \frac{\theta - \theta_{e2}}{\theta_{e1} - \theta_{e2}}, & \theta_{e2} \leq \theta \leq \theta_{e1} \\ 1, & \theta > \theta_{e1} \\ 0, & \theta < \theta_{e2} \end{cases} \quad \text{Equation 21}$$

where θ_{e1} is the moisture content beyond which full evaporation occurs and θ_{e2} is the moisture content below which evaporation is zero. For the overland flow domain, α^* varies between 1 when the depth of flow is at or above the depression storage and 0 when the depth of flow is below depression storage.

To distinguish between different runoff sources, the hydraulic mixing cell method was applied to HydroGeoSphere (Partington et al., 2011). This method traces discharge components from flux and storage information calculated by the model for rectangular cells. In each cell, the concentration of each discharge component equals the mass of the corresponding “tracer” divided by the volume of the cell and is altered according to inflows and outflow information of different nodes. As the volume of a cell can change according to the spatial discretization of the model domain, the results of the method are unique for a spatial discretization. Currently, the method distinguishes between (1) baseflow to the stream, (2) baseflow to overland areas -also called return flow-, (3) direct rainfall into the stream and (4) direct rainfall onto overland areas.

HydroGeoSphere is able to handle problems of different complexity with different numerical solution techniques (refer to Figure 7.4). The variably-saturated and coupled surface-subsurface system which has been simulated in this thesis is non-linear and is therefore solved with the Newton-Raphson method. The solution procedure consists of four steps: (1) discretization, (2) linearization, (3) matrix assembly and (4) iterative matrix solution with the Newton-Raphson and Gaussian elimination methods.

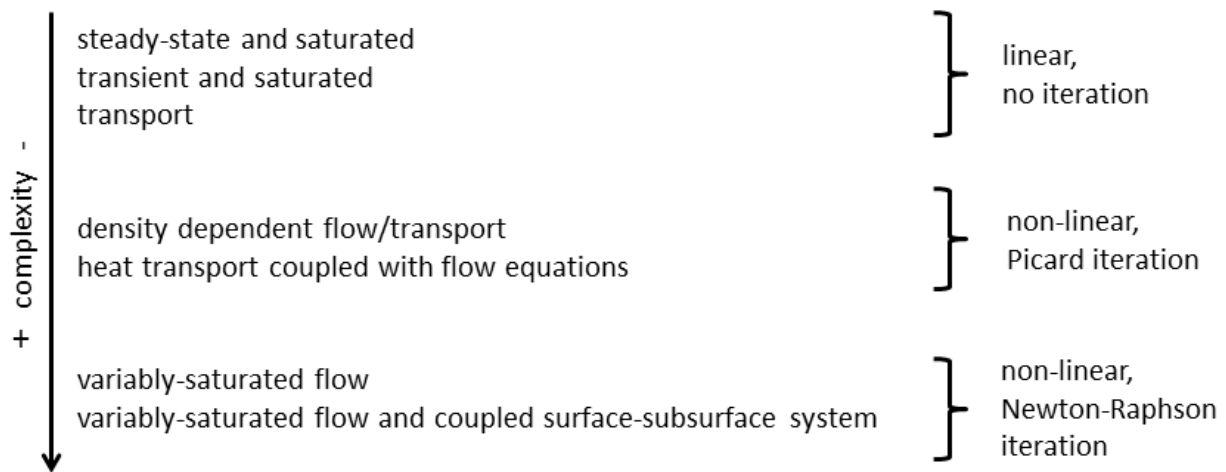


Figure 7.4: Overview about processes of different complexity implemented in HydroGeoSphere and their solution technique.

In HydroGeoSphere, grids can be **discretized** either with the finite element or the finite difference method (Figure 7.5). The main difference between the methods is the number of node connections taken into account for the discretization. While every node is connected to 26 other nodes in the finite element approach, it is only connected to 6 other nodes in the finite difference approach, because cross connections are ignored. Due to higher computation speed, the finite difference method was used in this study.

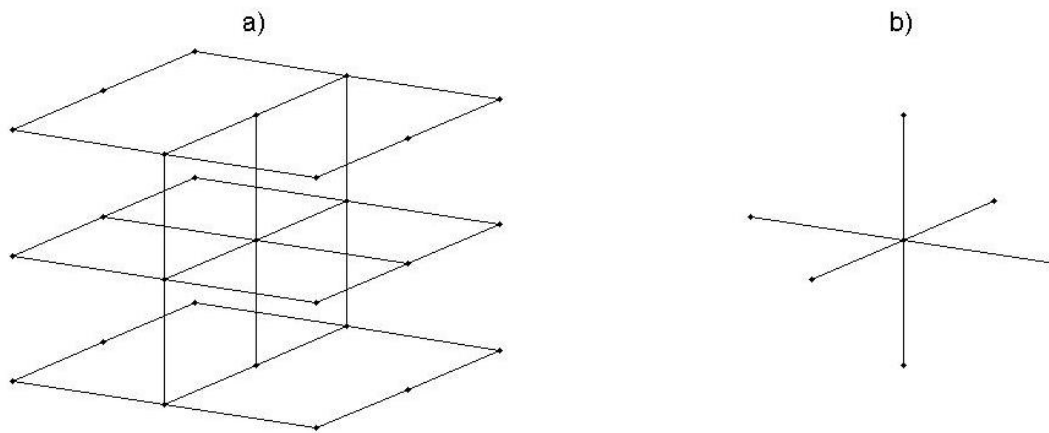


Figure 7.5: Illustration of node connections in the (a) finite element and (b) finite difference method (redrawn after Panday et al. 1993).

Discretization requires relating an equation to a volume. In the case of HydroGeoSphere, each node is surrounded by a virtual volume with a given length, width and height to enable the discretization of the mass balance and exchange fluxes. All model parameters like the unsaturated and saturated conductivities and evapotranspiration parameters are interpolated at the interfaces between the nodes (the boundaries of the nodal volumes).

The discretized version of the Richards' equation with the mass balance term of node "i" on the right and fluxes between nodes "i" and "j" on the left hand side is given below (Equation 22):

$$\sum_{j \in n_i} \left(\lambda_{ij+0.5}^{t+\Delta t} K S_{ij} (h_j^{t+\Delta t} - h_i^{t+\Delta t}) \right) + \Gamma_o^{t+\Delta t} + Q_i^{t+\Delta t} =$$

$$= \frac{v_i S_{wi}^{t+\Delta t} S_s}{\Delta t} (h_i^{t+\Delta t} - h_i^t) + [(\theta_s S_w)_i^{t+\Delta t} - (\theta_s S_w)_i^{t+\Delta t}] \frac{v_i}{\Delta t} \quad \text{Equation 22}$$

where $\lambda_{ij+0.5}^{t+\Delta t}$ represents the weighted value of relative permeability evaluated at the interface between the nodal volumes of "i" and "j" at time $t+\Delta t$, t denotes the time step (see description below), Δt is the change in time step, h the hydraulic head, v_i denotes the volume of influence of node "i", and $K S_{ij}$ is the saturated conductivity as a volume averaged value. The discretized function has to be solved for an unknown change in the pressure head ψ , so that the change in mass balance is equal to the flux divergence. The solution of this equation requires **linearization** and an **iterative solution** technique. In HydroGeoSphere, the Newton-Raphson method is used for linearization and iterative solution of non-linear equations in coupled surface-subsurface systems. The basic principle of the Newton-Raphson method is illustrated with the non-linear function $f(x) = x^3 - 2x^2 + 4$. The function has to be solved in a way that $f(x)$ becomes 0 for a given x . A first guess for the solution of the above given function would be $x=-1$ which yields $y=1$. As this is not the achieved result, a better solution can be found by adding an error term to x , so that $x=g-1$. If the equation is solved for $x=g-1$, the improved value for x approximately equals -1.14 which yields $y=-0.105$ which is much closer to the required solution. This procedure can be continued until $f(x)$ is as close as possible to the solution plus a given tolerance level. The method can be generalized as:

$$x_{n+1} = x_n - \frac{f(x_n)}{\frac{df}{dx}(x_n)} \quad \text{Equation 23}$$

where x_n is the first guess or initial value of the variable x , $f(x_n)$ is the value of the function for the given x_n , $\frac{df}{dx}(x_n)$ is the first derivative of the function $f(x_n)$, and x_{n+1} is the updated value for the variable x . The aim is to iterate the solution procedure until the change $x_n - x_{n+1}$ or the proportion $f(x_n) / \frac{df}{dx}(x_n)$ is below a given tolerance level. For the application to HydroGeoSphere, $f(\psi)$ is the discretized Richards' equation containing exchange and boundary fluxes as defined before.

In a multidimensional system e.g. a grid discretized with the finite difference method, the Newton-Raphson method takes the form:

$$J_{ij}^r \Delta \psi_{ij}^{t+\Delta t, r} = -f(\psi)_i^r \quad \text{Equation 24}$$

where J is the Jacobi-matrix which contains the partial derivatives of the function f(ψ) to the pressure head ψ for all nodes, $\Delta \psi$ is the change in pressure head, “r” the iteration step and “i” and “j” are node indices.

The next step of the solution procedure is the **assembly of the Jacobi-matrix** which is very important because the matrix contains more than 100,000 equations (ignoring the fact that boundary nodes have fewer connections and thus fewer equations) for the simulation of the smaller catchment investigated in this study. For illustration, the method to assemble the matrix and to reduce the number of stored equations are described for two 2D triangles with a total of 4 nodes. The Jacobi-matrices J_a and J_b of each element and the assembled matrix J can be written as:

$$J_a = \begin{bmatrix} a_{11} & a_{12} & a_{13} & 0 \\ a_{21} & a_{22} & a_{23} & a_{24} \\ a_{31} & a_{32} & a_{33} & a_{34} \\ 0 & 0 & 0 & 0 \end{bmatrix} \quad J_b = \begin{bmatrix} 0 & 0 & 0 & 0 \\ b_{21} & b_{22} & b_{23} & b_{24} \\ b_{31} & b_{32} & b_{33} & b_{34} \\ 0 & b_{42} & b_{43} & b_{44} \end{bmatrix}$$

$$J = \begin{bmatrix} a_{11} & a_{12} & a_{13} & 0 \\ a_{21} + b_{21} & a_{22} + b_{22} & a_{23} + b_{23} & a_{24} + b_{24} \\ a_{31} + b_{31} & a_{32} + b_{32} & a_{33} + b_{33} & a_{34} + b_{34} \\ 0 & b_{42} & b_{43} & b_{44} \end{bmatrix} \quad \text{Equation 25}$$

where a_{11} denotes the equation at node “1” and a_{12} denotes the equation to calculate the flux between nodes “1” and “2”. The two matrices J_a and J_b consist of a diagonal term (which contains the mass balance equation and all exchange fluxes) and an off-diagonal term (containing fluxes). As the solution has to be mass conservative, the diagonal term has to be equal to or larger than the sum of all off-diagonal terms. The off-diagonal term has the property that its upper part equals the lower part but with a negative sign, meaning that e.g. $a_{21} = -a_{12}$. By substituting upper parts with its lower counterparts, the number of equations can be substantially reduced. The actual **matrix solution procedure** uses the LU (‘lower upper’) decomposition method which splits the matrix J into an upper and a lower part. The decomposition is required for the Gaussian elimination procedure which is applied to solve the equation. For a description of this method, refer to e.g. Leader (2004).

HydroGeoSphere uses an **adaptive time stepping procedure** in which the time step is changed according to a time step multiplier. The multiplier is calculated for the maximum change in head, water content, flow depth and the number of Newton iterations. If the number of Newton iterations is below the maximum number defined by the user, the smallest of the 4 different

multipliers is selected for further usage. If the number of iterations is above the maximum value, the solution is restarted and the time step is halved. According to René Therrien (personal communication), the maximum number of Newton iterations should be set to 15 to allow rapid convergence. The solution of the coupled equation system is accepted if the residual of the equation $J_{ij}^r \Delta \psi_j^{t+\Delta t, r} = -f(\psi)_i^r$ is below a given absolute or relative convergence criterion. Hwang et al. (2014) compared computation demands for pre- and postprocessing (reading input and writing output data) to matrix assembly and matrix solution. For a variably saturated and coupled surface-subsurface flow system, they concluded that the matrix solution requires more time relatively to the other steps with increasing number of nodes.

Based on these results, the parallel version of HydroGeoSphere - which has also been applied in this thesis – developed by Hwang et al. (2014) focuses on the parallelization of the matrix solution process. The basic idea of the approach is to split the domain into a number of blocks. This creates boundary nodes between blocks, internal nodes which are only connected to nodes within one block, and a set of connection nodes linking internal to boundary nodes. On each thread, two internal node sets and three sets of boundary and connection nodes are computed. Hwang et al. (2014) state that this method requires interprocessor communication thus limiting the parallel version to a maximum of 64 cores.

7.2 Spatial and temporal discretization

The **spatial discretization** of the **Wüstebach** catchment has been performed by Sciuto and Diekkrüger (2010).¹ The model domain was discretized with a triangulated network consisting of 969 nodes at the 25 m grid scale, including 164 nodes for the channel, and 71 nodes at the 100 m grid scale (refer to the upper part of Figure 7.6 for illustration). In the vertical, 23 numerical layers down to a 1.5 m depth were used for the non-bedrock setups of both grid scales, and additional 185 numerical layers were used for the bedrock setups¹. The thickness of the numerical layers increased with depth, using 2.5 cm thickness between the land surface and 0.15 m depth, 5 cm thickness between 0.15 and 0.5 m depth and 10 cm thickness from 0.5 m depth onwards. For the 25 m setup, the subsurface had 22.287 nodes with an additional 969 nodes for the surface domain which was superimposed with the dual node approach. The bedrock added an additional 179.265 subsurface nodes. The refinement of the river bed was used to incorporate the different slopes of the flanks of the stream channel (refer to chapter 6.1). To avoid the river topography to penetrate to the bottom of the bedrock aquifer, the elevations of the stream channel at a depth of 2.5 m were changed. That means that between 1.5 and 2.5 m depth, the different slopes of the river bed flanks successively vanished.

¹ Text taken from Cornelissen et al. (2014)

¹ For all setups and at both model resolutions, the upper 5 cm correspond to the litter layer as suggested by Bogena et al. (2013). The lower part of Figure 7.6 illustrates the vertical discretization used at both resolutions. The non-bedrock setup only used the upper soil layer at both resolutions consisting of a number of soil layers assuming no influence of bedrock on hydrological processes. The second layer comprised the bedrock. At both resolutions the thickness of the bedrock at the lowest point in the catchment was 18.5 m. The large thickness was chosen because the base elevation has to be far below the zone taking part in the annual water cycle. For the two bedrock setups, soils of the first discretization layer between land surface and 1.5 m depth penetrated down to their maximum depth as given in the soil map of the test site ¹. This creates a bedrock topography with lowest elevations ($\hat{=}$ deepest mineral soil layer) in the central part of the catchment and highest elevations ($\hat{=}$ shallowest mineral soil layer) at the western and northern borders of the catchment.

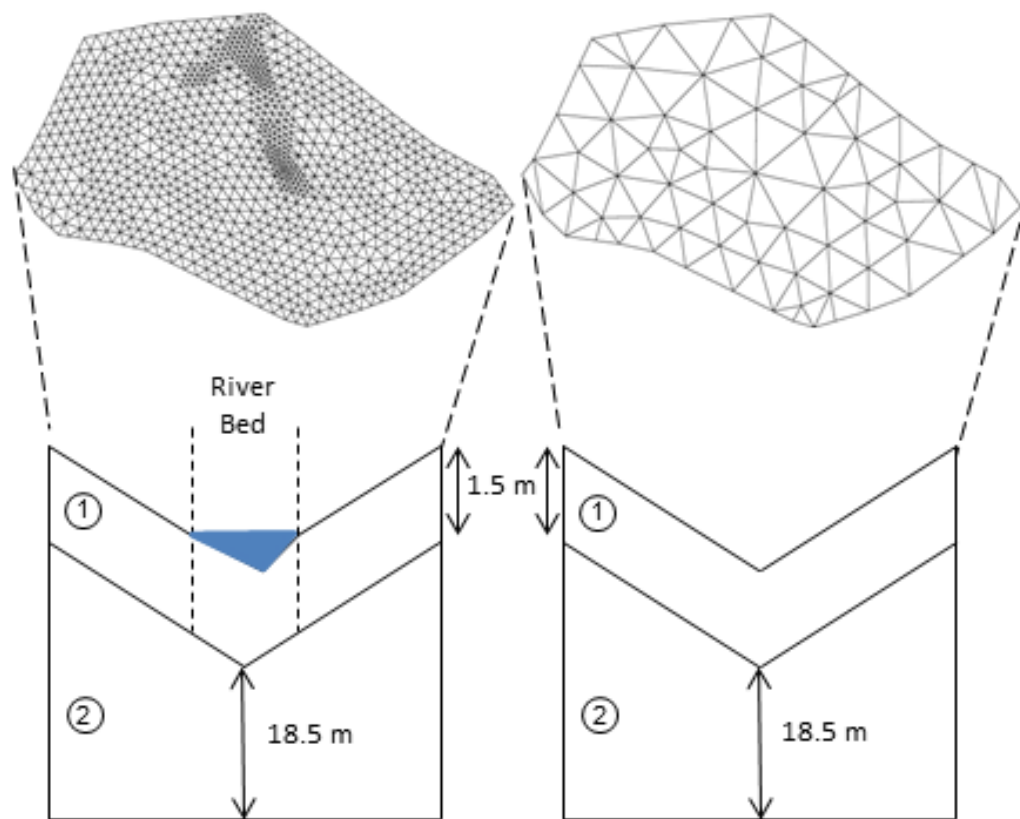


Figure 7.6: Illustration of the horizontal (top) and vertical (bottom) spatial discretization of the Wüstebach test site at 25 m (left) and 100 m (right) resolution. Numbers refer to different layers of the bedrock model setup.

¹ Text taken from Cornelissen et al. (2014)

The triangulated mesh for the **Erkensruhr** catchment was created in the context of this thesis. In the following, the grid creation process is briefly described.

In a first step, Erkensruhr catchment boundaries and the river network were determined with the ArcGIS SWAT Watershed Tool (Arnold et al., 1998). The program requires one parameter which is very subjective to choose: the minimum area of flow accumulation required for concentrated flow to occur. The smaller this parameter, the more tributaries are considered leading to an increasing computation time. In this study, the parameter was set to 19 ha which was a tradeoff between the representation of the Wüstebach stream network and the number of tributaries.

The second step involved cutting of the catchment area from the 10x10 m DEM of the whole Rur catchment (Land Surveying Office of North Rhine-Westphalia) with the coordinates of the Erkensruhr discharge station. In order to minimize computation time, the Erkensruhr mesh consisted of a riparian and a hillslope zone with different grid spacing distinguished by slope and distance to the river. The riparian zone was resolved in a 100x100 m and the hillslope zone in a 200x200 m spacing. The Wüstebach catchment was fully discretized with a 100x100 m spacing to facilitate the comparison with the independent Wüstebach simulation at 100x100 m. In the Erkensruhr setup, the delineation of the riparian area was achieved with slope information of the DEM. The riparian area included catchment parts with slopes larger than 15° and had a minimum distance of two grid units (200 m) to the river network.

The triangulation was performed with the GridBuilder tool (version 4.0 from 2002) developed by Rob McLaren from the University of Waterloo. GridBuilder uses the outer boundary and the boundary of the riparian area as constraints for the triangulation. Three parameters have to be defined for the mesh calculation: target element length, stretch factor (if an element is smaller than the target element length, it is multiplied by this factor) and node drop rate (influences number of nodes in an area where the target element lengths change). The stretch factor and the node drop rate both influence the number of elements at the borders of the riparian area. The parameters were chosen to minimize the number of nodes and the number of small elements at the boundary to the riparian areas. The following parameter values were chosen: 141.42136, 5, 5 (riparian area: 100x100 m grid spacing) and 282.84272, 2, 1 (all other areas: 200x200 m grid spacing). This procedure produced the grid illustrated in Figure 7.7. It consists of 5839 elements and 3031 nodes. In the vertical, the subsurface domain was 2 meters deep and was resolved in 28 numerical layers which increased thickness with increasing depth analogous to the discretization used at the Wüstebach catchment. In total, the subsurface had 84.868 nodes with additional 3031 nodes for the surface domain which is superimposed with the dual node approach. For all setups, a critical depth boundary was used for the 2D surface boundary nodes and no flow conditions were assigned to all other boundary nodes.

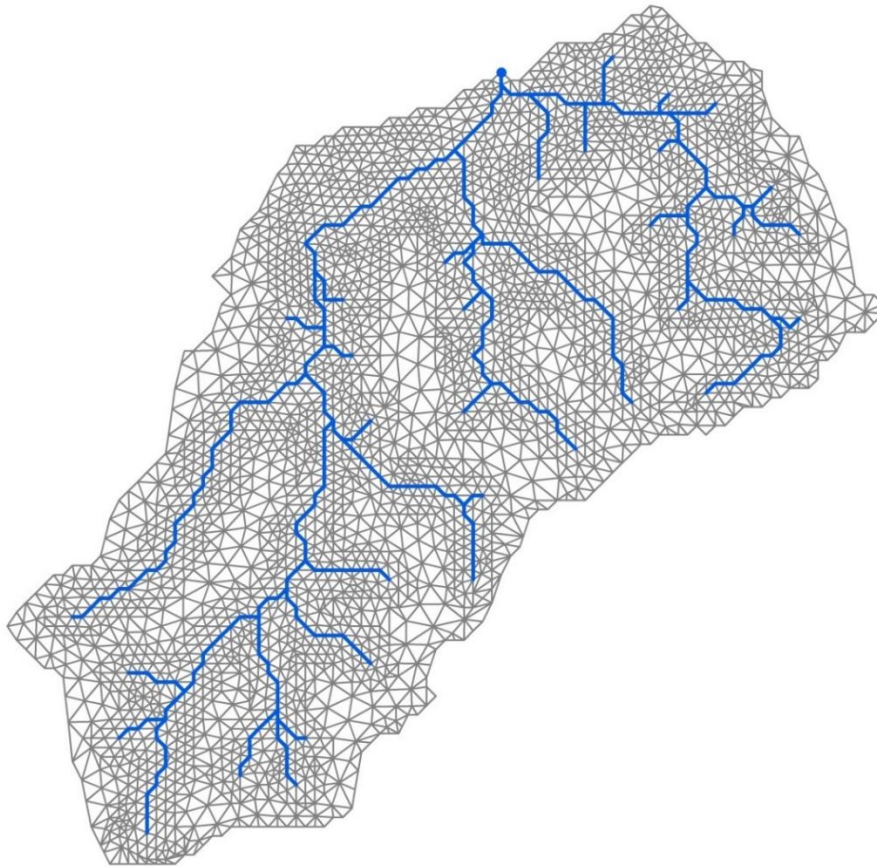


Figure 7.7: Illustration of the horizontal spatial discretization with river network and outlet of the Erkensruhr catchment.

7.3 Parameterization and calibration

7.3.1 Land use

Estimation of land use parameters of the Wüstebach has been conducted by Sciuto and Diekkrüger (2010); respective parameter values are reported in Table 7.1. In this thesis, the anoxic and oxic transpiration limiting saturations and the canopy storage parameter were calibrated as outlined in chapter 7.3.4. The Wüstebach catchment was assumed to be homogeneously covered with spruce. Thus, the following description focuses on the parameterization and parameter estimation of the Erkensruhr catchment.

For the Erkensruhr simulations with heterogeneous land use, the Moderate Resolution Imaging Spectroradiometer (**MODIS**) Leaf Area Index (LAI) data sets between 2003 and 2013 with a temporal resolution of 8 days and a spatial resolution of 1x1 km were used. The MODIS land use classification distinguishes between: Water, Evergreen needleleaf trees, Evergreen broadleaf trees, Deciduous needleleaf trees, Deciduous broadleaf trees, Shrub, Grass, Cereal crops, Broadleaf crops, Urban, Snow and ice and Barren/ sparse vegetation. Mean monthly LAI values for agriculture, grassland and deciduous broadleaf forests were computed as an arithmetic mean

of the 8-day LAI values. Figure 7.8 shows mean monthly LAI values for the three most important land use classes of the Erkensruhr catchment.

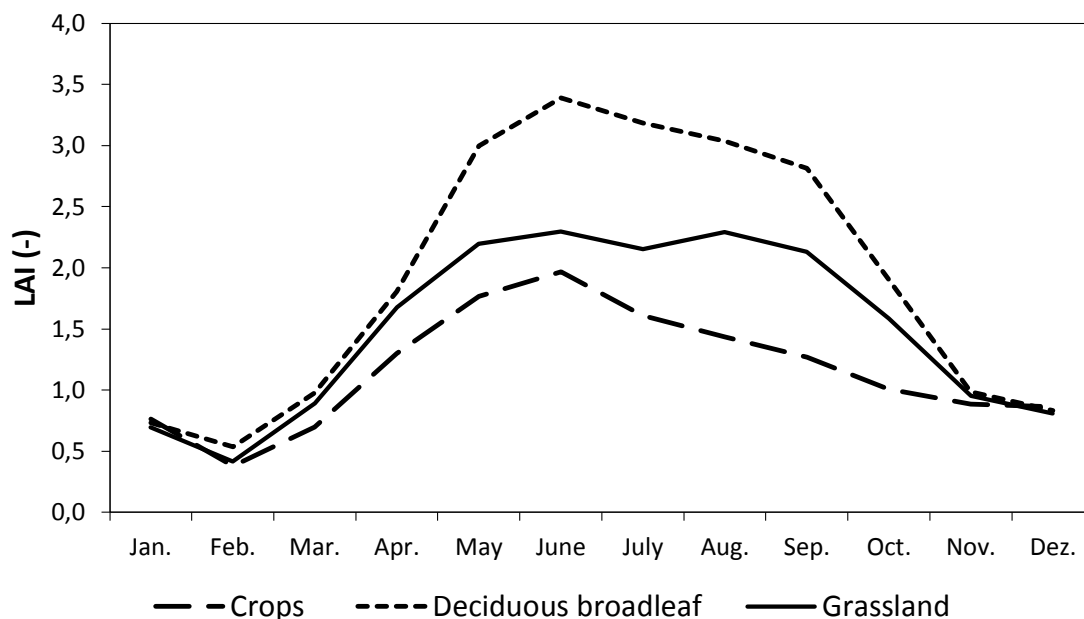


Figure 7.8: Mean monthly LAI for the three land use classes “crops, deciduous broadleaf forest and grassland” derived from MODIS data.

Meinen et al. (2009) and Dannowski & Wurbs (2003) reported the distribution of root biomass with soil depth for *Fagus sylvatica* and for extensive grassland. A polynomial function (4th degree) was fitted to the data for *Fagus sylvatica* ($R^2= 0.99$) and an exponential function to the extensive grassland ($R^2= 0.98$). HydroGeoSphere offers 4 different root distribution functions: constant, linear, quadratic and cubic decay (also refer to chapter 7.1). Figure 7.9 compares the empirically derived functions with the cubic and quadratic HydroGeoSphere root distribution functions. It is visible that the empirical function for the deciduous forest fits best to the quadratic decay function ($R^2=0.99$) and the exponential function fits best to the cubic decay function ($R^2=0.90$). Table 7.1 lists all vegetation parameters and the respective references that have been used in the simulation.

As outlined before, oxic and anoxic transpiration limits are calibrated for the Wüstebach catchments to an evapotranspiration fraction of 40% measured with eddy-covariance data from the Wüstebach catchment (refer to chapter 6.2.2). At the Erkensruhr, grassland is one of the main land use types (chapter 6.2.1). Measured actual evapotranspiration data from a nearby grassland site (Marius Schmidt (Research Center Jülich), personal communication) showed that grassland has a fraction of actual evapotranspiration of 60 % compared to local precipitation rates and is thus higher than estimates for the spruce forest Wüstebach. This observation made the adjustment of the oxic and anoxic transpiration limits for grassland areas necessary. They were set to a value which allowed transpiration to be unlimited if the saturation exceeds the

field capacity. As no measurements of actual evapotranspiration for a deciduous forest were available, the necessary parameters were taken unchanged from the Wüstebach catchment.

Table 7.1: Summary of used parameters for the Erkensruhr simulation study.

Land Use Class \ Parameter	Coniferous	Deciduous	Pasture/ Grassland	Agriculture	Urban
Mean annual LAI (-)	6.7 ^a	1.93 ^b	1.51 ^b	1.16 ^b	25.5 ^b
Evaporation depth (m)	0.2 ^a	Transferred			
Root depth (m)	0.5 ^a	1.8 ^c	0.35 ^d	1.0 ^e	Deactivation
Root and evaporation distribution function (-)	Quadratic ^a	Quadratic ^f	Cubic ^d	Quadratic ^e	
Transpiration fitting parameters (-)	0.3 ^a , 0.2, 1.0 ^a	Transferred			
Transpiration limiting saturations (Wilting point, Field capacity, Oxic, Anoxic) (-)	0.3 ^a , 0.4 ^a , 0.89 ^g , 0.97 ^g	Transferred	0.3 ^a , 0.4 ^a , 1.0, 1.0	Transferred	
Canopy storage (mm/per LAI)	0.8	0.83 ^h	1.0 ^h	2.5 ^h	15.0 ^e
Evaporation limiting saturations (min, max) (-)	0.3 ^a , 0.4 ^a	Transferred			

^a Sciuto and Diekkrüger, 2010, ^b MODIS data, ^c Breuer et al., 2003 (*Fagus sylvatica* on deep loam in Germany), ^d Values for extensive grassland by Dannowski and Wurbs (2003), ^e Assumption, ^f Meinen et al., 2009, ^g Cornelissen et al., 2014, ^h Mean interception capacities for grassland (1.5 mm), agriculture (2.9 mm) and *Fagus sylvatica* (1.6 mm) according to Breuer et al. (2003) and Mendel (2000) were divided by corresponding mean annual LAI according to MODIS data.

The simulation of forest growth between 1951 and 2000 required the definition of a time varying LAI. Due to the lack of measurements for this period, the LAI was taken from simulation results obtained with the process based forest hydrological model LWF-Brook90 developed by Hammel and Kennel (2001). Figure 7.10 shows resulting annual mean, maximum and minimum LAI values. In HydroGeoSphere, a time varying LAI influences the simulation of transpiration and evaporation by Equation 17 which is a function of the LAI and two dimensionless fitting parameters C_1 and C_2 (refer to chapter 7.1). If the parameter C_1 is 0.3, C_2 is 0.2 and the LAI is equal or above 2.7, the equation equals 1. This means that the canopy completely covers the ground at a LAI value of 2.7 not limiting the transpiration rate but reducing ground evaporation to zero. According to Figure 7.10, a LAI value above 2.7 was reached in the year 1963 and thus, evaporation from the ground was expected to be equal to zero from 1963 onwards.

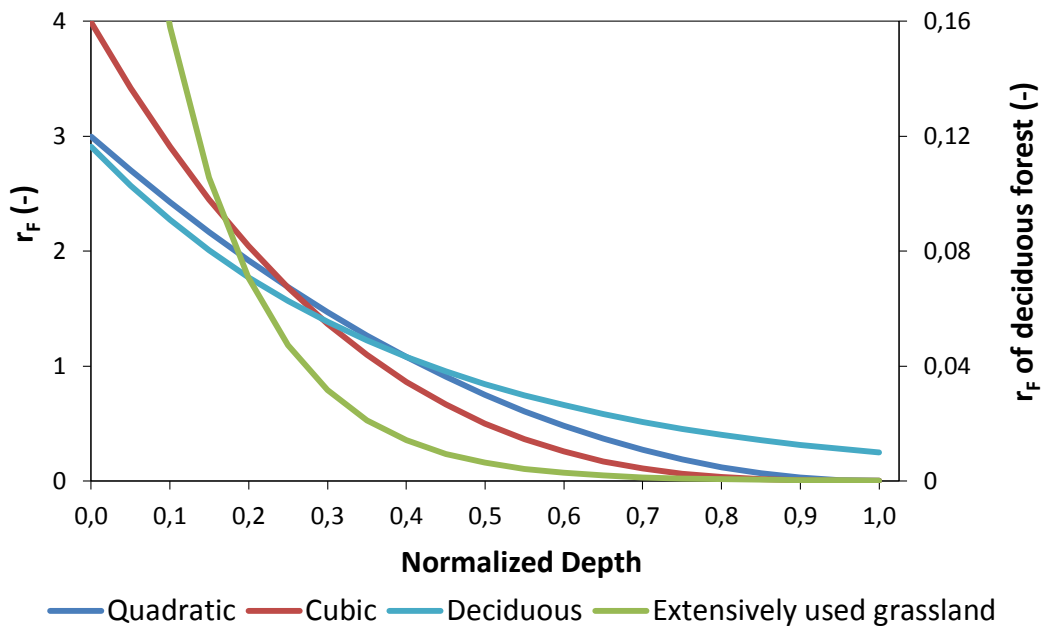


Figure 7.9: Comparison between empirically derived root extraction functions (r_F) for deciduous forest and extensive grassland with standard HydroGeoSphere root distribution functions.

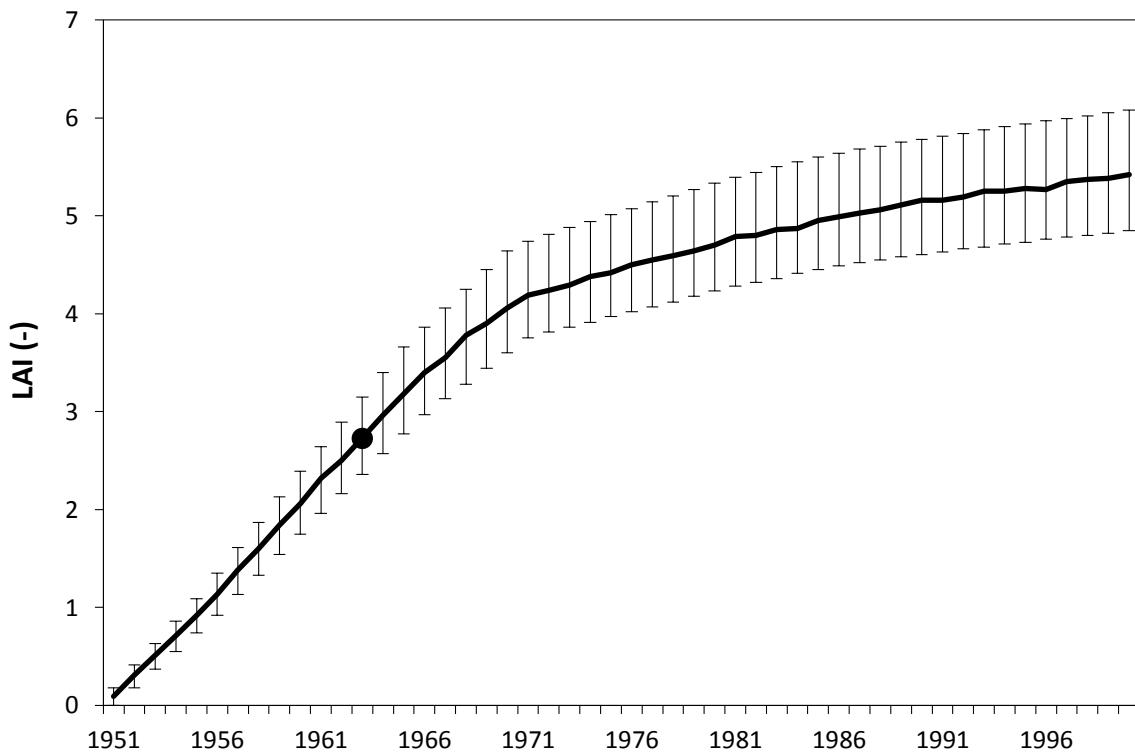


Figure 7.10: Minimum, maximum and mean annual LAI used for the long-term simulation study of forest growth in the Erkensruhr catchment (Hammel and Kennel, 2001). The mean LAI of 2.73 is highlighted with a black circle.

7.3.2 Soil

In HydroGeoSphere, the nonlinear relationship between pressure and saturation is described by the van-Genuchten-Mualem model (van Genuchten, 1980). The equation has already been introduced and illustrated with an example relationship in chapter 7.1. At the Wüstebach and the Erkensruhr catchments, van-Genuchten-Mualem parameters were derived from soil properties using the pedotransfer function of Rawls and Brakensiek (1985) and corrected for skeleton content according to Brakensiek and Rawls (1994).

Resulting parameters for the **Wüstebach** have been reported for each individual soil unit in Sciuto and Dieckkrüger (2010). In this chapter, van-Genuchten parameters are represented as area-weighted mean values in Table 7.2 for each soil type following their differentiation as described in chapter 6.2.5. Table 7.2 illustrates that the variability in van-Genuchten parameters between soil types was weak corresponding to the small variability in soil properties as shown in chapter 6.2.5. Histosol was the only soil type which significantly varied in soil properties and thus also in van-Genuchten parameters. Figure 7.11 exemplarily shows the pressure-saturation relationships for the soil types Cambisol, Gleysol and Histosol. The figure illustrates that Cambisol and Gleysol soils were characterized by a flat retention curve indicating that the dependency between pressure and saturation was weak. On the contrary, Histosol exhibited a steep retention curve and thus a strong dependency between the two variables. The difference is based on the fact that Histosol is a peat soil. As remaining soil types are dominated by silt (refer to Table 6.8), they show a retention curve steeper than that of Cambisol but flatter than that of Gleysol.

Table 7.2: Area weighted mean values of van-Genuchten parameters for the top two soil layers in the Wüstebach catchment (θ_s =porosity, θ_r =residual saturation, α and n being fitting parameters).

	Cambisol	Gleyic Cambisol	Gleysol	Histosol	Regosol	Stagnic Cambisol	Stagnic Eutric Gleysol	Stagnic Gleyic Cambisol
Layer 1								
θ_s (m ³ /m ³)	0.26	0.28	0.30	0.69	0.25	0.26	0.28	0.26
θ_r (m ³ /m ³)	0.04	0.05	0.06	0.01	0.05	0.05	0.06	0.04
α (1/m)	1.73	1.75	1.28	8.09	2.54	1.78	1.81	1.88
n (-)	1.32	1.31	1.19	1.55	1.32	1.30	1.29	1.31
Layer 2								
θ_s (m ³ /m ³)	0.12	0.10	0.14	0.21	0.17	0.15	0.17	0.14
θ_r (m ³ /m ³)	0.02	0.02	0.03	0.04	0.03	0.02	0.03	0.02
α (1/m)	1.44	1.44	1.25	1.26	1.44	1.44	1.44	1.44
n (-)	1.34	1.34	1.30	1.30	1.34	1.34	1.34	1.34

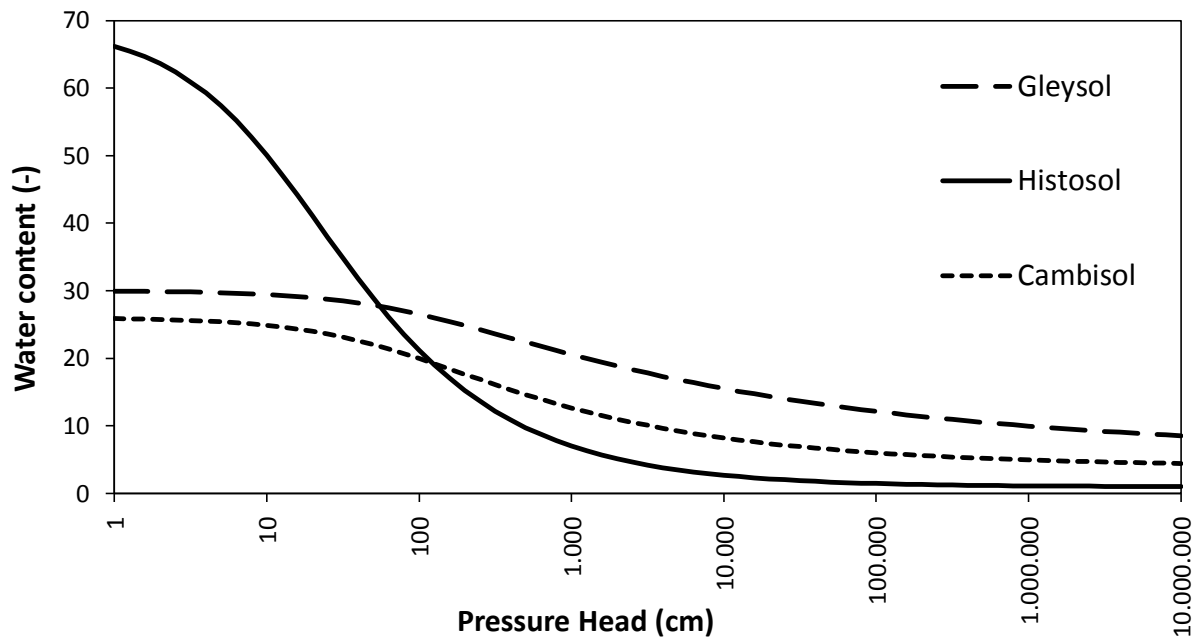


Figure 7.11: Illustration of the pressure-saturation curve for three example soil types from the Wüstebach catchment.

¹ At the **Wüstebach** catchment, a bedrock was added underneath the mineral soil layer. The parameterization of the bedrock followed Li et al. (2008) who reported van-Genuchten-Mualem parameters for Ordovician black shale of a Canadian catchment, assuming that these are comparable to the Devonian shale of the Wüstebach test site. This assumption is supported by the hydrogeological map for North Rhine-Westphalia (Stoltidis and Krapp, 1980) that reports typical saturated conductivity values from 10^{-5} to 10^{-6} m/s and maximum ranges from 10^{-4} to 10^{-8} m/s for the Wüstebach shale. Li et al. (2008) reported vertical saturated conductivities of 10^{-6} and lateral conductivities of 10^{-5} m/s.¹

For the **Erkensruhr** catchment, van-Genuchten parameters were calculated with the same method already applied at the Wüstebach catchment. Table 7.3 summarizes resulting parameter values as area-weighted mean values for the top two soil layers. Values for the soil type Histosol are not shown, because this soil type vanished during the aggregation process (chapter 6.2.5). Table 7.3 illustrates that the fitting parameter 'n' and the residual and saturated water contents are similar in the Wüstebach and in the Erkensruhr catchments, but α -values are much lower in the first soil layer at the Erkensruhr, meaning that higher soil moistures are maintained at pressure heads between 10 and 100,000 cm.

¹ Text taken from Cornelissen et al. (2014)

Table 7.3: Area weighted mean values of van-Genuchten parameters for the top two soil layers in the Erkensruhr catchment (θ_s =porosity, θ_r =residual saturation, α and n being fitting parameters).

	Cambisol	Vertisol	Gleysol	Planosol
Layer 1				
θ_s (m ³ /m ³)	0.26	0.24	0.45	0.23
θ_r (m ³ /m ³)	0.07	0.08	0.09	0.06
α (1/m)	0.94	0.65	2.71	0.98
n (-)	1.12	1.25	1.29	0.87
Layer 2				
θ_s (m ³ /m ³)	0.09	0.04	0.07	0.20
θ_r (m ³ /m ³)	0.03	0.01	0.02	0.06
α (1/m)	1.25	1.61	5.45	0.49
n (-)	1.11	1.26	1.41	0.79

7.3.3 Hydrological parameters

Based on the results of the sensitivity analysis conducted in the context of this thesis (chapter 8.1) and personal communication with model developers (René Therrien and Rob McLaren), hydrological parameters for channel and overland flow have been taken unchanged from Sciuto and Diekkrüger (2010) and are reported in Table 7.4.

Table 7.4: Parameters chosen for channel and surface flow. Parameter explanations can be found in chapter 7.1.

	Stream Channel	Overland Flow
Manning friction coefficients (s*m ^{1/3}):		
X direction	0.85	0.65
Y direction	0.85	0.65
Depression Storage (m)	0.0	0.25
Obstruction Storage (m)	0.25	0.25
Coupling Length (m)	1.00E-02	1.00E-02

7.3.4 Calibration and validation

¹ Calibration was performed for the Wüstebach with a split sample test using data from 2010 for calibration and 2011 for validation. Calibration was done manually.

The first aim of the calibration was to achieve a good agreement between observed and modeled soil moisture dynamics. The van-Genuchten-Mualem parameterization used in this study did include the influence of the skeleton content of the soil but soil sensor probes were not installed in skeleton rich soil parts. Rößler and Löffler (2010) identified the skeleton content of the soil as the main source of uncertainty in their soil moisture simulation. Thus, a calibration of residual water content was performed at 5, 20 and 50 cm depths. To compute new porosity values, the equation given below was used:

$$\theta_{sat_new} = \theta_{res_old} * a + (\theta_{sat_old} - \theta_{res_old}) \quad \text{Equation 26}$$

New porosity values (θ_{sat_new}) were calculated by adding the difference between the old residual saturation (θ_{res_old}) and porosity values (θ_{sat_old}) to the old residual saturations (θ_{res_old}) multiplied by the calibration factor a . Because temporal and spatial soil moisture variability decreases with depth (Manfreda et al., 2007), the measurements and their corresponding calibration factors were assumed to be representative for a certain soil layer. Measurements at 5 cm were assumed to be representative for **5-15 cm** depth, measurements at 20 cm for **15-35 cm** depth and measurements at 50 cm for **35-75 cm** depth. Changes in residual water contents and porosities only affect absolute soil moisture and not its temporal dynamics, because van-Genuchten-Mualem shape parameters were not calibrated. Thus, the multiplication factor for residual saturations calibrated at daily resolution was also used at hourly resolution. The multiplication factor was calibrated for the 25 m and 100 m resolutions to study the influence of changing resolution on the calibration of residual moisture ¹.

The second aim was to match the yearly amount of interception of the spruce canopy which was estimated to 20% with measured data from the Wüstebach catchment as outlined in chapter 6.2.3. In addition, the oxic and anoxic transpiration limiting saturations (refer to Equation 18) were calibrated to match annual discharge amounts and measured evapotranspiration between May and December 2010.

¹ The water balance calibration was performed at daily time steps for the 25 m and the 100 m resolutions. At hourly time steps, the two limiting saturations and the canopy storage parameter were adjusted to fit the interception and transpiration amounts simulated at daily time steps. The calibrated parameters for the non-bedrock setups were used unchanged for the bedrock setups ¹.

¹ Text taken from Cornelissen et al. (2014)

¹ The calibration success in relation to observed runoff was assessed at the **Wüstebach** with the Nash-Sutcliffe Coefficient (NSE; Nash and Sutcliffe, 1970), a measure for noise, the Coefficient of Determination (R^2) which is an indicator for systematic errors and the Percent Bias (PBIAS), which indicates a trend to over- or underestimate the measured data ¹.

At the **Erkensruhr**, Pearson's r which is the square root of the Coefficient of Determination (Correlation Coefficient), the Bias defined as the relation between simulated and observed mean discharge of a given time period, and the Coefficient of Variation (CV) which normalizes the variance with the mean value were used (also refer to chapter 3.4).

7.4 Simulation procedure

Hydrological modeling requires knowledge about the sensitivity of the model parameters. While the selection of parameters depends on the study aim, the model structure and results from previous studies, the size of the sampled parameter space is restricted by the computational demand of the model. The 3D structure and high spatial resolution of HydroGeoSphere (refer to chapter 7.1) is numerically demanding and thus time consuming. Therefore, the number of samples for the sensitivity analysis had to be restricted to 5 per parameter to allow for scale dependent sensitivity analysis for the 25 m and 100 m resolutions of the Wüstebach at daily time steps. These model setups were chosen because (1) the Wüstebach served as a reference for the Erkensruhr and (2) the computational demands of the Erkensruhr setup and of setups with hourly time steps were too large for a sensitivity analysis. The effect of nonlinear dependencies between parameters on their sensitivity (e.g. to reveal compensation effects) could not be investigated due to computational restrictions. Based on the calibration aims of the Wüstebach simulation as outlined in chapter 7.3.4 and results from other studies (Banks et al., 2011; Brunner et al., 2009b; Ebel et al., 2009; Li et al., 2008; Panday and Huyakorn, 2004; Sciuto and Diekkrüger, 2010), the sensitivity of the following 9 parameters to discharge dynamics, water balance, soil moisture dynamics and its standard deviation in 5, 20 and 50 cm depth was investigated:

- K_s and van-Genuchten parameter α (influencing infiltration and soil moisture dynamics),
- specific storage (influences soil moisture storage),
- root depth, LAI, canopy storage, anoxic and oxic transpiration limits (influencing water balance components, discharge and soil moisture dynamics),
- obstruction and depression storage (influencing discharge dynamics and amount),
- Manning friction coefficients in x and y (influence discharge dynamics)
- coupling length (influences infiltration).

¹ Text taken from Cornelissen et al. (2014)

In addition, the influence of numerical parameters (maximum head change, absolute and residual convergence, maximum number of Newton iterations) was investigated. Initial parameters were set equal to the values of Sciuto and Diekkrüger (2010). The investigated parameters and applied parameter ranges are shown in Table 7.5. Each simulation was conducted for the year 2010 with a half-year of spinup.

Table 7.5: Overview about parameters and corresponding change per simulation run considered in the sensitivity analysis.

Parameters	First run		Second run		Third run		Fourth run		Fifth run	
Land use										
Root depth (m)	-50%	0.25	-10%	0.45	0%	0.5	+10%	0.55	50%	0.75
LAI (-)	-50%	3.35	-10%	6.03	0%	6.7	+10%	7.37	50%	10.05
Anoxic limit (-)	-50%	0.43	-10%	0.77	0%	0.85	+10%	0.94	50%	0.97
Oxic limit (-)	-50%	0.85	-10%	0.87	0%	0.97	+10%	1.07	50%	1.46
Canopy Storage (mm)	-50%	0.10	-10%	0.18	0%	0.20	+10%	0.22	50%	0.30
Numerical										
Absolute convergence	-99%	1.0E-05	-90%	1.0E-04	0%	1.0E-03	+900%	1.0E-02	+9900%	1.0E-01
Residual convergence	-99%	1.0E-05	-90%	1.0E-04	0%	1.0E-03	+900%	1.0E-02	+9900%	1.0E-01
Newton iterations	-99%	4.0	-90%	8.0	0%	15.0	+900%	30.0	+9900%	60.0
Head control (m)	-99%	0.5	-90%	1.0	0%	2.0	+900%	10.0	+9900%	50.0*
Hydraulic										
Overland										
X-Manning Friction Coefficient (-)	-50%	0.325	-10%	0.585	0%	0.65	+10%	0.715	50%	0.975
Y-Manning Friction Coefficient (-)	-50%	0.325	-10%	0.585	0%	0.65	+10%	0.715	50%	0.975
Rill storage (m)	-50%	0.125	-10%	0.225	0%	0.25	+10%	0.275	50%	0.375
Obstruction Storage (m)	-50%	0.125	-10%	0.225	0%	0.25	+10%	0.275	50%	0.375
Coupling length (m)	-99%	1.0E-03	-90%	1.0E-02	0%	1.0E-01	+900%	1.0E+00	+9900%	1.0E+01*
Stream										
X-Manning Friction Coefficient (-)	-50%	0.425	-10%	0.765	0%	0.85	+10%	0.935	50%	1.275
Y-Manning Friction Coefficient (-)	-50%	0.325	-10%	0.585	0%	0.65	+10%	0.715	50%	0.975
Rill storage (m)	-50%	0.125	-10%	0.225	0%	0.25	+10%	0.275	50%	0.375
Obstruction Storage (m)	-50%	0.125	-10%	0.225	0%	0.25	+10%	0.275	50%	0.375
Coupling length (m)	-99%	1.0E-03	-90%	1.0E-02	0%	1.0E-01	+900%	1.0E+00	+9900%	1.0E+01*
Soil (independently for litter layer, 5 cm, 20 cm and 50 cm depth)										
Saturated Conductivity (m/s)	-99%	Variable	-90%	Variable	0%	Variable	+900%	Variable	+9900%	Variable
α (1/m)	-99%	Variable	-90%	Variable	0%	Variable	+900%	Variable	+9900%	Variable
Specific storage (1/m)	1.2E-4	Variable	1.2E-3	Variable	0%	1.2E-2	+900%	1.2E-1	+9900%	1.2E-0

*Values are unrealistically high but were included in the simulations due to consistency.

The Wüstebach was simulated at 2 different spatial resolutions (25, 100 m), 2 different temporal resolutions (daily, hourly) and with 2 different lower boundary conditions (with/without bedrock) which adds up to 8 different setups (refer to Table 7.6 for an overview). Four different setups were calibrated independently: 25 m and 100 m resolution at daily and hourly time steps (denoted d25, d100, h25 and h100). Setups including the bedrock underneath the mineral soil layer were not calibrated and are marked by the letter 'b' behind the abbreviation of the setups without bedrock (e.g. d25b). Calibration and validation was performed with a split-sample test with 2010 as calibration and 2011 as validation period both with a spin-up period of half a year. Initial conditions were set equal to the results of a 20 year warmup run.

When 2010 was initially chosen for calibration, measurements of actual evapotranspiration were not yet available and thus data quality was equally well in 2010 and 2011. With the availability of actual evapotranspiration measurements, the data base turned out to be better in 2011 than in 2010, but calibration was already finished with the data for 2010 with good results concerning discharge, actual evapotranspiration amounts and soil moisture dynamics. Thus, 2010 remained the calibration period. However, the influence of the choice of calibration period on model parameters and simulation results was investigated by recalibrating the Wüstebach 25 m setup at daily time steps without bedrock inclusion with data of 2011 (refer to chapter 8.2.3 for results).

The Erkensruhr simulation study consists of 10 different setups (refer to Table 7.6): 6 setups for the Wüstebach headwater catchment using the d100 setup and 4 for the Erkensruhr catchment. Each of the six simulations of the Wüstebach catchment had a unique combination of soil and land use parameter sets. In a first step, the land use of the reference setup (Wbach) was changed to deciduous forest (WbachDeci) and grassland (WbachGrass) while keeping all other inputs constant. In a second step, the fine resolution soil data from the Wüstebach was replaced by the low resolution soil data of the Erkensruhr and applied at the Wüstebach using the three different land use parameter sets: coniferous (WbachEsoilConi), deciduous (WbachEsoilDeci) and grassland (WbachEsoilGrass). Initial conditions were kept equal to those used for the high resolution Wüstebach simulations. The base setup of the Erkensruhr catchment (Erk) considered distributed soil data from the Erkensruhr, while land use, potential evapotranspiration and precipitation of the Wüstebach simulation were used. Spatial heterogeneity of land use, potential evapotranspiration and precipitation were introduced step-wise into the Erkensruhr setup leading to the 3 additional setups Erk_LN, Erk_LN_PET and Erk_LN_PET_P. Initial conditions were set equal to the results of a 10 year run. It should be noted that for the simulations of the Wüstebach catchment, a parallel HydroGeoSphere version of July 2012 was used while for the simulations of the Erkensruhr catchment, the parallel version of December 2014 was used which corrected a bug in the interception module. Thus, the canopy storage parameter which influences the maximum possible interception amount had to be recalibrated

for the Erkensruhr simulations. Differences arising from the usage of different versions are analyzed in chapter 8.3.3.

Table 7.6: Spatio-temporal resolution, applied soil and land use and abbreviation of simulations.

Abbreviation	Temporal Resolution	Spatial Resolution	Soil Data	Land Use	Additional Information
Wüstebach					
d25	Daily	25 m	Wüstebach	Coniferous	Calibration 2010
h25	Hourly				Calibration 2010
d25b	Daily				Bedrock
h25b	Hourly				Bedrock
d100	Daily	100 m			Calibration 2010
h100	Hourly				Calibration 2010
d100b	Daily				Bedrock
h100b	Hourly				Bedrock
Erkensruhr					
Wbach	Daily	100 m	Wüstebach	Coniferous	
WbachDeci			Wüstebach	Deciduous	
WbachGrass			Wüstebach	Grassland	
WbachEsoilConi			Erkensruhr	Coniferous	
WbachEsoilDeci			Erkensruhr	Deciduous	
WbachEsoilGrass			Erkensruhr	Grassland	
Erk			Erkensruhr	Coniferous	
Erk_LN			Erkensruhr	Distributed	
Erk_LN_PET			Erkensruhr	Distributed	Distributed PET
Erk_LN_PET_P			Erkensruhr	Distributed	Distributed PET and Precipitation
Wüstebach as part of Erkensruhr					
ErkWbach	Daily	100 m	Same as Erk		
ErkWbach_LN			Same as Erk_LN		
ErkWbach_LN_PET			Same as Erk_LN_PET		
ErkWbach_LN_PET_P			Same as Erk_LN_PET_P		
Long-term Simulation					
Erk_Orig	Daily	100 m	Erkensruhr	Coniferous	Climate data equal to Wüstebach setups
Erk_Kall					New climate data from Kall-Sistig
WbachEsoil_Orig	Daily	100 m	Wüstebach	Coniferous	Climate data equal to Wüstebach setups
WbachEsoil_Kall					New climate data from Kall-Sistig
Long-term simulation run (1951-2000)	Daily	100 m	Erkensruhr	Coniferous	New climate data from Kall-Sistig

In chapter 7.1, the method for separating different flow components available for HydroGeoSphere was described. Unfortunately, the baseflow filter version, which was available for the simulations in this thesis, was coupled to a HydroGeoSphere version which did not support spatially distributed data inputs in the form of grid files. This data format was, however, necessary to account for the heterogeneous potential evapotranspiration and precipitation patterns in simulations Erk_LN_PET and Erk_LN_PET_P. Therefore, the baseflow filter could only be applied for the Erkensruhr simulations with homogeneous climate input data.

Long-term discharge data of the Erkensruhr catchment offered the possibility to study the effect of a growing coniferous forest on water balance and evapotranspiration components. As the computation of the Erkensruhr simulations took several days for a 2.5 year simulation period, a simulation covering the growing period between 1951 and 2000 would have lasted at least two months. However, the large similarity between the discharge dynamics of the Wüstebach and the Erkensruhr (refer to Figure 6.13) allowed the important assumption that the Wüstebach catchment is representative for the whole Erkensruhr. Thus, the simulation of forest growth between 1951 and 2000 was conducted with the WbachEsoilConi setup with climate data from Kall-Sistig. Simulated discharge rates of this simulation were upscaled to match those of the Erkensruhr with a regression function (refer to chapter 6.2.4). Climate and precipitation data for the long term simulation differed from data used in the original simulation setups WbachEsoilConi and Erk (refer to chapter 6.2.2.). Therefore, respective simulation results of model runs with original and new climate data were compared for the years 2010 and 2011. Setups using original climate data are abbreviated WbachEsoil_Orig and Erk_Orig and setups with climate data from Kall-Sistig are abbreviated WbachEsoil_Kall and Erk_Kall.

7.5 Application of Variogram and Kriging methods

In this thesis, ¹ variogram and kriging calculations were performed using the following MATLAB functions:

The experimental variograms were calculated with the “variogram”- MATLAB function, and the theoretical variogram was fitted with the “variogramfit”-function. Kriging was performed with the “krig”-function, which is part of the Kriging Software Package by Dezhong Chu from the Woods Hole Oceanographic Institution. As the finer grid resolution had eight times more nodes than the existing soil moisture measurement network, the 105 closest nodes to the measurement points were selected with the “near” tool of the ArcGIS proximity toolbox.

The number of lags was chosen to be most representative for the distribution of data points. It varied between 15 and 30. For the measured data and the 25 m resolution, a spherical model was used. In the case of the 100 m resolution, a Gaussian model was applied, because it provided a better fit to the experimental variogram than the spherical model. The lag tolerance (50%), the maximum variogram distance (300 m), as well as the search radius for kriging (300 m) and the kriging block size of 10x10 m, remained unchanged.

The resulting patterns were tested for similarity with the Kappa statistics (Viera and Garrett, 2005). In addition, a correlation analysis of slope, relative elevation, porosity distribution, and topsoil measured/simulated soil moisture patterns was performed to find out if different spatial patterns drive the variability in soil moisture in the simulation and measurements. Because not all variables showed a normal distribution, the Spearman correlation coefficient was applied. Significance was tested using a student’s t-test with an alpha of 0.05 ¹.

¹ Text taken from Cornelissen et al. (2014)

8 Results and Discussions

8.1 Sensitivity analysis

The sensitivity analysis accounted for the variation of 31 different parameters (refer to Table 7.5 for a detailed overview of considered parameters). For each parameter, 5 simulation runs were conducted, one of them with unchanged parameter values and 4 with changed parameter values. Simulations with unchanged parameter values (in total 31) were used to investigate the intrinsic variability of water balance, soil moisture and run time resulting from the inaccuracy of the numerical solution procedure. In total, 155 simulations were performed for the Wüstebach setups at 25 m and 100 m resolution at daily time steps. In the case of mathematical inaccuracy, the results of the sensitivity analysis are reported as relative changes to the mean of all 31 reference simulations. In all other cases, results are reported as relative changes to a simulation chosen arbitrarily from the 31 simulations using equal parameter values. As the resulting variation originates from numerical inaccuracies, a “best case” simulation cannot be identified and thus the choice of the reference simulation was done arbitrarily. Sensitivity was investigated for the annual sums of 5 water balance components (discharge, infiltration, exfiltration, transpiration and interception), the run time, the annual mean and coefficient of variation of soil moisture and its standard deviation at 5, 20 and 50 cm depth and the coefficient of variation of discharge.

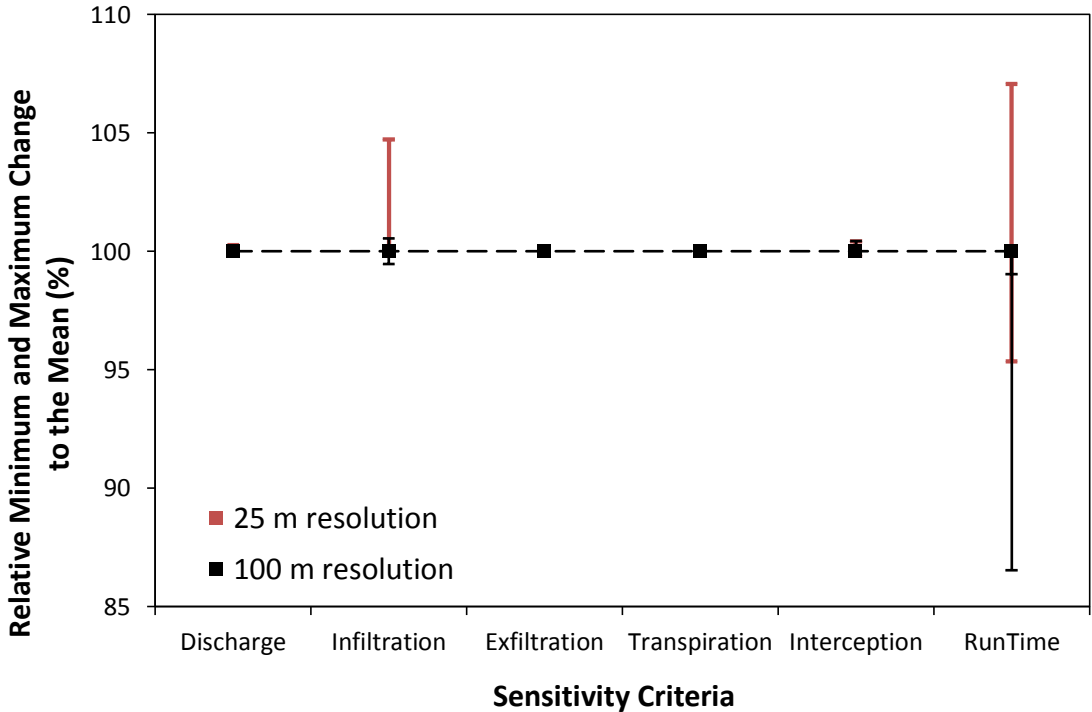


Figure 8.1: Maximum and minimum deviations of water balance components and run time from the mean of 31 simulations with equal parameter values. The figure expresses the sensitivity to the numerical solution procedure.

Figure 8.1 shows the variation in water balance components discharge, infiltration, exfiltration, transpiration and interception and run time due to the **inaccuracy of the numerical solution** procedure for the 25 m and 100 m resolution setups.

It is visible that only infiltration and run time exhibits variations larger than 1% at 25 m resolution. At 100 m resolution, run time is the only variable with notable variability.

In contrast to water balance components, soil moisture metrics and the coefficient of variation of discharge exhibited variations smaller than 1%. Variations of mean soil moisture and mean standard deviations were even lower than 0.2%. Generally, the 25 m resolution showed larger variations than the 100 m resolution setup with highest values occurring for the coefficient of variation of soil moisture standard deviation in 20 cm depth (1%).

The **sensitivity of water balance components** to a variation of chosen parameters by $\pm 10\%$ and $\pm 50\%$ is reported (refer to Table 7.5 for a detailed overview) for the 25 m setup in Figure 8.2 and in Figure 8.3 for the 100 m resolution. Positive parameter changes are indicated by green color, negative changes by red color and symbol size refers to the relative change in water balance components compared to the reference simulation. Filled circles indicate a decrease and “plus” symbols an increase in annual water balance sum.

Result of the 25 m resolution illustrated in Figure 8.2 showed some interesting features. First of all, infiltration and exfiltration were the most sensitive components as they reacted to changes of all parameters while interception was the least sensitive component. Furthermore, the parameters oxic and anoxic limit and the K_s of the litter layer turned out as the most sensitive parameters. The high sensitivity of transpiration to oxic and anoxic saturation limits is in line with observations by Sciuto and Diekkrüger (2010). Figure 8.2 also illustrates that the sensitivity of infiltration and exfiltration to saturated conductivity depended on the strength of change in the parameter. Whereas infiltration and exfiltration increased with a small decrease in K_s (factor 10), the two water balance components decreased with a large increase in saturated conductivity (factor 100). This unexpected behavior is in contrast to findings by e.g. Kværnø and Stolte (2012) who report an increase in infiltration with higher area weighted mean K_s . Consequences and reasons for this behavior are described in detail in chapter 8.3.1. Results for the 100 m resolution (Figure 8.3) were very similar to those outlined for the 25 m resolution with the exception that the sensitivity of water balance components to increases in litter layer K_s was much lower.

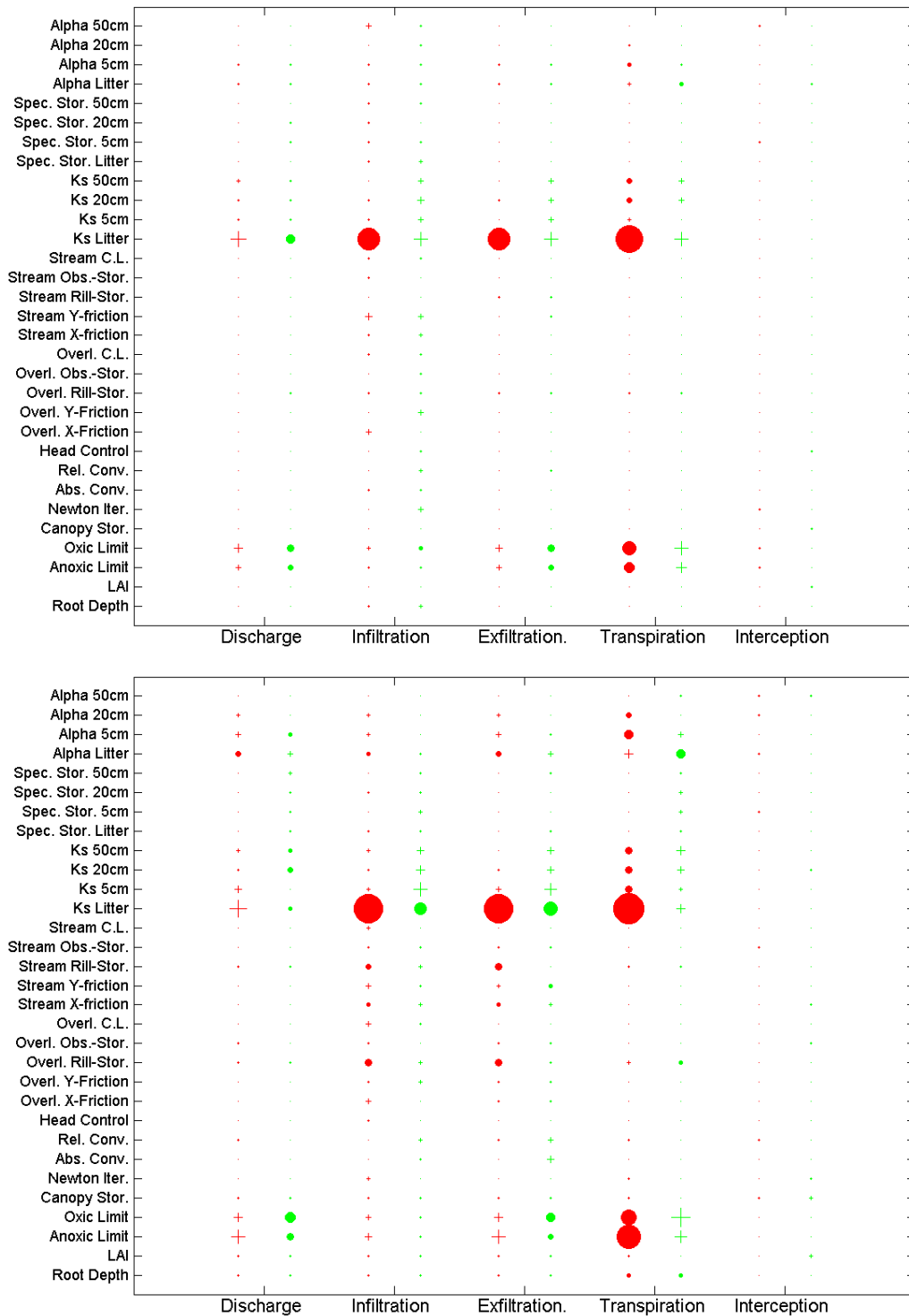


Figure 8.2: Sensitivity of water balance components to parameter change of $\pm 10\%$ (top) and $\pm 50\%$ (bottom) at 25 m resolution. Symbol size refers to relative changes in water balance components compared to the reference simulation. Filled circles indicate a decrease, "Plus" symbols an increase in water balance component due to a positive (green color) or negative parameter change (red color). Abbreviations: Spec. Stor. =Specific Storage; C.L. =Coupling Length; Obs.-Stor = Obstruction-Storage Length; Rill-Stor. =Rill-Storage Length; Overl. =Overland; Conv.=Convergence; Iter.= Iterations; Canopy Stor.=Canopy Storage.

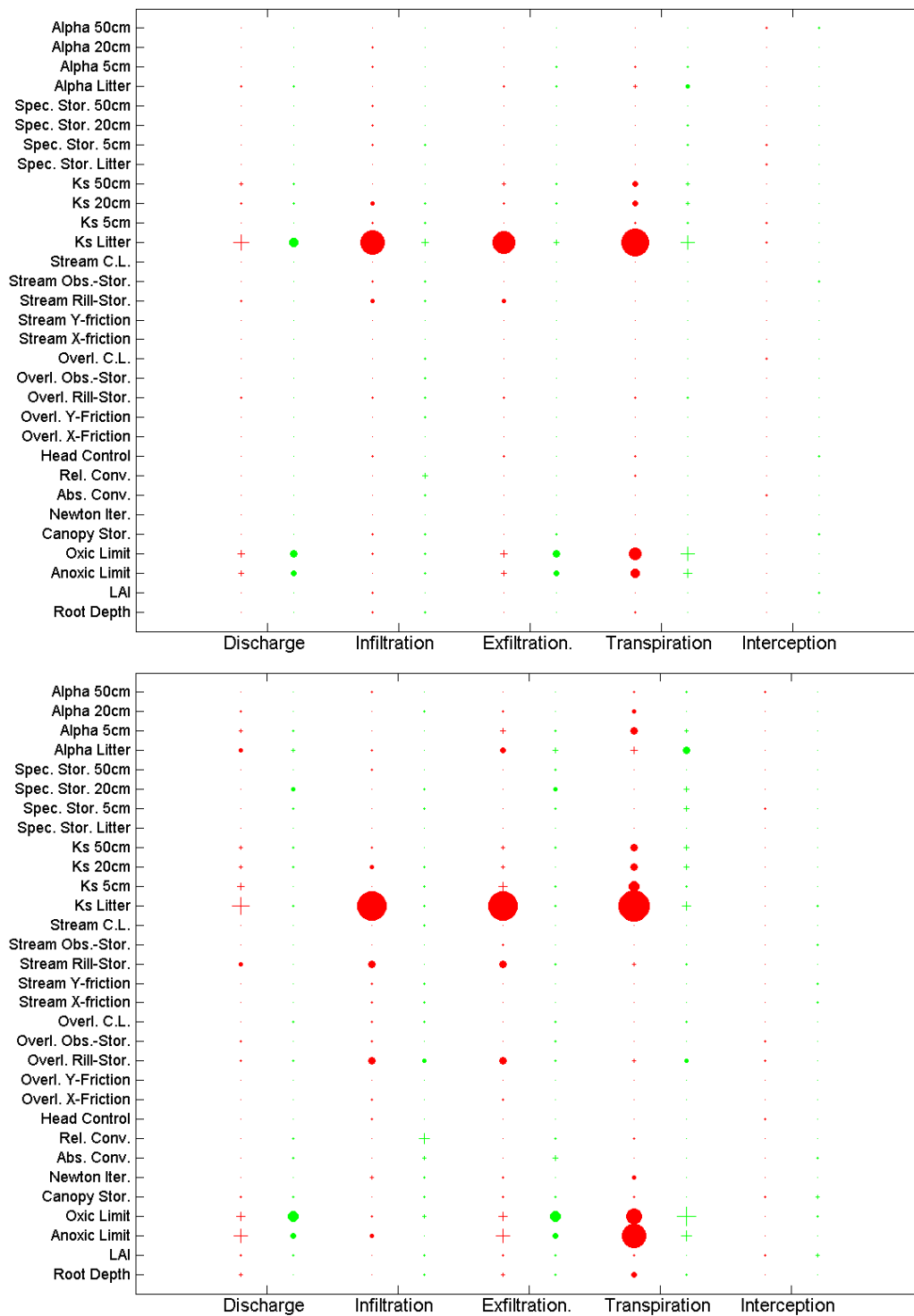


Figure 8.3: Sensitivity of water balance components to parameter change of $\pm 10\%$ (top) and $\pm 50\%$ (bottom) at 100 m resolution. Symbol size refers to relative changes in water balance components compared to the reference simulation. Filled circles indicate a decrease, "Plus" symbols an increase in water balance component due to a positive (green color) or negative parameter change (red color). Abbreviations: Spec. Stor. =Specific Storage; C.L. =Coupling Length; Obs.-Stor = Obstruction-Storage Length; Rill-Stor. =Rill-Storage Length; Overl. =Overland; Conv.=Convergence; Iter.= Iterations; Canopy Stor.=Canopy Storage.

In addition to water balance components, the **sensitivity of soil moisture** and of its standard deviation to parameter changes was investigated. Figure 8.4 shows the results for the 25 m resolution and Figure 8.5 for the 100 m resolution. It is important to note that the standard deviation depicted in Figures 8.4 and 8.5 measures the spatial variation in soil moisture and not its temporal variation.

Comparable to the sensitivity of water balance components, the oxic and anoxic limits and the litter layer K_s are the most sensitive parameters for soil moisture statistics at 25 m resolution. In addition, statistic metrics of soil moisture were sensitive to K_s values at 20 cm and 50 cm depth and the root depth. Interestingly, the sensitivity of the coefficient of variation was larger than that of mean values of soil moisture and its standard deviation. Run time was especially sensitive to changes in oxic, anoxic limits and K_s values but unlike statistical measures of soil moisture and discharge, run time exhibited sensitivity to all other parameters. It should be noted that positive and negative changes in mean and coefficient of variation of soil moisture were contradictory to each other at 5 and 20 cm depth. For example, at 5 cm depth, an increase in litter layer K_s resulted in an increase in coefficient of variation of soil moisture but a decrease in mean soil moisture. As the coefficient of variation is defined by the ratio of standard deviation to mean soil moisture, a large decrease in mean soil moisture results in an increase in the coefficient of variation as long as the decrease in the mean is larger than the decrease in its standard deviation. In chapter 2.2, it was outlined that the unimodal relationship between mean soil moisture and its (spatial) standard deviation is an important characteristics of soil moisture. The unimodal shape explains why an increase in soil moisture (e.g. for the K_s of the litter layer) at 5 cm depth resulted in a decrease in mean spatial standard deviation.

The bottom part of Figure 8.4 illustrates sensitivity results for a parameter change of $\pm 50\%$ at 25 m resolution. In addition to the already reported sensitivity to K_s , anoxic and oxic limits, the investigated statistics exhibited significant sensitivity to root depth, to the specific storage at all depths (mostly decreasing investigated metrics) and to the van-Genuchten parameter α which mostly resulted in a decrease in statistical measures. Comparable to results achieved with the smaller parameter change, the variation in the coefficient of variation was a lot larger than that of mean values of soil moisture and standard deviation. A decrease by the factor 100 in the relative convergence criterion influencing the solution time step strongly increases run time but the corresponding increase by a factor 100 did not lead to a decrease in run time of comparable magnitude.

In the following, main **differences between 100 m and 25 m resolution** in the sensitivity of statistical measures of soil moisture and discharge (Figures 8.4 and 8.5) are summarized. Largest differences between the two resolutions occurred for saturated conductivity values at 5, 20 and 50 cm depth, anoxic and oxic limits and run time. Resolution effects on sensitivity were not dependent on the intensity of parameter change. The different sensitivity of subsoil K_s resulted from the fact that subsoil K_s were volume averaged values of those used at 25 m resolution. As it

was outlined in chapters 3.2 and 3.3, parameters like K_s or the oxic and anoxic limits subsume subgrid variability and therefore, their absolute value and their sensitivity are scale-dependent. Run time was nearly equally sensitive to all parameters at 100 m resolution while at 25 m resolution, relative convergence was the most important parameter for run time. This result indicates that with increasing number of nodes, numerical parameters gain more importance for the run time.

In chapter 7.3.4, water balance components and soil moisture dynamics were defined as the primary calibration aims. Based on results of the sensitivity analysis, the anoxic and oxic saturation limits and the litter layer K_s were identified as having the largest influence on water balance components at both model resolutions. The canopy storage parameter did not show a large sensitivity in terms of interception at both resolutions which indicates that the applied parameter range was insufficient. Soil moisture dynamics was most sensitive to litter layer K_s , subsoil K_s and transpiration limiting saturations. As oxic and anoxic saturation limits altered water balance components as well as moisture and discharge dynamics, these parameters in addition to the canopy storage parameter were selected for calibration. The catchment mean soil moisture was adjusted by varying residual saturation and porosities as described in chapter 7.3.4. K_s values were not considered for calibration because a calibration to e.g. soil moisture dynamics would compensate for the missing bypass flow component in the model setup. As outlined in chapter 3.2, soil matrix and bypass flow can only be simulated with the Richards' equation if the equation is divided into a matrix and a bypass part as for example done in the method by Gerke and van Genuchten (1993). As this is not done in the current model setup, a calibration of the saturated conductivity was not performed.

At 25 m resolution, run time primarily depended on the relative convergence criterion but at 100 m resolution, run time varied nearly equally strong for all parameters. Thus, only relative convergence will be adjusted to influence computation time.

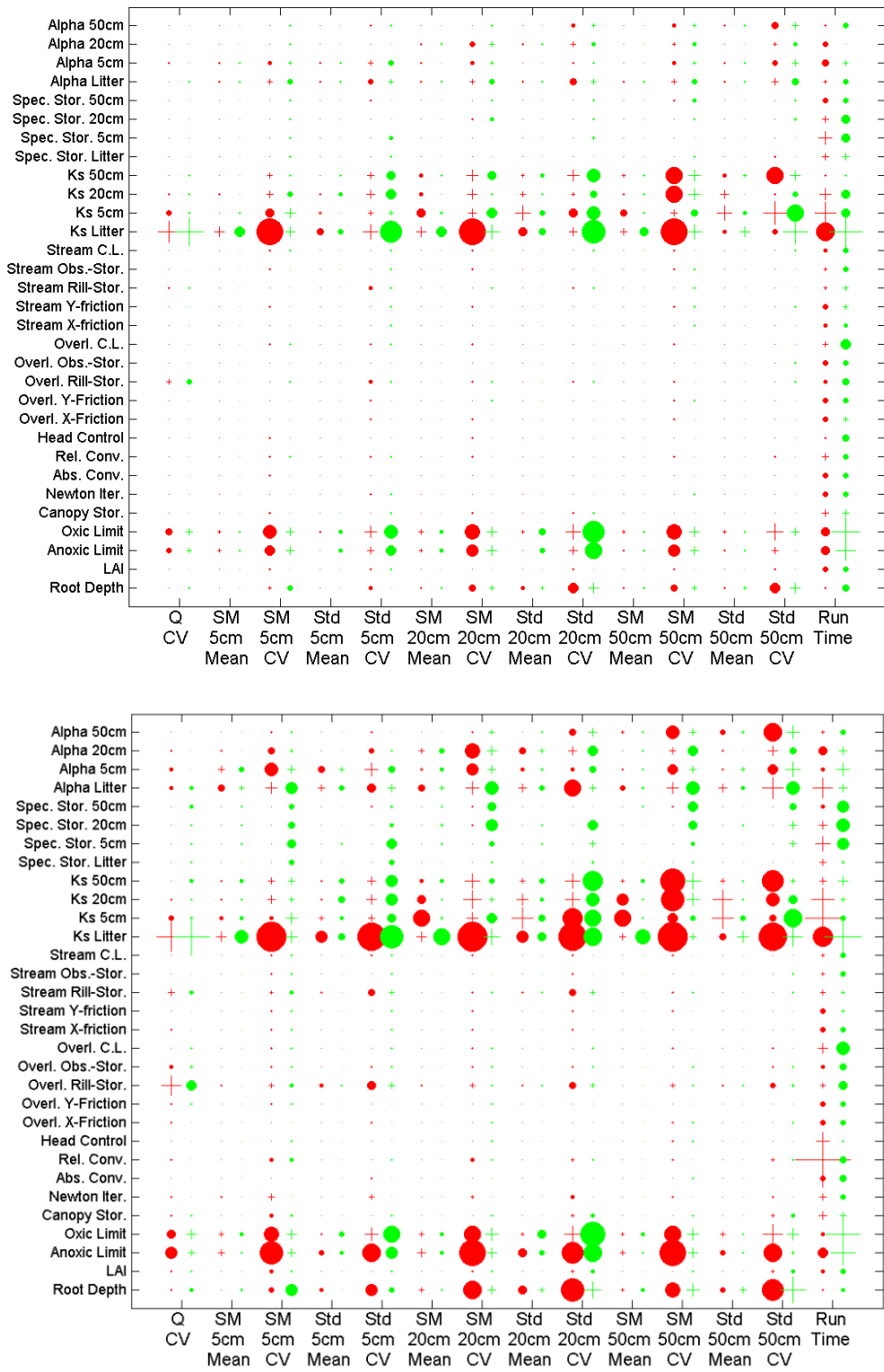


Figure 8.4: Sensitivity of the annual mean and coefficient of variation (CV) of soil moisture (SM) and its standard deviation (STD) in 5, 20 and 50 cm depth and the coefficient of variation (CV) of discharge (Q) to parameter change of $\pm 10\%$ (top) and $\pm 50\%$ (bottom) at 25 m resolution. Symbol size refers to relative changes in water balance components compared to the reference simulation. Filled circles indicate a decrease, "Plus" symbols an increase in water balance component due to a positive (green color) or negative parameter change (red color). Abbreviations: Spec. Stor. =Specific Storage; C.L. =Coupling Length; Obs.-Stor = Obstruction-Storage Length; Rill-Stor. =Rill-Storage Length; Overl. =Overland; Conv.=Convergence; Iter.= Iterations; Canopy Stor.=Canopy Storage.

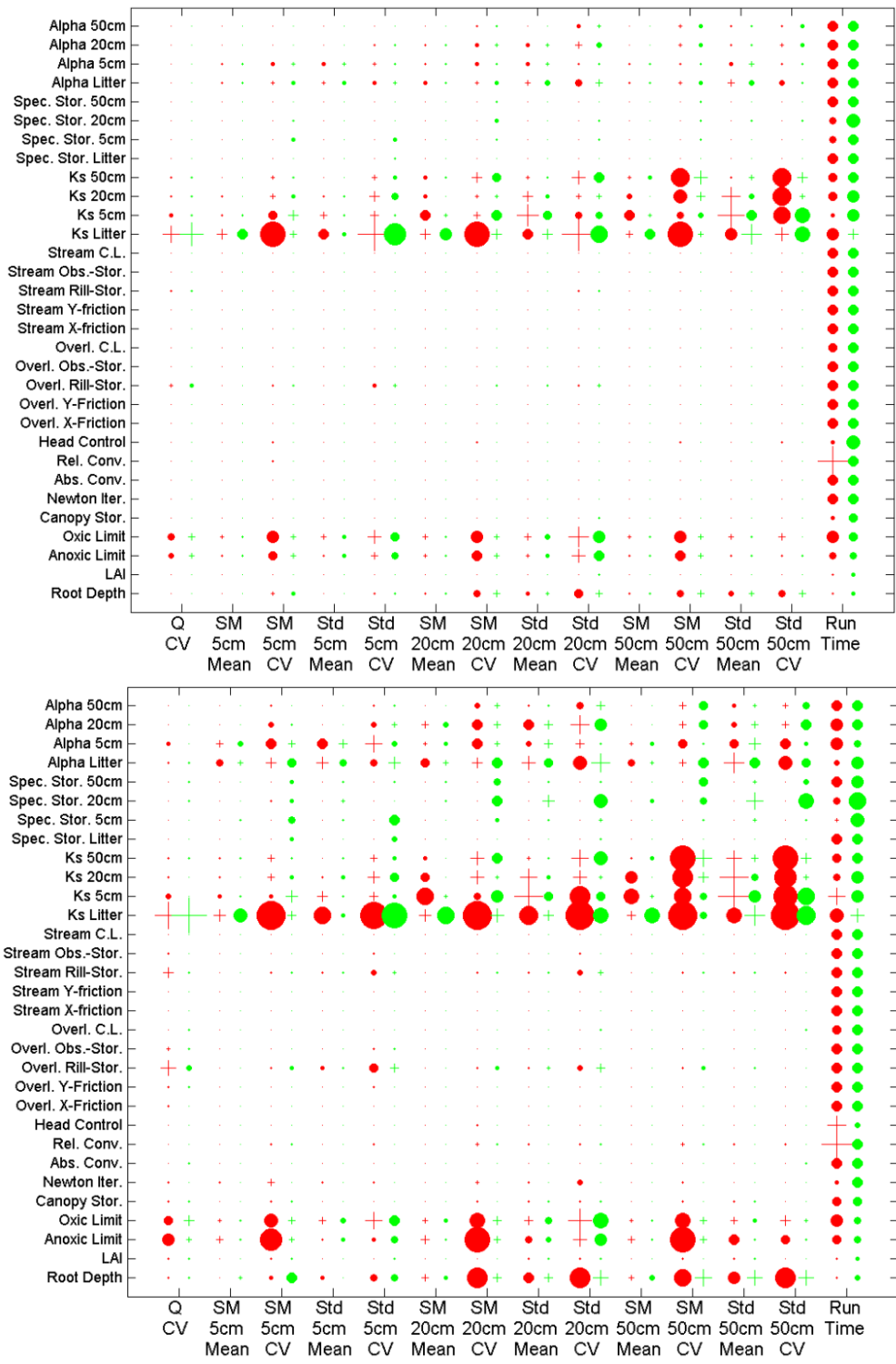


Figure 8.5: Sensitivity of the annual mean and coefficient of variation (CV) of soil moisture (SM) and its standard deviation (STD) in 5, 20 and 50 cm depth and the coefficient of variation (CV) of discharge (Q) to parameter change of $\pm 10\%$ (top) and $\pm 50\%$ (bottom) at 100 m resolution. Symbol size refers to relative changes in water balance components compared to the reference simulation. Filled circles indicate a decrease, "Plus" symbols an increase in water balance component due to a positive (green color) or negative parameter change (red color). Abbreviations: Spec. Stor. =Specific Storage; C.L. =Coupling Length; Obs.-Stor = Obstruction-Storage Length; Rill-Stor. =Rill-Storage Length; Overl. =Overland; Conv.=Convergence; Iter.= Iterations; Canopy Stor.=Canopy Storage.

8.2 Wüstebach

8.2.1 Influence of spatio-temporal resolution and of bedrock inclusion on water balance and discharge simulation

Chapter 8.2.1 is published in Cornelissen et al. (2014). Changes to the text include figure and table numbering and the replacement of formulations with “we” and “our”.

Figure 8.6a (black line) illustrates the discharge dynamics for 2010 (calibration) and 2011 (validation). In both years, a period of snowfall and snow melt was followed by a pronounced low flow period between May and mid-August. The end of the low flow period is marked by an abrupt discharge onset. In 2011, this onset is postponed to the beginning of December due to low rainfall amounts between August and November. The reference simulation ‘d25’ captured the low flow period well, apart from peak discharges (e.g. July 2010). Peak discharges are overestimated during the snowfall/snowmelt period and in the autumn of both years (Figure 8.6a red line).

Figure 8.6b and c illustrate the effect of spatial and temporal resolutions on the discharge simulation. Both figures show that a change in spatial or temporal resolution had a large effect on peak discharge simulation but marginal effect on low flow simulation. More interestingly, the effects of spatial and temporal scale were contradictory to each other. For precipitations higher than 10 mm, simulated peak discharges of d25 were larger than those of h25 but lower than those of d100. During August 2010, this pattern reversed, as peak discharges of d25 were lower than those of h25 but larger than those of d100.

According to Table 8.1, the interception amounted to 20% of the total precipitation for all simulations which fitted to the calibration aim defined in chapter 7.3.4. At daily resolution, interception amount only varied by 1 mm between calibration and validation period but at hourly resolution, interception amounts varied by up to 9 mm. Transpiration limiting saturations were calibrated to achieve a good match between simulated and observed discharge amounts (see Table 8.2 for calibrated parameters). Unfortunately, all simulations overestimated discharge amount during calibration by at least 39 mm and during validation of at least 21 mm. In chapter 7.3.4, it was outlined that the calibration seeks for a tradeoff between water balance compartments. With the parameters causing the overestimation of discharge, actual evapotranspiration between 1st May 2010 and 31st December 2010 was already overestimated by 57 mm and thus no additional parameter adjustment was applied. Generally, the higher temporal resolution simulated higher discharge amounts than the daily resolution.

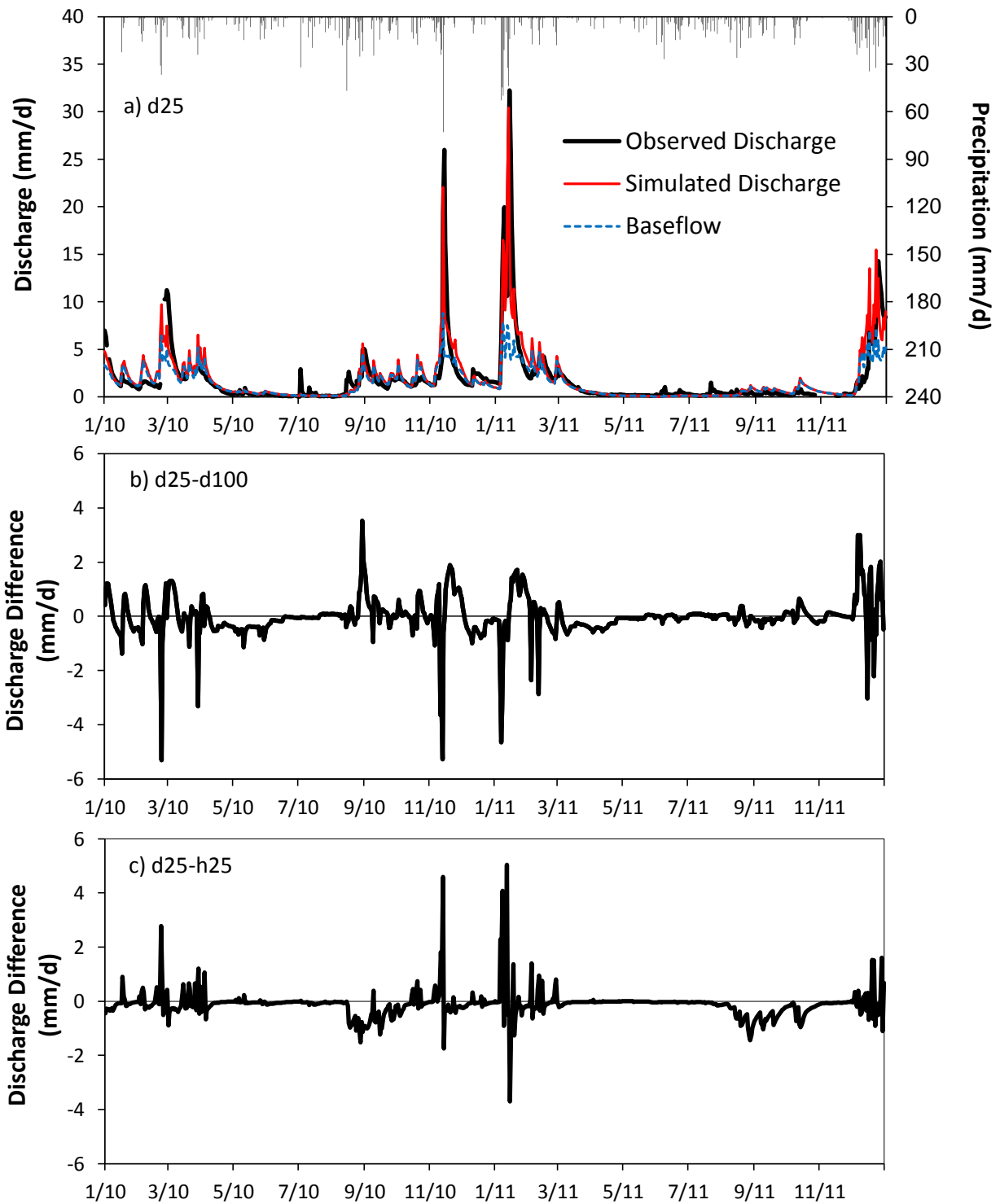


Figure 8.6: a: Observed and simulated total discharge and simulated baseflow for non-bedrock setup at 25 m resolution for daily time steps. b: Difference between non-bedrock setup at 25 m and 100 m resolution. Positive values indicate larger discharges at 25 m resolution. c: Difference between non-bedrock setup at 25 m resolution on daily and hourly time step. Positive values indicate larger discharges on daily resolution.

The simulation results presented in Figure 8.6a (blue line) and Table 8.1 showed that for all simulations, fast sub-surface flow was the main discharge component in the test site, accounting for at least 68% at 25 m and 61% at 100 m resolution. The contribution of baseflow to total discharge was not affected by a change in time step and cannot be compared between spatial resolutions as explained in chapter 7.1.

There were large differences in the discharge simulation between the bedrock and non-bedrock setups. Figure 8.7a shows the discharge difference between the d25 and d25b simulations. According to this graph, the discharge of the bedrock setup was higher during low flow periods but lower for the rest of the year. Spatial scale has a similar effect on discharge dynamics for bedrock and non-bedrock setups. For bedrock simulations, the effect of spatial resolution on discharge peaks is smaller than for the non-bedrock setups. The influence of temporal scale is very similar for the bedrock and non-bedrock setups comparing Figure 8.6c and Figure 8.7c. For the bedrock setup, total discharge during the calibration period was lower than that for non-bedrock setups at both temporal and spatial resolutions but transpiration rates were higher (Table 8.1). During validation, differences in total discharge between bedrock and non-bedrock setups were very low but transpiration rates were higher.

The discharge simulation results at both spatial and temporal resolutions show that subsurface flow is the dominant runoff generation process at the Wüstebach test site, which is in line with other studies, e.g. (Zehe et al., 2010). In the HydroGeoSphere simulation, fast subsurface flow originates from lateral flow. In addition to lateral flow, fast subsurface runoff can be induced by pipeflow, from fractures in the bedrock, by vertical macropores connected to these fractures or by lateral macropores in the unsaturated zone (Uchida et al., 2001). Due to large uncertainties in the parameterization of the macropore flow module implemented in HydroGeoSphere, macropore flow was not simulated. I assume that the inability of the model setup to simulate macropore flow is visible in the lack of discharge peaks in the summer and the lack of short term soil moisture dynamics. Kosugi et al. (2011) emphasized the importance of aquifers for discharge dynamics in a humid forested catchment in Japan. Kosugi et al. (2011) showed that a sequence of discharge peaks after a precipitation event corresponded to a sequence of water table changes in aquifers of different depths. The bedrock aquifer assumed for the model setup did not feature fast conducting fractures. Thus sharply rising discharge peaks resulting from fast subsurface flow through fractures could not be reproduced.

The results in Figure 8.6 also revealed that spatial and temporal scaling have an opposite effect on the simulation of discharge peaks if precipitation is higher than 10 mm. I attribute this behavior to the different scaling behavior of saturated conductivity values and van-Genuchten-Mualem shape parameters.

Table 8.1: Measured and simulated water balance components for the calibration (2010) and the validation period (2011) for all model setups.

	Calibration (2010)								Validation (2011)							
Precipitation (mm/y)	1226								1348							
Measured Discharge (mm/y)	608								630							
Potential Evapotranspiration (mm/y)	694								756							
Actual Evapotranspiration (mm/y)	377 ¹								596							
	Without bedrock				With bedrock				Without bedrock				With bedrock			
	Daily		Hourly		Daily		Hourly		Daily		Hourly		Daily		Hourly	
	<u>25 m</u>	<u>100 m</u>	<u>25 m</u>	<u>100 m</u>	<u>25 m</u>	<u>100 m</u>	<u>25 m</u>	<u>100 m</u>	<u>25 m</u>	<u>100 m</u>	<u>25 m</u>	<u>100 m</u>	<u>25 m</u>	<u>100 m</u>	<u>25 m</u>	<u>100 m</u>
Simulated Discharge (mm/y) ²	647	647	689	708	609	612	638	650	652	651	693	709	652	690	666	713
Baseflow (%)	82	77	82	77	86	85	86	85	66	61	68	64	72	75	73	75
Interception (mm/y)	248	248	251	248	246	248	246	238	248	247	239	242	251	247	237	237
Interception (%)	20	20	20	20	20	20	20	19	18	18	18	18	19	18	18	18
Transpiration (mm/y)	261	264	266	262	291	286	301	285	353	355	323	284	379	371	364	340
Actual Evapotranspiration (mm/y)	509	512	517	510	537	534	547	523	601	602	562	526	630	618	601	577
Coefficient of Determination (-)	0.66	0.55	0.69	0.64	0.68	0.58	0.72	0.64	0.75	0.72	0.75	0.74	0.76	0.72	0.77	0.76
Nash-Sutcliffe Coefficient (-)	0.65	0.54	0.68	0.63	0.65	0.51	0.66	0.53	0.75	0.71	0.75	0.74	0.76	0.69	0.76	0.72
Percent Bias (%)	-6.31	-6.35	-13.4	-16.5	-0.08	-0.68	-4.87	-6.94	-3.48	-3.40	-10.1	-12.7	-3.58	-9.62	-5.82	-13.3

¹=Measurements start on May 1st, 2010; ²= Yearly sums of simulated discharge exclude time steps with gaps of measured discharge)

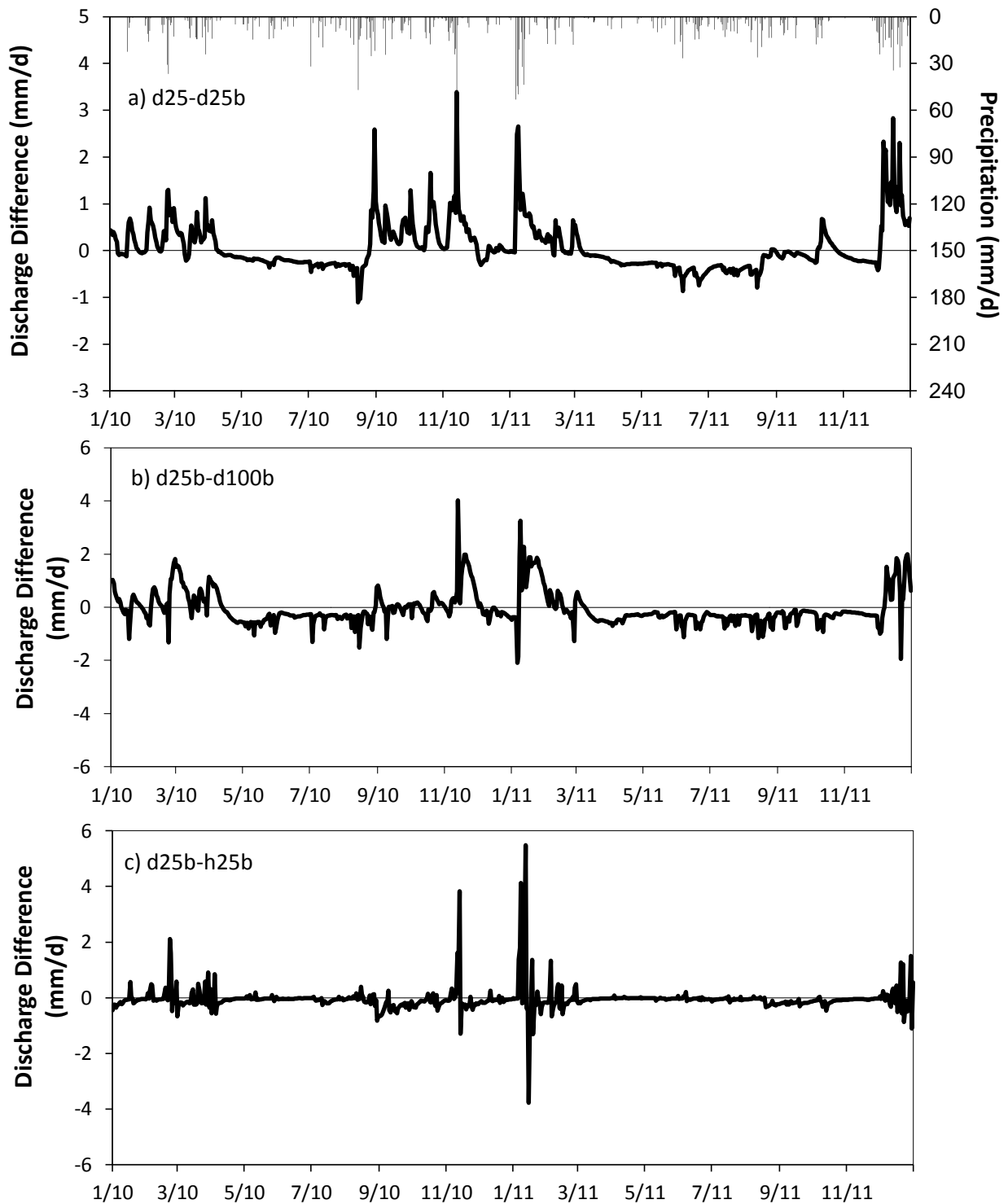


Figure 8.7: a: Difference in discharge between non-bedrock and bedrock setup at 25 m on hourly time steps. Discharges at hourly time steps were aggregated to daily time steps. Positive values indicate larger discharges for non-bedrock. b: Difference between 25 m and 100 m resolution for bedrock setup. Positive values indicate larger discharges at 25 m resolution. c: Difference between daily and hourly time step for the bedrock setup at 25 m resolution. Positive values indicate larger discharges on daily resolution.

Sciuto and Diekkrüger (2010) showed that a decrease in spatial resolution of HydroGeoSphere leads to a decrease in transpiration rate. Despite this, multiplication factors are only slightly higher, and the oxic limit is slightly smaller at the coarser resolution (see Table 8.2). The pronounced scale dependency found by Sciuto and Diekkrüger (2010) could be compensated in this study by the calibration of the residual saturations and porosities (refer to Young et al. (2009) regarding the influence of van-Genuchten-Mualem parameters on transpiration). Due to the lack of recalibration for the bedrock setup, the effect described by Sciuto and Diekkrüger (2010) became apparent for the bedrock setup, as the transpiration amounts were higher at the finer resolution by ~5 mm during calibration and 8 mm during validation (refer to Table 8.1).

Furthermore, Table 8.2 shows a temporal scaling problem of the canopy storage parameter as the amount of interception was different for validation and calibration. This result reveals that a dependency of the interception module concerning time steps cannot be accounted for by adjusting the provided parameters.

8.2.2 Influence of spatial resolution and of bedrock inclusion on temporal and spatial soil moisture variability at daily time steps

¹ Figure 8.8 (upper part) compares mean measured and simulated (d25) soil moisture dynamics. Due to the calibration of residual water contents, the seasonal trend was well captured at all depths (refer to Table 8.2 for calibration parameters) by the d25 and d100 simulations but the simulation quality of short term soil moisture dynamics decreased with depth. Therefore, the R^2 values were satisfactory (≥ 0.41) at both resolutions, especially during the calibration period at 5 cm (0.78) and 20 cm (0.76) depths.

At both resolutions, the bedrock setups simulated lower soil moisture values at all depths (refer to Figure 8.8 (lower part) for a comparison between d25 and d25b). This results from lower groundwater table for the bedrock setups and the nonlinear interconnection between transpiration and relative saturation shown in Equation 18. According to Equation 18, the transpiration increases beyond the anoxic saturation limit until it reaches the oxic saturation limit. At the finer resolution, the anoxic limit has been calibrated to 0.97 (Table 8.2) which corresponds to 46.6 vol.% soil moisture in 5 cm depth with a mean porosity of 0.48 after calibration. Whenever the soil moisture got below 46.6 vol.%, transpiration rate increased. During both simulation years, this happened on 485 days in the non-bedrock setup but on 582 days in the bedrock setup. Thus the transpiration rate increased in the bedrock setup and soil moisture values decreased accordingly ¹.

¹ Text taken from Cornelissen et al. (2014)

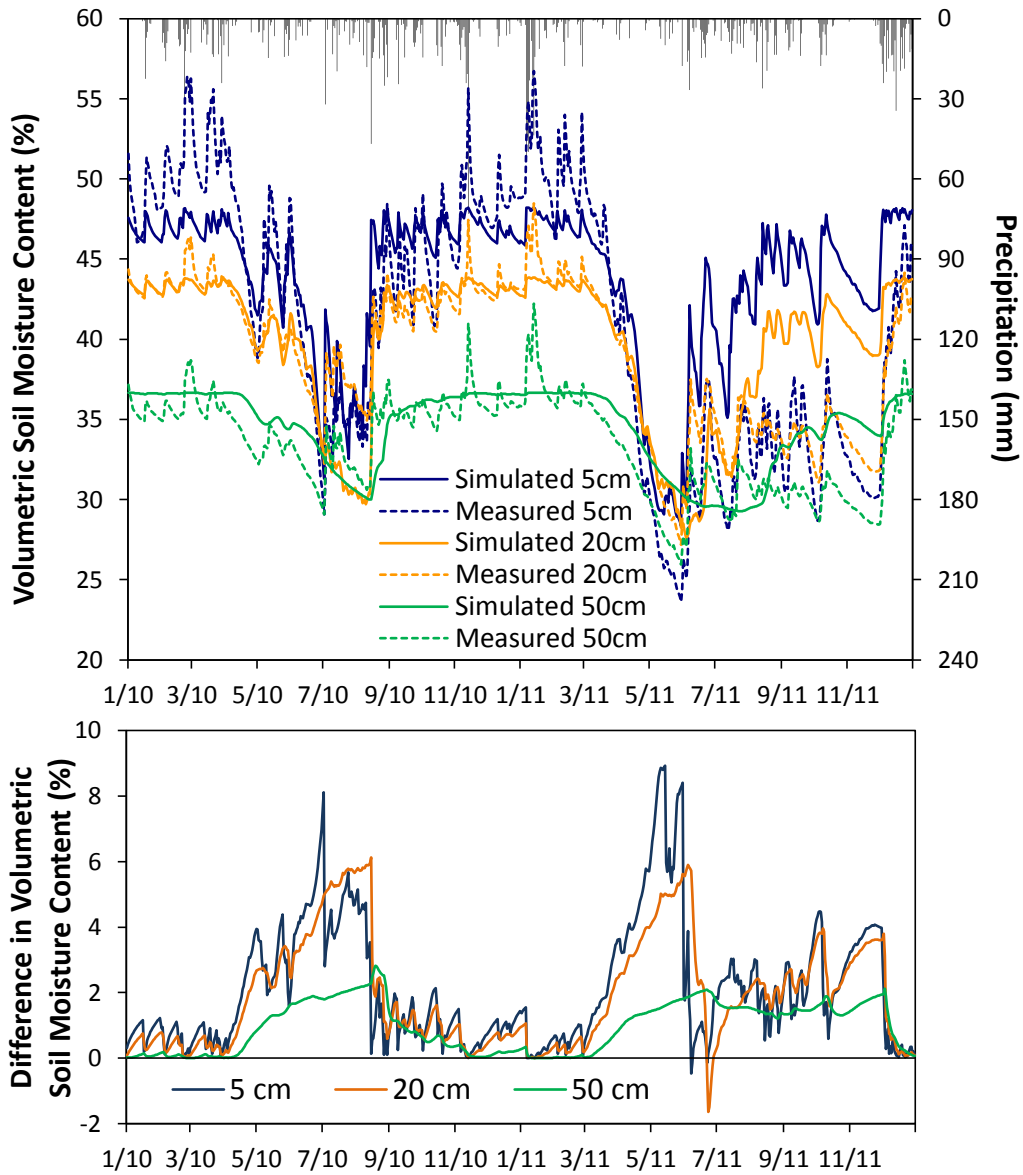


Figure 8.8: Upper part: Observed and simulated daily soil moisture dynamics at 25 m resolution for non-bedrock setup. Lower part: Difference between non-bedrock and bedrock setup at 25 m resolution. Positive values indicate larger soil moistures of the non-bedrock setup at 25 m resolution.

Table 8.2: Calibrated parameters at 25 m and 100 m resolutions for daily and hourly time steps.

	25 m daily	100 m daily	25 m hourly	100 m hourly
Canopy storage parameter (m)	0.0015	0.0015	0.00175	0.00195
Multiplication factor for residual saturation, 5 cm	5.4	5.6	5.4	5.6
Multiplication factor for residual saturation, 20 cm	4.6	4.7	4.6	4.7
Multiplication factor for residual saturation, 50 cm	3.3	3.3	3.3	3.3
Oxic limit	0.90	0.89	0.88	0.89
Anoxic limit	0.97	0.97	0.97	0.96

In the following, results of soil moisture modeling will be analyzed at three different depths. The description of results for topsoil moisture is taken from Cornelissen et al. (2014) and marked with cursive letters, results for 20 cm and 50 cm depth were added in the context of this thesis.

The relationship between measured and simulated mean soil moisture of the topsoil and its standard deviation displayed in the top part of Figure 8.9 shows a unimodal shape for measured soil moistures, with highest standard deviations (15%) between 35 and 40 vol.%. The shape of the simulated relationship compared well to the measured soil moisture, but the relationship was shifted to lower soil moisture values which partly omitted the decreasing part. The finer grid resolution simulated larger standard deviations than the coarser resolution. Differences between the setups with bedrock and without bedrock at 100 m resolution were very small but at 25 m resolution, differences were more pronounced and the 25b simulation was the only one reaching soil moisture values below 28 vol.%.

With increasing depth, the unimodal shape of the relationship for the measured soil moisture data subsequently changed into a linear dependency with higher standard deviations at higher soil moisture values (Figure 8.9, middle and lower part). At 20 cm depth, differences between simulations and measured data were smallest supporting the impression of Figure 8.8 that soil moisture simulation was best at 20 cm depth. The d25b setup showed a tendency for lower soil moisture values as already observed at 5 cm depth. The relationship between soil moisture and its standard deviation at 50 cm depth has a circular shape for all simulations (Figure 8.9, lower part). Figure 8.10 separates the circular shape at 50 cm depth for the d25 setup into patterns with a specific combination between the change in soil moisture and standard deviation.

Interestingly, some categories only occurred during a specific season of the year with a characteristic time length. For example, the category “periodic change” with very small changes in soil moistures and contradictory changes in standard deviation did only occur during winter periods and lasted between 12 and 14 weeks (winter 2010 and 2010/2011). In contrast, the category “decreasing soil moisture and standard deviation” occurred during all seasons except winter and lasted only 7 weeks. Shortest time spans were observed for the increase in both soil moisture and its standard deviation. The autumn of 2011 could not be linked to a certain category (denoted: “Other”) because the change in standard deviation was not linked to a certain change in soil moisture.

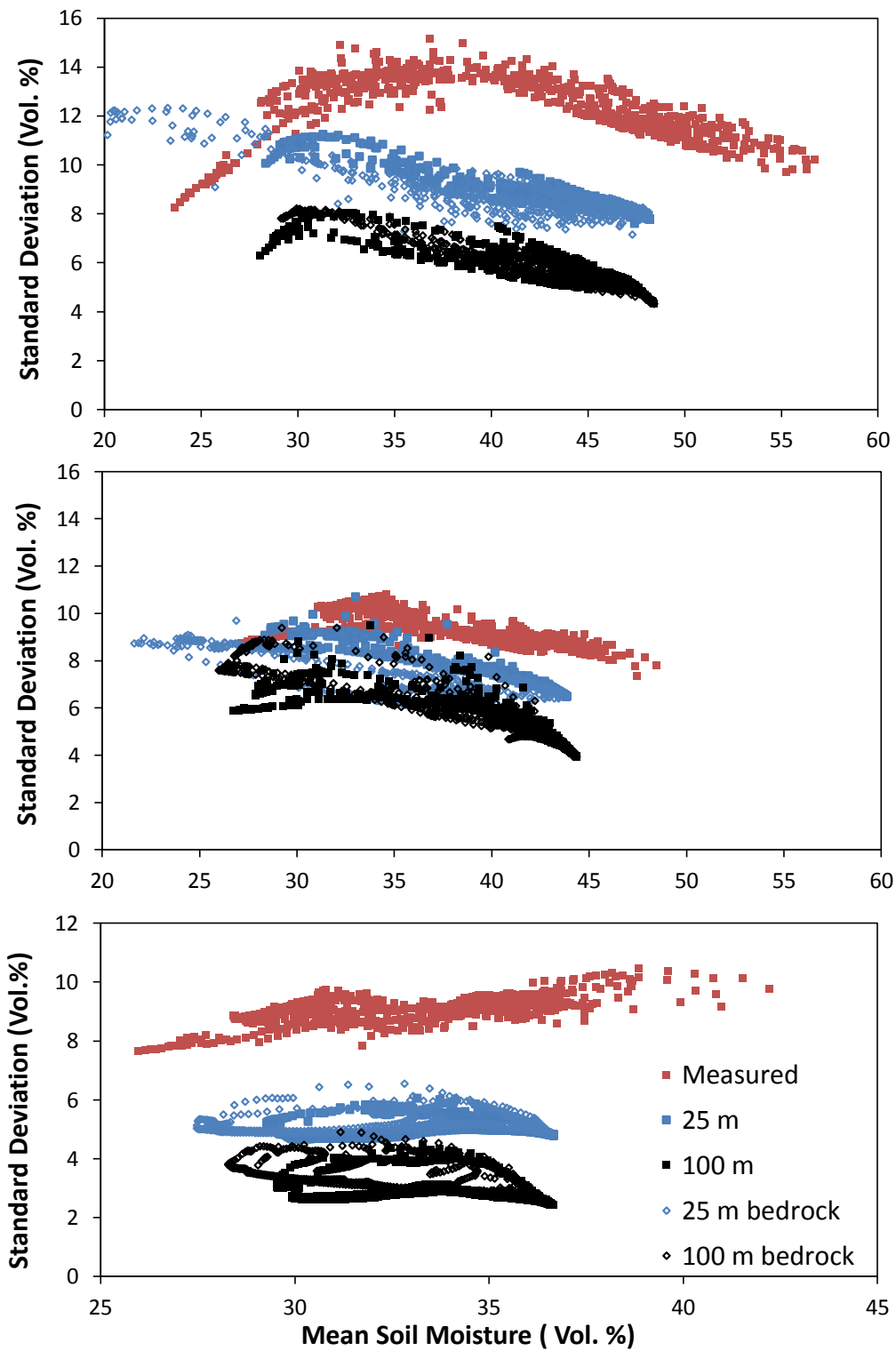


Figure 8.9: Relationship between mean soil moisture and its standard deviation in the topsoil for both model resolutions and both model setups compared with the measured soil moisture data at 5 cm (top), 20 cm (middle) and 50 cm (bottom). Beware of the different x- and y-axis limits in the bottom part of the figure!

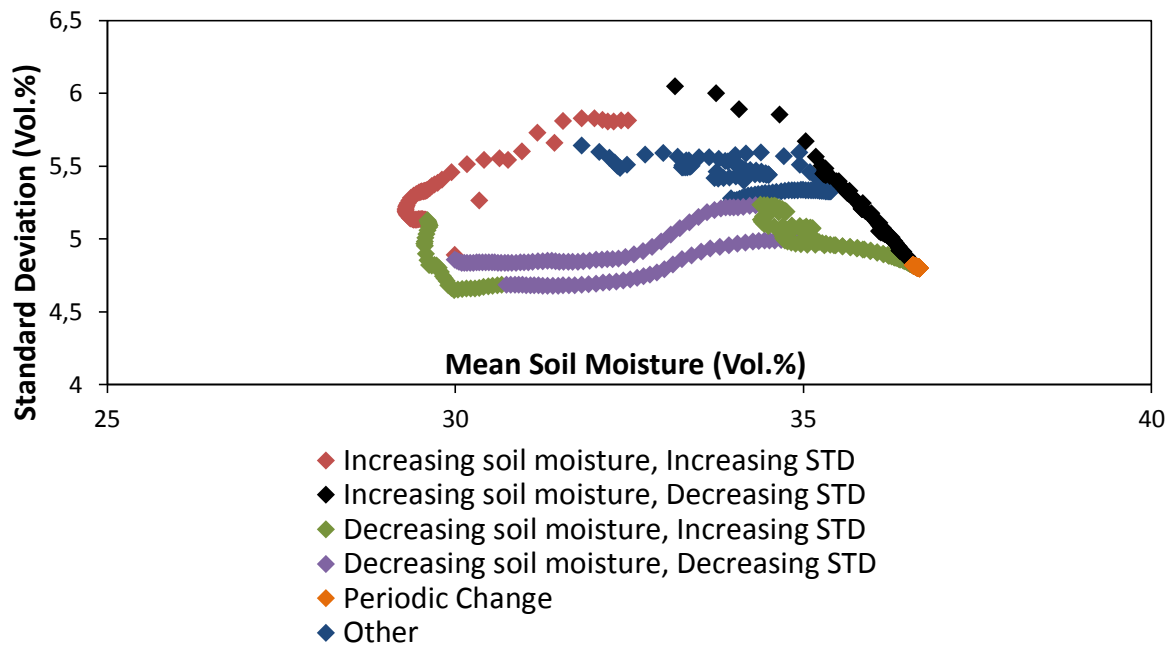


Figure 8.10: Relationship between mean soil moisture (SM) and its standard deviation (STD) at 50 cm depth for the d25 setup. The relationship is classified in six categories according to the temporal evolution of soil moisture and standard deviation.

As outlined in chapter 5, the autocorrelation structure of a distribution of soil moisture data can be described by its nugget, sill and range values. The sill-to-mean soil moisture relationship closely resembled the standard deviation-to-soil moisture relationship for measured and simulated data at all depths and was hence not analyzed in more detail. For the measured data, the range-to-soil moisture relationship did not show a clear trend in any depth but for the 25 m resolution, the relationship resembled the shape of the standard deviation-to-soil moisture relationship. At 100 m resolution, setups without bedrock showed a slight linear upward trend with increasing soil moisture at 5 and 20 cm depth while setups with bedrock showed a weak linear downward trend at 5 and 20 cm depth. At 50 cm depth, no clear relationship turned out.

Table 8.3 summarizes mean, minimum, maximum and standard deviation of range and sill values for all different setups at 5, 20 and 50 cm depth. Green colors highlight increases in range or sill between 5 to 20 cm depth and 20 to 50 cm depth of more than 10% and red colors indicate decreasing values of more than 10%. The patterns of decreases and increases in sill and range were very similar between bedrock and non-bedrock setups at both resolutions. In addition, absolute values were very similar between bedrock and non-bedrock setups at 25 m resolution. Range values at 25 m resolution increased between 5 and 20 cm but decreased between 20 and 50 cm. In contrast, measured data and simulations at 100 m resolution showed no significant changes between 5 and 20 cm but increased between 20 and 50 cm depth. Compared to measured data, mean, maximum and minimum range values at 20 m resolution were much higher in 5 and 20 cm depth indicating more homogeneity in soil moisture patterns. Range values at 100 m resolution were closer to those for measured data. This resulted from the usage

of different theoretical semivariograms. A Gaussian model at 100 m resolution was utilized instead of a spherical model used for measured data and the simulation at 25 m resolution because the fit between experimental and theoretical semivariogram was higher for the Gaussian model at 100 m resolution. The usage of the Gaussian model resulted in lower ranges. Sill values of all simulations were lower than those for measured data.

Example variograms are given in Figure 8.11 to Figure 8.13 for spatial soil moisture patterns shown in Figure 8.14 to Figure 8.19. Theoretical variograms for the d100 and d100b setups at 50 cm depth shown in the bottom left of Figure 8.13 for the wettest day obviously did not fit to the experimental variograms shown in the same plot. During very wet conditions (upper 5%), soil moisture data for the respective setups exhibited only little spatial heterogeneity with standard deviations lower than 3 vol.%. The low spatial variability and the occurrence of several sill-maxima (refer to Figure 8.13) made it impossible to properly fit a theoretical variogram for these days (~ 5% of all days) without heavily deteriorating the fit for all other days.

Table 8.3: Mean, minimum, maximum and standard deviation of range and sill values for simulated and measured soil moistures at 5, 20 and 50 cm depth. Green and red colors highlight increases and decreases in range or sill between 5 to 20 cm depth and 20 to 50 cm depth by $\geq 10\%$.

	5 cm		20 cm		50 cm		5 cm		20 cm		50 cm	
	Daily 25 m						Daily 25 m Bedrock					
	Range	Sill	Range	Sill	Range	Sill	Range	Sill	Range	Sill	Range	Sill
Min (m)	146	43	164	30	94	22	146	42	163	28	97	22
Max (m)	188	107	209	94	127	32	195	136	201	100	130	38
STD (m)	10	14	9	14	7	2	11	19	9	15	9	3
Mean (m)	159	54	178	41	100	23	162	58	182	42	107	25
	Daily 100 m						Daily 100 m Bedrock					
	Range	Sill	Range	Sill	Range	Sill	Range	Sill	Range	Sill	Range	Sill
Min (m)	98	14	101	12	114	4	109	14	116	12	113	3
Max (m)	127	65	140	88	187	18	143	70	153	91	223	23
STD (m)	6	11	6	13	16	3	6	13	8	19	30	5
Mean (m)	119	29	119	28	157	8	120	31	127	33	176	11
	Daily measured											
	Range	Sill	Range	Sill	Range	Sill						
Min (m)	92	76	94	52	117	62						
Max (m)	141	239	139	126	159	114						
STD (m)	10	34	9	14	6	10						
Mean (m)	123	164	114	89	135	90						

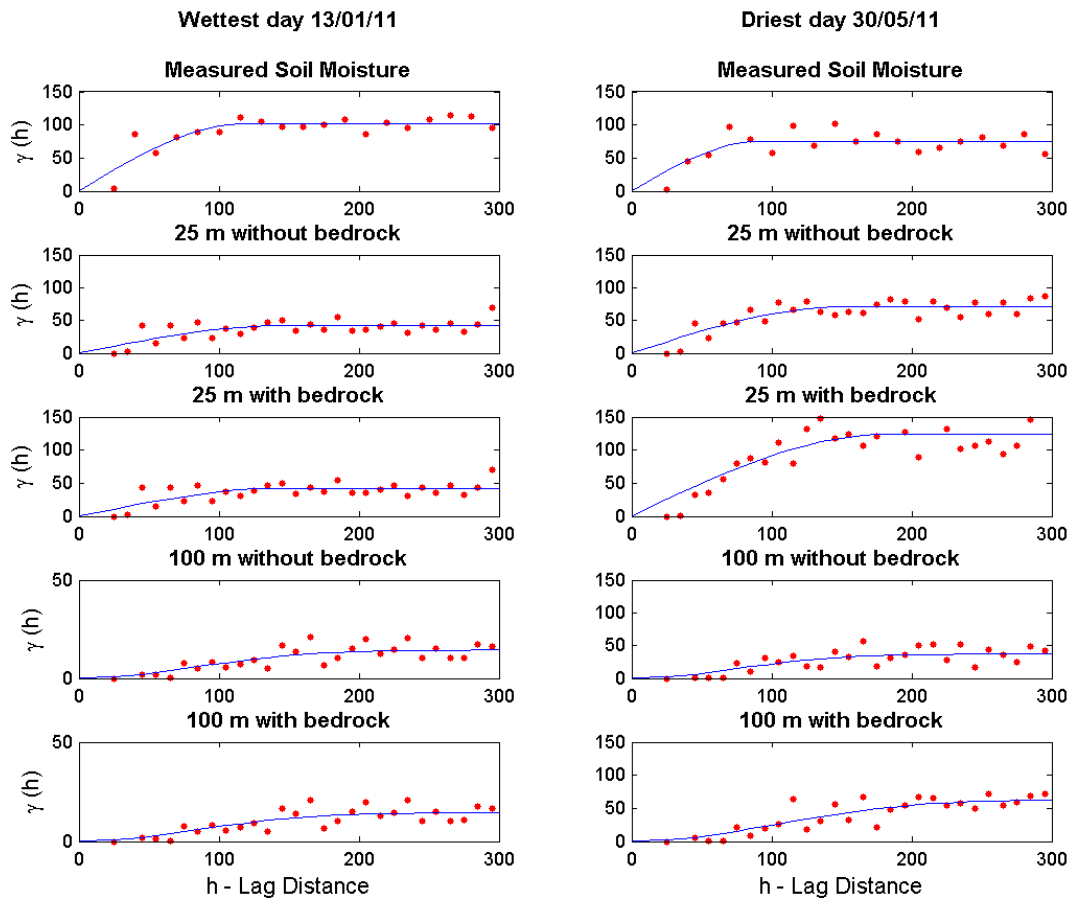


Figure 8.11: Variograms of measured (top row) and simulated soil moisture (second to last row) at the wettest (left column) and driest (right column) day in 5 cm depth. Variograms correspond to soil moisture patterns shown in Figure 8.14 and Figure 8.15.

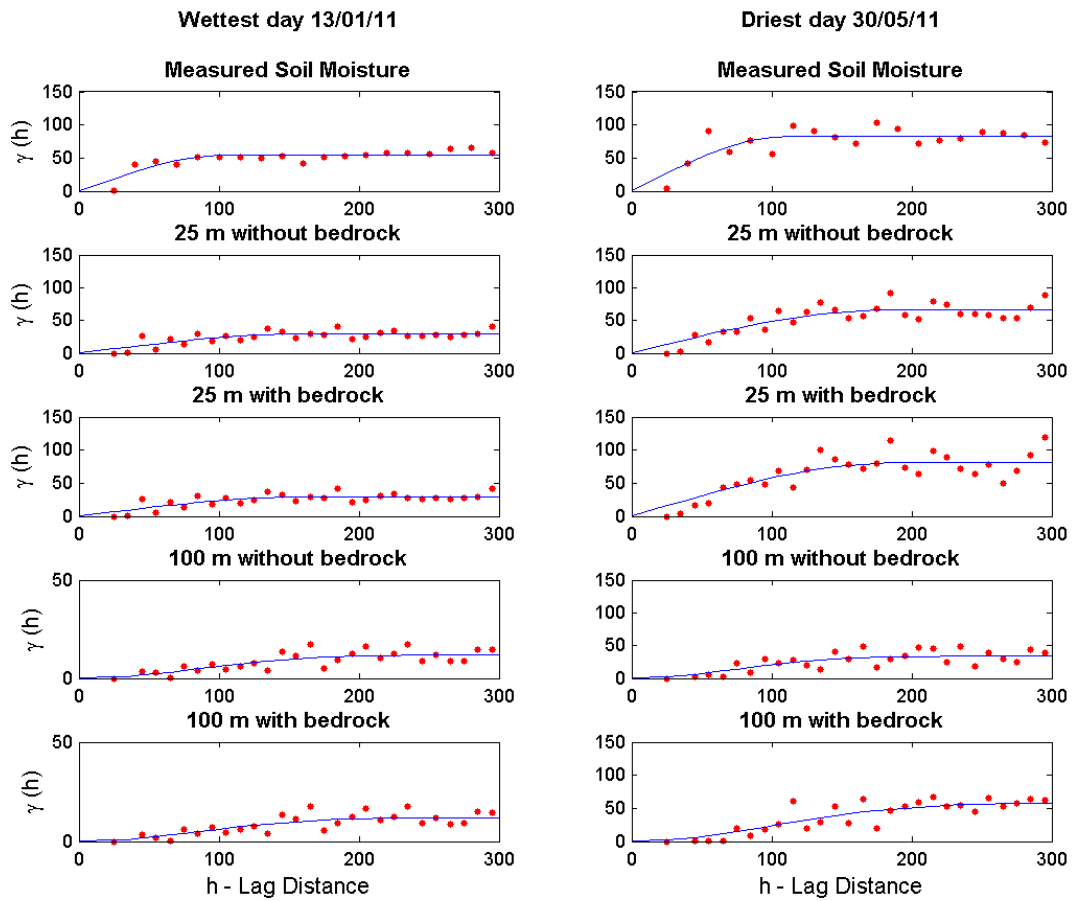


Figure 8.12: Variograms of measured (top row) and simulated soil moisture (second to last row) at the wettest (left column) and driest (right column) day in 20 cm depth. Variograms correspond to soil moisture patterns shown in Figure 8.16 and Figure 8.17.

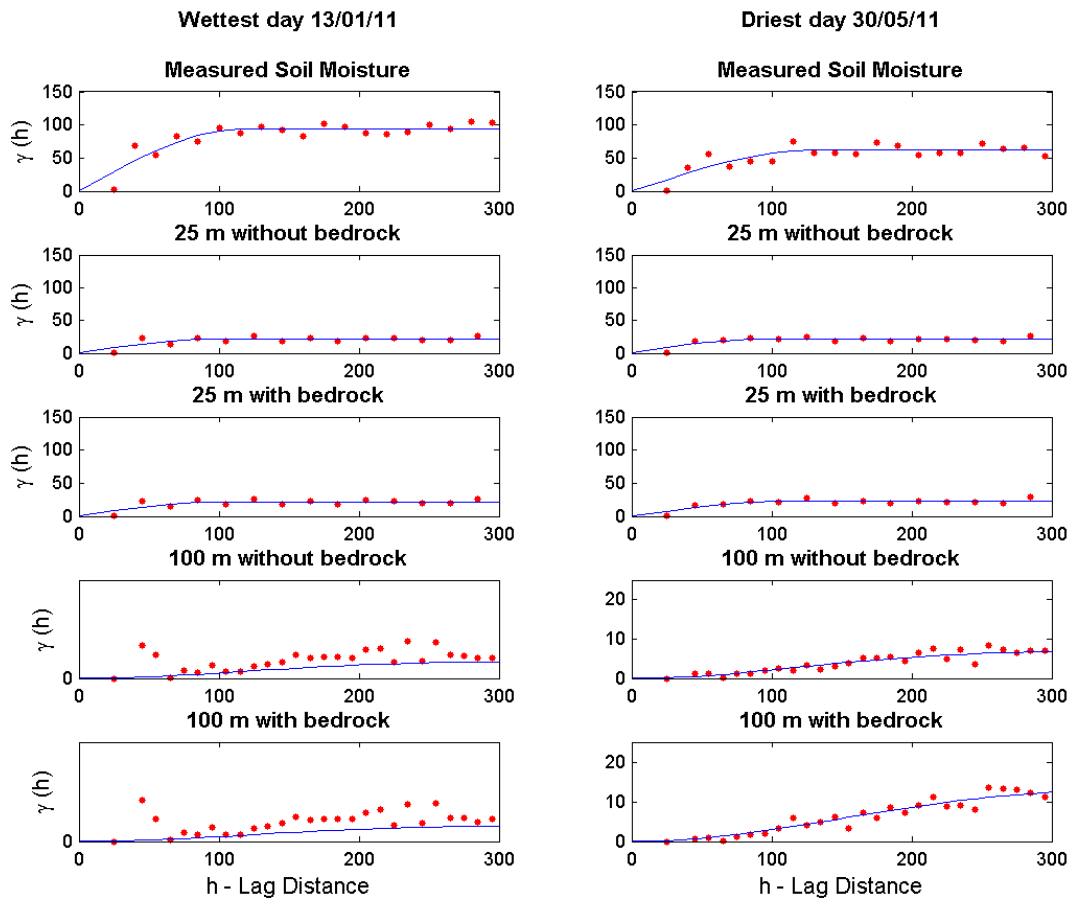


Figure 8.13: Variograms of measured (top row) and simulated soil moisture (second to last row) at the wettest (left column) and driest (right column) day in 50 cm depth. Variograms correspond to soil moisture patterns shown in Figure 8.18 and Figure 8.19.

Figures 8.14 and 8.15 depict the kriging results for the wettest (13.1.11) and driest (30.5.11) days of the simulation period at 5 cm depth. Black dots indicate the SoilNet measurement points and the nodes used for kriging. The white pixels represent the river. The measured pattern clearly followed the course and the source area of the river in the southeastern part of the catchment. In the western area, the measured pattern had a patchy structure. The d25 simulation closely resembled the measured pattern in the eastern part of the catchment, but missed a great part of the pattern in the western part. As expected, the spatial differentiation was smaller for the d100 simulation, but the source area of the river was still well represented. With decreasing soil moisture, the spatial pattern of both bedrock setups differed from that of the non-bedrock setup.

Figures 8.16 to 8.19 show kriging results for the same days but at 20 and 50 cm depth. With increasing depth, the measured pattern got more homogeneous in the eastern and western part but the river source area, the river bed and the outlet were still visible with higher soil moistures than neighboring areas. The simulated patterns only showed little changes between 5 and 20 cm depth. On the wet day, the pattern did not change except for dry spots at the 25 m resolution setups emerging in the western part of the catchment. The river source area and river outlet were still visible resulting in more pronounced differences between dry and wet areas of the catchment. At 50 cm depth, simulated patterns were very homogeneous, especially at 100 m resolution which nearly totally lacked a spatial differentiation. At both resolutions, the source area and the outlet seemed to have “dried out” with lower soil moistures in these areas compared to surrounding areas.

Table 8.4 summarizes mean annual Kappa values for all simulations and all different depths. The mean Kappa values at 5 and 50 cm depth were below 0.1 for every model setup, reflecting the impression from Figures 8.14, 8.15, 8.18 and 8.19 that the soil moisture pattern was not well represented in one part of the catchment. This finding will be explained in the next paragraph with a correlation analysis between topographic variables and soil moisture patterns and between soil parameters and soil moisture patterns. In addition, simulated soil moisture patterns at 50 cm depth did not resolve the river source area resulting in negative Kappa values at 25 m resolution. At 5 and 50 cm depth, mean KLoc values were below 0.2 but the histogram of the measured soil moisture values was moderately well represented by the simulation, as the KHisto values reached at least 0.5 at 5 cm and 0.29 at 50 cm for all model setups. Corresponding to the visual impression of Figures 8.8, 8.16 and 8.17, soil moisture simulation at 20 cm depth was best in terms of both dynamics (Figure 8.8) and patterns (Figures 8.16 and 8.17) thus KHisto reached values larger than 0.6 and KLoc reached values between 0.18 and 0.3.

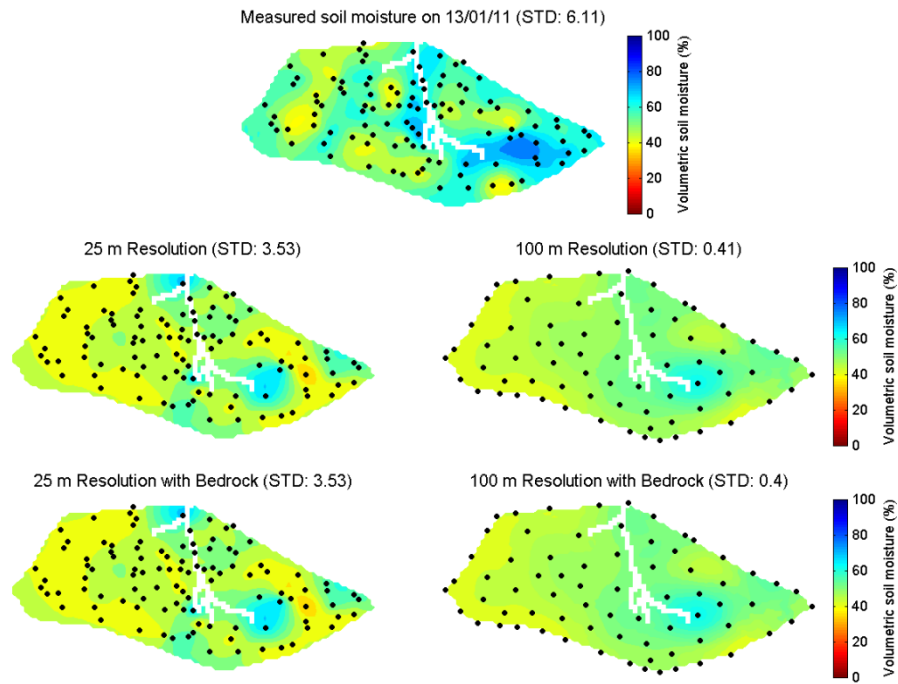


Figure 8.14: Spatial distribution of absolute soil moisture (vol. %) at 5 cm depth on 13.1.2011 for measured (top) and simulated data for 25 m (left) and 100 m (right) resolutions. The values in brackets refer to the mean standard deviation of the kriging algorithm.

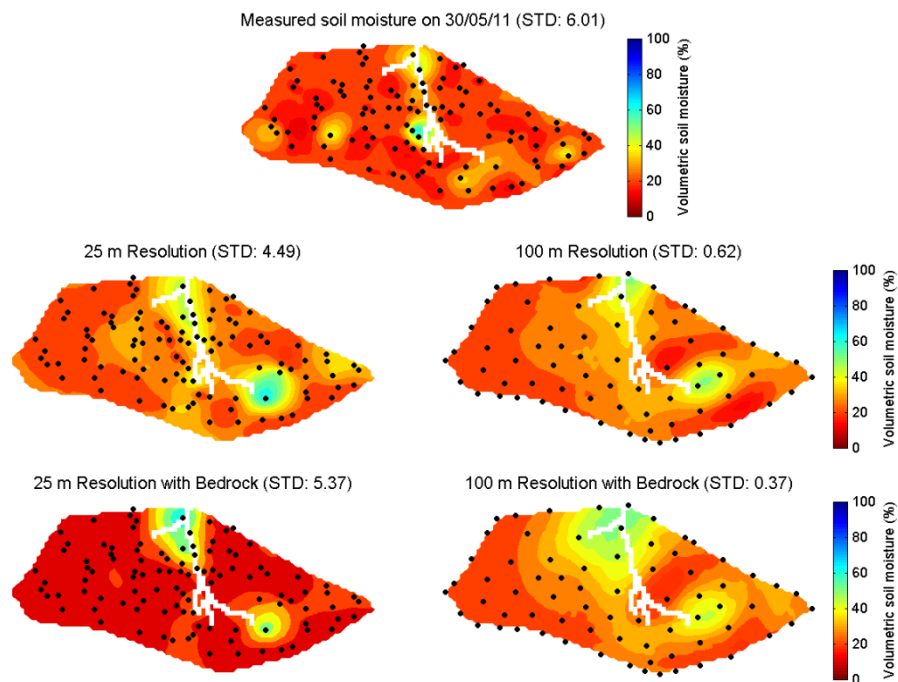


Figure 8.15: Spatial distribution of absolute soil moisture (vol. %) at 5 cm depth on 30.5.2011 for measured (top) and simulated data for 25 m (left) and 100 m (right) resolutions. The values in brackets refer to the mean standard deviation of the kriging algorithm.

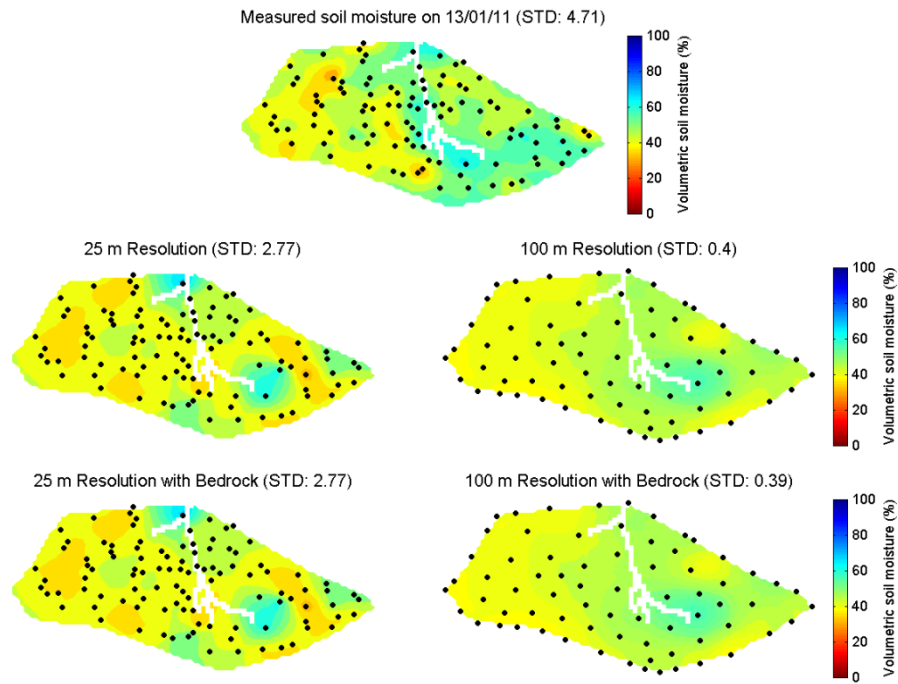


Figure 8.16: Spatial distribution of absolute soil moisture (vol. %) at 20 cm depth on 13.1.2011 for measured (top) and simulated data for 25 m (left) and 100 m (right) resolutions. The values in brackets refer to the mean standard deviation of the kriging algorithm.

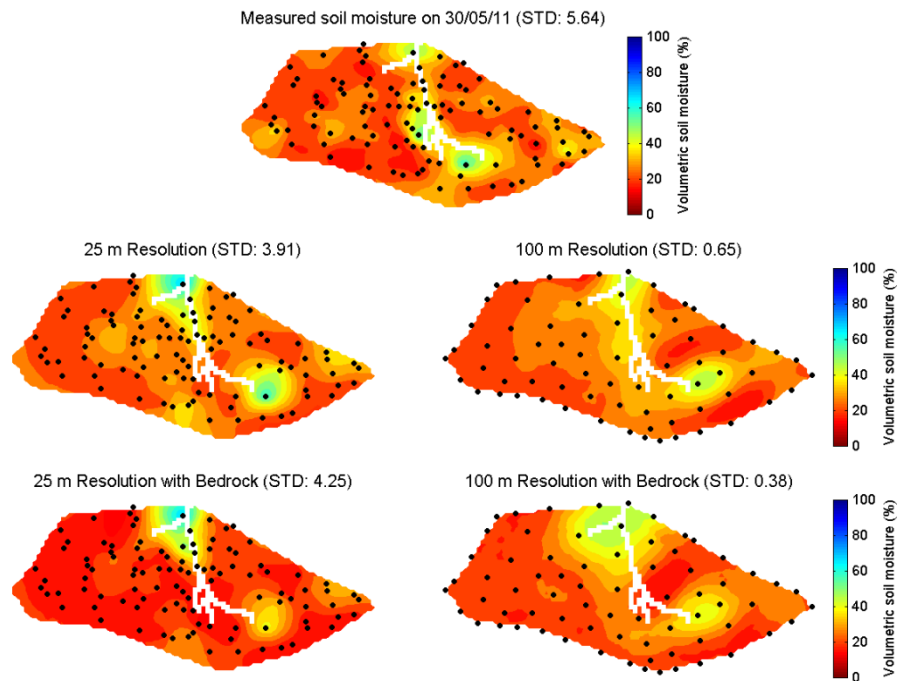


Figure 8.17: Spatial distribution of absolute soil moisture (vol. %) at 20 cm depth on 30.5.2011 for measured (top) and simulated data for 25 m (left) and 100 m (right) resolutions. The values in brackets refer to the mean standard deviation of the kriging algorithm.

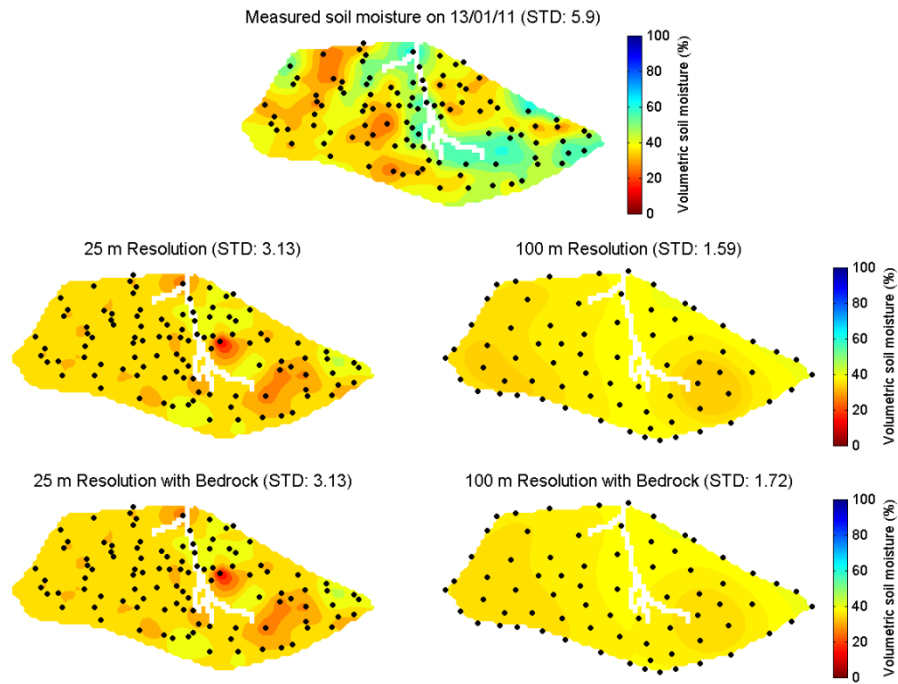


Figure 8.18: Spatial distribution of absolute soil moisture (vol. %) at 50 cm depth on 13.1.2011 for measured (top) and simulated data for 25 m (left) and 100 m (right) resolutions. The values in brackets refer to the mean standard deviation of the kriging algorithm.

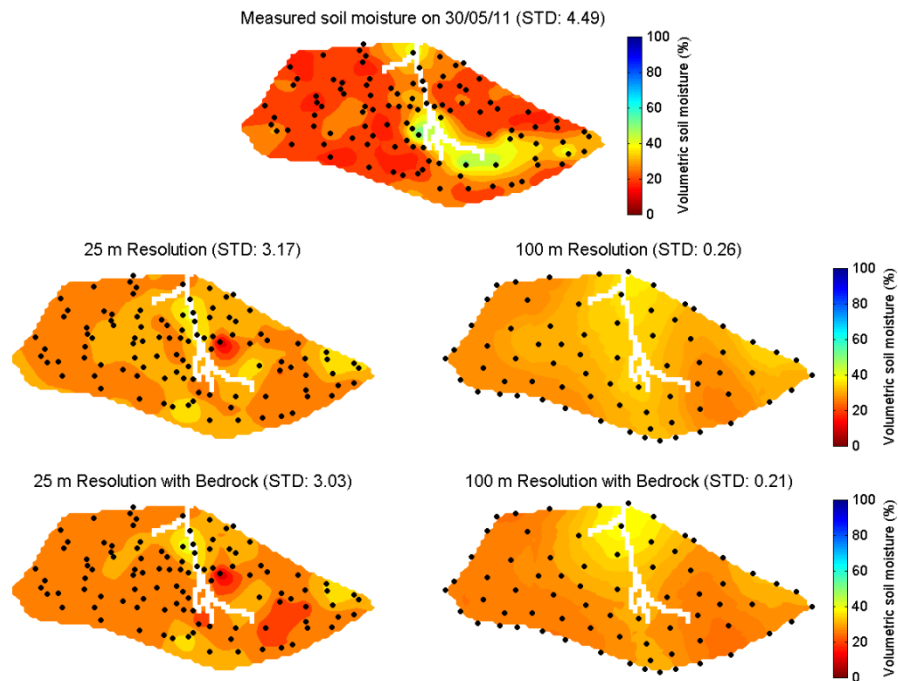


Figure 8.19: Spatial distribution of absolute soil moisture (vol. %) at 50 cm depth on 30.5.2011 for measured (top) and simulated data for 25 m (left) and 100 m (right) resolutions. The values in brackets refer to the mean standard deviation of the kriging algorithm.

Table 8.4: Kappa location, Kappa histogram and combined Kappa values for simulated and measured soil moistures at 5, 20 and 50 cm depth. Green and red colors highlight increases and decreases between 5 to 20 cm depth and 20 to 50 cm depth by $\geq 10\%$.

	Kappa Location			
	25 m	25 m Bedrock	100 m	100 m Bedrock
5 cm	0.12	0.15	0.12	0.11
20 cm	0.18	0.20	0.30	0.25
50 cm	-0.09	-0.03	0.18	0.16
	Kappa Histogram			
	25 m	25 m Bedrock	100 m	100 m Bedrock
5 cm	0.54	0.56	0.49	0.52
20 cm	0.67	0.63	0.69	0.64
50 cm	0.34	0.39	0.29	0.45
	Kappa			
	25 m	25 m Bedrock	100 m	100 m Bedrock
5 cm	0.07	0.08	0.06	0.06
20 cm	0.12	0.13	0.21	0.16
50 cm	-0.03	-0.01	0.05	0.07

To explain the moderate correspondence between measured and simulated soil moisture patterns, a correlation analysis (Spearman) between topographic and soil variables and soil moisture patterns was performed (Table 8.5). Results for topsoil moisture patterns show that porosity distribution and relative elevation explained the simulated soil moisture pattern. The measured soil moisture pattern was neither explained by topographic variables, as the correlation strengths only reached a maximum of -0.20, nor by porosity distributions as the correlation strengths only reached a maximum of 0.44. During drying, the correlation strength with relative elevation increased for all model setups. During wetting, the correlation strength with porosity distributions increased.

According to correlation coefficients summarized in Table 8.5, the correlation between the porosity (25 m resolution) and measured soil moisture pattern decreased between 5 and 20 cm by 28% but the correlation to relative elevation and slope increased. Like measured soil moisture patterns, correlations between simulated soil moisture patterns (25 m setups) and porosity decreased between 5 and 20 cm depth. In contrast, correlations to topographic variables decreased or remained constant instead of increasing. Only the correlation to the slope increased slightly for the d25b setup. Between 20 and 50 cm, all correlation strengths between topographic variables and measured soil moisture patterns and between topographic variables and simulated soil moisture patterns (25 m resolution) decreased. While the change of correlation with depths was comparable between measured and simulated soil moisture pattern for the 25 m resolution, the 100 m resolution setups showed different trends. While the decrease in correlation to porosity between 5 and 20 cm depth is in line with results of

measurements, correlation strengths to topographic variables only exhibit a very small change. Between 20 and 50 cm depth the correlation strengths of simulated pattern (100 m resolution) and topographic variables increased instead of decreasing for measured soil moisture patterns. Generally, correlations between relative elevation, porosities and simulated soil moisture patterns were higher and those between slope and simulated soil moisture patterns were lower in comparison to correlations with measured patterns.

As suggested by Sudicky et al. (2008) and Western et al. (2002), spatially distributed soil moisture measurements were used in addition to discharge values to improve the simulation results. In this study, simulated soil data initially incorporated the effect of skeleton content in the soil parameterization but measured soil moisture data originated from skeleton free soil parts. Thus, residual water content was adjusted to match simulated to measured soil data. The multiplication factors listed in Table 8.2 lead e.g. to a mean porosity of 0.48 (originally 0.28) for the d25 and 0.48 (originally 0.28) for d100 simulation at 5 cm depth. Thus, the application of high multiplication factors did not lead to physically unacceptable results.

A comparison of the temporal soil moisture dynamics with other studies is limited because the data used in these studies are either restricted in their temporal coverage (only event scale (Herbst and Diekkrüger, 2003), a few weeks (Noh et al., 2015) or a growing period (Wang et al., 2015)) or spatial coverage (Mahmood and Vivoni, 2011). Nevertheless, the general finding of Manfreda et al. (2007) that with increasing depth the temporal variability of soil moisture decreases but its spatial organization increases for measurements and simulation results can be confirmed. Recently, Fang et al. (2015) used ParFlow-CLM to simulate soil moisture dynamics and patterns in the Wüstebach catchment for 3 years and found that the incorporation of anisotropy in the saturated hydraulic conductivity improved the simulation of discharge and soil moisture dynamics. In the model intercomparison study by Koch et al. (submitted to journal), ParFlow-CLM provided better simulations of mean daily soil moisture dynamics than HydroGeoSphere and MIKE-SHE in terms of root mean square error but not in terms of correlation coefficient.

In general, all model setups reproduced the unimodal shape of the relationship between soil moisture and its standard deviation, but in the simulated relationships (Figure 8.9) the peak of the relationship was shifted towards lower soil moisture values. As the simulated range of soil moisture values was lower than the measured range, the decreasing arm of the relationship was not fully simulated. The lack of macropore flow hindered the soil moisture from reacting quickly to rainfall events in terms of short-term soil moisture changes and peak runoff response. Rosenbaum et al. (2012) assumed that the variability in wet soils was mainly controlled by lateral and vertical flow processes and the distribution of porosities. The results of correlation analysis confirm the hypothesis that porosity distribution is an important determinant of the soil moisture pattern because the correlation strength between porosity distributions and the moisture pattern increases with wetting. For example, on 13.1.11 (refer to Figure 8.14), the

correlation strength reached 0.98 for d100. Unfortunately, the results of hydrological simulations can neither confirm nor reject the hypothesis regarding flow processes because macropore flow processes were not represented in the HydroGeoSphere application. Rosenbaum et al. (2012) suggested that as the soil dries, the influence of evaporation and root water uptake increases, which reduces differences in soil moisture. Again, this result cannot be confirmed because the simulation missed the drying arm of the moisture-standard deviation relationship. In HydroGeoSphere the actual transpiration amount depends nonlinearly on soil moisture as shown in Equation 18. As the transpiration limiting saturations shown in Equation 18 and the vegetation parameterization were spatially constant, the heterogeneity of transpiration only depended on the soil moisture pattern (as potential evapotranspiration and precipitation were assumed to be spatially homogeneous throughout the catchment) and differences in soil properties. Due to the large degree of homogeneity in soil properties and resulting parameters (refer to chapter 7.3.2), the soil moisture pattern is likely the dominant control of transpiration heterogeneity. The bedrock simulations only marginally affected soil moisture simulation at both scales, and as such were not able to add additional insights in the model's capability to simulate spatial dynamics and their variability.

A Spearman correlation analysis between measured/simulated soil moisture patterns and topographic variables and porosity distributions was performed. Correlation strengths of simulated soil moisture patterns to relative elevation and porosity were higher but correlation strengths to slope were lower compared to measured soil moisture patterns at all depths. In addition, measured soil moisture patterns were not clearly correlated to either a topographic or porosity pattern which could have resulted from the simple linear correlation approach applied in this study and/or from the fact that an important pattern controlling soil moisture variability was not included in the analysis. *The results generally indicated that the simulation underestimated the complexity of the soil moisture pattern. Borchardt (2012) presented a map with the spatial distribution of the thickness of the top substrate layer of the Wüstebach test site. The spatial distribution of this layer corresponded well to the measured soil moisture pattern presented in Figures 8.14 to 8.19. It was also highly correlated to the moisture pattern in the western part of the catchment, which was not well captured by the simulation.* This result means that the applied spatial heterogeneity in maximum soil depth as derived from the soil map (Geological Survey NRW) in this study is either not correctly reported in the soil map or in the study of Borchardt (2012).

Famiglietti et al. (1998) found that the influence of topographic attributes on the soil moisture pattern and its variability increased with further drying of the catchment. In this study, the correlation between soil moisture and relative elevation increased, but the correlation with slope decreased with drying. This pattern was observed for both the measurements and the simulations.

Table 8.5: Mean Spearman coefficients among topographic variables, porosity distributions and soil moisture patterns. Values in bold are significant at an alpha of 0.05. Green and red colors highlight increases and decreases between 5 to 20 cm depth and 20 to 50 cm depth by $\geq 10\%$.

	5 cm					20 cm				
	Measured	25 m	100 m	100 m		Measured	25 m	100 m	100 m	
	Measured	25 m	Bedrock	m	Bedrock	Measured	25 m	Bedrock	m	Bedrock
Relative Elevation										
Measured	-0.06	-0.40	-0.38	-0.51	-0.53	-0.13	-0.38	-0.32	-0.53	-0.56
25 m	-0.06	-0.40	-0.38	-0.51	-0.53	-0.13	-0.38	-0.32	-0.53	-0.56
100 m	-0.04	-0.38	-0.36	-0.49	-0.51	-0.12	-0.37	-0.31	-0.51	-0.54
Slope										
Measured	-0.20	-0.05	-0.07	0.04	0.04	-0.21	-0.05	-0.10	0.06	0.04
25 m	-0.23	-0.05	-0.08	0.03	0.03	-0.25	-0.05	-0.11	0.05	0.04
100 m	-0.33	-0.12	-0.13	-0.17	-0.11	-0.37	-0.05	-0.06	-0.17	-0.13
Porosity										
25 m	0.36	0.64	0.62	0.61	0.58	0.26	0.32	0.32	0.42	0.41
100 m	0.44	0.71	0.69	0.91	0.85	0.41	0.39	0.38	0.61	0.57
Soil Moisture										
Measured	1.00	0.43	0.42	0.44	0.43	1.00	0.39	0.36	0.50	0.47
25 m	0.43	1.00	0.99	0.71	0.70	0.39	1.00	0.96	0.62	0.64
25 m Bedrock	0.42	0.99	1.00	0.70	0.70	0.36	0.96	1.00	0.56	0.59
100 m	0.44	0.71	0.70	1.00	0.96	0.50	0.62	0.56	1.00	0.94
100 m Bedrock	0.43	0.70	0.70	0.96	1.00	0.47	0.64	0.59	0.94	1.00
	50 cm									
	Measured	25 m	100 m	100 m						
	Measured	25 m	Bedrock	m	Bedrock					
Relative Elevation										
Measured	-0.11	-0.18	-0.13	-0.55	-0.65					
25 m	-0.11	-0.17	-0.13	-0.55	-0.65					
100 m	-0.09	-0.17	-0.12	-0.54	-0.64					
Slope										
Measured	-0.17	0.01	-0.03	0.14	0.18					
25 m	-0.19	0.01	-0.04	0.16	0.19					
100 m	-0.39	0.11	0.10	0.05	0.07					
Porosity										
25 m	0.22	0.33	0.35	0.51	0.48					
100 m	0.36	0.32	0.33	0.58	0.54					
Soil Moisture										
Measured	1.00	0.06	0.04	0.16	0.17					
25 m	0.06	1.00	0.96	0.50	0.47					
25 m Bedrock	0.04	0.96	1.00	0.47	0.45					
100 m	0.16	0.50	0.47	1.00	0.93					
100 m Bedrock	0.17	0.47	0.45	0.93	1.00					

8.2.3 Influence of calibration period on water balance and soil moisture dynamics

This chapter summarizes the effect of calibration period on calibration parameters, water balance and soil moisture simulation. As already outlined in chapter 7.4, Wüstebach simulations were calibrated for the year 2010 before measurements of actual evapotranspiration became available. As these measurements only start in May 2010, the year 2011 turned out to be more suitable for calibration. Thus, a comparison between simulation results achieved with different calibration periods had to be done.

Table 8.6: Measured and simulated water balance components in 2010 and 2011 for two simulations with different calibration periods.

	2010		2011	
Precipitation (mm/y)	1226		1348	
Measured Discharge (mm/y)	608		630	
Potential Evapotranspiration (mm/y)	694		756	
Actual Evapotranspiration (mm/y)	377 ¹		596	
	Calibration 2010	Calibration 2011	Calibration 2010	Calibration 2011
Simulated Discharge (mm/y) ²	647	645	652	651
Interception (mm/y)	248	251	248	272
Interception (%)	20	20	18	20
Transpiration (mm/y)	261	236	353	326
Actual Evapotranspiration (mm/y)	509	487	601	598
Coefficient of Determination (-)	0.66	0.66	0.75	0.75
Nash-Sutcliffe Coefficient (-)	0.65	0.65	0.75	0.75
Percent Bias (%)	-6.31	-6.12	-3.48	-3.43

(¹=Measurements start on May 1st, 2010; ²= Annual sums of simulated discharge exclude time steps with gaps in measured discharge)

Table 8.6 shows water balance components and performance measures of discharge simulation for the years 2010 and 2011 for two simulations where 2010 is either calibration period (calibration 2010) or validation period (calibration for 2011). Calibrating the model for 2011 slightly improved simulated water balance components for both years. The most striking change concerned the decrease of transpiration rate by 25 and 27 mm for 2010 and 2011. Additional water increased the soil storage and thus discharge amount remained constant. The quality of simulated discharge dynamics measured by Coefficient of Determination and Nash-Sutcliffe Coefficient showed no change.

The top part of Figure 8.20 compares simulated soil moisture dynamics (calibrated for 2011) to measured soil moisture; the bottom part shows simulated soil moisture for the two different calibration periods. The figure illustrates that the choice of calibration period had a large effect on soil moisture simulation at 5 cm depth but not on the simulation at 20 and 50 cm depth. This resulted from the large difference in measured volumetric soil moisture during autumn and winter between 2010 and 2011. Comparable to water balance components, soil moisture at 20 and 50 cm depth showed a slight improvement in terms of Nash-Sutcliffe-Coefficient when the model was calibrated for the year 2011 (refer to Table 8.7). At 5 cm depth, the Nash-Sutcliffe-Coefficient showed largest deviations between simulations with different calibration periods. In terms of calibration parameters, the multiplication factor for soil moisture at 5 cm depth exhibited the largest change due to the pronounced deviation in volumetric soil moisture between 2010 and 2011 (Table 8.8).

Table 8.7: Measures of soil moisture simulation performance at 5, 20 and 50 cm depth for two simulations with different calibration periods.

	2010					
	Calibration 2010			Calibration 2011		
	5 cm	20 cm	50 cm	5 cm	20 cm	50 cm
Coefficient of Determination (-)	0.77	0.75	0.47	0.77	0.75	0.45
Nash-Sutcliffe Coefficient (-)	0.72	0.33	0.26	-0.60	0.47	0.35
	2011					
Coefficient of Determination (-)	0.52	0.47	0.45	0.52	0.47	0.44
Nash-Sutcliffe Coefficient (-)	0.06	0.23	0.20	0.50	0.20	0.36

Table 8.8: Calibrated parameters for two simulations with different calibration periods.

	Calibration 2010	Calibration 2011
Canopy storage parameter (m)	0.0015	0.0019
Multiplication factor for residual saturation, 5 cm	5.4	4.0
Multiplication factor for residual saturation, 20 cm	4.6	4.6
Multiplication factor for residual saturation, 50 cm	3.3	3.1
Oxic limit	0.90	0.88
Anoxic limit	0.97	0.955

Based on these results, the choice of calibration period only had a minor effect on water balance and discharge simulation. This result was expected because the applied split sample test leads to two data sets that are “functionally equivalent” (Kirchner, 2006) concerning climate conditions and properties of underlying discharge processes. In contrast, large differences in measured topsoil moisture between 2010 and 2011 were apparent, affecting the calibration of residual saturation. Thus, it could not be decided if the choice of the calibration period improved or deteriorated soil moisture simulation results.

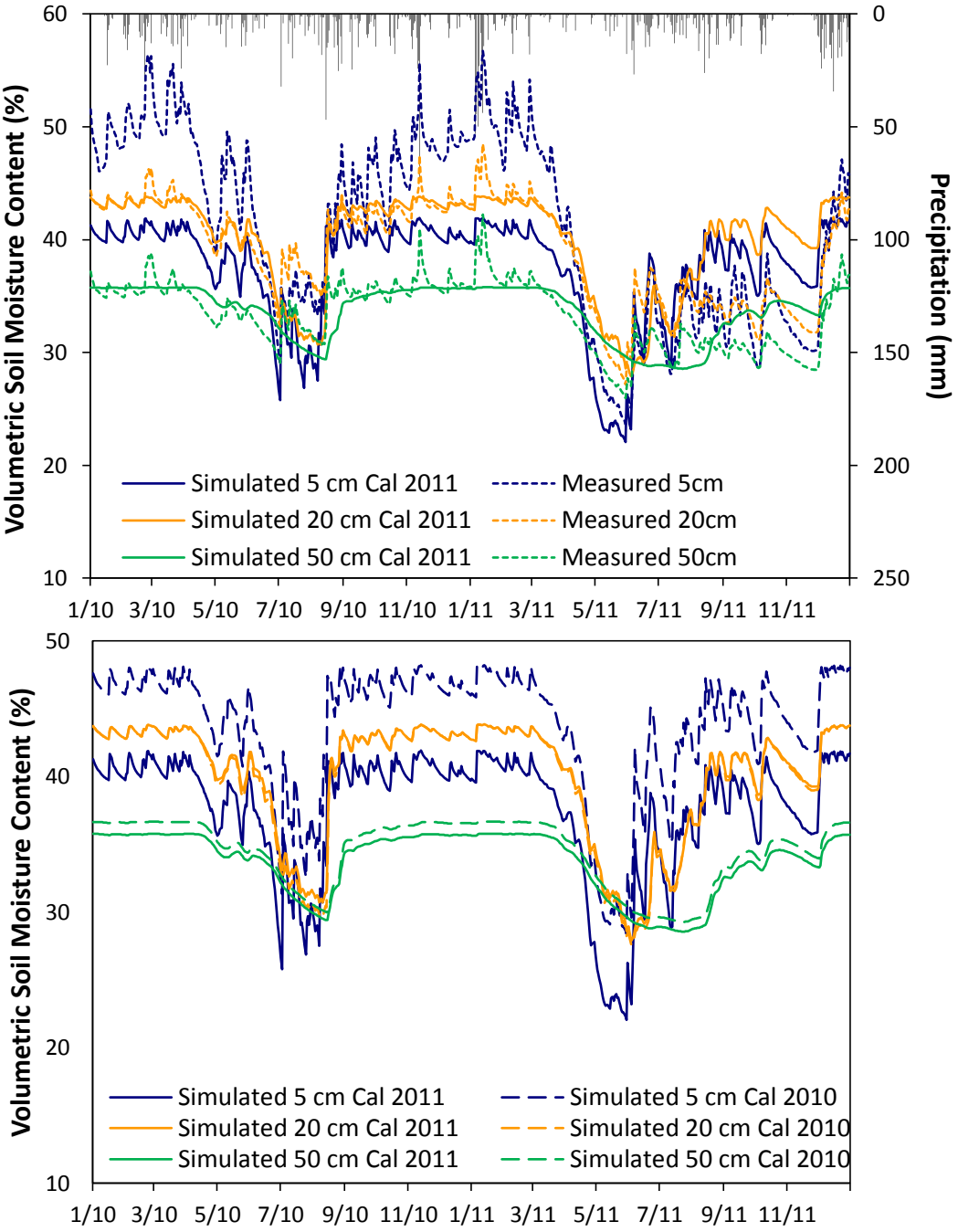


Figure 8.20: Upper part: Observed and simulated daily soil moisture dynamics calibrated for the year 2011. Lower part: Comparison between simulated soil moisture for the two different calibration periods 2010 and 2011.

8.2.4 Event scale soil moisture hysteresis

In 2012, Rosenbaum et al. found clockwise hysteresis of topsoil moisture at the event scale for moderate soil moisture content under heavy rainfall leading to pronounced and fast increase of soil moisture. In this chapter, measured and simulated event scale soil moisture and its standard deviation is analyzed for different soil moisture conditions under advective and convective precipitation events in order to reproduce Rosenbaum’s findings.

Following Rosenbaum et al. (2012), three soil moisture states are distinguished as follows: the dry soil moisture state occurs for soil moistures lower 30 vol. %, the intermediate between 30 and 47 vol. % and the wet state beyond 47 vol. % soil moisture. Events were selected if both simulated and measured soil moisture were part of the same soil moisture state and if the measured soil moisture changed by at least 2 vol. %. For the dry and wet state, no convective rainfall event leading to a sufficiently large increase in soil moisture could be identified. This was due to the small number of hours measured and simulated data shared at the dry state and due to the already high soil moisture during the wet state.

Table 8.9 summarizes absolute changes in simulated and measured soil moisture and standard deviation for each of the four selected events. The table illustrates some interesting patterns. First of all, increasing soil moisture always led to decreasing standard deviation in the model.

Table 8.9: Changes in simulated and measured soil moisture and standard deviation during four rainfall events with different rainfall characteristics and soil moisture contents.

	dry state		intermediate state				wet state	
	advective		convective		advective		advective	
	wet	dry	wet	dry	wet	dry	wet	dry
Rainfall (mm)	16.7	0.0	16.2	0.0	12.5	0.9	13.5	6.1
	Measurements							
Soil Moisture (%)	+3.1	-1.5	+4.0	-0.7	+7.0	-3.3	+3.1	-4.8
Standard Deviation (%)	+2.6	-1.6	+1.8	-0.5	-1.3	0.0	-1.1	+1.4
	Simulation							
Soil Moisture (%)	+7.1	-4.5	+1.7	-0.8	+2.0	-0.7	+0.6	-0.8
Standard Deviation (%)	-1.1	+0.8	-0.4	+0.2	-0.5	-0.1	-0.1	+0.3

Measured data showed an increase in standard deviation with wetting for the advective events at the dry and the convective event at the intermediate state but a decrease in standard deviation for the advective events at the intermediate and wet state. Secondly, simulated standard deviation changes were always smaller than measured ones as expected from the simulation results shown in Figure 8.9.

To illustrate the development of the relationship between soil moisture and its standard deviation, a convective rainfall event at the intermediate state and an advective event at the dry state are chosen as examples.

The convective rainfall event on 10.7.2010 (refer to Figure 8.21) brought 16.2 mm of rainfall in 3 hours. It increased both measured soil moisture (+4 vol. %) and its standard deviation (+1.8 vol. %). The decrease of both variables during the drying cycle was very slow as soil moisture only decreased by 0.7 vol. % and standard deviation by 0.4 vol. % in four days. Although the simulation captured the general trend of soil moisture dynamics, standard deviation decreased instead of increasing. The arrows in Figure 8.21 illustrate the clockwise development of the relationship between standard deviation and measured soil moisture. In the simulation, the wetting and drying path were nearly identical. Rosenbaum et al. (2012) explained hysteresis with spatial variability in throughfall. The fact that this variability was not resolved in the simulation explains the missing hysteresis pattern.

An advective rainfall event between the 31.5.2011 and 4.6.2011 brought 16.7 mm of rainfall distributed over 20 hours (Figure 8.22). Both simulated and measured soil moisture started at the dry state with lower values for measured soil moisture. Measured standard deviation increased during wetting and decreased during drying. Comparable to the convective rainfall event during the intermediate soil moisture state, simulated standard deviation increased with drying and decreased with wetting. Changes in simulated soil moisture were much larger than for the measured soil moisture while changes in simulated standard deviation were smaller. The relationship between soil moisture and its standard deviation (illustrated by arrows in Figure 8.22) did not show a hysteresis effect for both measurements and simulation. Instead, both relationships shared the same wetting and drying path although this effect was more pronounced for the simulated data. This pattern was also observable for the two other events summarized in Table 8.9 (advective at intermediate and wet moisture state) and thus these events are not shown in detail.

So, this chapter illustrates that the HydroGeoSphere simulation is not able to resolve hysteresis effects. In addition, simulated standard deviation always decreased during wetting but measured standard deviation decreased or increased during wetting dependent on pre-storm soil moisture.

Hysteresis at intermediate soil moisture was explained by Rosenbaum et al. (2012) with the spatial variability of throughfall. Interception measurements (refer to chapter 6.2.3) show an

increase of standard deviation with increasing precipitation amount approximately following a power law function given as $y=0.746*x^{0.682}$ with an R^2 of 0.86. Thus, at rainfall events of 15-16 mm investigated in this chapter, interception exhibits a standard deviation of 4.7-4.9 mm. A representation of this variability in HydroGeoSphere was not possible at the chosen spatial discretization of 25 and 100 m, because interception variability results from different distances between canopies and thus at spatial scales below 1 m.

The counterintuitive observation from measured soil moisture data that wetting increased variability instead of decreasing is explainable with the results described in chapter 8.2.2. It was shown that measured soil moisture data exhibited a convex shaped relationship between soil moisture and its standard deviation which means that the reaction of standard deviation to wetting can be either a decrease or an increase. As all simulations only captured the wetter part of the convex relationship, wetting always leads to a decrease in standard deviation and drying to an increase.

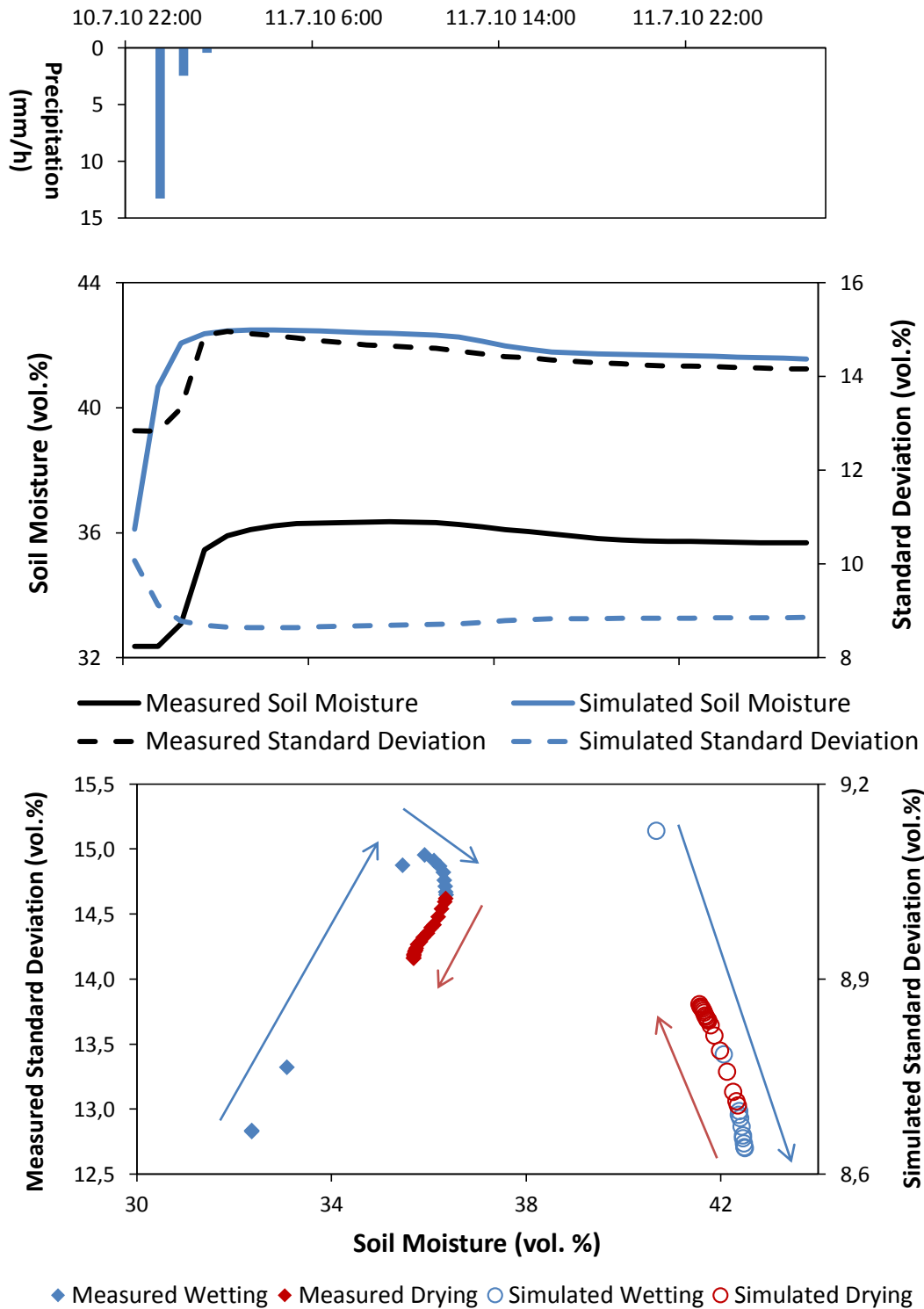


Figure 8.21: Hysteresis reaction after a convective rainfall at the intermediate soil moisture state between 10.7.2010 and 11.7.2010. Top part shows precipitation, center part soil moisture and standard deviation development, bottom part the soil moisture-to-standard deviation relationship for measured and simulated data.

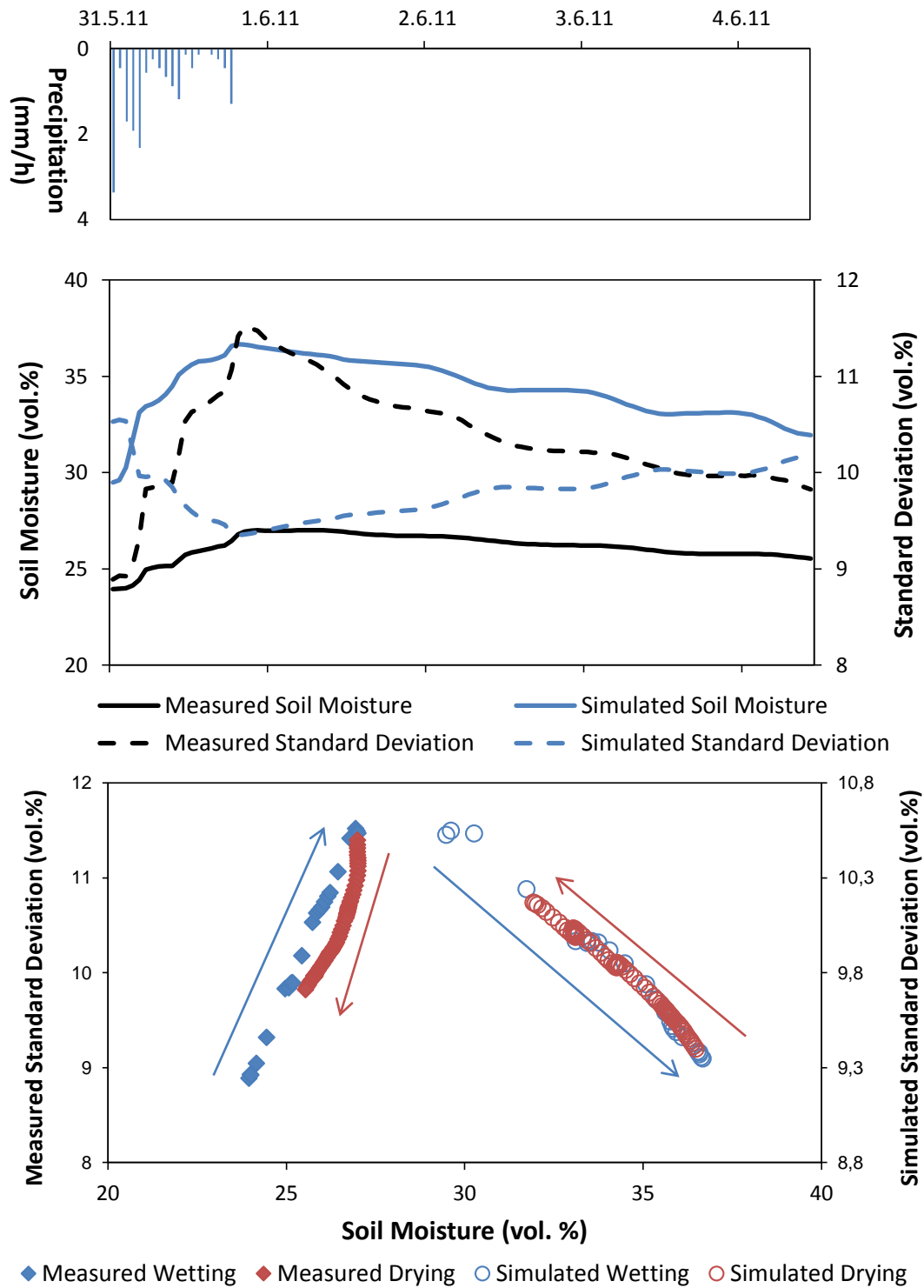


Figure 8.22: Hysteresis reaction after an advective rainfall at the dry soil moisture state between 31.5.2011 and 4.6.2011. Top part shows precipitation, center part the soil moisture and standard deviation development, bottom part the soil moisture-to-standard deviation relationship for measured and simulated data.

8.3 Erkensruhr

The following chapters (pages 144-157) have been submitted to Journal of Hydrology in August 2015. Changes to the text include figure and table numbering and the replacement of formulations with “we” and “our”.

8.3.1 Influence of mesoscale soil and land use parameters on the simulation of the headwater catchment

The top part of Figure 8.23 shows measured and simulated discharge rates for the original simulation of the Wüstebach (Wbach) and the simulation of the Wüstebach with soil data from the Erkensruhr (WbachEsoilConi) for the years 2010 and 2011. Observed discharge was characterized by a strong seasonality with a pronounced low flow period during the summer and high variability during snow dominated periods in the winter. Generally, both simulation scenarios reproduced the discharge dynamics well but overestimated peaks during the winter (due to an overestimation of snow melt by the snow model) and omitted some peaks during the summer. The usage of coarser soil data from the Erkensruhr (model scenario WbachEsoilConi) intensified the tendency to overestimate peak discharge rates. Small differences in discharge between the reference simulation Wbach and the simulations of the Wüstebach with deciduous (WbachDeci) and grassland vegetation (WbachGrass; middle section of Figure 8.23) showed that the sensitivity of discharge to changes in land use was weak. Higher discharge rates of WbachDeci and WbachGrass in late summer 2010 resulted from differences in LAI development and corresponding changes in interception. At the end of 2011, differences in discharge resulted from differences in soil moisture. The WbachDeci simulation had lower soil moistures in all depths than the Wbach simulation and therefore rainfall was primarily replenishing the water storage. The WbachGrass simulation had highest soil moisture at the same time and accordingly highest discharge rates. In the bottom part of Figure 8.23, differences between the reference simulation Wbach and the simulations with Erkensruhr soil data are shown for deciduous (WbachEsoilDeci) and grassland (WbachEsoilGrass) vegetation. Both simulations produced higher discharge rates during both years with an extreme overestimation during 2010 of the WbachEsoilDeci model scenario.

Figure 8.24 summarizes statistical measures of model performance for the hydrological winter 2010/2011 and - as a mean value - for the hydrological summer periods in 2010 and 2011.

All statistical measures varied stronger between simulations during summer than during winter because (1) differences in evapotranspiration simulation only became apparent during summer and (2) small changes in discharge amount and timing had a high impact on statistical measures during the low flow period. During winter, all model scenarios produced high statistical measures with correlation coefficients and coefficients of variation reaching values above 0.78 and bias values above 0.94.

Changing land use primarily affected the coefficient of variation during the hydrological summer with decreases for grassland and increases for deciduous forest. The correlation coefficient for grassland also decreased by 0.4. A change in soil data mainly influenced the bias and the coefficient of variation. The unique behavior of the simulation WbachEsoilDeci in terms of very high increases in bias and correlation coefficient compared to WbachDeci was already mentioned in the previous paragraph. The reason for this increase in simulation quality and the interplay between saturated conductivity, infiltration and antecedent soil moisture will be further analyzed in the discussion section.

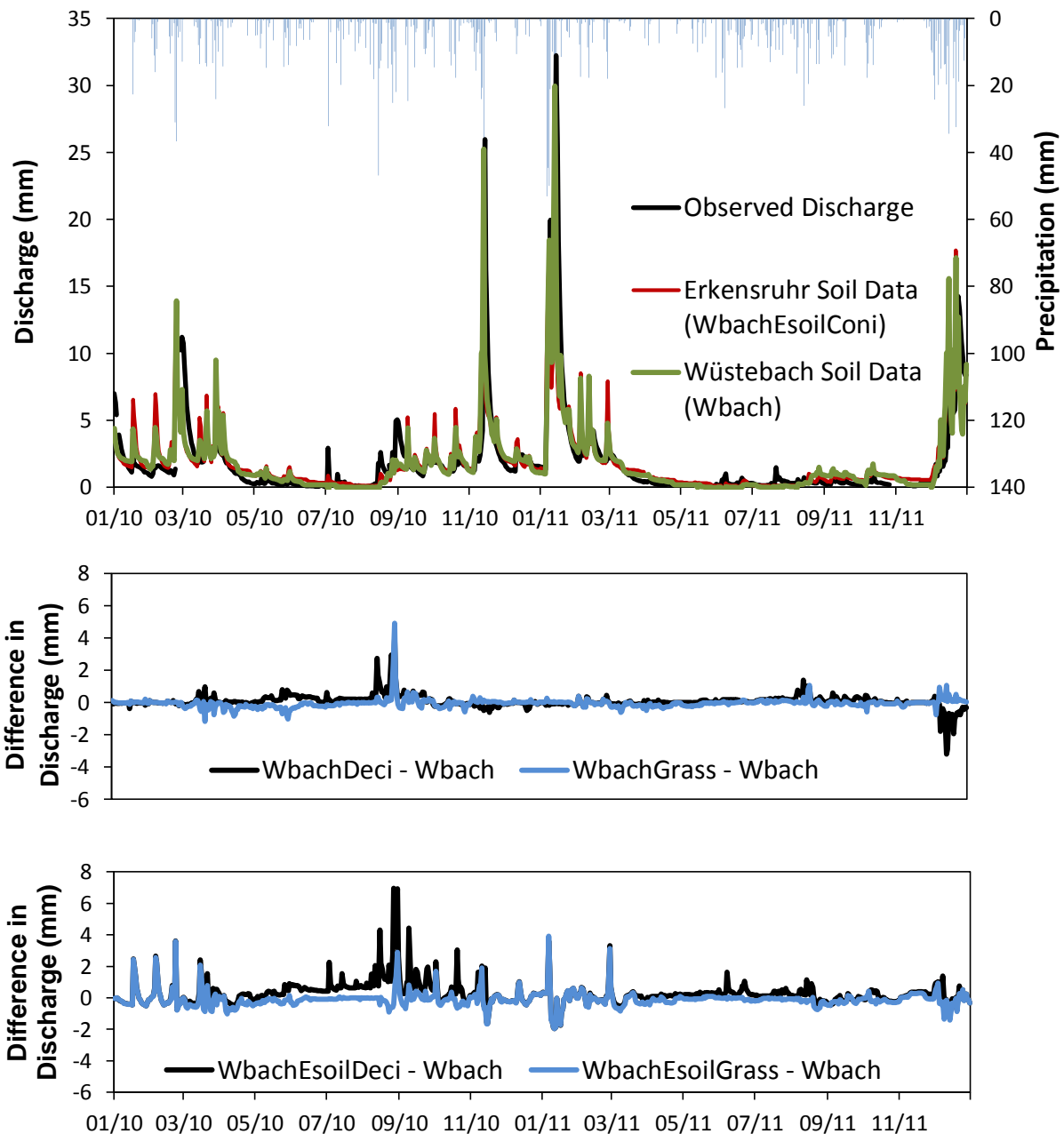


Figure 8.23: Top: Comparison of observed and simulated discharge of the Wüstabach for simulations with high-resolution soil data (Wbach) and low-resolution soil data (WbachEsoilConi). Middle: Discharge difference between simulations with changing land use. Bottom: Discharge difference between simulations with changing land use and soil data.

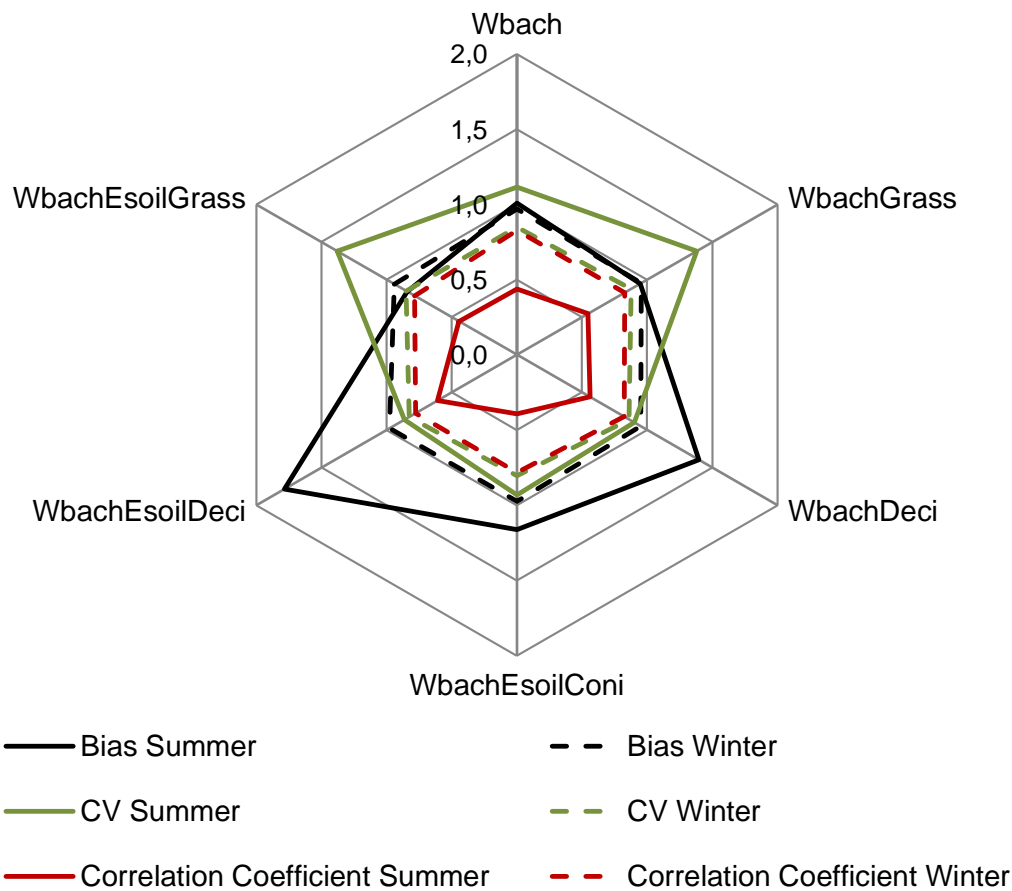


Figure 8.24: Bias (black line), coefficient of variation (CV; green line) and correlation coefficient (red line) in hydrological summer (solid lines) and winter (dashed lines) for the Wüstebach discharge simulations.

The water balance of the Wüstebach simulations (Table 8.10) showed some interesting features concerning evapotranspiration components and infiltration sums. The total amount of actual evapotranspiration significantly changed between different land uses with highest values for WbachGrass due to the changes in transpiration parameters (chapter 7.3.1). In 2010, the amount of actual evapotranspiration for the WbachDeci simulation equaled that of Wbach, but in 2011 evapotranspiration was larger by 50 mm. Infiltration sums and fractions of subsurface flow varied between years but not between simulation variants using the same soil data.

Comparing simulations with high-resolution soil data of the Wüstebach to those with larger scale Erkensruhr soil data, significant differences in the water balance components and in the fractions of subsurface flow became apparent. For both forested land uses, actual evapotranspiration decreased by 37 mm (2010) and 25 mm (2011) for coniferous and by 126 mm (2010) and 56 mm (2011) for deciduous forest. The decrease in evapotranspiration resulted from a decrease in infiltration sums by 77 mm (2010) and 62 mm (2011) for coniferous and by 113 mm (2010) and 89 mm (2011) for deciduous forest. Despite the decrease in infiltration

sums, discharge sums were much higher and as a result the fraction of subsurface flow decreased by 12-14% in 2010 and 6-7% in 2011. In contrast to the forest land uses, the WbachEsoilGrass scenario showed small changes in total evapotranspiration (≤ 27 mm) and correspondingly lowest variations in infiltration sums.

Table 8.10: Water balance components for Wüstebach simulations.

	2010					
	Wbach			Wbach		Wbach
	Wbach	WbachDeci	WbachGrass	EsoilConi	EsoilDeci	EsoilGrass
Rainfall (mm)	1226					
Potential ET ¹ (mm)	694					
Measured Discharge (mm)	608					
Transpiration (mm)	232	227	279	195	99	282
Evaporation (mm)	247	254	289	247	256	293
Actual Evapotranspiration (mm)	479	481	568	442	355	575
Discharge ² (mm)	611	657	591	647	764	587
Baseflow (%)	76	76	75	64	62	63
Infiltration (mm)	968	992	1011	891	879	954
	2011					
	Wbach			Wbach		Wbach
	Wbach	WbachDeci	WbachGrass	EsoilConi	EsoilDeci	EsoilGrass
Rainfall (mm)	1348					
Potential ET ¹ (mm)	756					
Measured Discharge (mm)	630					
Transpiration (mm)	272	312	290	247	250	306
Evaporation (mm)	273	283	314	273	289	325
Actual Evapotranspiration (mm)	545	595	604	520	539	631
Discharge ² (mm)	637	640	626	652	673	594
Baseflow (%)	62	64	60	56	58	53
Infiltration (mm)	894	959	960	832	870	896

¹ Evapotranspiration ² Sums of simulated discharge exclude time steps with gaps in measured discharge data.

In the context of the Erkensruhr study, soil moisture simulation results are compared between simulations but not with measurements. For a detailed comparison between simulated and measured soil moisture of the Wüstebach catchment, the reader is referred to Cornelissen et al. (2014) or to chapter 8.2.2.

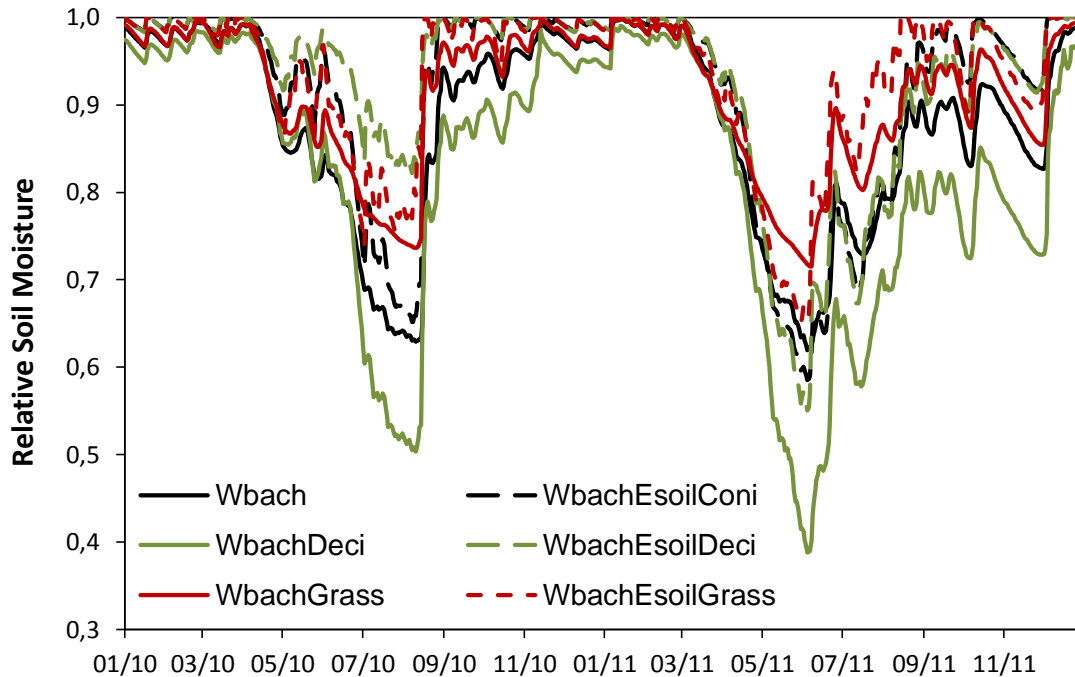


Figure 8.25: Soil moisture dynamics of the Wüstebach simulations at 20 cm depth.

There were large differences in simulated soil moisture dynamics between land use types at all depths. At 5 cm depth, differences were most pronounced during August and July 2010 when the WbachDeci simulation maintained soil moisture values above 0.5 while soil moisture for both the Wbach and the WbachGrass simulations dropped below 0.3. In August and July 2011, the WbachDeci simulation was again the wettest but differences to Wbach and WbachGrass were smaller. The Wbach and WbachGrass scenarios showed small differences at 5 cm depth, because their root depth (refer to Table 7.1) was comparably high with 0.5 m and 0.35 m respectively. At 20 cm depth, the WbachDeci scenario produced the lowest soil moisture in both years (Figure 8.25). During July and August of both years, WbachGrass and Wbach maintained soil moisture values of about 0.6 while WbachDeci dropped below 0.4 in 2011. In both years, the WbachGrass scenario produced the highest soil moisture. At 50 cm depth, a clear hierarchy following root depths was found in both years with highest moistures for WbachGrass (featuring the lowest root depth) and lowest values for WbachDeci (featuring the highest root depth). The usage of large scale soil data generally increased soil wetness and intensified short term soil moisture dynamics down to 50 cm depth. Differences were again most pronounced for the simulation with deciduous land use.

The relationship between mean soil moisture and its standard deviation showed little variations between different land use types at 5 cm depth (Figure 8.26). Simulations with Erkensruhr soil

data produced a steeper slope with higher standard deviations at the same moisture. This is attributed to the different number of soil units of the model scenarios (for the Wüstebach catchment the large scale soil map produced only 5 different soil units compared to 108 soil units when using the small scale soil map). As demonstrated recently by Qu et al. (2015), the shape of soil moisture to standard deviation relationship can be explained to a large extent by the spatial variance of soil hydraulic properties.

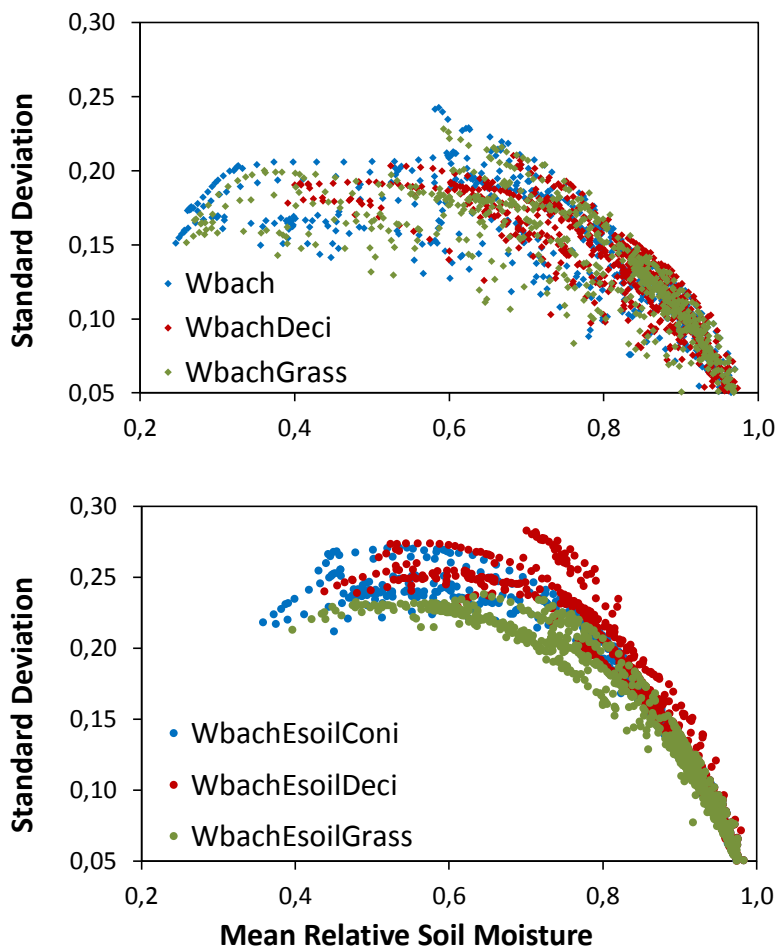


Figure 8.26: Relationship between mean soil moisture and its standard deviation for Wüstebach simulations at 5 cm depth with (top) Wüstebach and (bottom) Erkersruhr soil data.

Results of the Wüstebach simulations revealed a strong influence of (1) soil data on runoff generating processes and of (2) land use parameters on evapotranspiration components.

Usage of large scale soil data for the simulation of the Wüstebach catchment led to a decrease in infiltration and transpiration, and to a corresponding increase in discharge amount. Decrease in infiltration resulted from a higher antecedent wetness prior to precipitation events in the summer. In addition, Figure 8.25 showed pronounced short term soil moisture dynamics for all simulations with coarser soil data. Faster soil moisture dynamics was accompanied by faster groundwater level rise which hindered infiltration, decreased transpiration and accordingly increased the soil moisture storage thus limiting infiltration capacity.

Comparing water balance components (Table 8.10) between 2010 and 2011 showed that the effect described above was stronger in 2010 than in 2011. In April and May 2010 precipitation rates were larger than potential evapotranspiration rates but in April and May 2011 precipitation rates were lower. That significantly reduced soil moisture in 2011 thus dampening the effect of coarser soil data on runoff generation processes.

Pronounced soil moisture and groundwater level dynamics of the scenario with Erkensruhr soil data were partly explainable by higher saturated hydraulic conductivity. For example, at 5 cm below the litter layer, the saturated hydraulic conductivities of the Erkensruhr soil data were higher by a factor of 17 but alpha values were lower by 0.6. A synthetic experiment using the Wüstebach model scenario applying a rainfall rate exceeding the saturated conductivity of the Wüstebach soil dataset was performed. The experiment showed a decrease of 60% in infiltration and corresponding increase in surface runoff illustrating that (1) the sensitivity of hydrological processes to changes in saturated conductivity is large (also refer to chapter 8.1) and (2) the observed counter-intuitive decrease in infiltration rates due to higher saturated conductivity could be reproduced. This observation compared well to results of the sensitivity analysis which indicated a high dependency of soil moisture variability (coefficient of variation) and infiltration on saturated conductivities.

The observed high sensitivity of fast runoff sums and runoff generation mechanisms to changes in soil properties agreed well with the finding of many studies but the result that higher saturated conductivity led to an increase in fast runoff components contradicted to results reported in the literature for simulations with distributed hydrological models (Bormann et al., 2007; Herbst et al., 2006; Kværnø and Stolte, 2012).

To conclude, the observed increase in fast runoff components due to an increase in saturated conductivity resulted from a unique interplay between antecedent wetness, infiltration, groundwater level rise and transpiration which strongly depended on the difference between precipitation and potential evapotranspiration during spring. Although this interplay was an artifact because it occurred only for one model scenario, the effect was reproduced with a simple infiltration excess experiment.

The applicability of mesoscale land use parameters was validated with a comparison between evapotranspiration amounts simulated with Wüstebach soil data and values reported in the literature.

Simulated evapotranspiration of grassland amounted to 46% but literature values ranged between 36% for a measurement site in Germany with a precipitation of 800 mm (Harsch et al., 2009) and 60% at a grassland site near to the Erkensruhr catchment (Schmidt, personal communication). Data cited in Mendel (2000) ranged between 55% (with 800 mm precipitation) and 75% (with only 581 mm precipitation).

Despite the lack of calibration, simulated interception fractions for deciduous forest (17%) corresponded well to the value observed by Oishi et al. (2008) for a hardwood forest in the United States with a precipitation of 1091 mm. Mendel (2000) reported interception values between 5% and 48% for a beech forest. Simulated fractions of evapotranspiration (without interception) amounted to 25% but literature values ranged between 26% (Mendel, 2000) and 40% (Oishi et al., 2008).

The large range of evapotranspiration components for both land uses pointed to considerable uncertainty in evapotranspiration validation and thus expressed the need for additional land use specific evapotranspiration measurements.

8.3.2 Influence of parameter regionalization and spatially distributed input data on the simulation of the mesoscale catchment

In the following, the results of the four Erkensruhr simulations are analyzed separately for the whole Erkensruhr catchment and for the Wüstebach sub-catchment. Water balance results were only available for the Erkensruhr as HydroGeoSphere does not enable the export of water balance results for sub-catchments.

Erkensruhr simulations with homogeneous rainfall (Figure 8.27) heavily overestimated discharge amounts especially during autumn, because the applied rainfall originated from a climate station located in the southwestern – and thus wettest - part of the catchment. The usage of distributed precipitation substantially improved the discharge simulation of the Erkensruhr in terms of total sum, rising and falling limbs and low flows (Figure 8.28). However, discharge peaks were underestimated, possibly because the same interception and transpiration parameters were used for different precipitation inputs. At the Wüstebach outlet, discharge amounts were overestimated during the summer due to the influence of spatial discretization on topography and transpiration parameters as described in Sciuto and Diekkrüger (2010). The simulated discharge dynamics only slightly changed using distributed precipitation, but the total discharge amount was substantially reduced during winter and summer periods which caused a large underestimation during winter but an improvement in summer discharges.

The overestimation of simulated discharge amounts at the Erkensruhr and Wüstebach outlets caused bias values around 1.6 for the Erk and 1.3 for the ErkWbach model scenarios during summer (Figure 8.29). Bias values were lower during winter with values of 0.9 for the ErkWbach, ErkWbach_LN and ErkWbach_LN_PET scenarios. The correlation coefficient for the Erkensruhr simulations was considerably higher during winter (0.9) than during summer (0.47). As the correlation coefficient during winter was higher for the Erkensruhr simulations than for the independent Wüstebach simulations (refer to Figure 8.29), it can be assumed that the snow model used in both simulations performed better for the smoother discharge curve of the larger catchment.

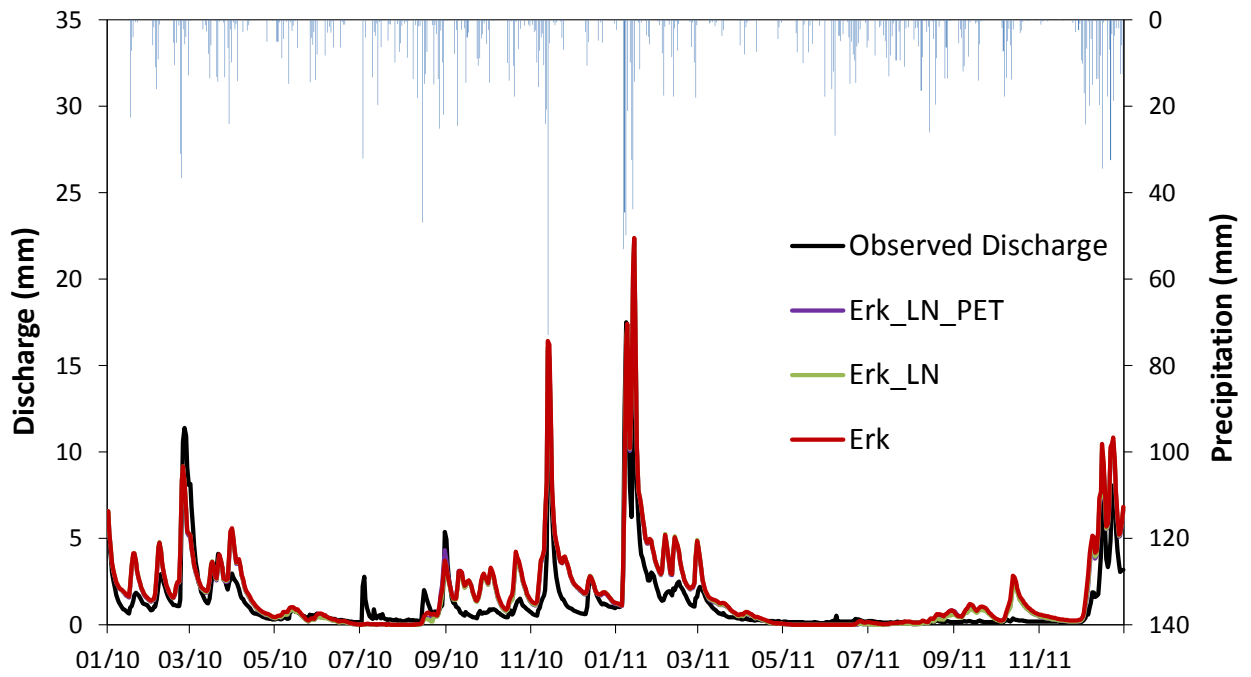


Figure 8.27: Observed and simulated discharge of the Erkensruhr for simulations with heterogeneous soil (Erk), heterogeneous soil and land use (Erk_LN), heterogeneous soil, land use and potential evapotranspiration (Erk_LN_PET).

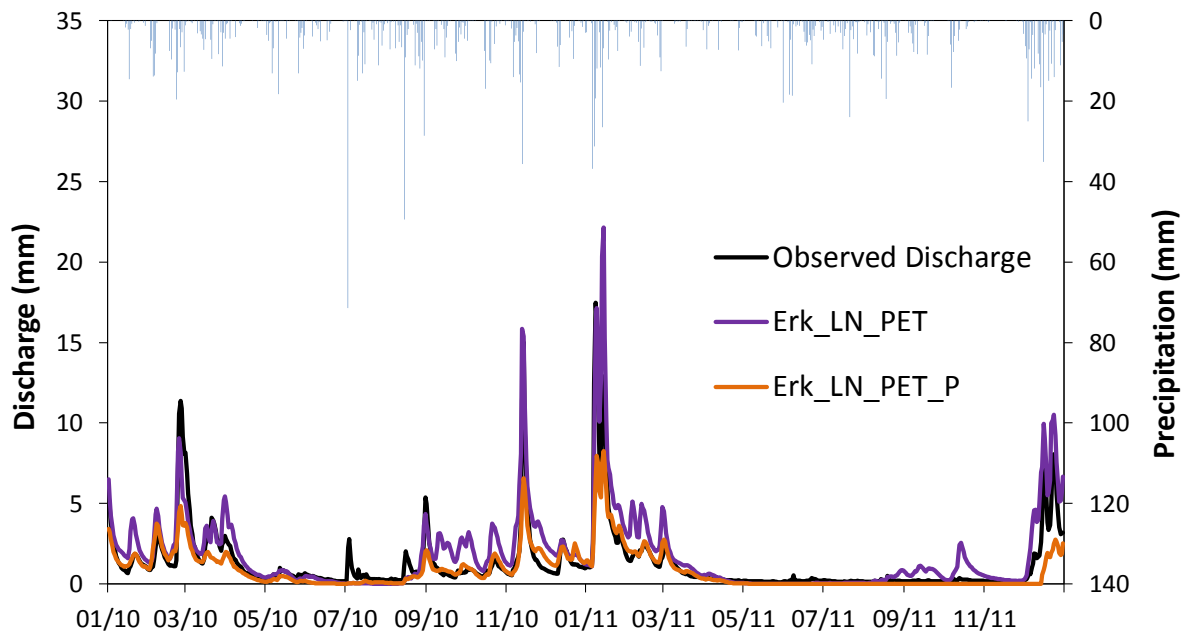


Figure 8.28: Observed and simulated discharge of the Erkensruhr for simulations with homogeneous (Erk_LN_PET) and distributed precipitation (Erk_LN_PET_P).

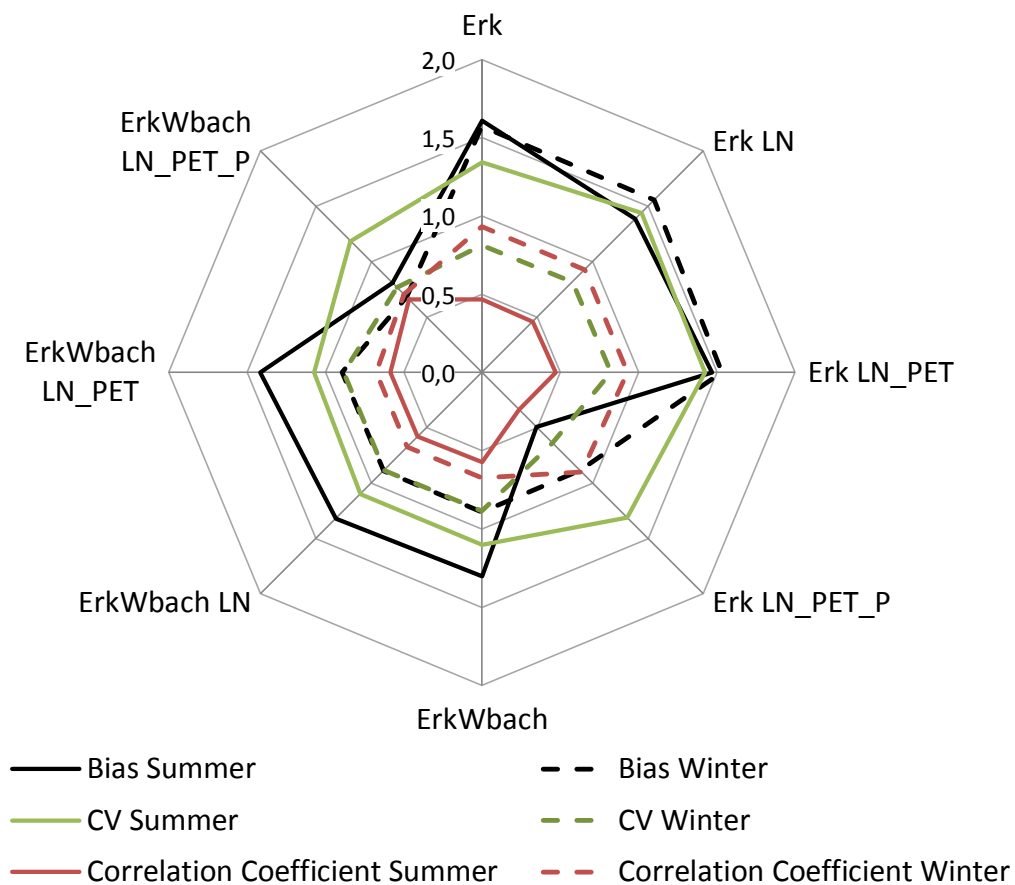


Figure 8.29: Bias (black line), coefficient of variation (CV; green line) and correlation coefficient (red line) in hydrological summer (solid lines) and winter (dashed lines) for the Erkensruhr discharge simulations.

Summer values of the correlation coefficient of the Erkensruhr simulations did not change with the inclusions of heterogeneous land use and heterogeneous potential evapotranspiration. The usage of distributed precipitation data improved the bias during summer and the coefficient of variation during winter. At the Wüstebach outlet, the usage of distributed precipitation improved the correlation coefficient in summer and winter but degraded the coefficient of variation in both summer and winter.

Interception amounts of the Erk simulation which considered spatially homogeneous coniferous land use throughout the catchment were slightly lower (by 15 mm) than that of Wbach and WbachEsoilConi with the same land use type (Table 8.11). The consideration of heterogeneous land use in the Erk_LN scenario slightly reduced interception. As already mentioned, the large scale soil data decreased simulated transpiration and infiltration amounts in the Wüstebach simulations independently of land use type. However transpiration of the Erk scenario was equal to that of the Wbach scenario and infiltration slightly increased.

Table 8.11: Water balance components for simulations of the Erkensruhr catchment.

	Erk		Erk_LN		Erk_LN_PET		Erk_LN_PET_P	
	2010	2011	2010	2011	2010	2011	2010	2011
Rainfall (mm)	1226	1348	1226	1348	1226	1348	956	902
Potential ET ¹ (mm)	694	756	694	756	694	757	694	757
Measured Discharge (mm)	524	396	524	396	524	396	524	396
Transpiration (mm)	226	272	268	286	260	305	283	332
Evaporation (mm)	265	289	278	306	288	312	265	267
Actual Evapotranspiration (mm)	491	561	546	592	548	617	548	599
Discharge (mm)	721	654	696	623	692	619	391	245
Subsurface Flow (%)	72	68	72	68	- ²	- ²	- ²	- ²
Infiltration (mm)	996	954	1024	980	1016	976	771	683

¹ Evapotranspiration ²Due to technical reasons, subsurface flow could not be calculated with the baseflow filter with gridded input data.

The total evapotranspiration amount increased when heterogeneous land use information was used. The consideration of distributed potential evapotranspiration did not alter total actual evapotranspiration amount and its components.

Figure 8.30 shows fractions of mean monthly evapotranspiration rates for coniferous (top), deciduous (middle) and grassland (bottom) vegetation. The simulated values were compared with measured eddy-covariance data in the case of coniferous and grassland vegetation and with literature values from Mendel (2000) in the case of deciduous vegetation.

For coniferous and grassland vegetation, the trend in mean monthly evapotranspiration was well simulated with a coefficient of correlation larger than 0.94. In the case of coniferous vegetation, the monthly evapotranspiration was overestimated between April and July and underestimated during August to December. Distributed precipitation rates improved the simulation between July and October meaning that the over- and underestimation for simulations with homogeneous precipitation was due to uncertainties in precipitation values and the calculation of potential evapotranspiration. For the grassland vegetation, mean evapotranspiration was overestimated during the winter and underestimated during the summer. Distributed precipitation only improved the simulation slightly during May to July. For deciduous vegetation, Figure 8.30 reveals largest deviations between simulated and measured data taken from literature (Mendel, 2000).

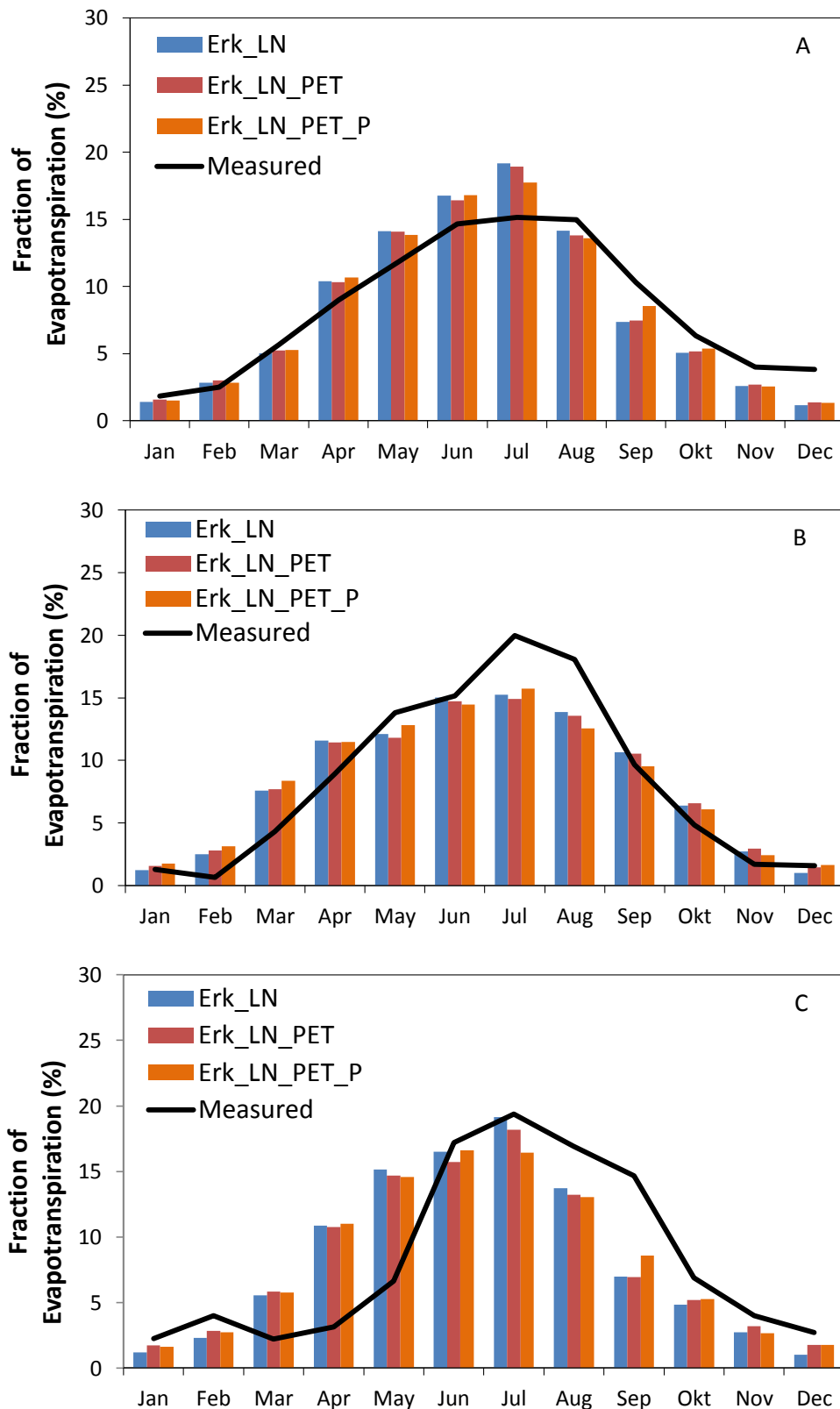


Figure 8.30: Measured and simulated mean monthly fraction of evapotranspiration rates for (A) coniferous, (B) grassland and (C) deciduous vegetation. Measured data refer to (A) eddy-covariance data from Graf et al. (2014), (B) eddy-covariance data from Schmidt (personal communication) and (C) mean monthly data from a low mountain catchment in northern Germany between 1969-1972 with a mean rainfall of 1066 mm (Mendel, 2000).

Figure 8.31 shows the pattern of simulated mean actual evapotranspiration given as a relative value of the evapotranspiration sum of 2010 and 2011. The pattern of the Erk scenario (top left in Figure 8.31) shows a clearly defined riparian and stream area with very high relative evapotranspiration values close to one. Driest conditions were found at the ridge of hills at the eastern, western and southern borders of the catchment. The pattern shown in the top right of Figure 8.31 for the Erk_LN scenario illustrates that the incorporation of heterogeneous land use enhanced evapotranspiration in the central part of the catchment covered with grassland. Distributed potential evapotranspiration decreased actual evapotranspiration in higher parts of the catchments (e.g. south-western border). The incorporation of distributed precipitation generally decreased the contribution of grassland areas to actual evapotranspiration.

Erkensruhr simulations revealed that the quality of the discharge simulation in terms of dynamics, amount and peak flow rates was most sensitive to differences in precipitation data. Spatially distributed land use parameterization only affected discharge amounts while spatially distributed potential evapotranspiration had a weak effect on discharge but a significant effect on the pattern of actual evapotranspiration during winter (not shown).

The influence of spatial precipitation patterns on hydrological simulations has been long under debate. For example Schuurmans and Bierkens (2007) and Arnaud et al. (2002) compared simulation results of distributed models using spatially distributed and spatially aggregated precipitation input. Schuurmans and Bierkens (2007) found that spatial variability of rainfall is necessary to simulate spatial variability in daily discharge, groundwater level and soil moisture content but not required for the general hydrological behavior. Arnaud et al. (2002) showed at two mesoscale catchments (103 and 22 km²) that differences in simulated discharge amount and peak flow rates decreased with increasing peak flow rate. In this study, differences in discharge rates between simulations with aggregated and spatially distributed precipitation increased with increasing peak flow. The high sensitivity of peak flow rates to precipitation sum and distribution highlights the extraordinary importance of meteorological forcing data in comparison to parameterization and parameter estimation efforts.

Mean monthly evapotranspiration was well simulated at the mesoscale catchment for coniferous forest and grassland (Pearson's r of ≤ 0.94) and to a lesser degree for deciduous vegetation (coefficient of correlation of ≤ 0.77) as these data were literature values and therefore the most uncertain (Mendel, 2000). Interestingly, the simulated trend improved when values were re-shifted in positive direction by one month, giving a coefficient of correlation of 0.94 revealing a systematic error in LAI and/or measured evapotranspiration data from Mendel (2000). The results indicated that using the same model-specific transpiration parameters for different land uses can be sufficient to reproduce monthly dynamics of evapotranspiration.

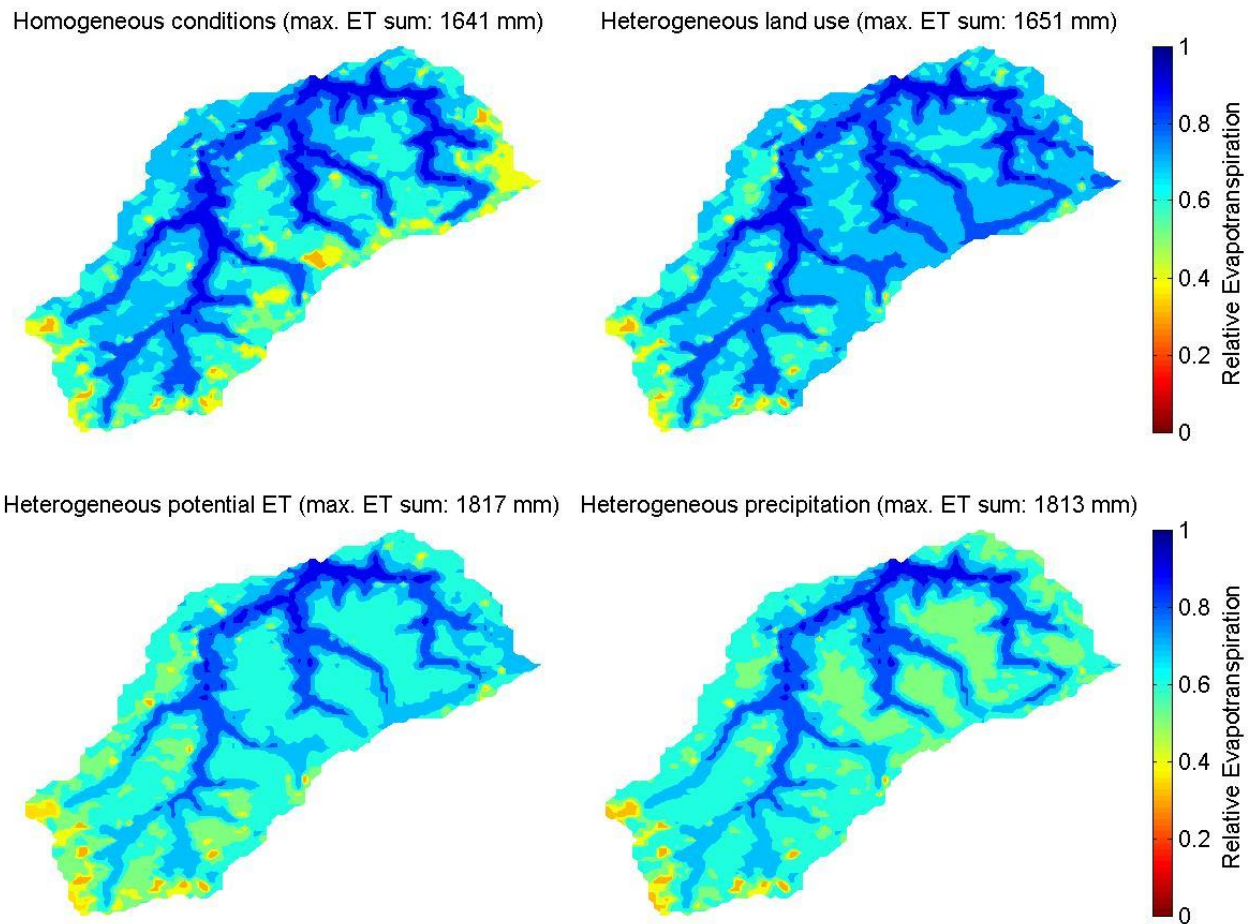


Figure 8.31: Pattern of actual evapotranspiration (ET) for simulations Erk (top left), Erk_LN (top right), Erk_LN_PET (bottom left) and Erk_LN_PET_P (bottom right). Evapotranspiration is given relative to the maximum of the actual evapotranspiration sums of 2010 and 2011 as specified in the brackets.

8.3.3 Influence of HydroGeoSphere version on water balance and soil moisture results at the Wüstebach and the Erkersruhr

In chapter 7.4, it was outlined that the version of HydroGeoSphere used for the Erkersruhr simulation study differed from the version used for the Wüstebach simulations. The new version was necessary because the older version did not support gridded precipitation and potential evapotranspiration input.

The present chapter summarizes differences in water balance and soil moisture between the two HydroGeoSphere versions. The comparison is done for the 100 m setup of the Wüstebach at daily time steps (d100) without bedrock and for the Erkersruhr setup with homogeneous land use, precipitation and potential evapotranspiration (Erk).

In Figure 8.32, the simulated discharge at the **Wüstebach** catchment is compared between the two different model versions so as between simulations and observation. In general, differences in discharge simulation results between model versions were restricted to the autumn

(September to November) in both years. The changes in discharge simulation were also visible in simulated water balance components summarized in Table 8.12. Discharge amount was lower for simulation with newer model version by 57 mm (2010) and 49 mm (2011). In 2010, performance measures listed in Table 8.12 were slightly higher in both years for the newer model version probably caused by improvements in low flow period and peaks discharges in September and October. Due to the correction of a bug (no details given by model developer) in the interception model, interception simulated with the new model version increased by 57 mm (2010) and 52 mm (2011). The corresponding decrease in transpiration overcompensated for this increase with a decrease of 82 mm (2010) and 95 mm (2011). As a result, total actual evapotranspiration amount decreased by 25 mm (2010) and 41 mm (2011). Decreases in total evapotranspiration and discharge amount of 82 (2010) and 90 mm (2011) pointed to differences in soil moisture simulation which are illustrated in Figure 8.33.

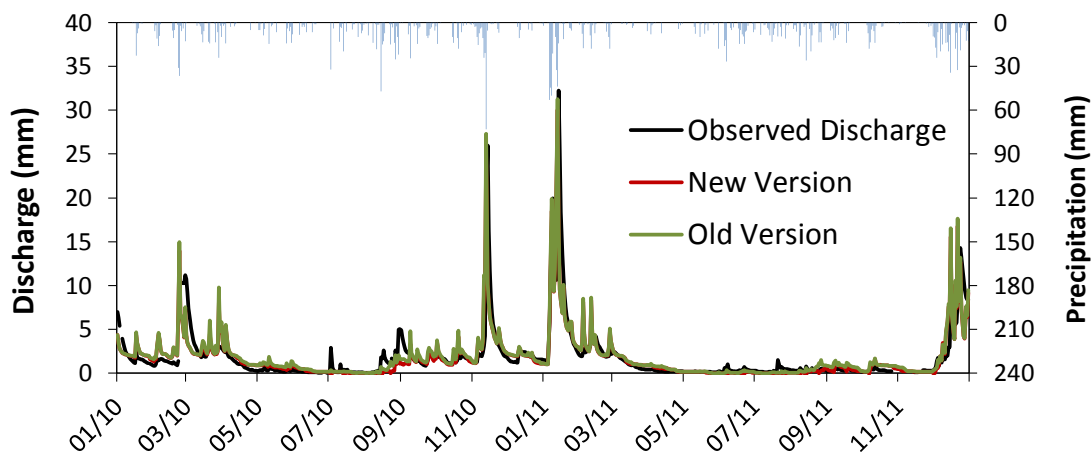


Figure 8.32: Comparison of measured and simulated discharge rates at the Wüstebach catchment with two different model versions.

Soil moisture simulation was highly sensitive to model version. Figure 8.33 shows that short term soil moisture dynamics during autumn and winter intensified at all depths with the new model version in comparison to observations and to results from the old model version. This improvement led to slight increases in the R^2 value at all depths in 2010. Due to the pronounced summer drying, the NSE decreased at all depths in comparison to the old model version (Table 8.13). On the contrary, the strong soil moisture drying during summer 2011 led to general improvement in soil moisture simulation in the new model version, reflected in the increase in R^2 and NSE at all depths in 2011 (Table 8.13). The enhanced soil moisture drying in the summer resulted from increased interception and explained the decreases in transpiration rate and discharge. Pronounced short term soil moisture dynamics during autumn and winter simulated with the new model version were not fully explainable. A difference in the effect of saturated conductivity on infiltration was most likely causing changes in short term soil moisture simulation.

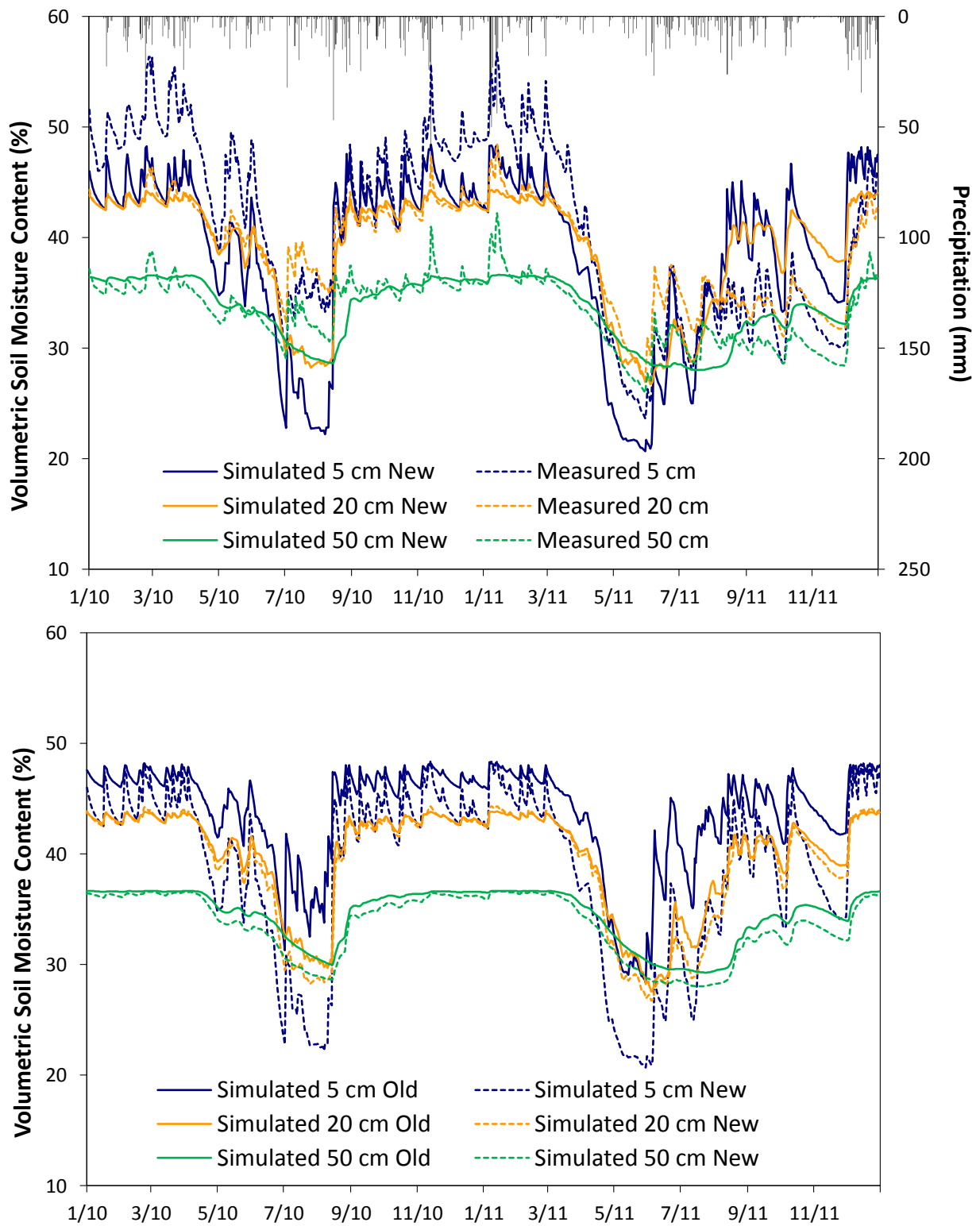


Figure 8.33: Upper part: Observed and simulated daily soil moisture dynamics with the new HydroGeoSphere version. Lower part: Comparison between soil moisture simulated with two different versions.

Table 8.12: Measured and simulated water balance components at the Wüstebach in 2010 and 2011 for two simulations with different model versions.

	2010		2011	
Precipitation (mm/y)	1226		1348	
Measured Discharge (mm/y)	608		630	
Potential Evapotranspiration (mm/y)	694		756	
Actual Evapotranspiration (mm/y)	377 ¹		596	
	Old Version	New Version	Old Version	New Version
Simulated Discharge (mm/y) ²	647	590	651	602
Interception (mm/y)	248	305	247	301
Interception (%)	20	25	18	22
Transpiration (mm/y)	264	182	355	260
Actual Evapotranspiration (mm/y)	512	487	602	561
Coefficient of Determination (-)	0.55	0.57	0.72	0.73
Nash-Sutcliffe Coefficient (-)	0.54	0.57	0.71	0.72
Percent Bias (%)	-6.35	3.00	-3.40	4.43

(¹=Measurements start on May 1st, 2010; ²= Annual sums of simulated discharge exclude time steps with gaps in measured discharge)

Table 8.13: Measures of soil moisture simulation performance at 5, 20 and 50 cm depth for two simulations with different model versions.

	Old Version			New Version		
	2010					
	5 cm	20 cm	50 cm	5 cm	20 cm	50 cm
Coefficient of Determination (-)	0.77	0.75	0.46	0.81	0.78	0.53
Nash-Sutcliffe Coefficient (-)	0.65	0.46	0.34	0.00	-0.12	0.18
	2011					
Coefficient of Determination (-)	0.49	0.41	0.39	0.62	0.51	0.59
Nash-Sutcliffe Coefficient (-)	-0.31	0.19	0.34	0.59	0.29	0.54

In summary, the change in model version has a larger impact on soil moisture simulation than all other investigated influence factors like spatial or temporal discretization (chapter 8.2.2), bedrock inclusion (chapters 8.2.1 and 8.2.2) and the choice of calibration period (chapter 8.2.3). The corrected bug in the interception model explains the different interception amounts which

result in a decrease in discharge, transpiration and mean soil moisture. Unfortunately, the source of this strong deviation in simulation results could not be explained with the version history provided by the model developers. It has to be noted that the reported differences do not deteriorate the general conclusions of chapter 8.2.1 and 8.2.2 that bypass flow and variability in root water uptake could improve simulation results and that the simulation of soil moisture patterns improves with higher spatial model resolution, but is not sensitive to temporal resolution.

In the following, the influence of HydroGeoSphere model version on simulation results for the **Erkensruhr** with the model setup including homogeneous land use, potential evapotranspiration and rainfall (Erk) is described. Figure 8.34 shows simulated discharge of two different model versions and observed discharge. The old version produced higher discharge rates in autumn of both years which indicates differences in soil moisture storages at the end of the summer. During the rest of the years, the differences between model versions were marginal.

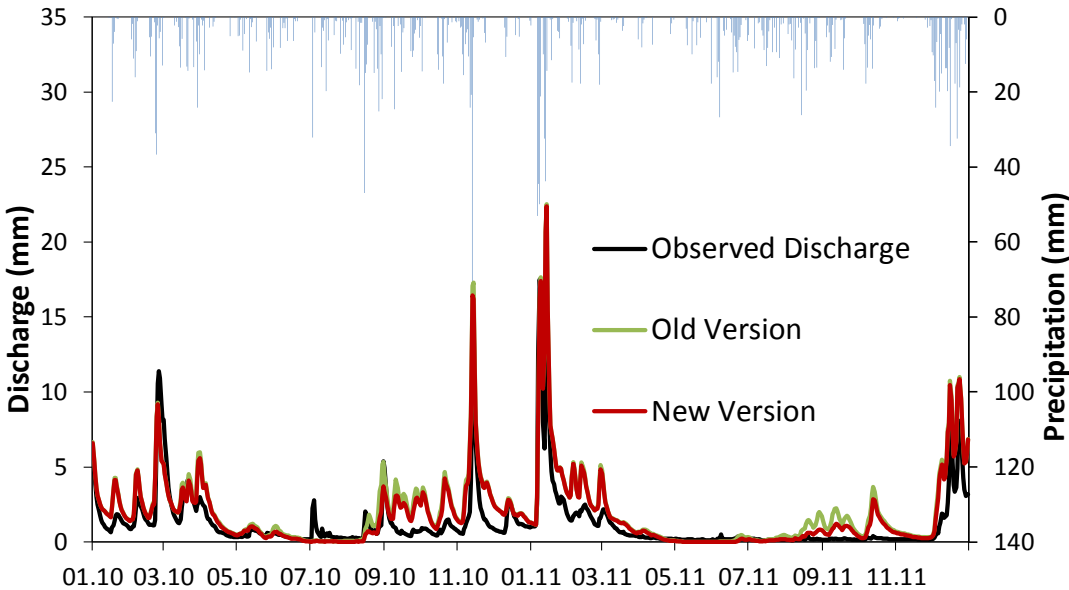


Figure 8.34: Observed and simulated discharge of the Erkensruhr for simulations with the old and new HydroGeoSphere model version.

Table 8.14 compares simulated water balance components between model versions and summarizes measures of discharge performance. Performance measures supported the impression of Figure 8.34 that differences between versions were most pronounced during autumn. In contrast, the coefficient of variation and the correlation coefficient slightly improved for the simulation with the old model version during summer.

Table 8.14: Water balance components for the Erkensruhr in simulations with the old and new HydroGeoSphere model version.

	Erk_old_version		Erk_new_version	
	2010	2011	2010	2011
Rainfall (mm)	1226	1348	1226	1348
Potential ET (mm)	694	756	694	756
Measured Discharge (mm)	524	396	524	396
Transpiration and Evaporation (mm)	327	387	257	306
Interception (mm)	160	166	234	255
Actual Evapotranspiration (mm)	487	553	491	561
Discharge (mm)	786	716	721	654
Exchange Balance (mm)	-47	79	14	133
Discharge Performance Measures				
	Summer	Winter	Summer	Winter
Bias	2.17	1.61	1.61	1.57
Correlation Coefficient	0.50	0.93	0.47	0.93
Coefficient of Variation	1.26	0.80	1.34	0.81

Evapotranspiration components showed larger differences between model versions. Comparable to results from the Wüstebach catchment, the interception amount dropped by 74 mm and 89 mm. This result was expected because the main difference between the versions is a fixed bug in the interception model. The surplus in precipitation into the catchment turned nearly completely to an increase in transpiration. Although the output from evapotranspiration was nearly equal between the model versions, discharge amount increased by 65 mm in 2010 and 62 mm in 2011 which resulted in a difference in the exchange balance (negative values indicate storage withdrawal, positive values storage refill) of 61 mm in 2010 and 54 mm in 2011. This indicated a systematic difference in the simulation of the soil moisture storage.

8.4 Long-term Simulation

This chapter describes results of the long-term simulation of forest growth. In the first part, the influence of different climate data sets on water balance and discharge simulation is investigated for the setups WbachEsoilConi (100 m resolution Wüstebach with Erkensruhr soil data) and Erk (Erkensruhr setup with homogeneous land use and climate conditions). The new climate data set used for the long-term simulation and the original climate data set used for all Wüstebach simulations are applied to both setups. Details about the new climate data set are given in chapter 6.2.2. In the second part, the results of the 50 year long simulation of forest growth performed with the setup WbachEsoilConi are presented. This setup was assumed representative for the Erkensruhr because of the large similarity in discharge dynamics illustrated in chapter 6.2.4.

Table 8.15 compares measured precipitation, calculated potential evapotranspiration sums, resulting simulated actual evapotranspiration and discharge amounts between the original and the new climate data set used for simulations of the Wüstebach (abbreviated as Wbach_Orig and Wbach_Kall) and Erkensruhr (abbreviated as Erk_Orig and Erk_Kall) catchments. In comparison to original climate data, annual precipitation significantly reduced by 144 mm in 2010 and 156 mm in 2011, but potential evapotranspiration only slightly decreased by 13 mm (2010) and 37 mm (2011). At both catchments, the decrease in precipitation resulted in a strong reduction in simulated discharge. Actual evapotranspiration only slightly changed. The Erk_Kall simulation showed a reduction in discharge of 156 mm (2010) and 144 mm (2011) and a change in actual evapotranspiration of 3 mm (2010) and 6 mm (2011). At the Wüstebach catchment, actual evapotranspiration slightly increased by 10 mm (2010) and 5 mm (2011), but discharge decreased by 145 mm (2010) and 142 mm (2011). Compared to observed discharge amounts, the reduction in discharge improved the simulation at the Erkensruhr catchment but deteriorated the discharge simulation at the Wüstebach catchment. This result corresponds to the observation described in chapter 6.2.2 that precipitation rates at the Wüstebach catchment are much higher than those at the Erkensruhr catchment, which is characterized by a marked decrease in precipitation from west to east. As the Wüstebach catchment is in the most western part of the Erkensruhr catchment, precipitation rates in the eastern part of the Erkensruhr are overestimated by approximately 300 mm. As a result, precipitation rates from the Wüstebach used for the Erkensruhr led to an overestimation of simulated discharge at the Erkensruhr outlet (chapter 8.2.2). Decreasing precipitation at both catchments thus reduced quality of the Wüstebach simulation but increased quality of the Erkensruhr simulation.

Figure 8.35 compares discharge curves of the simulations Erk_Orig and Erk_Kall with observed discharge. In compliance with the decrease in measured precipitation, discharge reduced during the whole year for the Erk_Kall simulation, resulting in an overall increase in simulation quality in terms of NSE from 0.55 to 0.68 in 2010 and 0.66 to 0.83 in 2011. The effect of new climate data on simulated discharge at the Wüstebach catchment illustrated in Figure 8.36 is comparable to

the effect at the Erkenruhr catchment with the exception that the reduction in precipitation rate only affected the NSE in 2010 which reduced from 0.57 to 0.46. In contrast to the NSE, the R^2 values were not affected by a change in climate data.

Table 8.15: Measured and simulated water balance components for simulations of the Wüstebach and the Erkenruhr with new and original climate data for 2010 and 2011.

	Erk_Orig		Erk_Kall		WbachOrig		Wbach_Kall	
	2010	2011	2010	2011	2010	2011	2010	2011
Rainfall (mm)	1226	1348	1082	1192	1226	1348	1082	1192
Potential Evapotranspiration (mm)	694	756	681	719	694	756	681	719
Measured Discharge (mm)	524	396	524	396	608	630	608	630
Transpiration (mm)	257	306	264	302	195	247	210	257
Evaporation (mm)	234	255	230	253	247	273	242	269
Actual Evapotranspiration (mm)	491	561	494	555	442	520	452	526
Discharge (mm)	721	654	565	510	647 ¹	652 ¹	502 ¹	510 ¹

¹= Annual sums of simulated discharge exclude time steps with gaps in measured discharge)

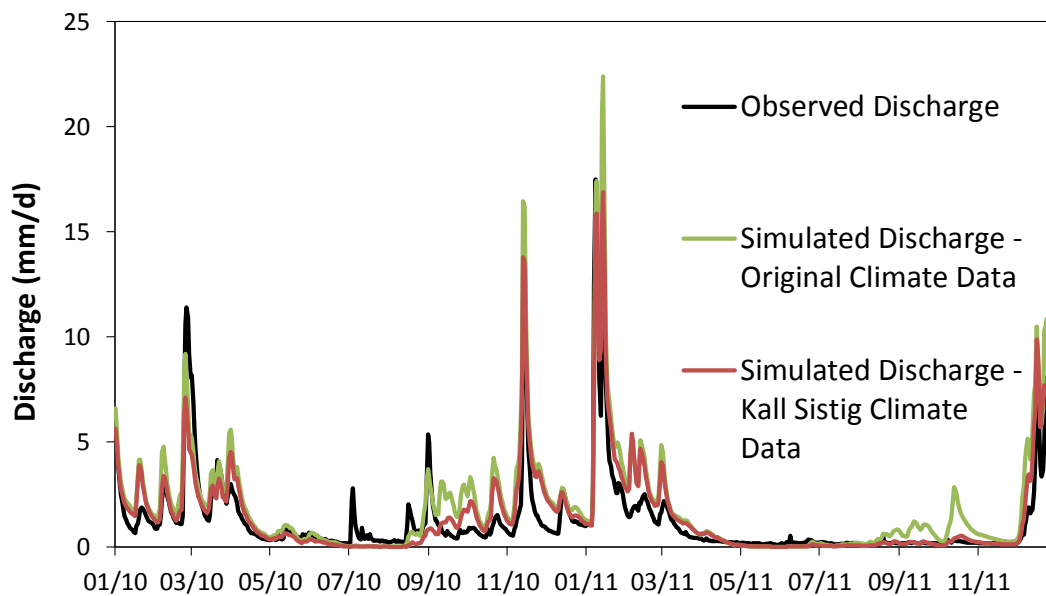


Figure 8.35: Observed and simulated total discharge of the Erk setup for different climate inputs.

In summary, different climate data sets mainly affect total discharge amount but did not deteriorate the simulation of actual evapotranspiration. This result also suggests that the evapotranspiration parameter values can be applied to both climate data sets. A reliable simulation of evapotranspiration and its components is very important for the 50-year long simulation run, especially during the first two decades when LAI is changing rapidly.

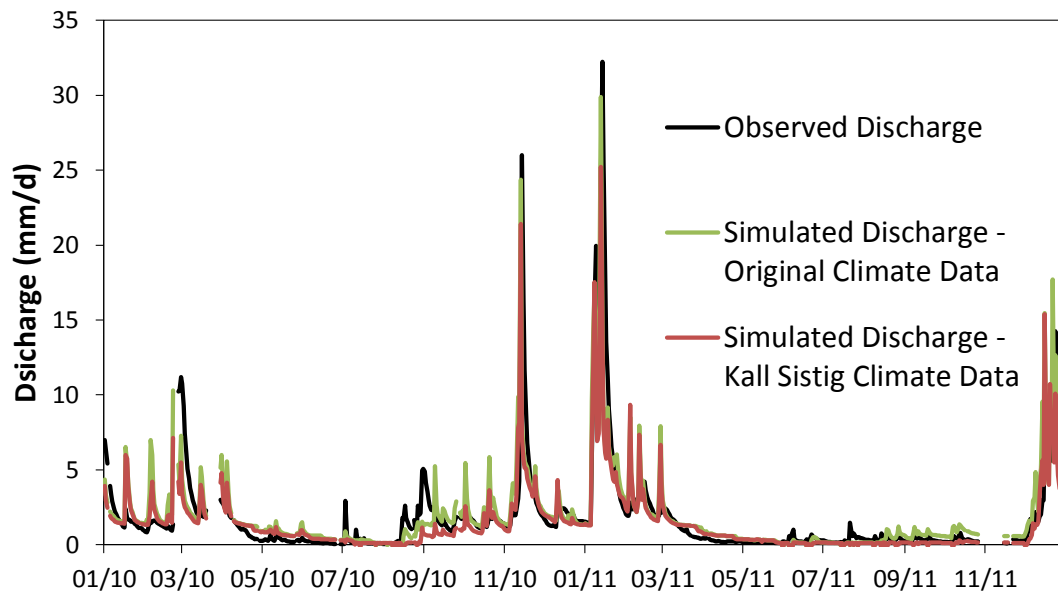


Figure 8.36: Observed and simulated total discharge of the WbachEsoilConi setup for different climate inputs.

First simulations with changing LAI revealed serious problems with the HydroGeoSphere interception routine between 1951 and 1959. The maximum possible interception in 1951 amounts to 29 mm ($\text{LAI of } 0.1 \times \text{canopy storage of } 0.8 \text{ mm} \times \text{number of days in a year}$) which equals a precipitation fraction of 3%. In Figure 8.37, the blue line illustrates simulated interception by the internal model routine. In 1951, interception simulated with the internal routine accounted for 25% of precipitation which equals 237 mm. Interception calculated with the equations given in the official manual (Aquanty, 2013) confirm this simulation result. Thus, internal routine and documented equations compare well, but for a time frame where the calculated interception is obviously false. Panday & Huyakorn (2004) report a different set of interception equations for HydroGeoSphere which led to the expected interception amount of 7 mm equaling a fraction of 0.8%. Between 1960 and 2000, simulated interception fraction was similar for the model output and given equations. As the development of interception during the first decade was neither captured by the model calculation nor by the equations given in the manual, canopy evaporation and ground precipitation were calculated outside HydroGeoSphere following Panday & Huyakorn (2004). For the subsequent model run, canopy storage was set to zero to avoid internal interception calculation; input time series of potential evapotranspiration and precipitation were altered according to calculated canopy evaporation. In addition, the canopy storage parameter was recalculated to match 20% of interception between 1951 and 2000 (dashed line in Figure 8.37).

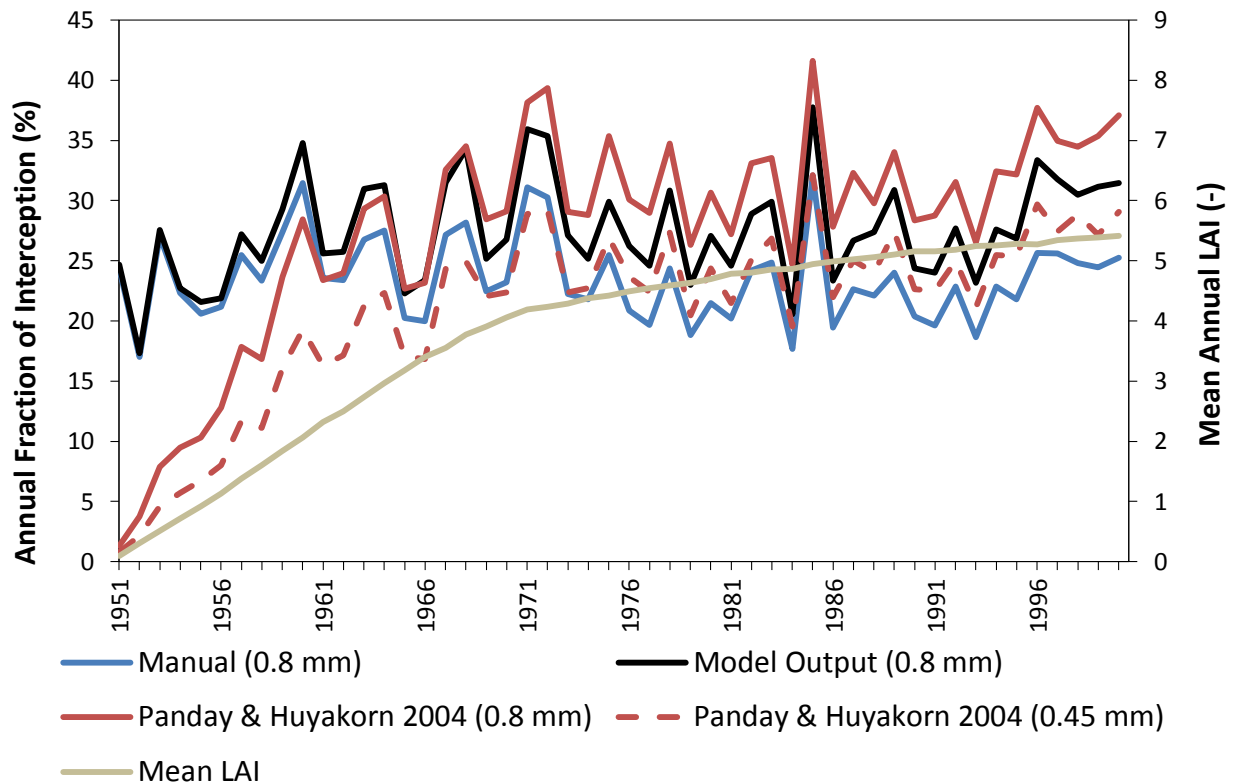


Figure 8.37: Annual fractions of interception between 1951 and 2000 calculated with HydroGeoSphere (black line), the equation given in the model manual (blue line), the equation given in Panday & Huyakorn (2004) with a canopy storage of 0.8 mm (solid red line) and 0.45 mm (dashed red line) and mean LAI (grey line).

It has to be noted that the false interception routine had been already recognized by the author for the HydroGeoSphere version used for the Wüstebach study. The interception routine was not replaced for the Wüstebach simulations because the output of the applied model version was restricted to ground precipitation. Thus, storage changes and canopy evaporation calculated with equations from Panday & Huyakorn (2004) could not be compared to the internal calculation. Based on these restrictions, it was decided to accept the obviously false canopy storage of 1.5 mm per LAI reported in the Wüstebach study (Table 8.2). For the Erkensruhr study, the canopy storage was recalibrated to 0.8 mm and model outputs and internal calculations matched well.

In the following, results of the 50-year simulation of forest growth are reported and discussed. Simulated water balance components and precipitation inputs are given as mean values for five-year periods between 1951 and 2000 in Figure 8.38. Error bars indicate wettest and driest years per 5-year period. Observed precipitation varied between 5-year periods with wettest conditions between 1981 and 1990 (\varnothing 940 mm) and driest conditions between 1971 and 1975 (\varnothing 760 mm), but did not exhibit a clear trend during the 50 years. Corresponding to changes in mean precipitation rates, simulated discharge amounts reached their maximum in the period 1981-1985 with 530 mm and their minimum between 1971 and 1975 with only 260 mm. Trends in

simulated actual evapotranspiration can be divided into two different time intervals that reflect the development of simulated evapotranspiration components and mean annual LAI. The first interval ranged from 1951 to 1965 and the second interval comprised all other years until the end of 2000. During the first interval, precipitation decreased by 90 mm, simulated actual evapotranspiration by 110 m, but discharge increased by 10 mm. In the following years, the amount of actual evapotranspiration increased again by 90 mm, while precipitation increased by only 20 mm and discharge decreased by 80 mm. According to Figure 8.38, mean water balance (storage) values varied between +20 mm (1951-1955) and -29 mm (1991-1995) which means that the model was able to maintain the water balance close to zero with a mean water balance error of 5 mm per year varying between zero (1964) and 8 mm (1961).

Interestingly, the decrease in actual evapotranspiration during the time interval 1951 to 1965 of 100 mm was not due to the decrease in precipitation, but resulted from the change in actual evapotranspiration components. Due to the applied parameterization, ground evaporation decreased very fast during this time frame (by 330 mm) and the increase in transpiration and interception evaporation (110 mm each) was not able to fully compensate for the decrease in ground evaporation.

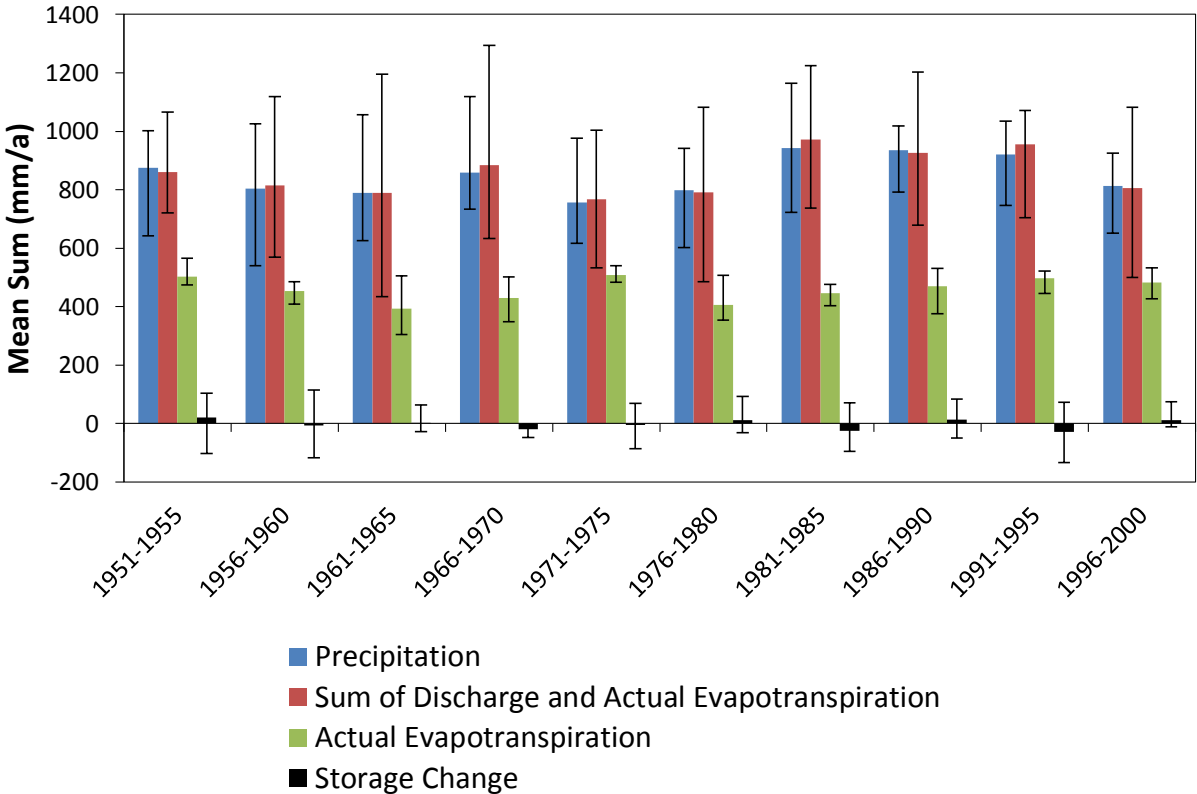


Figure 8.38: Simulated Water balance components per 5-year period of the 50-year simulation with the WbachEsoilConi setup. Error bars indicate maximum and minimum values during a five-year period.

The development of simulated evapotranspiration components and LAI is illustrated in **Figure 8.39** as mean values for five-year periods with error bars indicating minimum and maximum values per period. In the first five years, ground evaporation was the major evapotranspiration component and rapidly decreased until it reached zero in 1963. This development was expected by theoretical reflections in chapter 7.3.1. Simulated transpiration and interception evaporation showed a logistic growth comparable to that of the LAI. Transpiration amount exhibited large variation during five year periods, for example a variation of 90 mm between 1976 and 1980. The fraction of interception evaporation showed a constant increase during the simulation period.

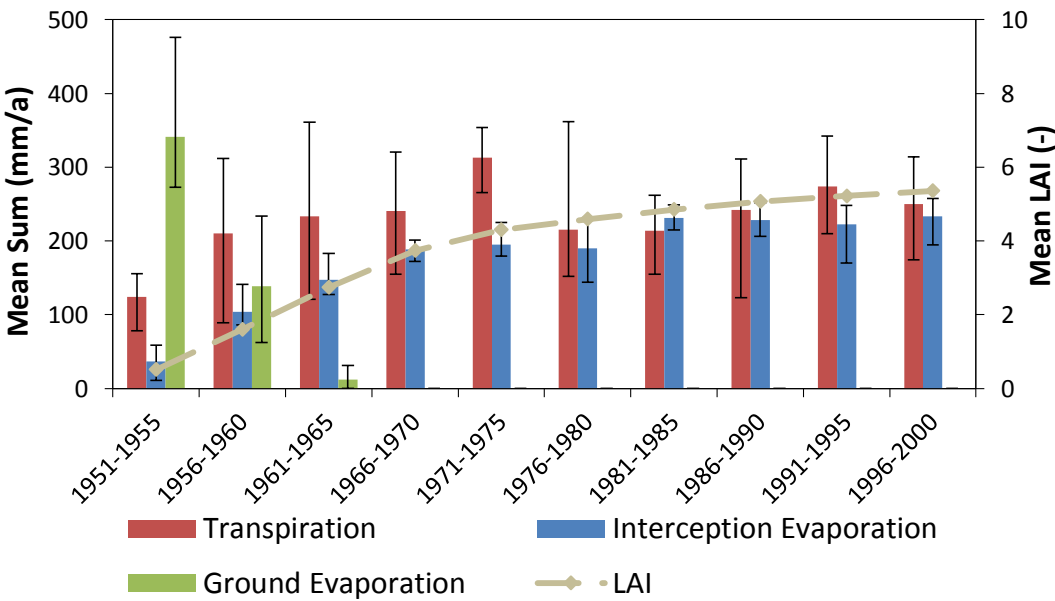


Figure 8.39: Actual evapotranspiration components and mean LAI per 5-year period between 1951 and 2000. Error bars indicate maximum and minimum values during a five-year period.

The long-term simulation exhibits years with pronounced drying characterized by a decrease in discharge below 100 mm. In Figure 8.40, the simulated water balance components, the simulated storage change and the measured discharge for the drying period between 1971 and 1973 are given. These years were selected because the addressed effect is most distinct. In 1971, precipitation rate dropped to 620 mm while actual evapotranspiration and discharge summed up to 700 mm, thus emptying soil moisture storage as illustrated in the negative storage change in Figure 8.40. In the following year, 1972, precipitation replenished soil moisture storage reducing discharge to 50 mm while actual evapotranspiration remained equally high. In 1973, discharge rate increased again due to the replenished soil moisture storage and due to increased precipitation (860 mm). Measured discharge rates from the Erkensruhr outlet did not drop below 100 mm but showed the same trend as the simulation.

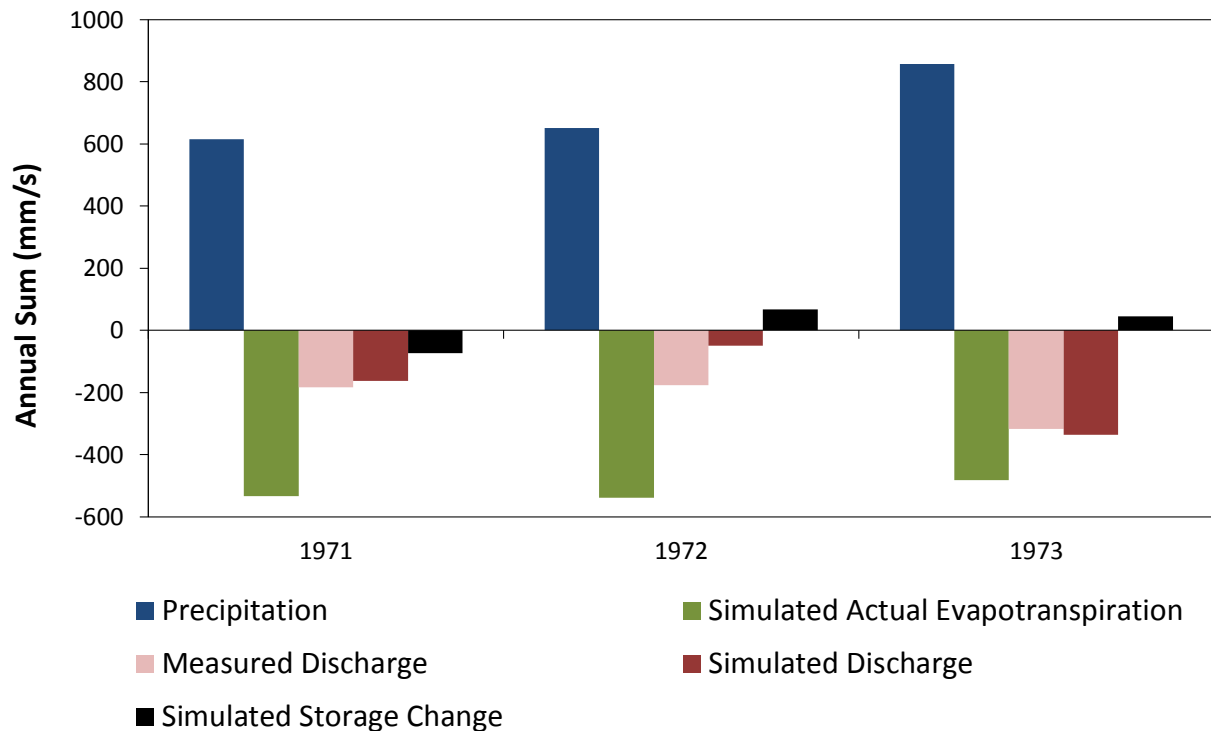


Figure 8.40: Simulated water balance components and measured discharge amount between 1970 and 1973.

Last but not least, Figure 8.41 compares measured discharge rates from the Erkensruhr outlet to simulated discharge rates which were upscaled from the Wüstebach to the Erkensruhr catchment (refer to chapter 6.2.4 for upscaling method). The figure clearly illustrates the close connection between precipitation and discharge rates which was well captured by the model. For the first two five-year periods, simulated and measured discharge rates compared very well with a mean deviation of only 20 mm. From 1971, deviations between simulation and measurements were higher with a mean value of 70 mm and a range of 50 to 130 mm.

In summary, the conducted simulation revealed a potential of HydroGeoSphere to simulate discharge dynamics and to sustain a balance between inputs (precipitation) and outputs (discharge and evapotranspiration) without drying or wetting trend over a 50-year long period. The simulation of evapotranspiration components currently suffers from the problems of the internal interception routine and from missing calibration of ground evaporation parameters.

Studies reporting measurements or simulation results following reforestation periods are rarely found. The need for a long-term continuous measurement of discharge and precipitation is the major restriction for reforestation experiments and makes deforestation studies easier to conduct (Robinson et al., 1991).

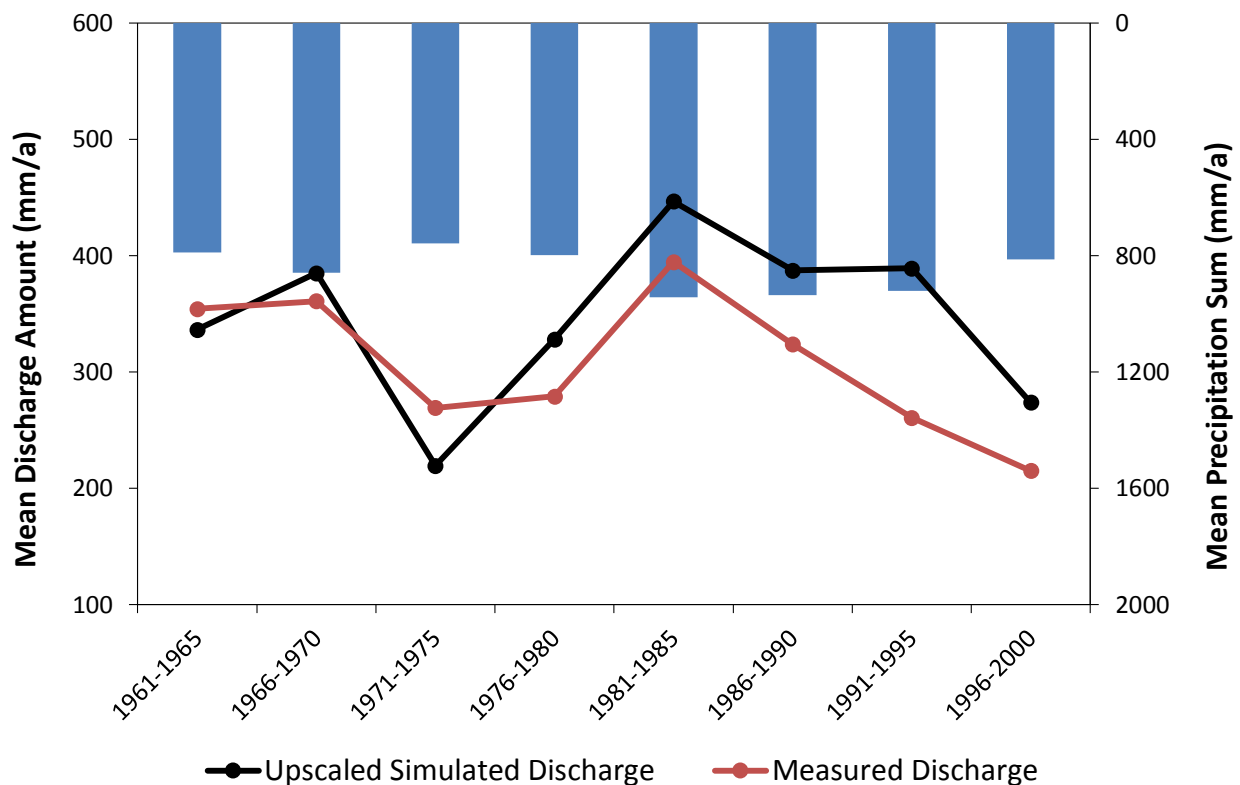


Figure 8.41: Comparison of upscaled simulated discharge to measured discharge amount between 1961 and 2000.

Andréassian (2004) summarized results from available studies on deforestation and afforestation and reported over 56 deforestation sites but only 15 afforestation experiments. Six of these have been reforested with coniferous trees and were undertaken on small experimental plots with a maximum size of 2.9 km² which is approximately 10% of the Erkensruhr catchment. For example, Robinson et al. (1991) presented water balance measurement results between 1971 and 1989 for an afforestation experiment of two formerly agriculturally used high moor fields near the Chiemsee in Germany. For a tree stand planted in 1969, they found a decrease in runoff by 40 %, an attenuation of peak flows, lower percolation and reduced storm runoffs. Similarly, Hudson et al. (1997) observed a decrease in discharge fraction by 19% over a 9-year period of spruce forest growth. Both studies agreed on the very high fraction of discharge directly after reforestation began. This is in contrast to the simulation results presented in this thesis. The difference might be due to the parameters of ground evaporation. Despite the broad data base at the Wüstebach, estimations of ground evaporation and transpiration fractions were not available and thus ground evaporation parameters were not calibrated. The lack of calibration can explain the very high amount of simulated ground evaporation during the first decade that overcompensated the dampening effect of low LAI on transpiration and interception.

Due to difficulties in finding a sufficient data base, simulation studies on the effects of reforestation are even rarer than measured water balance values. Recently, Salazar et al. (2013)

simulated mean annual water balance over 9 years for spruce stands with different age and found that the oldest stand (LAI of 7.8) had a lower discharge fraction of 16% in comparison to 25% at the youngest stand (LAI of 2.9). The impression that actual evapotranspiration increased with forest age, was approved by a 35-year long simulation with repeated climate cycles where spruce trees exhibited a linear increasing trend in actual evapotranspiration. These observations were in line with results from the Erkensruhr simulations.

In summary, an adjustment of the ground evaporation parameters was suggested by the finding of Robinson et al. (1991) and Hudson et al. (1997). Simulated development of the fraction of actual evapotranspiration at the Erkensruhr was in line with results of Hudson et al. (1997) and Salazar et al. (2013) when ground evaporation vanished. The comparison of measured to simulated discharge rates also indicated a systematic overestimation of discharge which was either due to low evapotranspiration or – comparable to results of the Erkensruhr simulations shown in chapter 8.3.2 – to overestimated precipitation inputs.

9 Conclusion and Outlook

In this thesis, headwater scale 3D-hydrological simulations with the model HydroGeoSphere, parameter regionalization and model validation with a 50-year long simulation for a mesoscale catchment were used to reveal potentials and limitations in the simulation of **soil moisture dynamics and patterns** and **unsaturated flow dynamics** at different spatial and temporal scales.

The applied methodology allowed (1) to identify a great potential of distributed hydrological models in simulating soil moisture patterns and dynamics, (2) to demonstrate that high spatial resolution is important for the simulation of soil moisture patterns but not for soil moisture dynamics, (3) to reveal the lack of bypass flow as a major limitation of model structure for the simulation of subsoil moisture dynamics, (4) to highlight the benefit of high-resolution hydrological simulations for parameter estimation of larger catchments by transferring calibrated evapotranspiration parameters, (5) to point out that a precipitation pattern is more important than other spatial input data for the simulation of discharge and (6) to show that the applied model is able to sustain a water balance closure among decades.

The broad data base available for this thesis allowed for the unique opportunity to compare simulated and measured soil moisture dynamics over a continuous time period of two years. Simulations of **soil moisture dynamics** agreed well with measured soil moisture dynamics, especially at 20 cm depth where some simulated peaks fully matched measured soil moisture peaks. Application of the 3D distributed model HydroGeoSphere at different spatial and temporal resolutions allowed to observe a small scale dependency in soil moisture dynamics resulting from weak spatial and temporal scale dependency of calibration parameters. The comparison of measured with simulated relationships between mean soil moisture and its standard deviation showed that the simulation did not reach the drying arm of the relationship. This indicated insufficient variability in root water uptake and evaporation although spatial variability of transpiration is represented in the model by its dependency on the distribution of soil moisture and soil properties.

In the investigated setups of HydroGeoSphere, fast subsurface flow originated from lateral soil matrix flow thus ignoring fast subsurface runoff induced by bypass flow. Missing bypass flow was visible in a lack of short term soil moisture dynamics especially at greater depths from 50 cm on. Due to large uncertainties in the parameterization of the macropore flow module implemented in HydroGeoSphere, the effect of missing macropore flow could not be quantified.

In contrast to soil moisture dynamics, **soil moisture patterns** simulated for the Wüstebach catchment exhibited larger differentiation in soil moisture at higher resolution. Although the higher resolution resulted in an improved soil moisture pattern, the comparison of simulated to measured soil moisture patterns generally showed limited agreement apart from river source

areas. A Spearman correlation analysis of measured and simulated soil moisture patterns to slope, porosity and relative elevation patterns revealed reasons for the insufficient match. Unlike simulated soil moisture patterns, measured soil moisture patterns showed no strong correlation to slope, porosity or relative elevation. This result allowed the interpretation that the model does not incorporate enough variability in state variables to simulate soil moisture patterns. At hourly time steps, soil moisture dynamics exhibit hysteresis cycles, which are most likely controlled by spatial variability in interception. Unfortunately, the spatial resolution of the model was not sufficient to represent these patterns resulting in a lack of hysteresis in soil moisture simulation at hourly time steps.

Unsaturated flow dynamics were generally well captured with all simulation runs. At the Wüstebach catchment discharge simulations agreed well with measured discharge dynamics regardless of spatial and temporal resolution. The model simulated the dominance of subsurface flow (which had been proven for forested catchments) independently of temporal and spatial resolution.

Using regionalized evapotranspiration parameters, discharge dynamics and monthly evapotranspiration for three different land use types (coniferous, deciduous forest and grassland) were well simulated at the mesoscale catchment. The good fit in monthly evapotranspiration highlighted the potential of using parameters from high-resolution simulations for the simulation of large scale catchments. A 50-year long simulation of forest growth captured annual and decadal discharge variability and did not exhibit any drying or wetting trend over the simulation period. Simulated development of evapotranspiration components agreed well with previous findings except for the first decade when ground evaporation reached very high values. This was due to missing calibration (resulting from lack of measurements) of ground evaporation parameters at the Wüstebach catchment.

At the Erkensruhr catchment, the major challenge was the adequate representation of spatial variability in land use, precipitation and potential evapotranspiration and not the representation of soil moisture patterns as was done at the Wüstebach catchment. The step-wise introduction of spatial variability in soil, land use, potential evapotranspiration and precipitation into the Erkensruhr model setup revealed distributed precipitation as the most important and distributed potential evapotranspiration as the least important of all spatial input patterns.

From a **methodological** point of view, simulation results at the Erkensruhr catchment clearly indicated that the direct transfer of parameters calibrated at a heavily instrumented test site to a mesoscale catchment is a promising alternative to classical calibration against runoff discharge and to statistically driven regionalization techniques. Simulations comparing the impact of different model versions and calibration periods on the simulation of unsaturated flow dynamics revealed large uncertainty arising from the employed model version. Unlike calibration period which had a minor effect on simulation quality and parameter values, the choice of model

version had a significant impact on the simulation of short term topsoil moisture dynamics and a minor effect on short term moisture at greater depths. In addition, the 50-year long simulation revealed bugs in the model internal calculation and/or output of the interception module, requiring the replacement of the model internal calculation routine with external calculations.

In summary, this thesis is a significant contribution to the question of potentials and limitations of high resolution unsaturated flow and soil moisture simulations with distributed hydrological models and to the challenges of parameter regionalization and model validation. Results (1) showed that distributed models support high-quality simulation of soil moisture dynamics, (2) identified bypass flow as the major source for improving simulation of soil moisture dynamics, (3) illustrated that the simulation of soil moisture patterns benefits from higher spatial model resolution, (4) highlighted that additional knowledge about drivers of soil moisture patterns and their interconnection is important for the improvement of distributed soil moisture modeling, and (5) stressed that the transfer of calibrated parameters from high-resolution hydrological simulations at small catchments is a promising method for parameters estimation of mesoscale catchments.

Based on the results of this study, it is recommended to use test sites similar to the Wüstebach catchment for different land use classes in order to enable high-resolution distributed hydrological simulation and to support parameter regionalization. A further assessment of the applied regionalization method, for example by comparing it to other approaches like multiple linear regression, is also proposed. Furthermore, it is necessary to incorporate more spatial heterogeneity into the high-resolution simulation to explore drivers of soil moisture. With estimates of transpiration – e.g. provided by sap-flux measurements - , all evapotranspiration components could be quantified, thus reducing uncertainties about transpiration and ground evaporation parameters. In addition, a model advancement concerning the incorporation of bypass flow to improve the simulation of unsaturated flow and soil moisture dynamics is strongly advocated.

10 Bibliography

- Aitken, A.P., 1973. Assessing systematic errors in rainfall-runoff models. *J. Hydrol.* 20, 121-136. doi:10.1016/0022-1694(73)90035-8
- Ala-aho, P., Rossi, P.M., Isokangas, E., Kløve, B., 2015. Fully integrated surface–subsurface flow modelling of groundwater–lake interaction in an esker aquifer: Model verification with stable isotopes and airborne thermal imaging. *J. Hydrol.* 522, 391–406. doi:10.1016/j.jhydrol.2014.12.054
- Allen, R.G., Pereira, L.S., Raes, D., Smith, M., 1998. FAO Irrigation and drainage paper No. 56. Rome Food Agric. Organ. U. N. 26–40.
- Anderson, M.G., Burt, T.P., 1990. Subsurface runoff. in: Anderson, M.G., Burt, T.P. (Eds.), *Process Studies in Hillslope Hydrology*. Wiley, Chichester, pp. 365-400.
- Anderson, M.G., Brooks, S.M., 1996. Hillslope Processes: Research Prospects. in: Anderson, M.G., Brooks, S.M. (Eds.), *Advances in Hillslope Processes*. Wiley, Chichester, pp. 5-32.
- Anderson, M.G., Bates, P.D., 2001. Hydrological Science: Model Credibility and Scientific Integrity. in: Anderson, M.G., Bates, P.D. (Eds.), *Model Validation: Perspectives in Hydrological Science*. Wiley, Chichester, pp. 1-10.
- Andréassian, V., 2004. Waters and forests: from historical controversy to scientific debate. *J. Hydrol.* 291, 1–27. doi:10.1016/j.jhydrol.2003.12.015
- Aquanty, 2013. HGS 2013: HydroGeoSphere - User Manual. Waterloo.
- Armbruster, M., Seegert, J., Feger, K.-H., 2004. Effects of changes in tree species composition on water flow dynamics–Model applications and their limitations. *Plant Soil.* 264, 13–24. doi:10.1023/B:PLSO.0000047716.45245.23
- Arnaud, P., Bouvier, C., Cisneros, L., Dominguez, R., 2002. Influence of rainfall spatial variability on flood prediction. *J. Hydrol.* 260, 216–230.
- Arnold, J.G., Srinivasan, R., Muttiah, R.S. Williams, J.R., 1998. Large area hydrologic modelling and assessment. Part I: Model development. *J. Am. Water Resour. As.* 34, 73-89. doi:10.1111/j.1752-1688.1998.tb05961.x
- Banks, E.W., Brunner, P., Simmons, C.T., 2011. Vegetation controls on variably saturated processes between surface water and groundwater and their impact on the state of connection. *Water Resour. Res.* 47, W11517. doi:10.1029/2011WR010544
- Bao, Z., Zhang, J., Liu, J., Fu, G., Wang, G., He, R., Yan, X., Jin, J., Liu, H., 2012. Comparison of regionalization approaches based on regression and similarity for predictions in ungauged catchments under multiple hydro-climatic conditions. *J. Hydrol.* 466-467, 37–46. doi:10.1016/j.jhydrol.2012.07.048
- Beckers, J., Smerdon, B., Wilson, M., 2009. Review of Hydrologic Models for Forest Management and Climate Change Applications in British Columbia and Alberta Forrex Forum, Forrex Forum for Research and Extension in Natural Resources. Forrex, Kamloops.
- Bergström, S., 1976. Development and application of a conceptual runoff model for Scandinavian catchments. SMHI Reports RH, No. 7, Norrköping, Sweden.
- Bernhofer, C., Aubinet, M., Clement, R., Grelle, A., Grünwald, T., Ibrom, A., Jarvis, P., Rebmann, C., Schulze, E.-D., Tenhunen, J.D., 2003. Spruce Forests (Norway and Sitka Spruce, Including Douglas Fir): Carbon and Water Fluxes and Balances, Ecological and Ecophysiological Determinants, in: Valentini, R. (Ed.), *Fluxes of Carbon, Water and Energy of European Forests*. Springer Berlin Heidelberg, Berlin, Heidelberg, pp. 99–123.

- Beven, K.J., Kirkby, M.J., 1979. A physically based, variable contributing area model of basin hydrology / Un modèle à base physique de zone d'appel variable de l'hydrologie du bassin versant. *Hydrol. Sci. Bull.* 24, 43–69. doi:10.1080/02626667909491834
- Beven K.J., Binley, A.M., 1992. The future of distributed models: model calibration and uncertainty prediction. *Hydrol. Process.* 6, 279–298. doi:10.1002/hyp.3360060305
- Beven, K.J., 2001. *Rainfall-runoff modelling - The Primer*. Wiley, Chichester.
- Beven, K., Binley, A., 2013. GLUE: 20 years on. *Hydrol. Process.* 28, 5897–5918. doi:10.1002/hyp.10082
- Blöschl, G., Sivapalan, M., 1995. Scale issues in hydrological modelling: a review. *Hydrol. Process.* 9, 251–290. doi:10.1002/hyp.3360090305
- Blöschl, G., 2001. Scaling in hydrology. *Hydrol. Process.* 15, 709–711. doi:10.1002/hyp.432
- Blöschl, G., Grayson, R., 2001. Spatial Observations and Interpolation. in: Grayson, R., Blöschl, G. (Eds.), *Spatial patterns in catchment hydrology: observations and modelling*. Cambridge University Press, Cambridge, pp 17-50.
- Blume, T., Zehe, E., Bronstert, A., 2009. Use of soil moisture dynamics and patterns at different spatio-temporal scales for the investigation of subsurface flow processes. *Hydrol. Earth Syst. Sci.* 13, 1215. doi:10.5194/hess-13-1215-2009
- Bogena, H.R., Huisman, J.A., Oberdörster, C., Vereecken, H., 2007. Evaluation of a low-cost soil water content sensor for wireless network applications. *J. Hydrol.* 344, 32–42. doi:10.1016/j.jhydrol.2007.06.032.
- Bogena, H.R., Herbst, M., Huisman, J.A., Rosenbaum, U., Weuthen, A., Vereecken, H., 2010. Potential of Wireless Sensor Networks for Measuring Soil Water Content Variability. *Vadose Zone J.* 1002–1013. doi:10.2136/vzj2009.0173
- Bogena, H.R., Huisman, J.A., Baatz, R., Hendricks Franssen, H.-J., Vereecken, H., 2013. Accuracy of the cosmic-ray soil water content probe in humid forest ecosystems: The worst case scenario: Cosmic-Ray Probe in Humid Forested Ecosystems. *Water Resour. Res.* 49, 5778–5791. doi:10.1002/wrcr.20463
- Borchardt, H., 2012. Einfluss periglazialer Deckschichten auf Abflusssteuerung am Beispiel des anthropogen überprägten Wüstebaches (Nationalpark Eifel). RWTH Aachen, Aachen. <http://darwin.bth.rwth-aachen.de/opus3/volltexte/2013/4567/>
- Bormann, H., Diekkrüger, B., Richter, O., 1999. Effects of spatial data resolution on the calculation of regional water balances. in: Diekkrüger, B., Kirkby, M., Schröder, U. (Eds.), *Regionalization in Hydrology*, IAHS-Publication 254, 193-202.
- Bormann, H., Diekkrüger, B., 2004. A conceptual, regional hydrological model for Benin (West Africa): validation, uncertainty assessment and assessment of applicability for environmental change analyses. *Phys. Chem. Earth Parts ABC* 29, 759–768. doi:10.1016/j.pce.2004.05.003
- Bormann, H., Breuer, L., Gräff, T., Huisman, J.A., 2007. Analysing the effects of soil properties changes associated with land use changes on the simulated water balance: A comparison of three hydrological catchment models for scenario analysis. *Ecol. Model.* 209, 29–40. doi:10.1016/j.ecolmodel.2007.07.004
- Bossa, A.Y., Diekkrüger, B., 2012. Estimating scale effects of catchment properties on modeling soil and water degradation. in: Seppelt, R., Voinov, A.A., Lange, S., Bankamp, D. (Eds.), *International Environmental Modelling and Software Society (iEMSS) 2012: International Congress on Environmental Modelling and Software. Managing Resources of a Limited Planet: Pathways and Visions under Uncertainty*, Sixth Biennial Meeting, Leipzig, Germany. <http://www.iemss.org/society/index.php/iemss-2012-proceedings>. ISBN: 978-88-9035-742-8
- Brakensiek, D.L., Rawls, W.J., 1994. Soil containing rock fragments: effects on infiltration. *Catena* 23, 99–110. doi:10.1016/0341-8162(94)90056-6

- Brammer, D.D., McDonnell, J.J., 1996. An Evolving Perceptual Model of Hillslope Flow at the Maimai Catchment. in: Anderson, M.G., Brooks, S.M. (Eds.), *Advances in Hillslope Processes*. Wiley, Chichester, pp. 35–60.
- Breuer, L., Eckhardt, K., Frede, H.-G., 2003. Plant parameter values for models in temperate climates. *Ecol. Model.* 169, 237–293. doi:10.1016/S0304-3800(03)00274-6.
- Bronstert, A., 1994. Modellierung der Abflussbildung und der Bodenwasserdynamik von Hängen., *Mitteilungen des Instituts für Hydrologie und Wasserwirtschaft der TU Karlsruhe*. Institut für Hydrologie und Wasserwirtschaft, Karlsruhe.
- Brunner, P., Cook, P.G., Simmons, C.T., 2009a. Hydrogeologic controls on disconnection between surface water and groundwater. *Water Resour. Res.* 45, W01422. doi:10.1029/2008wr006953,2009
- Brunner, P., Simmons, C.T., Cook, P.G., 2009b. Spatial and temporal aspects of the transition from connection to disconnection between rivers, lakes and groundwater. *J. Hydrol.* 376, 159–169. doi:10.1016/j.jhydrol.2009.07.023
- Camporese, M., Paniconi, C., Putti, M., Orlandini, S., 2010. Surface-subsurface flow modeling with path-based runoff routing, boundary condition-based coupling, and assimilation of multisource observation data. *Water Resour. Res.* 46, W02512. doi:10.1029/2008WR007536
- Castillo, A., Castelli, F., Entekhabi, D., 2015. An entropy-based measure of hydrologic complexity and its applications. *Water Resour. Res.* 51, 5145–5160. doi:10.1002/2014WR016035
- Chanson, H., 2001. *The hydraulics of open channel flow: an introduction*, 2nd ed. Elsevier, Amsterdam.
- Clark, M.P., Rupp, D.E., Woods, R.A., Tromp-van Meerveld, H.J., Peters, N.E., Freer, J.E., 2009. Consistency between hydrological models and field observations: linking processes at the hillslope scale to hydrological responses at the watershed scale. *Hydrol. Process.* 23, 311–319. doi:10.1002/hyp.7154
- Cornelissen, T., Diekkrüger, B., Giertz, S., 2013. A comparison of hydrological models for assessing the impact of land use and climate change on discharge in a tropical catchment. *J. Hydrol.* 498, 221–236. doi:10.1016/j.jhydrol.2013.06.016
- Cornelissen, T., Diekkrüger, B., Bogena, H.R., 2014. Significance of scale and lower boundary condition in the 3D simulation of hydrological processes and soil moisture variability in a forested headwater catchment. *J. Hydrol.* 516, 140–153. doi:10.1016/j.jhydrol.2014.01.060
- Cornelissen, T., Diekkrüger, B., Bogena, H.R. Transferring small scale parameterization to improve mesoscale catchment modelling. Submitted to *J. Hydrol* in August 2015.
- Dannowski, M., Wurbs, A., 2003. Spatial differentiated representation of maximum rooting depths of different plant communities on a field wood-area of the Northeast German Lowland. *Die Bodenkultur* 54, 93-108. <https://diebodenkultur.boku.ac.at/volltexte/band-54/heft-2/dannowski.pdf>.
- Davie, T., 2008. *Fundamentals of hydrology*, 2nd ed. Routledge, London.
- Deutsch, C.V., Journel, A.G., 1998. *GSLIB: Geostatistical Software Library and User's Guide*, 2nd ed. Oxford University Press.
- Diekkrüger, B., Söndgerath, D., Kersebaum, K.C., McVoy, C.W., 1995. Validity of agroecosystem models a comparison of results of different models applied to the same data set. *Ecol. Model.* 81, 3–29. doi:10.1016/0304-3800(94)00157-D
- Diekkrüger, B., 2003. Upscaling of Hydrological Models by Means of Parameter Aggregation Technique, in: Neugebauer, H.J., Simmer, C. (Eds.), *Dynamics of Multiscale Earth Systems*. Springer Berlin Heidelberg, Berlin, Heidelberg, pp. 145–165.

- Doble, R., Brunner, P., McCallum, J., Cook, P.G., 2011. An analysis of river bank slope and unsaturated flow effects on bank storage. *Ground Water* 50, 77–86.
doi:10.1111/j.1745-6584.2011.00821.x
- Drüe, C., Graf, A., Heinemann, G., Pütz, T., 2012. Observation of atmosphere-forest exchange processes at the new TERENO site Wüstebach. Presented at 20th Symposium on Boundary Layers and Turbulence, Boston, Mass, 9–13 Jul, AMS (American Meteorological Society).
<https://ams.confex.com/ams/20BLT18AirSea/webprogram/Paper209279.html>
- Dye, H.B., Houston, S.L., Welfert, B.D., 2011. Influence of Unsaturated Soil Properties Uncertainty on Moisture Flow Modeling. *Geotech. Geol. Eng.* 29, 161–169.
doi:10.1007/s10706-009-9281-0
- Ebel, B.A., Mirus, B.B., Heppner, C.S., VanderKwaak, J.E., Loague, K., 2009. First-order exchange coefficient coupling for simulating surface water–groundwater interactions: parameter sensitivity and consistency with a physics-based approach. *Hydrol. Process.* 23, 1949–1959. doi:10.1002/hyp.7279
- Famiglietti, J.S., Rudnicki, J.W., Rodell, M., 1998. Variability in surface moisture content along a hillslope transect: Rattlesnake Hill, Texas. *J. Hydrol.* 210, 259–281.
doi:10.1016/S0022-1694(98)00187-5
- Famiglietti, J.S., Ryu, D., Berg, A.A., Rodell, M., Jackson, T.J., 2008. Field observations of soil moisture variability across scales. *Water Resour. Res.* 44, W01423.
doi:10.1029/2006WR005804
- Fang, Z., Bogena, H., Kollet, S., Koch, J., Vereecken, H., 2015. Spatio-temporal validation of long-term 3D hydrological simulations of a forested catchment using empirical orthogonal functions and wavelet coherence analysis. *J. Hydrol.* 529, 1754–1767.
doi:10.1016/j.jhydrol.2015.08.011
- Fetter, C.W., 2001. *Applied Hydrogeology*, 4th ed. Prentice Hall, Upper Saddle River, New Jersey, USA.
- Freeze, R.A., Harlan, R.L., 1969. Blueprint for a physically-based digitally simulated hydrologic response model. *J. Hydrol.* 9, 237–258.
doi:10.1016/0022-1694(69)90020-1
- Frei, S., Fleckenstein, J.H., 2014. Representing effects of micro-topography on runoff generation and sub-surface flow patterns by using superficial rill/depression storage height variations. *Environ. Model. Softw.* 52, 5–18. doi:10.1016/j.envsoft.2013.10.007
- Furman, A., 2008. Modeling Coupled Surface–Subsurface Flow Processes: A Review. *Vadose Zone J.* 7, 741. doi:10.2136/vzj2007.0065
- Gandolfi, C., Facchi, A., Maggi, D., 2006. Comparison of 1D models of water flow in unsaturated soils. *Environ. Model. Softw.* 21, 1759–1764.
doi:10.1016/j.envsoft.2006.04.004
- Gerke, H.H., van Genuchten, M.T., 1993. A dual-porosity model for simulating the preferential movement of water and solutes in structured porous media. *Water Resour. Res.* 29, 305–319. doi:10.1029/92WR02339
- Goderniaux, P., Brouyère, S., Fowler, H.J., Blenkinsop, S., Therrien, R., Orban, P., Dassargues, A., 2009. Large scale surface–subsurface hydrological model to assess climate change impacts on groundwater reserves. *J. Hydrol.* 373, 122–138.
doi:10.1016/j.jhydrol.2009.04.017
- Graf, A., Bogena, H.R., Drüe, C., Hardelauf, H., Pütz, T., Heinemann, G., Vereecken, H., 2014. Spatiotemporal relations between water budget components and soil water content in a forested tributary catchment. *Water Resour. Res.* 50, 4837–4857.
doi:10.1002/2013WR014516

- Graham, D.N., Butts, M.B., 2005. Flexible, integrated watershed modelling with MIKE SHE. in: Singh, V.P., Frevert, D.K. (Eds.), *Watershed Models*. CRC Press, Boca Raton, Florida, USA, pp. 245–271.
- Granier, A., 1987. Evaluation of transpiration in a Douglas-fir stand by means of sap flow measurements. *Tree Physiol.* 3, 309–320. doi:10.1093/treephys/3.4.309
- Grayson, R.B., Western, A.W., Chiew, F.H.S., Blöschl, G., 1997. Preferred states in spatial soil moisture patterns: Local and nonlocal controls. *Water Resour. Res.* 33, 2897–2908. doi:10.1029/97WR02174
- Gupta, H.V., Sorooshian, S., Yapo, P.O., 1999. Status of automatic calibration for hydrologic models: Comparison with multilevel expert calibration. *J. Hydrologic Eng.* 4, 135–143. doi: 10.1061/(ASCE)1084-0699(1999)4:2(135)
- Gupta, H.V., Kling, H., Yilmaz, K.K., Martinez, G.F., 2009. Decomposition of the mean squared error and NSE performance criteria: Implications for improving hydrological modelling. *J. Hydrol.* 377, 80–91. doi:10.1016/j.jhydrol.2009.08.003
- Hammel, K., Kennel, M. (2001): Charakterisierung und Analyse der Wasserverfügbarkeit und des Wasserhaushalts von Waldstandorten in Bayern mit dem Simulationsmodell BROOK90. In: Schriftenreihe des Wissenschaftszentrums Weihenstephan für Ernährung, Landnutzung und Umwelt der technischen Universität München und der bayrischen Landesanstalt für Wald und Forstwirtschaft 185.
- Hao, Z., Singh, V., 2015. Integrating Entropy and Copula Theories for Hydrologic Modeling and Analysis. *Entropy* 17, 2253–2280. doi:10.3390/e17042253
- Harsch, N., Brandenburg, M., Klemm, O., 2009. Large-scale lysimeter site St. Arnold, Germany: analysis of 40 years of precipitation, leachate and evapotranspiration. *Hydrol. Earth Syst. Sci.* 13, 305–317. doi:10.5194/hess-13-305-2009
- Hauck, C., Barthlott, C., Krauss, L., Kalthoff, N., 2011. Soil moisture variability and its influence on convective precipitation over complex terrain. *Q. J. R. Meteorol. Soc.* 137, 42–56. doi:10.1002/qj.766
- Hentschel, R., Bittner, S., Janott, M., Biernath, C., Holst, J., Ferrio, J.P., Gessler, A., Priesack, E., 2013. Simulation of stand transpiration based on a xylem water flow model for individual trees. *Agric. For. Meteorol.* 182–183, 31–42. doi:10.1016/j.agrformet.2013.08.002
- Herbst, M., Diekkrüger, B., 2003. Modelling the spatial variability of soil moisture in a micro-scale catchment and comparison with field data using geostatistics. *Phys. Chem. Earth Parts ABC* 28, 239–245. doi:10.1016/S1474-7065(03)00033-0
- Herbst, M., Diekkrüger, B., Vanderborght, J., 2006. Numerical experiments on the sensitivity of runoff generation to the spatial variation of soil hydraulic properties. *J. Hydrol.* 326, 43–58. doi:10.1016/j.jhydrol.2005.10.036
- Holländer, H.M., Bormann, H., Blume, T., Buytaert, W., Chirico, G.B., Exbrayat, J.-F., Gustafsson, D., Hölzel, H., Krauß, T., Kraft, P., Stoll, S., Blöschl, G., Flüher, H., 2014. Impact of modellers' decisions on hydrological a priori predictions. *Hydrol. Earth Syst. Sci.* 18, 2065–2085. doi:10.5194/hess-18-2065-2014
- Horton, R., 1933. The role of infiltration in the hydrologic cycle. *Trans. Am. Geophys. Union* 14, 446–460.
- Hu, W., Shao, M., Han, F., Reichardt, K., 2011. Spatio-temporal variability behavior of land surface soil water content in shrub-and grass-land. *Geoderma* 162, 260–272. doi:10.1016/j.geoderma.2011.02.008
- Hudson, J.A., Crane, S.B., Robinson, M., 1997. The impact of the growth of new plantation forestry on evaporation and streamflow in the Llanbrynmair catchments. *Hydrol. Earth Syst. Sci.* 1, 463–475. doi:10.5194/hess-1-463-1997

- Huysmans, M., Dassargues, A., 2009. Application of multiple-point geostatistics on modelling groundwater flow and transport in a cross-bedded aquifer (Belgium). *Hydrogeol. J.* 17, 1901–1911. doi:10.1007/s10040-009-0495-2
- Hwang, H.-T., Park, Y.-J., Sudicky, E.A., Forsyth, P.A., 2014. A parallel computational framework to solve flow and transport in integrated surface–subsurface hydrologic systems. *Environmental Modelling & Software* 61, 39–58. doi:10.1016/j.envsoft.2014.06.024
- hydro & meteo GmbH & Co. KG, 2012. Analyse der Radarniederschläge für das hydrologische Jahr 2011. Bericht an den Wasserverband Eifel-Rur.
- Ivanov, V.Y., Fatichi, S., Jenerette, G.D., Espeleta, J.F., Troch, P.A., Huxman, T.E., 2010. Hysteresis of soil moisture spatial heterogeneity and the “homogenizing” effect of vegetation. *Water Resour. Res.* 46, W09521. doi:10.1029/2009WR008611
- Janssen, P.H.M., Heuberger, P.S.C., 1995. Calibration of process-oriented models. *Ecological Modelling* 83, 55–66. doi:10.1016/0304-3800(95)00084-9
- Jin, X., Xu, C.-Y., Zhang, Q., Singh, V.P., 2010. Parameter and modeling uncertainty simulated by GLUE and a formal Bayesian method for a conceptual hydrological model. *J. Hydrol.* 383, 147–155. doi:10.1016/j.jhydrol.2009.12.028
- Jost, G., Schume, H., Hager, H., 2004. Factors controlling soil water-recharge in a mixed European beech (*Fagus sylvatica* L.)–Norway spruce [*Picea abies* (L.) Karst.] stand. *Eur. J. For. Res.* 123, 93–104. doi:10.1007/s10342-004-0033-7
- Kampf, S.K., Burges, S.J., 2007. A framework for classifying and comparing distributed hillslope and catchment hydrologic models. *Water Resour. Res.* 43, W05423. doi:10.1029/2006WR005370
- Kirchner, J.W., 2006. Getting the right answers for the right reasons: Linking measurements, analyses, and models to advance the science of hydrology: *Water Resour. Res.* 42, W03S04. doi:10.1029/2005WR004362
- Kirkby, M.J., 1988. Hillslope runoff processes and models. *J. Hydrol.* 100, 315–339. doi:10.1016/0022-1694(88)90190-4
- Klemes, V., 1983. Conceptualization and Scale in Hydrology. *J. Hydrol.* 65, 1-23. doi:10.1016/0022-1694(83)90208-1
- Kling, H., Gupta, H., 2009. On the development of regionalization relationships for lumped watershed models: The impact of ignoring sub-basin scale variability. *J. Hydrol.* 373, 337–351. doi:10.1016/j.jhydrol.2009.04.031
- Koch, J., Cornelissen, T., Fang, Z., Bogena, H.R., Diekkrüger, B., Kollet, S., Stisen, S. Inter-comparison of three distributed hydrological models with respect to 1 seasonal variability of soil moisture patterns at a small forested catchment. Submitted to *J. Hydrol.* in May 2015.
- Kollet, S.J., Maxwell, R.M., 2008. Capturing the influence of groundwater dynamics on land surface processes using an integrated, distributed watershed model. *Water Resour. Res.* 44, W02402. doi:10.1029/2007WR006004
- Korres, W., Reichenau, T.G., Schneider, K., 2013. Patterns and scaling properties of surface soil moisture in an agricultural landscape: An ecohydrological modeling study. *J. Hydrol.* 498, 89–102. doi:10.1016/j.jhydrol.2013.05.050
- Korres, W., Reichenau, T.G., Fiener, P., Koyama, C.N., Bogena, H.R., Cornelissen, T., Baatz, R., Herbst, M., Diekkrüger, B., Vereecken, H., Schneider, K., 2015. Spatio-temporal soil moisture patterns – A meta-analysis using plot to catchment scale data. *J. Hydrol.* 520, 326–341. doi:10.1016/j.jhydrol.2014.11.042
- Kosugi, K., Fujimoto, M., Katsura, S., Kato, H., Sando, Y., Mizuyama, T., 2011. Localized bedrock aquifer distribution explains discharge from a headwater catchment. *Water Resour. Res.* 47, W07530. doi:10.1029/2010WR009884

- Koyama, C.N., Korres, W., Fiener, P., Schneider, K., 2010. Variability of Surface Soil Moisture Observed from Multitemporal C-Band Synthetic Aperture Radar and Field Data. *Vadose Zone J.* 9, 1014–1024. doi:10.2136/vzj2009.0165
- Kristensen, K.J., Jensen, S.E., 1975. A model for estimating actual evapotranspiration from potential evapotranspiration. *Nordic Hydrol.* 6, 170–188. doi: 10.2166/nh.1975.012.
- Kværnø, S.H., Stolte, J., 2012. Effects of soil physical data sources on discharge and soil loss simulated by the LISEM model. *CATENA.* 97, 137–149. doi:10.1016/j.catena.2012.05.001
- Leader, J.J., 2004. Numerical analysis and scientific computation. Pearson Addison-Wesley, Boston.
- Legates, D.R., McCabe, G.J., 1999. Evaluating the use of “goodness-of-fit” Measures in hydrologic and hydroclimatic model validation. *Water Resour. Res.* 35, 233–241. doi:10.1029/1998WR900018
- Lehmkuhl, F., Loibl, D., Borchardt, H., 2010. Geomorphological map of the Wüstebach (Nationalpark Eifel, Germany)—an example of human impact on mid-European mountain areas. *J. Maps* 6, 520–530. doi:10.4113/jom.2010.1118
- Li, M., Shao, Q., Zhang, L., Chiew, F.H.S., 2010. A new regionalization approach and its application to predict flow duration curve in ungauged basins. *J. Hydrol.* 389, 137–145. doi:10.1016/j.jhydrol.2010.05.039
- Li, Q., Unger, A.J.A., Sudicky, E.A., Kassenaar, D., Wexler, E.J., Shikaze, S., 2008. Simulating the multi-seasonal response of a large-scale watershed with a 3D physically-based hydrologic model. *J. Hydrol.* 357, 317–336. doi:10.1016/j.jhydrol.2008.05.024
- Lussem, U., Waldhoff, G., 2013. Land use classification of 2012 for the Rur catchment. TR32DB. doi:10.5880/TR32DB.9.
- Mahmood, T.H., Vivoni, E.R., 2011. Breakdown of hydrologic patterns upon model coarsening at hillslope scales and implications for experimental design. *J. Hydrol.* 411, 309–321. doi:10.1016/j.jhydrol.2011.10.011
- Maidment, D., 1993. *Handbook of Hydrology.* McGraw-Hill, New York.
- Manfreda, S., McCabe, M.F., Fiorentino, M., Rodríguez-Iturbe, I., Wood, E.F., 2007. Scaling characteristics of spatial patterns of soil moisture from distributed modelling. *Adv. Water Resour.* 30, 2145–2150. doi: 10.1016/j.advwatres.2006.07.009
- Mauder, M., Cuntz, M., Drüe, C., Graf, A., Rebmann, C., Schmid, H.P., Schmidt, M., Steinbrecher, R., 2013. A strategy for quality and uncertainty assessment of long-term eddy-covariance measurements. *Agric. For. Meteorol.* 169, 122–135. doi:10.1016/j.agrformet.2012.09.006
- Maxwell, R.M., 2009. Coupled Surface–Subsurface Modeling across a Range of Temporal and Spatial Scales. *Vadose Zone J.* 8, 823. doi:10.2136/vzj2009.0117
- Maxwell, R.M., Putti, M., Meyerhoff, S., Delfs, J.-O., Ferguson, I.M., Ivanov, V., Kim, J., Kolditz, O., Kollet, S.J., Kumar, M., Lopez, S., Niu, J., Paniconi, C., Park, Y.-J., Phanikumar, M.S., Shen, C., Sudicky, E.A., Sulis, M., 2014. Surface-subsurface model intercomparison: A first set of benchmark results to diagnose integrated hydrology and feedbacks. *Water Resour. Res.* 50, 1531–1549. doi:10.1002/2013WR013725
- McDonnell, J.J., 1990. A Rationale for Old Water Discharge Through Macropores in a Steep, Humid Catchment. *Water Resour. Res.* 26, 2821–2832. doi:10.1029/WR026i011p02821
- Meinen, C., Hertel, D., Leuschner, C., 2009. Biomass and morphology of fine roots in temperate broad-leaved forests differing in tree species diversity: is there evidence of below-ground overyielding? *Oecologia* 161, 99–111. doi:10.1007/s00442-009-1352-7.

- Mendel, H., 2000. Elemente des Wasserkreislaufs: eine kommentierte Bibliographie zur Abflußbildung. Analytica, Berlin.
- Moriasi, D.N., Arnold, J.G., Van Liew, M.W., Bingner, R.L., Harmel, R.D., Veith, T.L., 2007. Model evaluation guidelines for systematic quantification of accuracy in watershed simulations. *Trans Asabe* 50, 885–900.
- Morton, A., Suárez, M., 2001. Kinds of Models. in: Anderson, M.G., Bates, P.D. (Eds.), *Model validation: Perspectives in hydrological science*. Wiley, Chichester, pp. 11–21.
- Mualem, Y., 1976. A new model for predicting the hydraulic conductivity of unsaturated porous media. *Water Resour. Res.* 12, 513–522. doi:10.1029/WR012i003p00513
- Nash, J.E., Sutcliffe, J.V., 1970. River flow forecasting through conceptual models part I—A discussion of principles. *J. Hydrol.* 10, 282–290. doi:10.1016/0022-1694(70)90255-6
- Noh, S.J., An, H., Kim, S., Kim, H., 2015. Simulation of soil moisture on a hillslope using multiple hydrologic models in comparison to field measurements. *J. Hydrol.* 523, 342–355. doi:10.1016/j.jhydrol.2015.01.047
- Oishi, A.C., Oren, R., Stoy, P.C., 2008. Estimating components of forest evapotranspiration: A footprint approach for scaling sap flux measurements. *Agric. For. Meteorol.* 148, 1719–1732. doi:10.1016/j.agrformet.2008.06.013
- Oliver, M.A. (Ed.), 2010. *Geostatistical Applications for Precision Agriculture*. Springer, Heidelberg, London, New York.
- Oudin, L., Andréassian, V., Perrin, C., Michel, C., Le Moine, N., 2008. Spatial proximity, physical similarity, regression and ungaged catchments: A comparison of regionalization approaches based on 913 French catchments. *Water Resour. Res.* 44, W03413. doi:10.1029/2007WR006240
- Pan, F., Peters-Lidard, C.D., 2008. On the Relationship Between Mean and Variance of Soil Moisture Fields. *J. Am. Water Resour. Assoc.* 44, 235–242. doi: 10.1111/j.1752-1688.2007.00150.x
- Panday, S., Huyakorn, P.S., 2004. A fully coupled physically-based spatially-distributed model for evaluating surface/subsurface flow. *Adv. Water Resour.* 27, 361–382. doi:10.1016/j.advwatres.2004.02.016
- Partington, D., Brunner, P., Simmons, C.T., Therrien, R., Werner, A.D., Dandy, G.C., Maier, H.R., 2011. A hydraulic mixing-cell method to quantify the groundwater component of streamflow within spatially distributed fully integrated surface water–groundwater flow models. *Environ. Model. Softw.* 26, 886–898. doi:10.1016/j.envsoft.2011.02.007
- Partington, D., Brunner, P., Frei, S., Simmons, C.T., Werner, A.D., Therrien, R., Maier, H.R., Dandy, G.C., Fleckenstein, J.H., 2013. Interpreting streamflow generation mechanisms from integrated surface-subsurface flow models of a riparian wetland and catchment. *Water Resour. Res.* 49, 5501–5519. doi:10.1002/wrcr.20405
- Patzner, K.M., 2004. *Die Transpiration von Waldbäumen als Grundlage der Validierung und Modellierung der Bestandestranspiration in einem Wassereinzugsgebiet des Flusses 'Ammer'*. Universität München.
- Qu, W., Bogaen, H.R., Huisman, J.A., Vanderborght, J., Schuh, M., Priesack, E., Vereecken, H., 2015. Predicting subgrid variability of soil water content from basic soil information: predict soil water content variability. *Geophys. Res. Lett.* 42, 789–796. doi:10.1002/2014GL062496
- Rahman, M., Sulis, M., Kollet, S.J., 2014. The concept of dual-boundary forcing in land surface-subsurface interactions of the terrestrial hydrologic and energy cycles. *Water Resour. Res.* 50, 8531–8548. doi:10.1002/2014WR015738
- Rawls, W.J., Brakensiek, D.L. 1985. Prediction of soil water properties for hydrologic modeling, in: Jones, E, Ward, T.J. (Eds.), *Proceedings of the symposium watershed management in the eighties*, Denver, pp. 293–399.

- Refsgaard, J.C., Storm, B., 1996. Construction, calibration and validation of hydrological models. in: Abbott, M.B., Refsgaard, J.C. (Eds.), *Distributed hydrological modelling*. Kluwer Academic, Dordrecht, pp. 41-54.
- Richter, D., 1995. Ergebnisse methodischer Untersuchungen zur Korrektur des systematischen Meßfehlers des Hellmann-Niederschlagsmessers. in: *Berichte des Deutschen Wetterdienstes* 194.
- Ringgaard, R., Herbst, M., Friborg, T., 2014. Partitioning forest evapotranspiration: Interception evaporation and the impact of canopy structure, local and regional advection. *J. Hydrol.* 517, 677–690. doi:10.1016/j.jhydrol.2014.06.007
- Robinson, M., Gannon, B., Schuch, M., 1991. A comparison of the hydrology of moorland under natural conditions, agricultural use and forestry. *Hydrol. Sci. J.* 36, 565–577. doi:10.1080/02626669109492544
- Romano, N., 2014. Soil moisture at local scale: Measurements and simulations. *J. Hydrol.* 516, 6–20. doi:10.1016/j.jhydrol.2014.01.026
- Rosenbaum, U., Bogaen, H.R., Herbst, M., Huisman, J.A., Peterson, T.J., Weuthen, A., Western, A.W., Vereecken, H., 2012. Seasonal and event dynamics of spatial soil moisture patterns at the small catchment scale. *Water Resour. Res.* 48, W10544. doi: 10.1029/2011WR011518.
- Rößler, O., Löffler, J., 2010. Potentials and limitations of modelling spatio-temporal patterns of soil moisture in a high mountain catchment using WaSiM-ETH. *Hydrol. Process.* 2182–2196. doi:10.1002/hyp.7663
- Ryu, D., Famiglietti, J.S., 2006. Multi-scale spatial correlation and scaling behavior of surface soil moisture. *Geophys. Res. Lett.* 33, L08404, doi:10.1029/2006GL025831
- Salazar, O., Hansen, S., Abrahamsen, P., Hansen, K., Gundersen, P., 2013. Changes in soil water balance following afforestation of former arable soils in Denmark as evaluated using the DAISY model. *J. Hydrol.* 484, 128–139. doi:10.1016/j.jhydrol.2013.01.036
- Samaniego, L., Kumar, R., Attinger, S., 2010. Multiscale parameter regionalization of a grid-based hydrologic model at the mesoscale. *Water Resour. Res.* 46, W05523. doi:10.1029/2008WR007327.
- Schulla, J., 2015. Model description WaSiM. Available for download (last checked: 03.11.2015): http://www.wasim.ch/downloads/doku/wasim/wasim_2015_en.pdf
- Schume, H., Jost, G., Hager, H., 2004. Soil water depletion and recharge patterns in mixed and pure forest stands of European beech and Norway spruce. *J. Hydrol.* 289, 258–274. doi:10.1016/j.jhydrol.2003.11.036
- Schuermans, J.M., Bierkens, M.F.P., 2007. Effect of spatial distribution of daily rainfall on interior catchment response of a distributed hydrological model. *Hydrol. Earth Syst. Sci.* 11, 677–693. doi:10.5194/hess-11-677-2007
- Schwärzel, K., Menzer, A., Clausnitzer, F., Spank, U., Häntzschel, J., Grünwald, T., Köstner, B., Bernhofer, C., Feger, K.H., 2009. Soil water content measurements deliver reliable estimates of water fluxes: A comparative study in a beech and a spruce stand in the Tharandt forest (Saxony, Germany). *Agric. For. Meteorol.* 149, 1994–2006. doi: 10.1016/j.agrformet.2009.07.006
- Sciuto, G., Diekkrüger, B., 2010. Influence of soil heterogeneity and spatial discretization on catchment water balance modeling. *Vadose Zone J.* 9, 955–969. doi:10.2136/vzj2009.0166
- Shrestha, P., Sulis, M., Masbou, M., Kollet, S., Simmer, C., 2014. A scale-consistent terrestrial systems modeling platform based on COSMO, CLM, and Parflow. *Mon. Wea. Rev.* 142, 3466-3483. doi:10.1175/MWR-D-14-00029.1

- Sidele, R.C., Tsuboyama, Y., Noguchi, S., Hosoda, I., Fujieda, M., Shimizu, T., 2000. Stormflow generation in steep forested headwaters: a linked hydrogeomorphic paradigm. *Hydrol. Process.* 14, 369–385. doi:10.1002/(SICI)1099-1085(20000228)14:3<369
- Simmer, C., Masbou, M., Thiele-Eich, I., Amelung, W., Bogena, H., Crewell, S., Diekkrüger, B., Ewert, F., Franssen, H.-J.H., Huisman, J.A., Kemna, A., Klitzsch, N., Kollet, S., Langensiepen, M., Löhnert, U., Mostaquimur Rahman, A.S.M., Rascher, U., Schneider, K., Schween, J., Shao, Y., Shrestha, P., Stiebler, M., Sulis, M., Vanderborght, J., Vereecken, H., van der Kruk, J., Waldhoff, G., Zerenner, T., 2014. Monitoring and Modeling the Terrestrial System from Pores to Catchments – the Transregional Collaborative Research Center on Patterns in the Soil-Vegetation-Atmosphere System. *Bull. Am. Meteorol. Soc.* 150904101253006. doi:10.1175/BAMS-D-13-00134.1
- Šimůnek, J., van Genuchten, M.Th., Šejna, M., 2005. The HYDRUS-1D software package for simulating the one-dimensional movement of water, heat, and multiple solutes in variably-saturated media. Version 3.0. HYDRUS Softw. Ser. 1. Dep. of Environ. Sci., Univ. of California, Riverside, CA
- Singh, V.P., Woolhiser, D.A., 2002. Mathematical Modeling of Watershed Hydrology. *J. Hydrol. Eng.* 7, 270-292. doi:10.1061/(ASCE)1084-0699(2002)7:4(270)
- Singh, V.P., 2010. Entropy theory for movement of moisture in soils. *Water Resour. Res.* 46, W03516. doi:10.1029/2009WR008288
- Singh, V.P., 2011. Hydrologic Synthesis Using Entropy Theory: Review. *J. Hydrol. Eng.* 16, 421–433. doi:10.1061/(ASCE)HE.1943-5584.0000332
- Sivapalan, M., Kalma, J.D., 1995. Scale problems in hydrology: Contributions of the Robertson Workshop. *Hydrol. Process.* 9, 243–250. doi:10.1002/hyp.3360090304
- Smith, R.E., Woolhiser, D.A., 1971. Overland Flow on an Infiltrating Surface. *Water Resour. Res.* 7, 899–913. doi:10.1029/WR007i004p00899
- Soulsby, C., Tetzlaff, D., Dunn, S.M., Waldron, S., 2006. Scaling up and out in runoff process understanding: insights from nested experimental catchment studies. *Hydrol. Process.* 20, 2461–2465. doi:10.1002/hyp.6338
- Stephan, K., 2003. Möglichkeiten der Aggregation heterogener Eingangsdaten für eine prozessorientierte hydrologische Simulation der Wasserflüsse am Beispiel des Untersuchungsgebietes der Oberen Leine. Universität Bonn. <http://hss.ulb.uni-bonn.de/2003/0192/0192.pdf>
- Stockinger, M.P., Bogena, H.R., Lücke, A., Diekkrüger, B., Weiler, M., Vereecken, H., 2014. Seasonal soil moisture patterns: Controlling transit time distributions in a forested headwater catchment. *Water Resour. Res.* 50, 5270–5289. doi:10.1002/2013WR014815
- Stoltidis, I., Krapp, L., 1980. Hydrological map NRW. 1:25.000, sheet 5404. State Agency for Water and Waste of North Rhine-Westfalia, Düsseldorf.
- Sudicky, E.A., Jones, J.P., Park, Y.J., Brookfield, A.E., Colautti, D., 2008. Simulating complex flow and transport dynamics in an integrated surface-subsurface modeling framework. *Geosci. J.* 12, 107–122. doi:10.1007/s12303-008-0013-x
- Sulis, M., Meyerhoff, S.B., Paniconi, C., Maxwell, R.M., Putti, M., Kollet, S.J., 2010. A comparison of two physics-based numerical models for simulating surface water–groundwater interactions. *Adv. Water Resour.* 33, 456–467. doi:10.1016/j.advwatres.2010.01.010
- Tesemma, Z.K., Wei, Y., Peel, M.C., Western, A.W., 2015. Including the dynamic relationship between climatic variables and leaf area index in a hydrological model to improve streamflow prediction under a changing climate. *Hydrol. Earth Syst. Sci.* 19, 2821–2836. doi:10.5194/hess-19-2821-2015

- Tetzlaff, D., McDonnell, J.J., Uhlenbrook, S., McGuire, K.J., Bogaart, P.W., Naef, F., Baird, A.J., Dunn, S.M., Soulsby, C., 2008. Conceptualizing catchment processes: simply too complex? *Hydrol. Process.* 22, 1727–1730. doi:10.1002/hyp.7069
- Uchida, T., Kosugi, K., Mizuyama, T., 2001. Effects of pipeflow on hydrological process and its relation to landslide: a review of pipeflow studies in forested headwater catchments. *Hydrol. Process.* 15, 2151–2174. doi: 10.1002/hyp.281
- Van Genuchten, M.Th., 1980. A closed-form equation for predicting the hydraulic conductivity of unsaturated soils. *Soil Sci. Soc. Am. J.* 44, 892–898.
- Van Genuchten, M. Th., Nielsen, D.R., 1985. On describing and predicting the hydraulic properties of unsaturated soils. *Annales Geophysicae*, 3, 615-628.
- Vereecken, H., Kamai, T., Harter, T., Kasteel, R., Hopmans, J., Vanderborght, J., 2007. Explaining soil moisture variability as a function of mean soil moisture: A stochastic unsaturated flow perspective. *Geophys. Res. Lett.* 34, L22402. doi:10.1029/2007GL031813
- Vereecken, H., Huisman, J.A., Bogaert, H., Vanderborght, J., Vrugt, J.A., Hopmans, J.W., 2008. On the value of soil moisture measurements in vadose zone hydrology: A review. *Water Resour Res* 44, W00D06. doi:10.1029/2008WR006829
- Verstraeten, W.W., Muys, B., Feyen, J., Veroustraete, F., Minnaert, M., Meiresonne, L., Schrijver, A.D., 2005. Comparative analysis of the actual evapotranspiration of Flemish forest and cropland, using the soil water balance model WAVE. *Hydrol. Earth Syst. Sci.* 9, 225–241. doi:10.5194/hess-9-225-2005
- Viera, A.J., Garrett, J.M., 2005. Understanding interobserver agreement: the kappa statistic. *Fam Med.* 37, 360–363.
- Voeckler, H.M., Allen, D.M., Alila, Y., 2014. Modeling coupled surface water – Groundwater processes in a small mountainous headwater catchment. *J. Hydrol.* 517, 1089–1106. doi:10.1016/j.jhydrol.2014.06.015
- Vrugt, J.A., Gupta, H.V., Bouten, W., Sorooshian, S. 2003. A Shuffled Complex Evolution Metropolis algorithm for optimization and uncertainty assessment of hydrologic model parameters, *Water Resour. Res.* 39, 1201. doi:10.1029/2002WR001642
- Vrugt, J.A., ter Braak, C.J.F., Clark, M.P., Hyman, J.M., Robinson, B.A., 2008. Treatment of input uncertainty in hydrologic modeling: Doing hydrology backward with Markov chain Monte Carlo simulation. *Water Resour. Res.* 44, W00B09. doi:10.1029/2007WR006720
- Waldhoff, G., 2012. Enhanced land use classification of 2008 for the Rur catchment. TR32DB. doi:10.5880/TR32DB.1
- Wang, T., Franz, T.E., Zlotnik, V.A., You, J., Shulski, M.D., 2015. Investigating soil controls on soil moisture spatial variability: Numerical simulations and field observations. *J. Hydrol.* 524, 576–586. doi:10.1016/j.jhydrol.2015.03.019
- Weill, S., Altissimo, M., Cassiani, G., Deiana, R., Marani, M., Putti, M., 2013. Saturated area dynamics and streamflow generation from coupled surface–subsurface simulations and field observations. *Adv. Water Resour.* 59, 196–208. doi:10.1016/j.advwatres.2013.06.007
- Western, A.W., Grayson, R.B., Blöschl, G., 2002. Scaling of soil moisture: a hydrologic perspective. *Annu. Rev. Earth Planet. Sci.* 30, 149–180. doi:10.1146/annurev.earth.30.091201.140434
- Western, A.W., Zhou, S.L., Grayson, R.B., McMahon, T.A., Blöschl, G., Wilson, D.J., 2004. Spatial correlation of soil moisture in small catchments and its relationship to dominant spatial hydrological processes. *J. Hydrol.* 286, 113–134. doi:10.1016/j.jhydrol.2003.09.014
- Willmott, C.J., 1981. On the validation of models. *Phys. Geogr.* 2, 184–194. doi:10.1080/02723646.1981.10642213

- Woolhiser, D.A., 1996. Search for physically based runoff model—A Hydrologic El Dorado. *J. Hydr. Eng.* 122,122–129. doi:10.1061/(ASCE)0733-9429(1996)122:3(122)
- Xu, C.Y., 2002. WASMOD – The water and snow balance modeling system. in: Singh, V.J., Frevert, D.K. (Eds.), *Mathematical Models of Small Watershed Hydrology and Applications*. Water Resources Publications LLC, Highlands Ranch, CO, USA, pp. 555–590.
- Xu, H., Xu, C.-Y., Chen, H., Zhang, Z., Li, L., 2013. Assessing the influence of rain gauge density and distribution on hydrological model performance in a humid region of China. *J. Hydrol.* 505, 1–12. doi:10.1016/j.jhydrol.2013.09.004
- Young, M.H., Caldwell, T.G., Meadows, D.G., Fenstermaker, L.F., 2009. Variability of soil physical and hydraulic properties at the Mojave Global Change Facility, Nevada: Implications for water budget and evapotranspiration. *J. Arid Environ.* 73, 733–744. doi: 10.1016/j.jaridenv.2009.01.015.
- Zacharias, S., Bogena, H., Samaniego, L., Mauder, M., Fuß, R., Pütz, T., Frenzel, M., Schwank, M., Baessler, C., Butterbach-Bahl, K., Bens, O., Borg, E., Brauer, A., Dietrich, P., Hajsek, I., Helle, G., Kiese, R., Kunstmann, H., Klotz, S., Munch, J.C., Papen, H., Priesack, E., Schmid, H.P., Steinbrecher, R., Rosenbaum, U., Teutsch, G., Vereecken, H., 2011. A Network of Terrestrial Environmental Observatories in Germany. *Vadose Zone J.* 10, 955. doi:10.2136/vzj2010.0139
- Zehe, E., Gräff, T., Morgner, M., Bauer, A., Bronstert, A., 2010. Plot and field scale soil moisture dynamics and subsurface wetness control on runoff generation in a headwater in the Ore Mountains. *Hydrol. Earth Syst. Sci.* 14, 873–889. doi:10.5194/hess-14-873-2010
- Zhang, Y., Wegehenkel, M., 2006. Integration of MODIS data into a simple model for the spatial distributed simulation of soil water content and evapotranspiration. *Remote Sens. Environ.* 104, 393–408. doi:10.1016/j.rse.2006.05.011

Further Acknowledgements

MODIS LAI data were taken from: Land Processes Distributed Active Archive Center (LP DAAC), 2003-2013, Leaf Area Index - Fraction of Photosynthetically Active Radiation 8-Day L4 Global 1km (MOD15A2): NASA EOSDIS Land Processes DAAC, USGS Earth Resources Observation and Science (EROS) Center, Sioux Falls, South Dakota (<https://lpdaac.usgs.gov>), accessed April 17, 2014.

Measurement and processing of eddy covariance and precipitation data of the Rollesbroich test site were provided by Marius Schmidt from the central service project Z3 of the TR32 project.

Web References

Variogramfit-function for MATLAB:

<http://www.mathworks.com/matlabcentral/fileexchange/25948-variogramfit> (last checked on 13/11/13).

Chu, D., 2004. The GLOBEC Kriging Software Package. Wood Hole Oceanographic Institution. http://globec.whoi.edu/software/kriging/easy_krig/easy_krig.html (last checked on 13/11/13).